

NARROWBAND PASSIVE SYSTEMS THEORY WITH APPLICATIONS
TO POSITIONING AND NAVIGATION

by

JOSÉ MANUEL FONSECA DE MOURA
Engenheiro Electrotécnico, Instituto Superior Técnico,
Universidade Técnica de Lisboa
(1970)

M.S., Massachusetts Institute of Technology
(1973)

E.E., Massachusetts Institute of Technology
(1973)

SUBMITTED IN PARTIAL FULFILLMENT OF THE REQUIREMENTS
FOR THE DEGREE OF DOCTOR OF SCIENCE
at the
MASSACHUSETTS INSTITUTE OF TECHNOLOGY
June, 1975

Signature of Author ~~Jose Manuel Fonseca de Moura~~
Department of Electrical Engineering and Computer Science

Certified by ~~Walter D. Sullivan~~ Thesis Supervisor

Accepted by ~~Walter D. Sullivan~~
Chairman, Departmental Committee on Graduate Students



NARROWBAND PASSIVE SYSTEMS THEORY WITH
APPLICATIONS TO POSITIONING AND NAVIGATION

by

JOSÉ MANUEL FONSECA DE MOURA

Submitted to the Department of Electrical Engineering and Computer Science on April 7, 1975 in partial fulfillment of the requirements for the Degree of Doctor of Science.

ABSTRACT

This thesis considers the passive tracking problem with narrowband and linear constraints on geometry and motion.

In Part I we develop a model explicitly exhibiting the nonhomogeneous received wavefield structure induced by the spatial baseline (e.g. observer's array) and/or temporal diversity (e.g. source motion). The model encompasses the basic phenomena of many practical situations, and is sufficiently simple to lend itself to analytical studies.

We pursue the fundamental question of global parameter identifiability (with emphasis on passive ranging), examine the structure, and global and local performance of the optimal and suboptimal receivers, and, by considering two limiting geometries (distant and close observer), derive analytical intuitively pleasing expressions bounding the mean square performance. We study the issues of spatial/temporal factorability and coupling, focussing on the implications of the processing complexity and identifiability nonsingularity.

In Part II, we develop a practical hybrid solution to the passive tracking problem, which achieves a compromise between global parameter identifiability and receiver complexity, and analyse the Hybrid Algorithm's behavior and sensitivity to the underlying modeling assumptions (linear path perturbations). We apply the preceding theory on passive tracking to positioning (air traffic control, underwater acoustics) and navigation (orbiting and geostationary satellites), discussing in detail the tradeoffs among attainable accuracies, geometry, and statistical parameters.

Finally, we present Monte Carlo simulations showing the existence of regions of convergence for the theoretical and simulated results.

THESIS SUPERVISOR: Arthur B. Baggeroer
TITLE: Associate Professor of Electrical and Ocean
Engineering

DEDICATION

To My Parents

Maria José Fonseca de Moura

and

José Saraiva de Moura

ACKNOWLEDGEMENTS

I would like to express my gratitude to several people:

Prof. A. B. Baggeroer, for his advice and support throughout my stay at M.I.T.. The inumerous technical discussions we had, greatly contributed to shape and develop this work.

Dr. K. Senne who, as a reader, I met frequently for the last two and a half years; his knowledge and advice had a direct influence in the evolution of the thesis.

Prof. H. L. Van Trees, whose original interest first intröduced me to the subject.

Prof. A. Willsky, for his willingness to serve as a reader, and for his many useful comments.

My former officemate, Prof. Jose' P. Albuquerque, from Pontificia Universidade Católica, Brasil, whose companionship made easier, in all regards, the first three years at M.I.T.

My officemates, K. Theriault (whom I bothered with all sorts of questions, and who read part of the manuscript), R. Pusey, L. Metzger, and S. Robinson for the many interesting discussions.

Eleanor Montesano, who typed most of the thesis; Diane Eulain, and my wife Teresa for helping with the typing. Phyllis Handle (from the R.L.E. Drafting Room) and Margie Streeter for making the drawings and technical

illustrations. Their expertise improved enormously the readability of the manuscript.

My parents, for their continued love and support.

My wife Teresa and my daughter Barbara for all they have given me.

I also want to acknowledge the following organizations:

Information Processing Center and Project Mac (and its Macsym program) at M.I.T.;

Instituto de Alta Cultura, and Instituto Superior Técnico for having provided the financial means, supporting my graduate education at M.I.T..

TABLE OF CONTENTS

	Page
TITLE PAGE	1
ABSTRACT	2
ACKNOWLEDGEMENT	4
TABLE OF CONTENTS	7
LIST OF TABLES	14
LIST OF FIGURES	14
LIST OF SYMBOLS AND ABBREVIATIONS	22
Part I	
GLOBAL ACQUISITION VIA MAXIMUM LIKELIHOOD TECHNIQUES	25
Chapter I	
MOTIVATION . MODEL . SYNOPSIS	26
1. Introduction	26
2. Positioning and Navigation	27
3. Model	29
4. Perspective of Present Work in Relation to Other's on Passive Tracking. Synopsis	33
Chapter II	
SYNTHETIC ARRAYS WITH STATIONARY SOURCES (SASS)	37
1. Geometric Model	38
1.1 Stationary Array-Stationary Source ..	40
1.2 Moving Array-Stationary Source	41
2. Receiver Design	48
3. Generalized Ambiguity Function	53
3.1 Approximate Analysis of GAF	59
3.2 General Case	65

	Page
4.	Performance Analysis 73
4.1	Cramer-Rao Performance Analysis 78
4.1.1	Short Observation Interval Analysis of the Cramer-Rao Bounds 82
4.1.2	Asymptotic Behavior of the Cramer- -Rao Bounds 88
4.1.3	Very Long Baseline Staved Array 96
4.1.4	Graphical Representation of the Cramer-Rao Bounds 99
4.2	Global Performance 103
4.2.1	$E (A_{j\epsilon}^2 \epsilon)$ 105
4.2.2	Probability of a Diversion 106
4.2.3	$E (A_{j\epsilon}^2 \epsilon^c)$ 109
4.2.4	Performance Graphical Analysis 111
4.3	Limiting Behavior of the ML-Algorithm 116
Chapter III	STATIONARY (OMNIDIRECTIONAL) ARRAYS WITH MOVING SOURCES (SAMS ₀) 120
1.	Model 121
2.	Receiver Design 127
3.	Generalized Ambiguity Function 129
3.1	Polynomial Approximations to the Range Phase Difference 131
3.2	General Case 137
4.	Performance Analysis 145
4.1	Short Observation Interval Analysis (Distant Observer) 147
4.1.1	Full SAMS ₀ Problem 147
4.1.2	Range Angle Estimation (SASS) 158

	Page
4.1.3 Range Velocity Estimation - - Applications to Navigation	159
4.1.4 Velocity Angle Estimates	162
4.2 Long Observation Interval Analysis (Close Observer)	164
4.3 Graphical Display of the Cramer-Rao Bounds	166
4.4 Global Performance	172
4.4.1 Probability of Error and Total Number of Grid Cells	173
4.4.2 Graphical Analysis of the Total Performance Bounds	178
4.5 Asymptotic Behavior of the ML-Algorithm	180
Chapter IV SYNTHETIC ARRAY WITH MOVING SOURCE (SAMS)	183
1. Model	184
2. Receiver Structure	188
3. Decoupled Spatial Temporal SAMS Structure	193
3.1 Ambiguity Structure	195
3.2 Computation of the Inverse of the Mean Square Spread Matrix	201
4. Coupled Spatial Temporal SAMS Structure	207
4.1 Ambiguity Structure	211
4.1.1 Asymptotic Behavior	212
4.1.2 Coupled Ambiguity Structure	214
4.2 Mean Square Spread Matrix	229
4.2.1 Det M	230

	Page
4.2.2	Mean Square Parameters Spread 235
4.2.3	Parameter-Errors Cross Correlations 240
	Summary of the Chapter 247
Part II	APPLICATIONS TO POSITIONING AND NAVIGATION 249
Chapter V	THE HYBRID ALGORITHM : A PRACTICAL SOLUTION TO THE PASSIVE TRACKING ... 250
1.	Hybrid Algorithm 251
2.	Global Acquisition 254
3.	Phase Tracker 255
3.1	Random Accelerations Motion Model .. 256
3.2	Linearized Mathematical Equivalent to the Extended Kalman-Bucy Filter . 258
3.3	Linearized Decoupled Range Loop 261
3.4	EKB Linearized Performance Versus ML-Performance 265
3.5	EKB Nonlinear Behavior 267
4.	Sensitivity of ML-Global Acquisition to Path Perturbations 274
5.	Hybrid Algorithm Error Analysis 279
6.	Regions of Behavior for the Hybrid Algorithm 280
Chapter VI	APPLICATIONS TO NAVIGATION AND POSITIONING. SIMULATION 285
1.	Air Traffic Control Precision Landing 286
1.1	Problem Description 286
1.2	Hybrid Algorithm 289
1.2.1	Model 289

	Page
1.2.2 Nominal Parameter Values	290
1.2.3 Review of ML-Performance Results ...	291
1.3 ML-System Curves	294
1.4 Related Hybrid Algorithm Issues	299
1.4.1 Sensitivity of the ML-Receiver to Path Perturbations	299
1.4.2 Extended Kalman-Bucy Linearized Performance	300
1.4.3 Average Time for Cycle Skipping	301
1.5 Conclusion	301
2. Passive Positioning Via Underwater Acoustics	305
2.1 Underwater Acoustic Model	305
2.2 Nominal Parameter Values	308
2.3 Review of ML-Mean Square Performance Results	309
2.4 ML-System Curves	310
2.5 Linearized Performance of Extended Kalman-Bucy Filter	317
2.6 RMS Range Phase Variation and Cycle Skipping	318
2.7 Summary	321
3. Precision Navigation Via Satellites and other Navigational Aids	322
3.1 Orbiting Satellites	324
3.2 Geostationary Satellites	327
3.2.1 Discrete Ambiguity Function in the Fresnel Zone	329
3.2.2 Discrete Mean Square (Local) Performance in the Fresnel Zone	332

	Page
3.3	Discrete Ambiguity and Performance for Geostationary Satellites 334
3.4	Global Acquisition Strategy for a Constellation of Geostationary Satellites 336
3.5	Commercial Avionics Surveillance with Geostationary Satellites 340
3.5.1	Model Consideration 342
3.5.2	ML-Mean Square Performance 343
3.5.3	ML-System Discussion 344
3.5.4	Extended Kalman-Bucy Filter Perfor- mance 348
	Conclusion 350
4.	Monte Carlo Simulation Results 352
4.1	Algorithms Implementation 353
4.2	Confidence Intervals Associated with Statistical Averages 354
4.3	Simulation Results 355
Chapter VII	CONCLUSIONS . EXTENSIONS 360
1.	Conclusions 360
2.	Extensions 365
	BIBLIOGRAPHY 368
Appendix A	GENERALIZED AMBIGUITY FUNCTION 373
1.	Introduction 373
2.	Polynomial Approximation 375
2.1	Linearized Analysis 375
2.2	Quadratic Analysis 377
2.2.1	Radial Acceleration GAF Type 283

	Page
2.2.2 General Quadratic GAF	386
2.3 Third Order Approximation	391
2.4 General Expression of GAF	395
Appendix B MEAN SQUARE SPREAD MATRIX COMPUTATION	398
Appendix C ASYMPTOTIC BEHAVIOR OF THE MEAN SQUARE SPREAD MATRIX	405
1. General Derivation	405
2. Limiting Behavior of Diagonal Elements	410
3. Limiting Behavior of Principal Minors	411
4. SAMS ₀ - Mean Square Spread Matrix ...	415
5. Very Long Baseline Interferometry (Range/Bearing)	416
Appendix D TAYLOR SERIES APPROXIMATION TO 4 - -DIMENSIONAL SAMS-MEAN SQUARE SPREAD MATRIX	421
Biographical Note	426

LIST OF TABLES

		Page
IV-1	Spatial Quadratic Parameter's Definition	217
V-1	Regions of Behavior for the Hybrid Algorithm	281
VI-1	Numerical Values for Precision Landing	291
VI-2	Root Mean Square Path Variation	300
VI-3	Nominal Values for Passive Acoustic Positioning	308
VI-4	Data on Navigational Satellites	324
VI-5	Nominal Values for Commercial Avionics Surveillance	342
VI-6	Simulated Configuration Parameters	355

LIST OF FIGURES

I-1	Typical Navigational Configurations	28
I-2	Passive Sonar	29
I-3	Passive Tracking Global Geometry	31
I-4	Doppler Type Modulations	34

LIST OF FIGURES (cont.)

	Page
II-1 Planar Geometry for a Stationary Source	38
II-2-a Stationary Array-Stationary Source Geometry	40
II-2-b Moving Array-Stationary Source Configuration	42
II-3 Modulations on Temporal Signal Structure	44
II-4 Source in Far-Field (Linear Approximation)	45
II-5 Source in Fresnel Zone (Quadratic Approximation)	46
II-6 Coarse Search ML-Algorithm	52
II-7 (3-Dim.) Range/Angle Ambiguity Structure ($X=1/4$)	58
II-8 (Contour) Range/Angle Ambiguity Structure ($X=1/4$)	58
II-9 Linearized Ambiguity Sinc Function	60
II-10 Quadratic (Fresnel) Ambiguity Structure With Local/Asymptotic Approximations	62
II-11 Cornu Spiral	62
II-12 Line of Sight Definition for 3-Dimensional Plots	66
II-13 (3-Dim.) Range/Angle Ambiguity Structure ($X=1/40$)	67
II-14 (Contour Range/Angle Ambiguity Structure ($X=1/40$))	67
II-15 Range/Angle Ambiguity Structure ($X=6$)	68
II-16 Geometric Interpretations of X Parameter	80
II-17 Asymptotic Behavior of Single Mean Square Spread Matrix, SASS parameter	91
II-18 Asymptotic Behavior of Mean Square Spread Matrix Range Parameter (SASS)	91

	Page
II-19 Asymptotic Behavior of MSSM Angle Parameter (SASS)	91
II-20 Asymptotic Behavior of Cross-Correlation for SASS Parameters	91
II-21 Long Baseline (3-Element) Staved Linear Array	97
II-22 Inverse Range Mean Square Spread Versus X	100
II-23 Inverse Angle Mean Square Spread Versus X	100
II-24 Range/Angle Cross-Correlation Versus X	100
II-25 Range Standard Deviation Versus X	102
II-26 Angle Standard Deviation Versus X	102
II-27 Range Standard Deviation Versus Bearing Angle	102
II-28 Probability of Diversion Versus Sign. En/ Noise Ratio	110
II-29 Probability of Diversion Versus Total Number of Cells	110
II-30 Det M versus X	114
II-31 Probability of Diversion versus X	110
II-32 Total Range Mean Square Error Versus X	114
II-33 Total Angle Mean Square Error Versus X	114
III-1 (Eliminated)	-
III-2 Stationary Array/Moving Source	123
III-3 Integral of $\cos X^3$ Versus Integration Interval	133
III-4 Squared Generalized 3th Sinc Functions	133
III-5 Squared Generalized Sinc Functions up to 3th Order	133
III-6 Viewing Angles for 3-Dimensional Plots	137

	Page	
III-7	Same as II-7	58
III-8	Same as II-8	58
III-9	(3-Dim.) Range/Velocity Ambiguity Structure (X=1/4)	138
III-10	(Contour) Range/Velocity Ambiguity Structure (X=1/4)	138
III-11	(3-Dim.) Velocity/Angle Ambiguity Structure (X=1/4)	139
III-12	(Contour) Velocity/Angle Ambiguity Structure (X=1/4)	139
III-13	(3-Dim.) Range/Velocity Ambiguity Structure (X=1/16)	141
III-14	(3-Dim.) Range/Velocity Ambiguity Structure (X=1/16)	141
III-15	(Contour) Range/Velocity Ambiguity Structure (X=1/16)	141
III-16	Main Lobe Ellipsoidal Structure	143
III-17	(Cramer-Rao Bound) Equivalent Range Performance Geometries	156
III-18	Satellite Tracking Geometry	159
III-19	Doppler Configuration	165
III-20	Range Mean Square Spread Versus X	167
III-21	Angle Mean Square Spread Versus X	167
III-22	Speed Mean Square Spread Versus X	167
III-23	Cross Correlation Versus X	169
III-24	Range Cramer-Rao Bound Versus Bearing	169
III-25	Speed and Angle Cramer-Rao Bound Versus Bearing	169
III-26	Range Cramer-Rao Bound Versus Range (X=cte)	171
III-27	Cross-Correlation Versus Bearing	171

	Page
III-28 Det M Versus X	176
III-29 Probability of a Diversion X	171
III-30 Speed Total ML-Performance Versus X	179
III-31 Angle Total ML-Performance Versus X	179
III-32 Range Total ML-Performance Versus X	179
IV-1 Stationary Array/Moving Source (a) Positioning (b) Navigation	183
IV-2 SAMS-Planar Geometry	186
IV-3 Ambiguity Resolution of Signs of V and Sin θ_t in SAMS	188
IV-4 Time Varying Spatial Structure	194
IV-5 Sequential Beam Steering	196
IV-6 Source Dynamics Within a Resolution Cell of the Linear Array	199
IV-7 Decoupled Receiver Structure	200
IV-8 Spatial Temporal Coupled Curvature	208
IV-9 Geometry	208
IV-10 Range Function Decomposition	210
IV-11 Locus on $\nabla_{v\theta_t}$	222
IV-12 Reduction of Double to Single Integration	226
IV-13 (a) Equivalent SASS Problem (b) Triangular Shading	228
IV-14 Cross-Coupling. Dependence on θ_t -angle	234
IV-15 Spatial/Temporal Symmetric and Parallel Configuration	242
IV-16 (Closest Approach) SAMS Geometry	243
IV-17 Range/Velocity Cross-Correlation Versus $\cos\theta_\ell$ (Closest Approach Geometry)	243

	Page	
IV-18	SAMS Parallel Geometry	245
IV-19	Range/Velocity Cross-Correlation Versus X_1 (Paralell Geometry)	245
V-1	Absolute Phase Evolution	252
V-2	Global Acquisition/Tracking Hybrid Algorithm	253
V-3-a	EKB-Mathematical Model (Polar Coordinates)	259
V-3-b	EKB-Decoupled Structure	259
V-4	Mathematical Equivalent for Signal Source Channel and EKB Range Loop	260
V-5	EKB Decoupled Range Loop: (a) Phase Lock Range Loop (b) F(s) Block Diagram	263
V-6	EKB Range "Lock in" Points	266
V-7	EKB Simulation Results	268
V-8	Cycle-Skipping Phenomena	269
V-9	Average Time for Cycle Skipping Versus SNR for several values of Q	272
V-10	Root Mean Square Range Path Variation Versus Acquisition Time, for several values of Q	272
V-11	Decomposition of the Mean Square Error at the ML-Processor Output	278
V-12	Typical Regions of Behavior for Hybrid Algorithm	282
V-13	Hybrid Algorithm	284
VI-1	Landing Geometry	287
VI-2	3-Dimensional Ambiguity Associated with Single Linear Array	288
VI-3	Precision Landing Geometry	289
VI-4	Range Accuracy Versus SNR	296

	Page	
VI-5	SNR Versus Range	296
VI-6	Acquisition Time Versus Range for two Range Accuracy Requirements	296
VI-7	Speed Accuracy Versus SNR	296
VI-8	Practical Solution to Passive Landing	302
VI-9	Range Accuracy (Two Different Flight Turbulence Conditions) Versus Acquisition Time	303
VI-10	Underwater Acoustic Geometries	306
VI-11	Mean Square Performance Versus SNR ($SAMS_0$)	312
VI-12	Mean Square Performance Versus A priori Range Uncertainty	312
VI-13	SNR Versus Range	312
VI-14	Range Performance Versus SNR (SASS)	315
VI-15	Range Performance Versus A priori Range Uncertainty	315
VI-16	SNR Versus Range	315
VI-17	Range Performance Versus Range	315
VI-18	EKB Mean Square Performance Versus SNR	312
VI-19	Underwater Acoustic Positioning Modes of Behavior	320
VI-20	Orbiting Satellite With Moving Platform Geometry	325
VI-21	Range Accuracy Versus Acquisition Time for Ship Navigation Satellite Problem	326
VI-22	Moving Platform / Geostationary Satellites	328
VI-23	Discrete SASS	329
VI-24	DGAF for an Over Sampled Array	332

		Page
VI-25	Commercial Avionics Surveillance with Geostationary Satellites	340
VI-26	Number of Updates Versus Apriori Range Uncertainty	345
VI-27	Speed Accuracy Versus Acquisition Time	348
VI-28	SASS - Simulation Results	356
VI-29	SAMS _o - Simulation Results	357
A-1	Complex Impulse Response of Complex Filter	379
C-1	Long Baseline (3-element) Staved Linear Array	416

LIST OF ACRONYMS . NOTATION

A = parameter vector

$A_i(.)$ = Airy Function

$A_o = \begin{bmatrix} R_o \\ v_o \\ \text{Sin } \theta \end{bmatrix}$ = parameter vector associated with SAMS_o

$A_s = \begin{bmatrix} R_o \\ \text{Sin } \theta \end{bmatrix}$ = parameter vector associated with SASS

α = signal to noise ratio in noise band with loop

\tilde{b} = complex Rayleigh parameter

B_L = noise bandwidth of PLL

C = wave propagation speed

$\Delta A_i = A_i - \bar{A}_i$

$\Delta_M A_i = A_{i_{\text{Max}}} - A_{i_{\text{min}}} = \text{apriori uncertainty associated with parameter } A_i$

\bar{E}_r = average received energy

ϵ = event that a decision error occurred

ϵ^{ML} = errors associated with ML-receiver

ϵ^{EKB} = errors associated with EKB

EKB = Extended Kalman-Bucy Filter

f = carrier frequency

FIM = Fisher Information Matrix

F(.) = Fresnel Integral

$\phi(A, \bar{A})$ = Generalized Ambiguity Structure

G = Energy to Noise Ratio Gain

GAF = Generalized Ambiguity Function

HA = Hybrid Algorithm

J = Fisher Information Matrix
 \bar{J}_r = average frequency for cycle skipping
 t = space dimension
 L = array length
 $\tilde{L}(A, \bar{A})$ = log - ML - function
 λ = wavelength = c/f
 M = total number of grid cells
 M = mean square spread matrix = MSSM
 ML = Maximum Likelihood
 N_o = Measurement Noise Level
 P = radiated power
 P_{ii} = (i,i) element of error covariance propagated by Riccati equation
 $\frac{2P}{N_o}$ = signal to noise ratio
 PLL = Phase Locked Loop
 ψ = random component of phase incoherent model
 $\psi(A, \bar{A})$ = signal autocorrelation function
 Q = driving noise power level
 $R(t, \mathbf{l}), R(t), R(\mathbf{l})$ = range function
 R_o = range parameter
 ρ_{ij} = error cross-correlation
 $SAMS$ = Synthetic Array/Moving Source
 $SAMS_o$ = Stationary Array with Omnidirectional sensor/Moving Source
 $SASS$ = Synthetic Array / Stationary Source
 SNR = Signal to Noise Ratio

$\Sigma_R^{1/2}$ = root mean square range path variation

Σ_R = mean square path variation

$2\sigma_b^2$ = Rayleigh parameter standard deviation

Δ_{gl} , Δ_{loc} , Δ_{tot} = global, local, total root mean square performance bound

T = Total observation time interval

T_{acq} = acquisition time

$T_{skp} = J_R^{-1}$ = average time between cycle skips

TS = Taylor Series

θ_l , θ_t , θ = spatial, temporal, bearing angles

$u(t)$ = driving noise

V = source speed

VT = source travel

$w(t)$ = measurement noise

WF = Wave Front

$W_c = 2\pi f$

Ω = parameter space

X = diversity parameter = $\frac{L}{2R_o}$ or $\frac{VT}{2R_o}$

Y = $\frac{1}{X}$

Z = L or VT

PART I

GLOBAL ACQUISITION VIA MAXIMUM
LIKELIHOOD TECHNIQUES

- Chapter I MOTIVATION . MODEL . SYNOPSIS
- Chapter II SYNTHETIC ARRAYS WITH STATIONARY SOURCES
 (SASS)
- Chapter III STATIONARY (OMNIDIRECTIONAL) ARRAYS WITH
 MOVING SOURCES (SAMS₀)
- Chapter IV SYNTHETIC ARRAY WITH MOVING SOURCE (SAMS)

Chapter I

MOTIVATION.MODEL.SYNOPSIS

1. Introduction

Passive situations, where no use of an active radar or sonar is involved, arise in a variety of fields: In Oceanography, when locating drifting buoys collecting meteorological, oceanographic or ocean floor earthquake data [Wes72],[Por73],[Spi74]; in Meteorology, when tracking radiosondes, or balloon-borne devices measuring the wind of the upper atmosphere [Ack72],[Beu72],[IEE75]; in passive sonar, when positioning submersibles (animals, ships, or instrumentation) in the ocean and on the ocean floor [Bas72]; in Navigation, when obtaining a position fix, by processing the signals emitted by a beacon, or a satellite, [Beu74], [Fio70], [McD73]; in Radioastronomy, when sensing the natural radiation from distant celestial objects or the coherent emission from man-made satellites [Cou73]; in Air Traffic Control when processing the signals transmitted from an airplane.

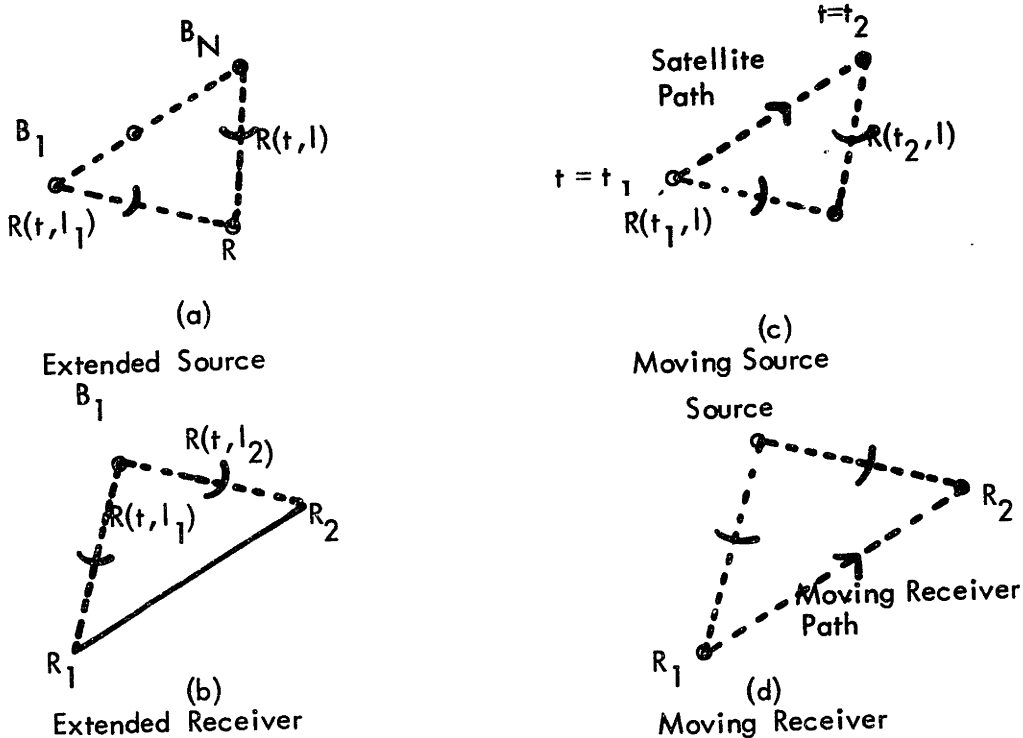
In all these practical applications one faces the problem of locating a moving or stationary source from noisy observations of the source signature. This thesis is concerned with the analysis and design of receivers for these passive estimation problems, for which the available measure-

ments are the radiations emitted by the source itself.

2. Positioning and Navigation

In the above applications one is interested in determining the relative source/receiver geometry. The ultimate geographical location of both can then be found from the a priori knowledge of the absolute position of either. We classify the passive tracking as a navigation or a positioning problem if it is the receiver's or the source's location, respectively, that is to be determined.

Figure 1 shows some typical navigational configurations. The basic characteristic of (a) and (b) is the spatial separation or baseline either at the source (beacons B_1 to B_N), or at the receiver. In (c) and (d) this separation is synthetically generated in time by the source and/or receiver motions. In the two former cases the configuration is stationary, not changing significantly during the time observation interval; the navigation problem is solved from the modifications induced on the signals by the overall spatial diversity; in the two latter cases the signal is modulated by the relative dynamics. In general, due to the non-negligible source and/or receiver spatial extent and the relative dynamics, one will have a coupled spatial and temporal diversity signal structure.



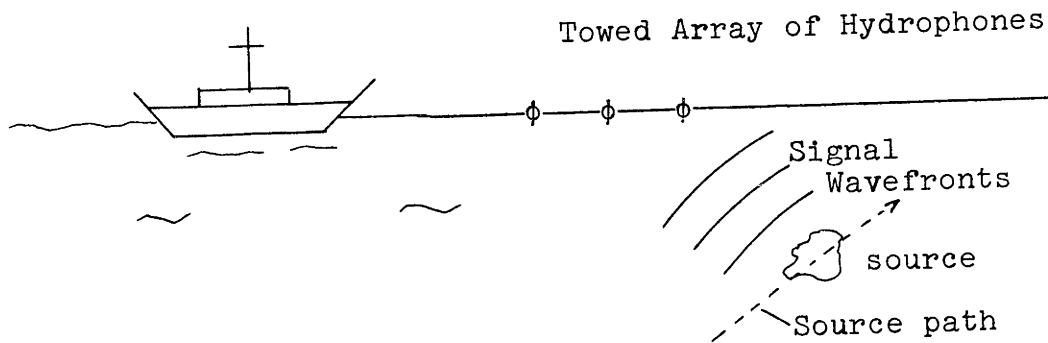
Typical Navigational Configurations

Figure 1

To each one of the navigational geometries there corresponds a twin positioning geometry, where a stationary or moving receiver tracks a stationary or moving source. Given the dualism, we restrict the discussion most of the time to positioning configurations alone. We concentrate on the fundamental aspects, common to all problems, of source/receiver parameter identifiability, of optimal and suboptimal receivers design, and of performance analysis.

3. Model

Figure 2 illustrates the passive tracking problem on a sonar context. A moving source (MS) emits some type of



Passive Sonar

Figure 2

radiation (source signature) which propagates through the surrounding medium and is sensed by the receiving devices, hereafter called sensors or array elements.

The source signature is either random or deterministic in nature, and depends on both time and space. The global geometry and the relative source/receiver dynamics affect the spatial and temporal field distribution characteristics; they induce modulations on the spatial and temporal signal structure, as reflected, at distinct points in space and instants in time, by differences of arrival times (delays), of measured frequency content (Doppler), of signal strength

(spherical spreading,attenuation). If the source signature is structurally known, the passive tracking relates to a (stochastic) decision upon the source energy distribution function, as sensed by the receiver, on a space/time domain, or on its Fourier dual, a wavenumber/frequency space.

There are two modelling issues: The first involves the wavefield's structure, while the second concerns the global geometry and the relative dynamics.

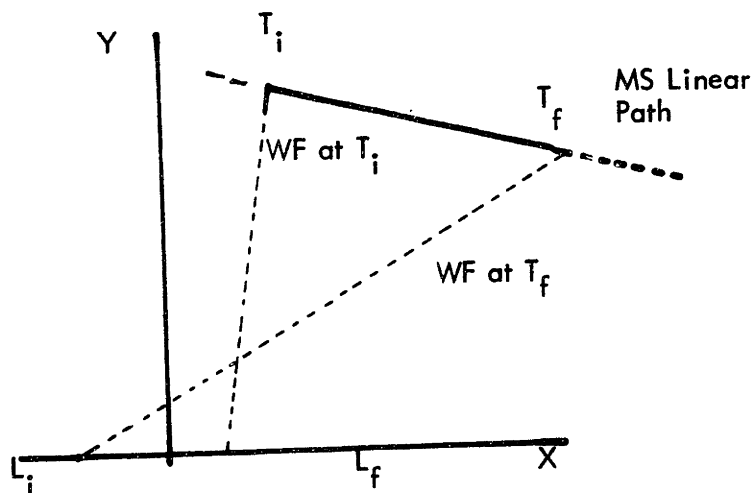
This thesis is restricted to a simple class of random wavefields, namely that of narrowband signals multiplied by a Rayleigh-Gaussian random parameter. The signals are imbedded in an additive, spatially homogeneous, temporally white Gaussian noise process. This Rayleigh-Gaussian parameter reflects, besides propagation losses and other model inaccuracies, the fundamental constraint of lack of absolute phase reference. As a consequence, the passive tracking is to be achieved from the higher order phase modulations and not from the absolute phase reference (travel time delay).

We assume a planar geometry with linear constraints, i.e.:

i) The receiving aperture either is omnidirectional or is a linear structure;

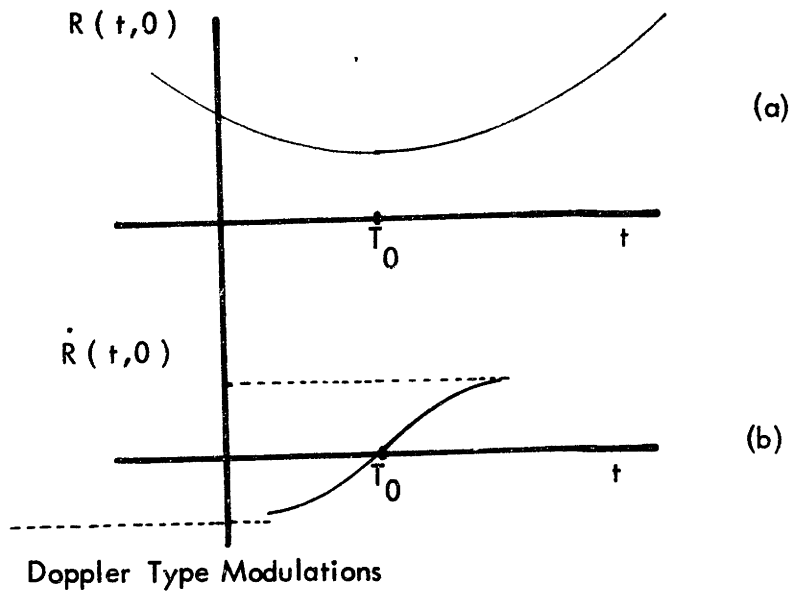
ii) The source/receiver dynamics are either stationary (no relative motions) or linear, e.g. the source follows a deterministic constant-speed linear path, as displayed in

Figure 3. In Chapter V we discuss a more realistic model, where this nominal linear path is disturbed by random accelerations.



Passive Tracking Global Geometry
Figure 3

With the above assumptions the resulting wavefield distribution exhibits in time and space a "narrowband" modulated structure, and thus is temporally nonstationary and spatially inhomogeneous. With reference to Figure 3, the distance between the source and the linear array's geometric center assumes the parabolic form of Figure 4a, thereby inducing the time varying Doppler of Figure 4b.



Doppler Type Modulations
Figure 4

At the point T_0 of stationary Doppler (closest point of approach) the line defined by the array's geometric center and the source is normal to the path. Many practical positioning and navigation techniques are based on this elementary observation.

Although the ideal tracking system would use all the available information conveyed by the received wavefields, we concentrate the analysis on the phase modulations of the narrowband signals, ignoring in particular the observed changes in the signal strength occurring either across the extended receiving aperture, or during the finite time observation interval. These are only of practical significance when, for example, the total array dimensions are much larger

than the source/receiver separation, representing higher order corrections not pursued here. The passive tracking reduces then to a (nonlinear) phase demodulation problem.

4. Perspective of Present Work in Relation to Other's on Passive Tracking. Synopsis

The narrowband passive tracking has received considerable treatment in the literature, e.g. [Bas72], [Kol68], [Mac69]. Most of the work makes three important simplifying assumptions:

S1: Planar Wavefronts: The curvature of the incoming wavefronts is assumed linear (either at a global or local level);

S2: Decoupling: The spatial and temporal aspects are decoupled;

S3: Finite Parameter Context: The relative source/receiver dynamics are stationary or deterministic.

Under S1 through S3 the problem reduces to a "bearings only" situation, where the observable source/receiver parameter is the bearing angle, and/or the source (radial) velocity. Ranging is accomplished by either an auxiliary active system, or by ad hoc procedures like simple triangulation or Doppler counting.

To our knowledge, only recently, [Ban71], [Ban73], some preliminary analytical work with the (spatial) curvature of the wavefronts has been reported. We further note that inhomogeneous fields have received little attention in other applied areas. Of course an exception to this is Optics [IEE74], where quadratic type approximations to the wavefront curvature are common in Fresnel diffraction studies. Another area where the measurement of the nonlinear modulations of the signals spatial structure is emerging as a means of exploiting the wavefront curvature is in seismic profiling [Bag74], [Tan69]. Still another area where a mixture of plane and nonhomogeneous waves is considered, is in wave theory, when finding the distribution of a field scattered by a rough surface [Bec63].

In [Mo73a], [Mo73b] we studied passive narrowband tracking when only S1 is assumed. The motions were modelled by a stochastic finite dimensional dynamical system. A spatial/time integrated approach, with planar wavefront structure, was developed based on first order approximations to the infinite-dimensional filter. Analysis substantiated by Monte Carlo simulations, showed that the filter only tracked local dynamics, lacking global range observability.

We concentrate in this thesis on the fundamental issues of global range (and the remaining source parameters) identifiability. We incorporate explicitly in the model

the spatially inhomogeneous, and/or the temporally non-stationary character of the wavefields (spatial and temporal curvature). The absence of hypothesis S1 is the essential underlying characteristic of the present work.

Chapters II to IV assume S3, i.e. classes of stationary or deterministic motions, with the passive tracking fitting a finite parameters estimation problem. In Chapters II and III, S2 is naturally imbedded in the formulation, by restricting the analysis to either stationary geometries (Chapter II), where no significant temporal diversity occurs, or to point sources and omnidirectional sensors (Chapter III), where no meaningful spatial diversity is available. Chapter IV considers spatially extended receivers and moving sources, with the analysis focussing on the implications of space/time factorability and space/time coupling.

In Chapter V we generalize the class of motions to include dynamics generated by a finite dimensional stochastic system. We study a "hybrid" practical solution to the problem, resulting from a compromise between two conflicting requirements, i) global identifiability of the relative source/receiver geometry, and ii) minimization of the receiver's complexity.

Chapter VI discusses applications of the theory and results developed in the preceding chapters to three problems of practical significance: 1) precision landing in

air traffic control; 2) underwater acoustic positioning; and 3) navigation by passive means, with orbiting and geostationary satellites. In Chapter VI we also present the results of Monte Carlo Simulation studies.

Chapter VII reviews the main conclusions and expands on possible generalizations and extensions of the present work.

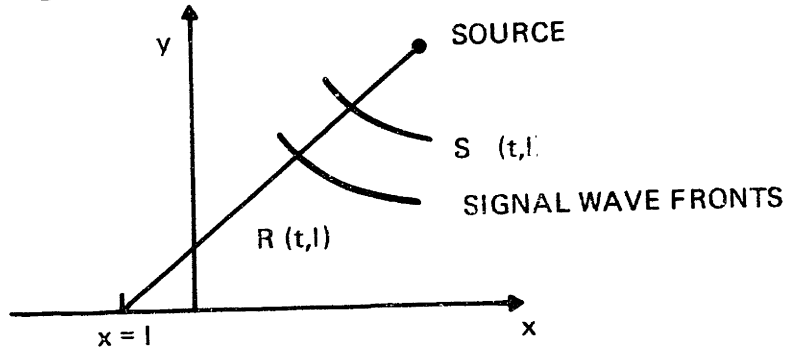
Chapter II

Synthetic Arrays with Stationary Sources (SASS)

In this chapter we study a class of narrowband passive tracking systems which arise in two extreme situations of practical significance. In the first a Stationary Array detects and estimates the location of a Stationary Source. In the second a Moving Omnidirectional observer generating a synthetic Array tracks a Stationary Source. We refer to both as Synthetic Array with Stationary Source (SASS). We consider the simplest estimation hierarchy, namely that of a finite parameter estimation model. In section 1, the model is described in detail. We emphasize the space/time geometric dualism between both problems, and establish in which sense they are equivalent. In section 2 a practical implementation to the maximum likelihood receiver is presented. In section 3 we study the generalized ambiguity function which characterizes the fundamental structure of the processor. In section 4 we consider the error constraints on this receiver, derive performance bounds, and discuss threshold effects.

1. Geometric Model

As described in chapter I, we assume a planar geometry, illustrated in Figure 1, and a point source radiating



Planar Geometry for a Stationary Source

Figure 1
narrow band signals, which at time t and point l in space
are given by

$$S(t, l) = \sqrt{2} \operatorname{Re}\{\tilde{s}(t, l) \exp j\omega_c t\} \quad 1$$

The wavefronts at the receiving aperture are

$$r(t, l) = \sqrt{2} \operatorname{Re}\{\tilde{r}(t, l) \exp j\omega_c t\} \quad 2a$$

with

$$\tilde{r}(t, l) = \tilde{s}(t, l) + \tilde{w}(t, l) \quad 2b$$

The signal complex envelope is

$$\tilde{s}(t, \ell) = \sqrt{\frac{E_r}{LT}} \tilde{\delta} \exp\left[j \frac{2\pi}{\lambda} R(t, \ell)\right] \quad 2c$$

where

E_r = total received energy during the observation interval $[-\frac{T}{2}, \frac{T}{2}]$, and by an array of dimension parameter L ;

$R(t, \ell)$ = distance (range) at time t from the source to the array element at location ℓ ;

$$\lambda = \frac{2\pi f}{c} = \frac{\omega}{c} = \text{wavelength}$$

$$\tilde{\delta} = b \exp(j\psi)$$

with b a Rayleigh distributed random variable and ψ uniformly distributed in $[0, 2\pi]$. We note that $\tilde{\delta}$ is a complex Gaussian r.v. with

$$E \tilde{\delta} = 0 \quad 3a$$

$$E |\tilde{\delta}|^2 = 2\sigma_b^2 \quad 3b$$

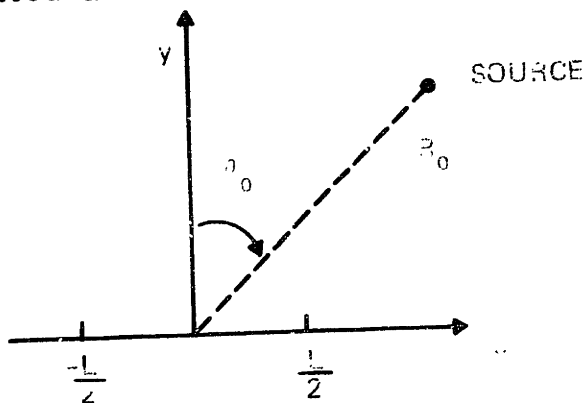
which accounts for model inaccuracies due for example to variations on the radiated signal power about some nominal value, fading in the transmission medium, etc. More importantly, from a structural point of view, the unknown phase ψ represents the lack of knowledge of the absolute phase (incoherent receiver). This is a fundamental constraint, modeling the

fact that global range estimation is achieved from the modulation induced on the signal structure and not from the absolute phase reference.

The complex noise $\tilde{w}(t, \ell)$ is assumed spatially homogeneous and temporarily wide-band ("white"), Gaussian with spectral height N_0 .

1.1 Stationary Array-Stationary Source

In this case the point, stationary source is being tracked by a linear stationary array. Figure 2a details the geometry and the parametrization to be used. The linear array is oriented along the x-axis and the source



Stationary Array - Stationary Source Geometry

Figure 2-a

parameter vector is

$$A = \begin{bmatrix} R_0 \\ \sin\theta \end{bmatrix}$$

We note the choice of $\sin\theta$ over the angle parameter itself, corresponding to a wavenumber type dependence for the space/time processing techniques. This removes from the model the ambiguity characteristic of a linear array, namely that it can only solve for

$$\theta_0 \in [-\frac{\pi}{2}, \frac{\pi}{2}]$$

as it is immediately apparent from equation 5 below. We will refer nevertheless to this parameter as the bearing angle or bearing information.

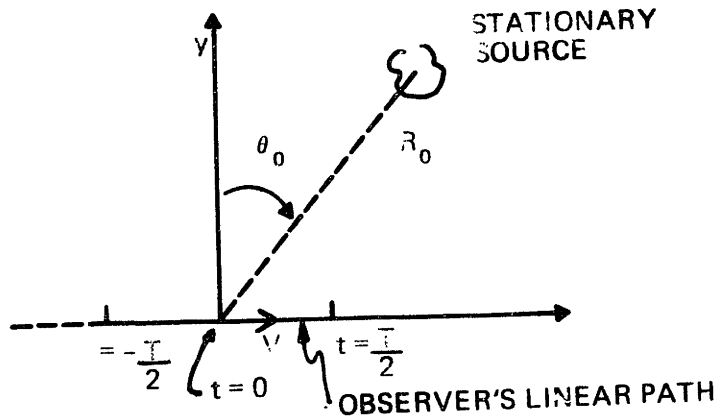
The range function at the array location is

$$R(t, \ell) = \{R_0^2 + \ell^2 - 2\ell R_0 \sin\theta_0\}^{1/2} \quad \ell \in [-\frac{L}{2}, \frac{L}{2}], t \in [-\frac{T}{2}, \frac{T}{2}] \quad 5$$

We observe from equation 5 that the source parameters are imbedded in the spherical curvature of the incoming wavefronts as observed across the array (targets in the near field).

1.2 Moving Array-Stationary Source

In this problem a moving omnidirectional sensor locates a stationary source. It is assumed that the observer motion is perfectly known with respect to a rigid framework and is constrained to a linear path with constant speed v . Fig. 2b shows the parametrization to be used.



Moving Array / Stationary Source Configuration

Figure 2-b

The source parameter vector is, as in the preceding case,

$$A = \begin{bmatrix} R_0 \\ \sin\theta_0 \end{bmatrix}$$

The range at time t is given by

$$R(t) = \{R_0^2 + v^2 t^2 - 2vt R_0 \sin\theta_0\}^{1/2} \quad \begin{array}{l} t \in [-\frac{T}{2}, \frac{T}{2}] \\ L \in [-\frac{L}{2}, \frac{L}{2}] \end{array} \quad 6$$

Equation 6 represents the range function in terms of the source parameters at the middle point of the observation interval. This introduces no a priori reference location assumptions, and allows further algebraic simplifications of the final results.

We note that we have assumed here, that the omnidirectional sensor is a nonlinear array with dimension parameter L .

Identification of the length ℓ with vt in equations 5 and 6 emphasizes the theoretical similarity underlying the measurement of the source parameters in both applications. The quantitative results for one problem can be immediately translated into the other by substituting L for vT or vice versa. We let in the sequel

$$z = \frac{L}{2} \tag{7a}$$

or

$$z = \frac{vT}{2} \tag{7b}$$

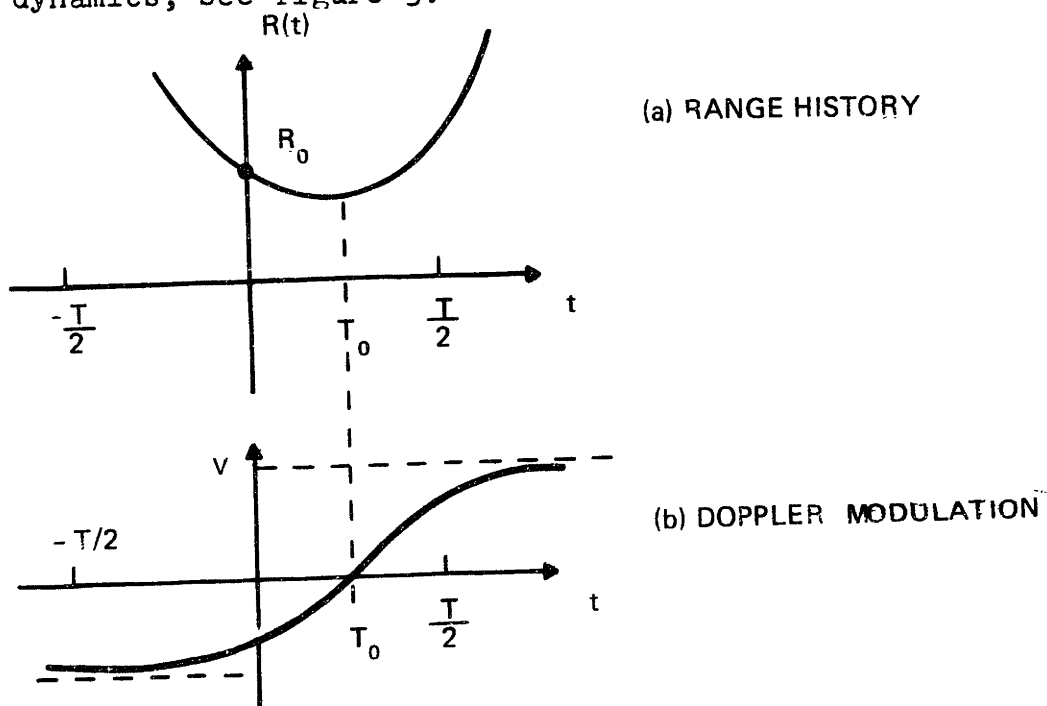
and define the spatial variable

$$x = \ell \text{ or } x=vt \tag{7c}$$

depending on the specific application, alluding simply to a Synthetic Array with Stationary Source (SASS) when referring to either problem.

The mathematical equivalence of the two situations stresses the space/time dualism between them. In the Stationary Array/ Stationary Source context the spherical curvature of the

incoming wavefronts induces a nonlinear spatial modulation on the signal, which is measured by the spatially extended linear array. With the moving omnidirectional configuration the range and angle information are conveyed by the nonlinear temporal modulations induced on the signal structure by the relative dynamics, see figure 3.



Modulations on Temporal Signal Structure

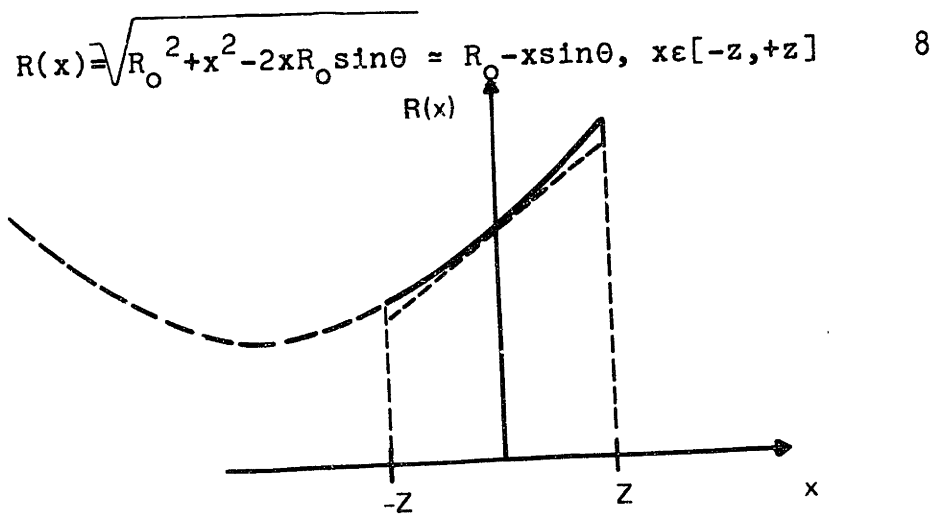
Figure 3

This can be contrasted with a Synthetic Aperture Radar (SAR) system.

SAR is an airborne system following a prescribed path (observer's motion constraints), and carrying the scanning beam illuminating the terrain. The observer's motion has the net effect of generating a longer, effective baseline array. The reflected echo arrives at the SAR system,

phase modulated by the relative motion. These modulations give to the 2-dimensional signal a structure similar to an FM-modulated signal, compressing the signal in the angle direction (referred to as azimuth in the SAR jargon). The SAR recovers the range from an active modulation, while the azimuth is estimated from the "passive" modulations induced by the relative motions. The SASS problem with omnidirectional sensor described in section 1.2 represents the other extreme, where no "active" range measurement occurs. In other words the global target parameters are to be constructed only from the modulations induced by the relative motions.

The range phase, equations 5 or 6, can be approximated by truncated Taylor series expansions. For targets in the far-field, known in optics as the Fraunhofer zone, a linear expansion is valid, see figure 4, and the phase is



Source in Far-Field (Linear Approximation)

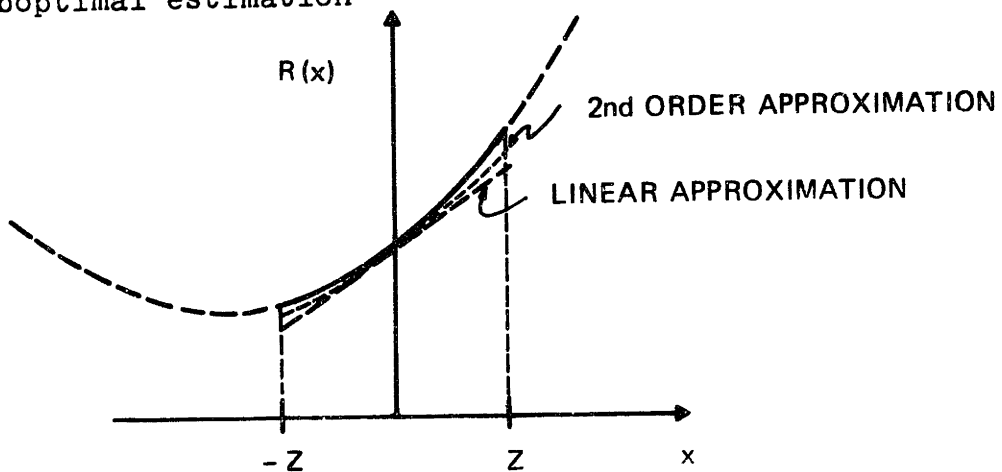
The wavefronts are practically planar at the front end of the receiver, and given the incoherent phase model assumed with lack of any phase reference, convey no range information.

For targets in the so called Fresnel zone a second order expansion is appropriate as displayed in figure 5, leading to

$$R(x) = R_0 - x \sin \theta + \frac{(x \cos \theta)^2}{2R_0}, \quad x \in [-Z, +Z] \quad 9$$

The range may now be observed from the second order modulations induced on the spatial/temporal signal structure.

A suboptimal estimation



Source in Fresnel Zone (Quadratic Approximation)

Figure 5

algorithm, recovering the source parameters, may be developed by first tracking the Doppler and the Doppler rate by means of, for example, second or third order phase locked loops, and then performing the nonlinear transformation

$$\sin\theta = -\dot{R}_o \quad 10a$$

$$R_o = \frac{1 - \dot{R}_o^2}{\ddot{R}_o} \quad 10b$$

where

$$\overset{(1)}{R}_o = \left. \frac{d^i R(x)}{dx^i} \right|_{x=0} \quad 10c$$

We conclude that, in order to reconstruct the source receiver separation (range), extended apertures measuring the higher order effects have to be synthesized.

Given the high costs involved in building very large arrays, it is apparent that, in most applications, the stationary array with stationary source of section 1.1 will have smaller ranges of applicability than the moving omnidirectional sensor with stationary array of section 1.2, for which one has, in many cases, the possibility of synthesizing larger apertures by enlarging the observation interval.

2. Receiver Design

Under the "white" and Gaussian assumptions on the noise and Rayleigh parameter statistics, the optimum receiver for the parameter estimation problem described above is a Maximum Likelihood (ML) processor, essentially consisting of a matched filter followed by an envelope detector, e.g., Van Trees [Va71b]. The filter maximizes on the parameter space a monotonic function of the ML-function (its natural logarithm). The log ML-function is [Va71b]

$$\ln \Lambda_1(A) = \frac{1}{N_0} \frac{\bar{E}_r / N_0}{1 + \frac{\bar{E}_r}{N_0}} |\tilde{L}(\bar{A})|^2 \quad 11a$$

where A is the parameter vector

$$\bar{E}_r = (2\sigma_b^2)E_r = \text{average received energy}$$

$$|\tilde{L}(\bar{A})|^2 = \int_{-\frac{T}{2}}^{\frac{T}{2}} dt \int_{-\frac{L}{2}}^{\frac{L}{2}} d\mathbf{r} |\tilde{r}(t, \mathbf{l}) \tilde{s}^*(t, \mathbf{l}, \bar{A})|^2 \quad 11b$$

Notation 1) The inner product in equation 11b will be abbreviated by

$$|\tilde{L}(\bar{A})|^2 = |\langle \tilde{r}, \tilde{s}(\bar{A}) \rangle|^2 \quad 11c$$

2) * stands for complex conjugation.

3) To avoid cumbersome expressions, we avoid the explicit functional dependence of the several quantities on all variables and/or source parameters, showing only those variables of most concern in the specific argument, e.g., the signal will generally be represented by $\tilde{s}(t)$ or $\tilde{s}(t, \ell)$, although on occasion we use $\tilde{s}(t, \ell, A)$.

The ML-estimator is in practice unrealizable since it requires the (stochastic) maximization of $|\tilde{L}(\bar{A})|^2$ over the (continuous) parameter space Ω . A practical suboptimal receiver can however be constructed by exploiting the signal autocorrelation and the noise statistics.

Substituting the value of the received signal as given by equation 3 in the expression of the log ML-function we obtain

$$|\tilde{L}(\bar{A})|^2 = |\langle \tilde{s}(A), \tilde{s}(\bar{A}) \rangle + \langle \tilde{w}, \tilde{s}(\bar{A}) \rangle|^2 \quad 11d$$

where A and \bar{A} represent the actual and scanning parameter values respectively.

In the absence of the additive measurement noise the output of the ML-receiver is

$$|\tilde{L}(\bar{A})|^2 = |\langle \tilde{s}(A), \tilde{s}(\bar{A}) \rangle|^2 = |\psi_s(A, \bar{A})|^2 = \phi_s(A, \bar{A}) \quad 12$$

which is a scaled version of the so called generalized ambiguity function, as discussed in the next section. The noise component in equation 11d

$$\tilde{w}(\bar{A}) = \langle \tilde{w}, \tilde{s}(\bar{A}) \rangle \quad 13a$$

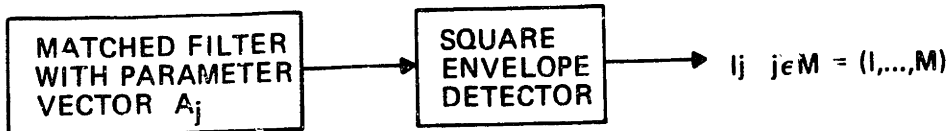
is a Gaussian complex random variable with zero mean and variance N_0 .

At two scanning points $A_1, A_2 \in \Omega$

$$\begin{aligned} & E[(\tilde{L}(A_1) - \psi(A, A_1))(\tilde{L}(A_2) - \psi(A, A_2))^*] \\ & = E[\tilde{w}(A_1)\tilde{w}^*(A_2)] = \psi(A_1, A_2) \end{aligned} \quad 13b$$

This expression shows that, as \bar{A} is scanned over Ω , the noise samples at the output of the matched filter exhibit a cross-correlation given in terms of the signal auto-correlation function. Because this function has essentially a

finite extent, to be determined in the sequel, we define a coherence or correlation distance in Ω . Points whose separation is greater than this distance, lead to noise components $\tilde{W}(\vec{A})$ at the output of the ML-processor which are uncorrelated. This suggests a two step implementation for the ML-algorithm. The first, substitutes the continuous by a discretized search, where the scanned points are separated by the coherence distance. The region of interest is divided in cells (whose form and number M is to be determined subsequently). In each cell block we assume that the parameter vector takes only a fixed value (e.g. the center of the cell). With this discrete structure for Ω , we perform a crude maximization of the log ML-function, by computing it at all grid vertices, and choosing the point at which it is maximum. The receiver performs a "largest of" M -ary hypothesis decision with uncorrelated signals, and, at this stage, consists of a 2-dimensional bank of matched filters followed by square envelope detectors (we will return in more detail to this point later in the chapter when discussing the global performance). Figure 6 illustrates the "largest of" receiver.



Coarse Search ML-Algorithm

Figure 6

The coarse search returns a crude estimate

$$\tilde{A}_{m\ell} = A_1 \quad 14a$$

for which

$$l_1 = \max_{j \in M} l_j \quad 14b$$

In the second step the mechanization accomplishes a local maximization of the log ML-function about $\tilde{A}_{m\ell}$. This can be done by a finer search procedure, or by any other method, e.g., a steepest-descent.

As a final comment we note that this approach in two steps to the ML-receiver was first taken by Woodward in the context of (active) radar range measurements [Woo 55], and is referred to, in the frequency estimation literature, as Frequency Shift Keying techniques (FSK).

3. Generalized Ambiguity Function

As discussed in the previous section the statistical behavior of the ML-receiver is determined by $\phi_S(A, \bar{A})$. We make a preliminary:

Definition 1 - The Signal Autocorrelation Function is

$$\psi(A, \bar{A}) = \langle \tilde{s}_n(A), \tilde{s}_n(\bar{A}) \rangle \quad 15a$$

where $\tilde{s}_n(A)$ stands for a normalized version of the signal given by

$$\tilde{s}_n(A) = \frac{1}{\sqrt{LT}} \exp j \frac{2\pi}{\lambda} [t - R(t, \ell, A)], t \in [-\frac{T}{2}, \frac{T}{2}], \ell \in [-\frac{L}{2}, \frac{L}{2}] \quad 15b$$

We have then:

Definition 2 - The Generalized Ambiguity Function (GAF) is given by

$$\phi(A, \bar{A}) = |\psi(A, \bar{A})|^2 \quad 15c$$

Substitution of equation 15b in Definition 2 leads to

$$\phi(A, \bar{A}) = \left| \frac{1}{LT} \int_{-\frac{T}{2}}^{\frac{T}{2}} dt \int_{-\frac{L}{2}}^{\frac{L}{2}} d\ell \exp j \frac{2\pi}{\lambda} \Delta R(t, \ell, A, \bar{A}) \right|^2 \quad 15d$$

where the range phase difference is

$$\Delta R(t, \ell, A, \bar{A}) \triangleq R(t, \ell, A) - R(t, \ell, \bar{A})$$

We observe the properties

Property 1: $\phi(A, A) = 1$

Property 2: $\phi(A, \bar{A}) \leq \phi(A, A)$

Applying these definitions to the SASS context, and working with the general variable x , the GAF is

$$\phi(A, \bar{A}) = \left| \frac{1}{2Z} \int_{-Z}^Z dx \exp \left[j \frac{2\pi}{\lambda} \Delta R(x, A, \bar{A}) \right] \right|^2 \quad 16$$

with Z defined in 7a or 7b, and the range phase difference given by

$$\Delta R(x, A, \bar{A}) = \sqrt{R_0^2 + x^2 - 2xR_0 \sin\theta} - \sqrt{\bar{R}_0^2 + x^2 - 2x\bar{R}_0 \sin\theta} \quad 17$$

Equation 16 can be renormalized

$$\phi(A, \bar{A}) = \left| \frac{1}{2} \int_{-1}^1 dz \exp j \frac{2\pi Z}{\lambda} \left[\sqrt{r_0^2 + z^2 - 2zr_0 \sin\theta_0} - \sqrt{\bar{r}_0^2 + z^2 - 2z\bar{r}_0 \sin\theta_1} \right] \right|^2 \quad 18a$$

$$\text{where } z = \frac{x}{Z} \quad 18b$$

$$r_o = \frac{R_o}{Z} \quad 18c$$

Since GAF plays an important role in evaluating the ability of the ML-receiver in locating the source it is of importance to have a clear idea of its structure. From active radar systems theory one knows that a desirable ambiguity pattern is impulsive, i.e., a narrow spike at the source location in the parameter space and zero elsewhere. This idealized ambiguity function is physically unrealizable due to the volume invariance of the time frequency radar ambiguity function, but it suggests an optimal limiting form to look for when designing the radar modulating signal.

In the passive problem we have no control over the signal design, since it is radiated by the source. Our task is to analyse the structure of GAF in order to quantify the receiver's capability of locating the target.

We observe that GAF is not a function of the vector difference

$$A-\bar{A},$$

but it also depends on the actual source parameter values. This contrasts with Woodward's Frequency-Time Ambiguity Function in radar, but is similar to the dependence of the

ambiguity function found when echolocating high velocity and accelerating targets with active systems [Kel 65].

We note that this thesis does not deal with the important questions of designing the array geometry and the weighting pattern of the array. We restrict the analysis to linear structure with uniform shadings, since we are addressing the basic questions of identifiability of the source parameters and of the ultimate performance bounds in the least complex situation of practical significance, namely that of spatially homogeneous and temporally white background noise.

In the presence of directional noise sources, higher order array processing techniques may be required, shaping the array beam pattern to the statistical environment, providing for null cancellations at the wave number space direction of the noise interference, at the cost of undesirable sidelobes and/or deterioration in performance in the presence of the white background noise alone. We will not pursue here these high resolution array processing techniques, since they represent second order type complications of the problem, but refer the reader to [Bag71] and [Van 75] where these methods are dealt with, in the "bearings only" context.

Figures 7 and 8 present a 3-dimensional, and a contour plot of GAF for typical values of the parameters. The function exhibits a main peak centered at the source location, whose contours are essentially ellipses, and some subsidiary structure outside the main lobe. In the absence of the additive observation white noise the output of the filters is a point in this curve, and the maximum-likelihood (ML) estimates are the parameters for the matched filter whose output leads to the absolute maximum of the function. In the presence of measurement disturbances, the noise contribution at the filter's output may lead to an absolute maximum which is in error. In order to quantify the statistics of these errors we need a better quantitative understanding of GAF, namely the dimensions of its main lobe, and the size of any secondary peak in the subsidiary GAF structure, i.e., outside the main lobe. This will be done using both graphical and analytical techniques.

In Appendix A we do an approximate analysis of GAF by assuming polynomial approximations to the phase range difference. We also derive bounds on the rate of fall off of the ambiguity structure, both for these approximations and for the general expression. Here we restrict our attention to the main results therein, and combine them with a pictorial

Figure 7

(3-Dim.) Ran / Ang. Ambig. Struct. (X=1/4)

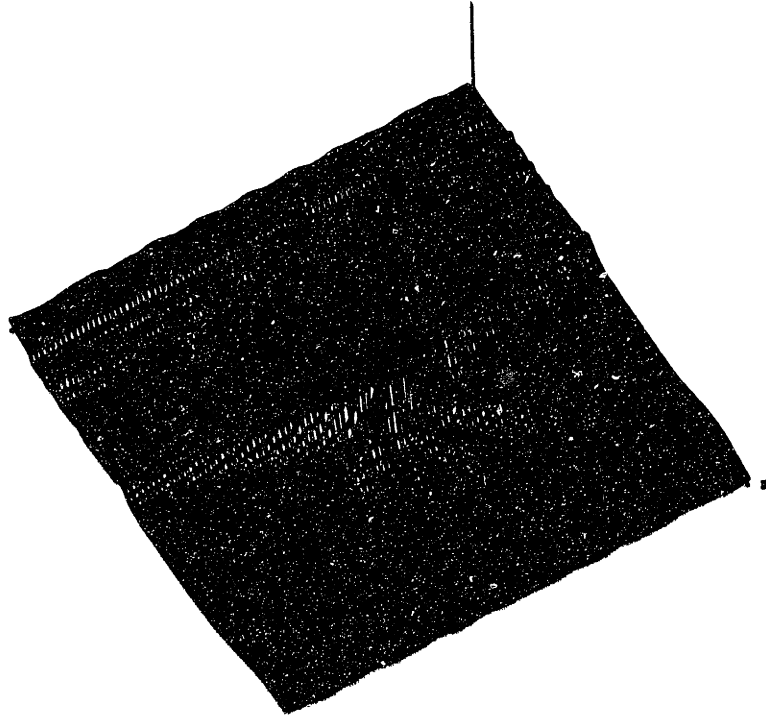
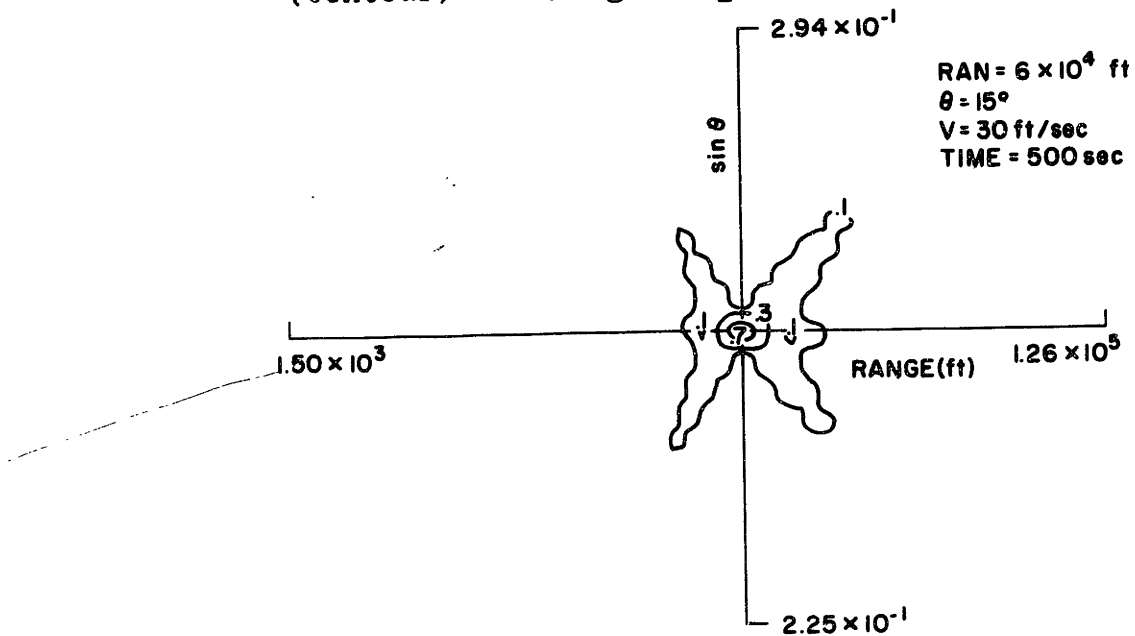


Figure 8

(Contour) Ran/Ang Ambig. Struct. (X=1/4)



representation of GAF for several values of the important parameters, to obtain a complete qualitative and quantitative evaluation of GAF.

3.1 Approximate Analysis of GAF

In Appendix A we have approximated the range phase differences by a polynomial expansion

$$\Delta R(x, A, \bar{A}) \approx \sum_{i=0}^n \Delta_i x^i \quad 19a$$

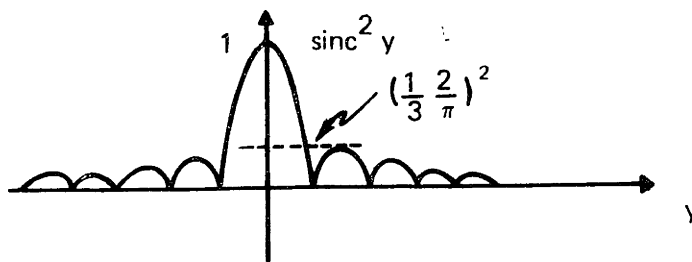
where we define

$$\Delta_i \triangleq \frac{1}{i!} \Delta R_o^{(i)} = \left[\frac{d^i R(x, A)}{dx^i} - \frac{d^i R(x, \bar{A})}{dx^i} \right] \Big|_{x=0} \quad 19b$$

For a linearized expansion the GAF has a sinc² structure

$$\phi(A, \bar{A}) \approx \text{sinc}^2 \left[\frac{2\pi}{\lambda} \Delta(\sin\theta)Z \right] = \left| \frac{\sin \frac{2\pi}{\lambda} \Delta(\sin\theta)Z}{\frac{2\pi}{\lambda} \Delta(\sin\theta)Z} \right|^2 \quad 20$$

as illustrated in Figure 9.



Linearized Ambiguity Sinc Structure

Figure 9

The maxima decrease monotonically, as we depart from the origin, along the angle parameter axis with the second maximum reduced to about 4.5% of the value at the origin.

The ambiguity pattern is constant along the range parameter axis, and the linearized GAF presents no range focusing ability. This is not surprising, since, as remarked before, the range is estimated from the higher order modulations induced on the signal structure by the waveform curvature, and not from the absolute phase reference. In analogy with optics, this amounts to say that, for targets at the Fraunhoff zone, the incoming waveforms are planar at the observer site, with no information on the range being conveyed to the passive receiver. The bearing is measured from the linear delays recorded either across the array or by the moving observer along its linear path.

For a quadratic approximation and along the radial line

$$\Delta \dot{R}=0 \implies \Delta(\sin\theta)=0, \quad 21$$

the ambiguity function is approximated by

$$\phi(A, \bar{A}) = \left| \frac{1}{\Sigma} F(\Sigma) \right|^2 \quad 22a$$

where

$$\Sigma = \sqrt{\frac{\pi}{\lambda} \Delta\left(\frac{\cos^2 \theta}{R_0}\right)} \quad Z \quad 22b$$

and $F(\cdot)$ is the (exponential) Fresnel Integral, whose graph in the complex plane gives the Cornu Spiral.

The ambiguity function along the radial-acceleration axis, parameter $\Delta \ddot{R}_0$, is shown in Figure 10, with the first minimum occurring at

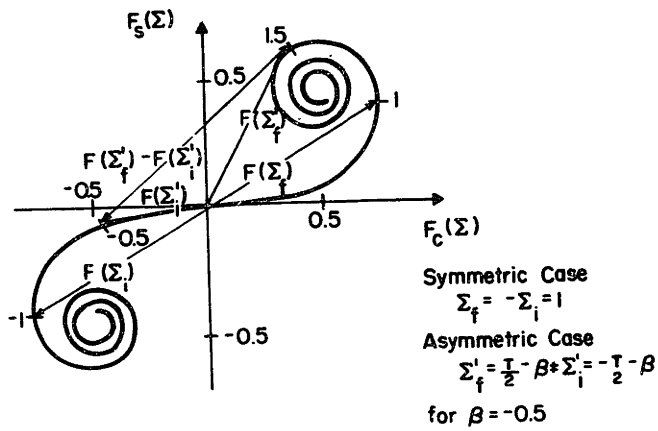
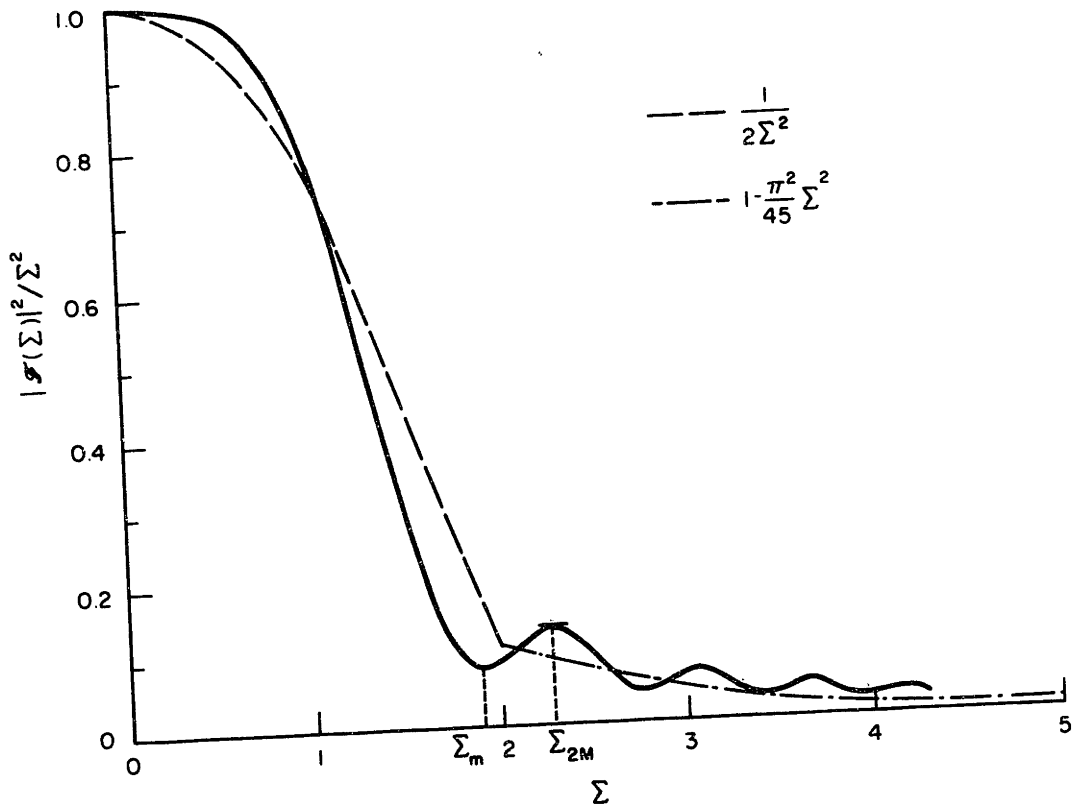
$$\Sigma_m \approx 1.9 \quad 23a$$

and the second local maxima at

$$\Sigma_{2M} \approx 2.26 \quad 23b$$

Figure 10

Quadr. (Fresnel) Amb. Struct. W. Loc./Asympt. App.



Cornu Spiral

Figure 11

where

$$\phi(A,A) \approx .132 \quad 23c$$

i.e., it is reduced to about 13% of its maximum value 1, at the origin. By establishing the equivalence of the signal correlation function

$$\psi(A,\bar{A}) = \frac{1}{\Sigma} F(\Sigma) \quad 24$$

with a certain Confluent Hypergeometric Function, we apply in the Appendix known developments (Abramowitz and Stegun [Abr65])

to obtain local (about $\Sigma=0$), and asymptotic (large Σ) expansions, respectively equation A-41 and equation A-42. From the latter, we find that the rate of fall-off for the ambiguity function along the radial-acceleration line is

$$\phi(A,\bar{A}) \approx \frac{1}{2\Sigma^2} \quad 25$$

The general expression of GAF for the quadratic phase approximation is

$$\phi(A, \bar{A}) \cong \left| \frac{1}{\Delta \Sigma} [F(\Sigma_f) - F(\Sigma_i)] \right|^2 \quad 26a$$

where

$$\Delta \Sigma = \Sigma_f - \Sigma_i \quad 26b$$

and

$$\Sigma_f = \sqrt{\Delta_2} \left(Z + \frac{\Delta_1}{2\Delta_2} \right) \quad 26c$$

$$\Sigma_i = \sqrt{\Delta_2} \left(-Z + \frac{\Delta_1}{2\Delta_2} \right) \quad 26d$$

In terms of the Cornu Spiral representation of the Fresnel Integral the vector

$$F(\Sigma_f) - F(\Sigma_i) \quad 27$$

is a running vector based on the spiral, i.e., with both end points on the curve as illustrated for a specific example on figure 11.* The ambiguity function has the intuitive interpretation of being given by the modulus squared of this vector, divided by the square of the distance of the arguments $\Sigma_f - \Sigma_i$.

* See page 62

3.2 General Case

We study graphically the structure of GAF as given by the exact expression 16. The signal correlation function is

$$\psi(A, \bar{A}) = \frac{1}{2Z} \int_{-Z}^Z dx \exp\left\{j \frac{2\pi}{\lambda} \Delta R(x, A, \bar{A})\right\} \quad 31a^*$$

and GAF

$$\phi(A, \bar{A}) = |\psi(A, \bar{A})|^2 \quad 31b$$

We presented in Figures 7 and 8 a 3-dimensional, and a contour plot, of GAF for source parameters given by

$$A_a = \begin{bmatrix} R_{0a} \\ \sin \theta_a \end{bmatrix} = \begin{bmatrix} .6 \times 10^5 \text{ feet} \\ \sin 15^\circ \end{bmatrix}$$

with the geometric parameter

$$X = \frac{Z}{R_0} = \frac{1}{4}$$

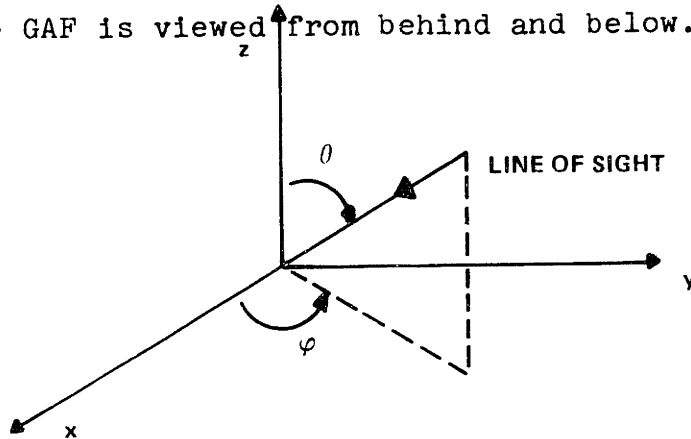
The line of sight for the 3-dimensional plot is given by the angles θ and ϕ illustrated in figure 12. For figure 7 these parameters are

* Equations 28 to 30 have been eliminated

$$\theta = 150^\circ$$

$$\phi = 210^\circ$$

i.e., the GAF is viewed from behind and below.



Line of Sight Definition for 3-Dimensional Plots

Figure 12

Figures 13 and 14 show the ambiguity structure for a smaller value of the x geometric parameter, namely

$$x = \frac{1}{40}$$

Reducing x (smaller array or shorter observation interval, or equivalently for the same synthetic aperture, larger range) results in a flatter main lobe, with a larger ridge.

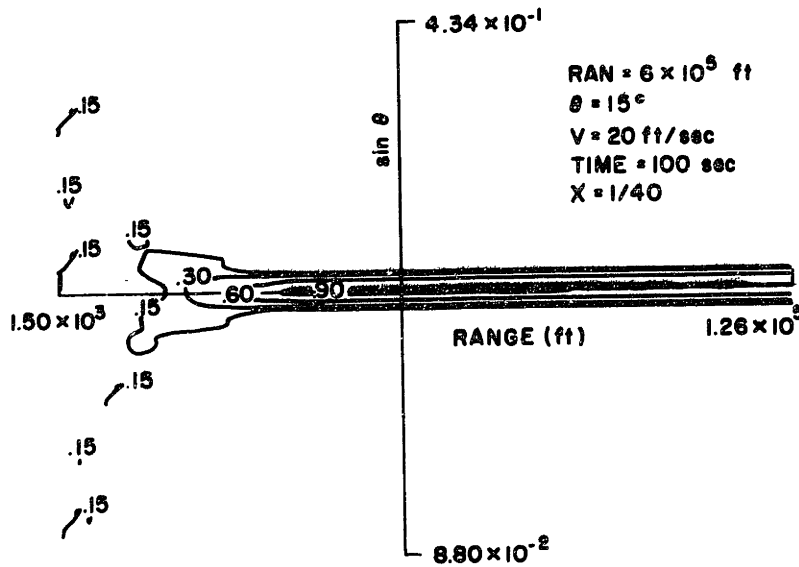
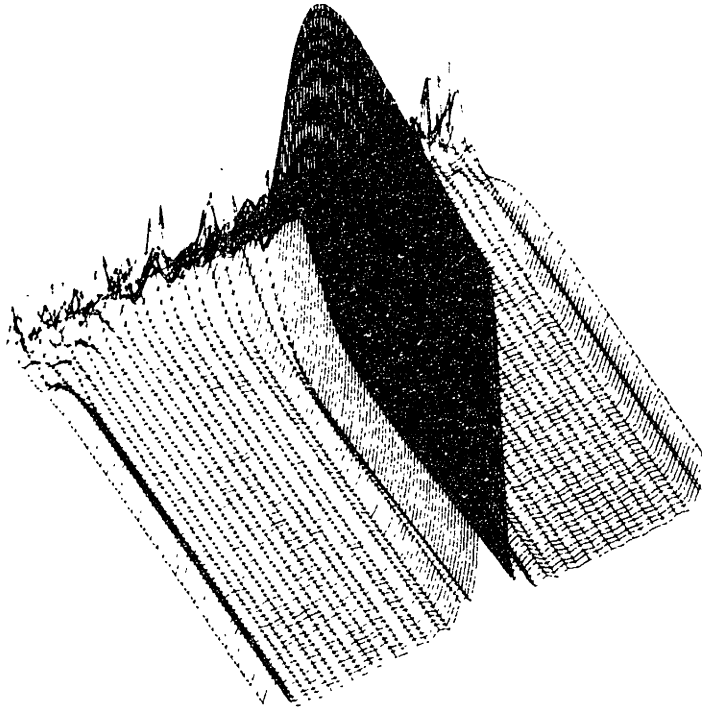
This illustrates that, whenever all the other conditions are identical (e.g. source-receiver separation, signal-noise ratio), the simultaneous range and angle focusing requires larger synthetic arrays, as we would expect. In the next section we will quantify these statements.

Finally, figure 15 displays the ambiguity pattern for a large value of x

$$x = 6,$$

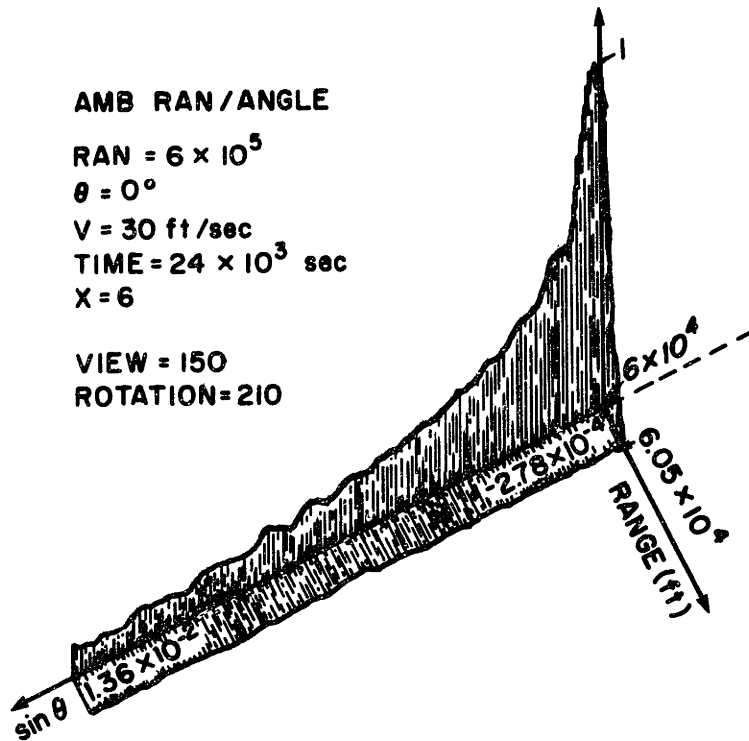
(3-Dim.) Ran/Ang Ambig. Struct. (X=1/40)

Figure 13



(Contour) Ran/Ang Ambig. Struct. (X= 1/40)

Figure 14



(3-Dim.) Ran/Ang Ambig. Struct.(X=6)

Figure 15-a

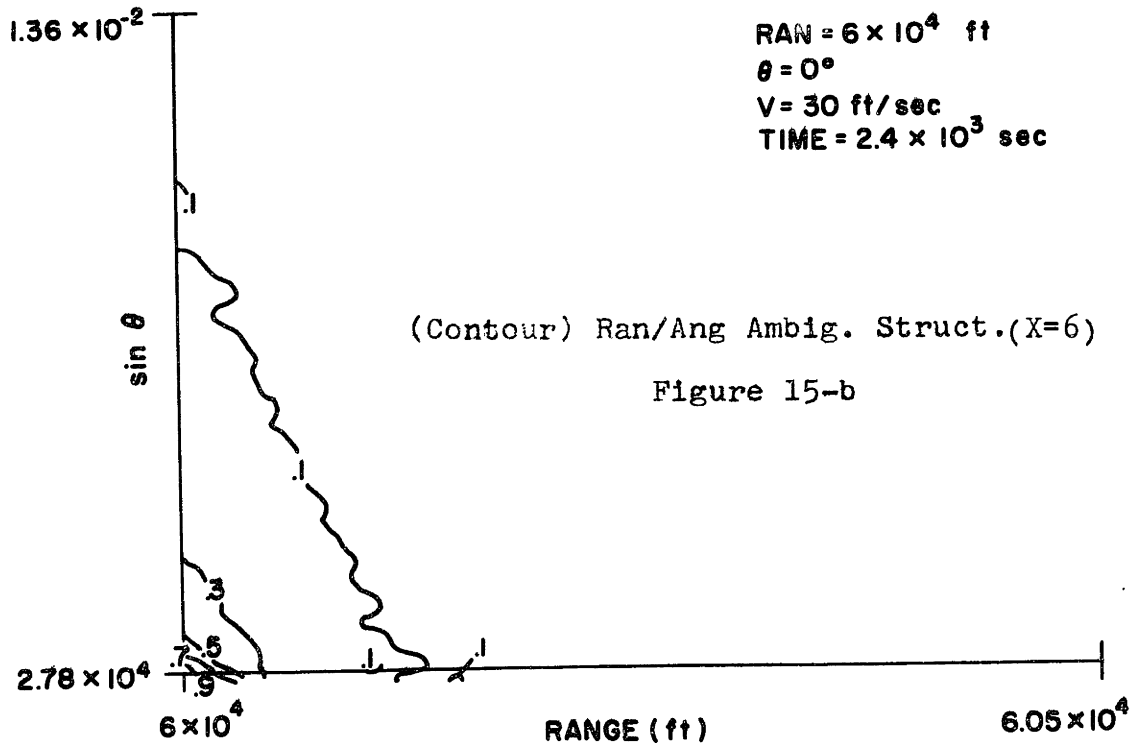


Figure 15-b

referred to as the close observer configuration. This picture shows the behavior of GAF asymptotically, as the (synthetic) array length grows compared to the source/receiver separation.

We note the changes in scale on the different pictures. Along the $\sin\theta$ -axis the ambiguity function has been scanned at points whose positions were determined by the sinc^2 structure of equation 20, i.e., the elementary interval between scanning points was

$$\Delta(\sin\theta) \approx \frac{1}{n} \frac{\lambda}{2L}, \quad n \text{ some integer} \geq 2 \quad 32$$

Along the range-axis the scale is essentially the same on figures 8 and 14, but has drastically changed on figure 15, reflecting the sharper lobe one gets for large X-parameter.

The graphs display the peaked structure of GAF, and show that outside the main lobe the secondary peaks are negligible.

A local and an asymptotic analysis can be pursued in much the same terms as in the previous paragraphs. The local analysis essentially determines the structure of the main lobe of GAF. We only note here, that, from the graphic displays, the equal height contours on the main lobe are approximately ellipses. Because for higher dimensions this

generalizes to ellipsoids we refer it as the GAF's main lobe ellipsoidal structure. Given this ellipsoidal structure, the dimensions of the main lobe are determined from a second order analysis of GAF on the parameter space Ω , i.e., on the errors on the parameters (not to be confused with the second order analysis carried out in Appendix A, which is in the time variable). This will be done in section 4 where we discuss the ML-receiver's performance.

We close the section with a brief discussion of the bounds on the subsidiary ambiguity pattern. They are derived in the Appendix, by application of the Method of Stationary Phase, and are summarized by equations A-63, A-65, and A-67. The bounds at each point

$$\bar{A} = \begin{bmatrix} \bar{R}_0 \\ \frac{1}{\sin\theta} \end{bmatrix}$$

of the parameter space Ω depend on the behavior of the range phase difference at that point in the observation interval $[-Z, Z]$, namely on the order n of the first nonzero derivative of the range phase difference in x , $x \in [-Z, Z]$. If n is even

$$\phi(A, \bar{A}) \sim \left[\frac{1}{Z} \frac{\Gamma(1/n)}{n \sqrt{\frac{2\pi}{\lambda} \frac{(n)}{\Delta R(x_0)/n!}}} \right]^2 \quad 33a$$

If n is odd >1

$$\phi(A, \bar{A}) \sim \left[\frac{1}{Z} \frac{\Gamma(1/n) \cos \frac{\pi}{2n}}{\sqrt[n]{\frac{2\pi}{\lambda} \Delta R^{(n)}(x_0)/n!}} \right]^2 \quad 33b$$

where $x_0 [-Z, Z]$ is the point where the lower order derivatives vanish at $\bar{A}\epsilon\Omega$. For $n=1$

$$\phi(A, \bar{A}) \sim \left[\frac{1}{2Z} \frac{2\pi}{\lambda} \left(\frac{1}{|\Delta \dot{R}(Z)|} + \frac{1}{|\Delta \dot{R}(-Z)|} \right) \right]^2 \quad 33c$$

Equations 33 exhibit the decaying of the ambiguity pattern in terms of the inverse of a certain power of the errors of the least order nonvanishing derivative at x_0 , i.e., in terms of

$$\binom{(n)}{(\Delta R)}^{-2/n};$$

we refer to this rate of decaying as the GAF hyperbolic rate of fall-off. We note that for the problem at hand, and except for degenerate condition (endfire), $n=1$ or $n=2$.

Summarizing, in this section we analysed the ambiguity pattern for the SASS problem with narrowband passive signals. For targets in the far-field no range focusing is possible, and the stationary array/stationary source problem reduces to the classical passive bearing measurement problem. The moving omnidirectional sensor with stationary array compares conceptually to the "passive" azimuth measurement in SAR systems (see discussion at the end of section 1). The ambiguity function has a sinc^2 structure which is constant along the range axis. For targets in the Fresnel zone (quadratic approximation), or in the near field, the ambiguity structure is concentrated on a main lobe, and no significant sidelobes arise, since by a bounding procedure, coupled to the pictorial representation of GAF, we have concluded that the limiting behavior of GAF, for large parameter errors, is essentially negligible. We can then extrapolate the graphic displays to the whole parameter space, by assuming that the ambiguity function is concentrated in its main lobe and is zero in the remaining space.

4. Performance Analysis

In section 2 we described a practical implementation of the maximum likelihood (ML-) receiver consisting of two stages. On the first, one assumes that the parameter space is discretized by a grid. The algorithm performs a coarse search, aiming at the grid point which is closest to the actual parameter values. On the second step a finer search about the previous value returns the approximate ML-estimate. In other words, the direct global maximization of the ML-function is accomplished by first performing a multiple hypothesis decision ("largest of" type receiver) which chooses a cell from the assumed discrete grid, and secondly by maximizing the ML function (or equivalently its logarithm), locally, on the chosen cell of the parameter space.

In this section we discuss the estimation errors induced by the above algorithm, and find bounds constraining its performance.

Let A_j represent the j th component of the source parameter vector A . From the above description, the mean square error on the estimate A_{jml} will be

$$\begin{aligned} E(A_j^2 | \epsilon) &\triangleq E[(A_j - A_{jml})^2] = \\ &= E(A_j^2 | \epsilon) \Pr(\epsilon) + E(A_j^2 | \epsilon^c) (1 - P_r(\epsilon)) \end{aligned} \quad 34$$

where:

ϵ is the event that a decision error or diversion occurred, i.e., that the wrong grid interval was chosen by the "largest of" receiver; ϵ^c is the complement of ϵ , i.e., the event that no diversion occurred, and the correct cell has been chosen on the first step; $\text{Pr}(\epsilon)$ is the probability of the event ϵ .

The computation of the various quantities in equation 34 depends on the design and dimension of the grid discretizing the parameter space. Given the ellipsoidal structure of the ambiguity function (section 3) we assume an ellipsoidal mode grid, i.e., that the grid cell blocks are approximately ellipsoids. The size of these elementary cells is determined from the dimensions of the main lobe of GAF. Retaining up to second order terms on its Taylor series expansion about the actual value A_a of the source parameters, leads to

$$\begin{aligned} \phi(A, A_a) \approx & \phi(A_a, A_a) + \left[\nabla_A \phi(A, A_a) \Big|_{A=A_a} \right]^T \Delta A + \\ & + \frac{1}{2} \sum_{i,j} \frac{\partial^2 \phi(A, A_a)}{\partial A_i \partial A_j} \Big|_{A=A_a} \Delta A_i \Delta A_j \end{aligned} \quad 35a$$

where

$$\Delta A = A - A_a = \begin{bmatrix} \text{---} \\ A_j - A_{j a} \\ \text{---} \end{bmatrix} \quad 35b$$

$$\nabla_A \cdot = \text{grad}_A \cdot \quad 35c$$

Since

$$\phi(A_a, A_a) = 1$$

and by direct substitution

$$\nabla_A \phi(A, A_a) \Big|_{A=A_a} = 0 \quad 36$$

the GAF is approximated by

$$\phi(A, A_a) \cong 1 - \Delta A^T M \Delta A \quad 37$$

where we used the

Definition The Mean Square Spread Matrix (MSSM) M is given by

$$M = -\frac{1}{2} \left[\frac{\partial^2 \phi(A, A_a)}{\partial A_i \partial A_j} \Big|_{A=A_a} \right]_{i,j} \quad 38$$

We note that, given the quadratic approximation 37, the spread matrix quantifies the extension of the main lobe of GAF, which in turn determines the coherence distance of the noise samples referred to in section 3. Let

$$Q(\Delta A) = \Delta A^T M \Delta A, \quad 39a$$

then

$$\phi(A, A_a) \cong 1 - Q(\Delta A) \quad 39b$$

The ambiguity function will have a stationary point, which is a maximum, at

$$A = A_a$$

if, besides 68, we also have

$$M > 0$$

40

i.e., whenever $Q(\Delta A)$ is a positive definite quadratic form. Since the ambiguity function is by definition

$$\phi(A, A_a) \geq 0 \quad 41$$

we see from equation 39b, that its first minimum occurs approximately when

$$Q(\Delta A) = 1 \quad 42$$

This equation 42 dimensions the ellipsoide defining the elementary cell of the discrete grid. Its form and size are determined by M , in particular by its eigenvalues and eigenvectors. Because this matrix plays also an important role on the Cramer-Rao performance analysis we postpone its detailed study to the next paragraph.

The exact computation of equation 34 is difficult in general. We resort first to the calculation of bounds for the mean square error. A well known and general bound results from the Cramer-Rao inequality, e.g., [Va 71b]. This is done next. We return then to the definition of the MSE and evaluate directly an approximation, bounding the right hand side (RHS) of expression 37. Finally, we discuss under which conditions the estimation algorithm

is efficient, i.e., when is its performance accurately predicted by the Cramer-Rao bounds, or when and where do threshold effects occur, with the processor's expected performance deteriorating faster than predicted by the Cramer-Rao bound.

4.1 Cramer-Rao Performance Analysis

It is well known that if

$$\Lambda_{\epsilon} = [\sigma_{ij}^2]$$

is the error covariance matrix of the parameter estimates, then

$$\Lambda_{\epsilon} \geq J^{-1}, \quad 43$$

where J is the Fisher Information Matrix (FIM). For the general signal model described in section 1, FIM is given by (e.g., Van Trees [Va71b])

$$J = [J_{ij}] = -E \left[\frac{\partial^2 \ln \Lambda_{\mathbf{1}}(A)}{\partial A_i \partial A_j} \right] \quad 44a$$

Under general regularity conditions, satisfied by this problem, one can interchange the partial derivatives with the expectation operator. Doing this, and replacing the log-ML function, as given by equation 11, we get

$$J_{ij} = -\frac{1}{2} G' \left. \frac{\partial^2 \phi(A, A_a)}{\partial A_i \partial A_j} \right|_{A=A_a} \quad 44b$$

where G' is a multiplicative gain

$$G' = 2 \frac{\bar{E}_R}{N_O} \frac{\bar{E}_R}{N_O + \bar{E}_R} \quad 44c$$

Recalling the matrix M defining the ellipsoidal structure of the GAF main lobe we can rewrite FIM as

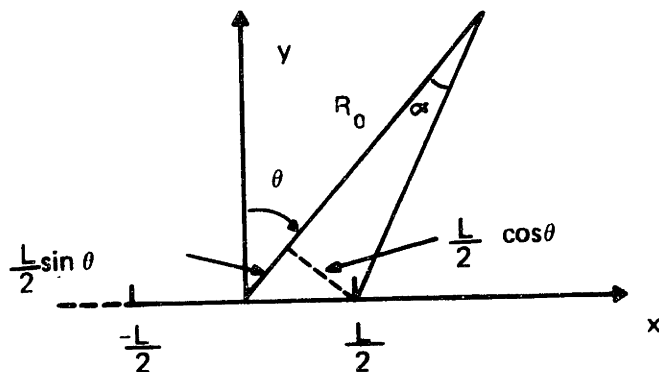
$$J = G' M \quad 45$$

The spread matrix M is computed in Appendix B, where closed form expressions are presented.

We observe that the elements of M , apart scaling factors (equation B-39), are only functionally dependent on the bearing angle θ and

$$X = \frac{Z}{R_O} \quad 46$$

From figure 16 one obtains



Geometric Interpretation of X Parameter

$$\tan \alpha = \frac{X \cos \theta}{1 - X \sin \theta}$$

Figure 16

47

i.e., X relates directly to the angle α spanned by the receiver at the source location R_0 . For a broadside geometry

$$\theta = 0$$

48a

and

$$\tan \alpha = X$$

48b

As in the delay/Doppler radar, the elements of \mathbf{M} are additively given by two terms. With active systems, e.g., Appendix in [Va 71b]

$$M_{11} = \bar{t}^2 = \int_{-\infty}^{\infty} t |\tilde{s}(t)|^2 dt \quad 49a$$

and

$$M_{22} = \bar{w}^2 = \int_{-\infty}^{\infty} w |\tilde{s}(jw)|^2 \frac{dw}{2\pi} \quad 49b$$

$$M_{12} = \bar{t} \bar{w} \quad 49c$$

where $\tilde{s}(jw)$ is the Fourier transform of $s(t)$. In radar, and except in multitone applications, these quantities can usually be made zero by convenient choice of the time origin and carrier frequency. With the passive problem, and inspecting equations B-25 through B-38, we see that, for a broadside geometry, i.e., $\theta=0^\circ$

$$M_1 \sin\theta = 0 \quad 50$$

i.e., the first moment is centralized.

Due to the analytical complexity of the closed form expressions defining the bounds, equations through B-38, and aiming at getting a more intuitive quantitative description of the bounds, we continue, by first doing a local analysis

via a Taylor series expansion. Secondly we study its asymptotic behavior, as the array length increases without bound. Finally, we plot the Cramer-Rao bounds as computed exactly with a digital computer, and compare these results with the local asymptotic expressions.

4.1.1 Short Observation Interval Analysis of the Cramer-Rao Bounds

For most of the applications, we face the fact that the geometric parameter X will be small. As long as

$$X = \frac{L}{2R_0} \quad \text{or} \quad X = \frac{vT}{2R_0} < 1 \quad 51$$

a Taylor Series (TS) analysis is valid, and leads to meaning full results. Accordingly, we consider here this type of approach.

Truncation after the first nonzero term leads to

$$M \cong \left(\frac{2\pi}{\lambda} \right)^2 \left[\begin{array}{l} \frac{\cos^4 \theta X^4}{45} \quad R_0 \frac{11 \sin \theta \cos^2 \theta X^4}{45} \\ = \quad R_0^2 \frac{X^2}{3} \end{array} \right] \quad 52a *$$

For the Cramer-Rao bounds we are also interested on the inverse matrix

*Similar expressions for the diagonal elements of M , for the short observation interval analysis, have also been arrived at, with a somewhat different argument, by Bangs [Ban71], and Bangs and Schultheiss [Ban73].

$$M^{-1} \cong \left(\frac{\lambda}{2\pi}\right)^2 \begin{bmatrix} \frac{45}{\cos^4 \theta X^4} & -\frac{33 \sin \theta}{R_0 \cos^2 \theta X^2} \\ \text{---} & \text{---} \\ = & \frac{3}{R_0^2} \frac{1}{X^2} \end{bmatrix} \quad 52b$$

The determinant is

$$\text{Det } M \cong \left(\frac{2\pi}{\lambda}\right)^4 \frac{R_0^2 \cos^4 \theta X^6}{3^3 X^5} \left[1 + \frac{3}{5X^7} (-11 \cos^2 \theta + 29 \sin^2 \theta) X^2\right] \quad 52c$$

We remark that, in the expression of Det M, the coefficient of X^8 has been computed using the higher order terms contributing to it, but not shown in equation 52a.

The eigenvalues and eigenvectors for M are, up to first order, given by

$$\lambda_{R_0} \cong \left(\frac{2\pi}{\lambda}\right)^2 \frac{\cos^4 \theta X^4}{45} \quad e_{R_0} \cong \begin{bmatrix} 1 \\ 0 \end{bmatrix} \quad 53a$$

$$\lambda_{\sin \theta} \cong \left(\frac{2\pi}{\lambda}\right)^2 \frac{R_0^2 X^2}{3} \quad e_{\sin \theta} \cong \begin{bmatrix} 0 \\ 1 \end{bmatrix} \quad 53b$$

The Cramer-Rao bounds are obtained by readjusting M^{-1} by a gain. From Equations 43 and 45 we obtain

$$\Lambda_{\epsilon} = \begin{bmatrix} \Lambda_{R_0} & \Lambda_{R_0} \sin \theta_0 \\ \text{---} & \text{---} \\ = & \Lambda_{\sin \theta} \end{bmatrix} \geq G^{-1} M^{-1} \quad 54$$

The standard deviations are

$$\sigma_{R_0} = \Lambda_{R_0}^{1/2} \geq \left[\frac{1}{\frac{2\bar{E}_R}{N_0} \frac{\bar{E}_R}{N_0 + \bar{E}_R}} \left(\frac{\lambda}{2\pi} \right)^2 \right]^{1/2} 3\sqrt{5} \frac{1}{\cos^2 \theta X^2} \quad 55a$$

$$\sigma_{\sin \theta} = \Lambda_{\sin \theta}^{1/2} \geq \left[\frac{1}{\frac{2\bar{E}_R}{N_0} \frac{\bar{E}_R}{N_0 + \bar{E}_R}} \left(\frac{\lambda}{2\pi} \right)^2 \right]^{1/2} \frac{\sqrt{3}}{R_0} \frac{1}{X} \quad 55b$$

Recalling that

$$\bar{E}_R = \text{average received energy} = P_n T_L (2\sigma_b^2) \quad 55c$$

where we renormalized the received power as

$$P_n = \frac{P}{\left(\frac{R_0}{R_r} \right)^2} \quad 55d$$

with R_o^r standing for the nominal range of operation for which the system has been designed.

The bracketted term in equations 55a and 55b can be rearranged as

$$G^{-1/2} = \left[1 + \frac{N_o}{P_n (2\sigma_b^2)} \frac{1}{LT} \right]^{1/2} \frac{1}{\sqrt{\frac{2P}{N_o} (2\sigma_b^2) \left(\frac{2\pi}{\lambda}\right)^2}} \frac{R_o}{R_o^r} \frac{1}{\sqrt{LT}} \quad 56a$$

Define

$$SNR_{eq} = \frac{2P(2\sigma_b^2)}{N_o} \left(\frac{2\pi}{\lambda}\right)^2 \quad 56b$$

$$SNR_{eff} = \frac{SNR_{eq}}{\left(\frac{R_o}{R_o^r}\right)^2} \quad 56c$$

$$\alpha = \left[1 + \frac{N_o}{2P_n \sigma_b^2} \frac{1}{LT} \right]^{1/2} \quad 56d$$

SNR_{eq} is an equivalent signal to noise ratio taking into account the channel Rayleigh fading (factor $2\sigma_b^2$), and the effect of the modulation index

$$\beta = \frac{2\pi}{\lambda} \quad 56e$$

SNR_{eff} is the effective signal to noise ratio at the receiver level, after normalizing the emitted power with the inverse of the square distance. This normalization accounts for the spherical geometry of the signals propagation, i.e., that the radiated energy is uniformly spread on a (2-dimensional) sphere centered at the source location, and which expands as the observer gets further apart.

The gain can now be rewritten as

$$G^{-1/2} = \frac{\alpha}{\sqrt{\text{SNR}_{\text{eff}}}} \frac{1}{\sqrt{LT}} \quad 57$$

The standard deviations

$$\sigma_{R_o} \geq \frac{\alpha}{\sqrt{\text{SNR}_{\text{eff}} LT}} \frac{3\sqrt{5}}{\cos^2 \theta X^2} = \frac{1}{\sqrt{\text{SNR}_{\text{eff}} LT}} g_{R_o}(\theta, X) \quad 58a$$

$$\sigma_{\sin} \geq \frac{\alpha}{\sqrt{\text{SNR}_{\text{eff}} LT}} \frac{\sqrt{3}}{R_o X} = \frac{1}{\sqrt{\text{SNR}_{\text{eff}} LT}} g_{\theta}(R_o, X) \quad 58b$$

In these expressions, we separated the dependence of the standard deviations on the parameters, into two factors. The first is due to power level considerations, and involves detailed model specifications. The second reflects how the modulations induced on the signal spatial/temporal structure affect the performance. We see that, the bearing estimation

is fundamentally dependent on linear effects (e.g., linear delay across the array or observed Doppler). The range performance deteriorates with X^{-2} , as it is intuitively clear, from the fact that the range focusing is essentially achieved from the second order effects (e.g., spherical curvature of the incoming wavefronts with the stationary array-stationary source; and chirp modulations induced on the signal temporal structure by the relative dynamics, with the moving omnidirectional sensor with stationary source). We also note that σ_{R_0} increases monotonically as we go from broadside to end fire, as a consequence of a reduction on the effective array length. The angle estimation grows worse as the source/receiver separation increases.

Finally the cross correlation between the errors on the parameter estimates, as predicted by the Cramer-Rao inequality is

$$\rho_{R_0, \sin\theta} \cong \frac{M^{-1}_{12}}{\sqrt{M^{-1}_{11} M^{-1}_{22}}} \cong - \frac{11 \sin\theta X}{\sqrt{15}} \quad 59$$

For small X the errors are almost uncorrelated. A similar conclusion could be taken from the eigenvalues of M , as given by 53a and 53b. They show that up to truncation to the lowest nonzero power of X for the eigenvalues, the estimation problem is essentially uncoupled.

4.1.2 Asymptotic Behavior of the Cramer-Rao Bounds

In Appendix C we study the asymptotic behavior of the elements M_{ij} as the geometric parameter

$$x = \frac{z}{R_0} \rightarrow \infty \quad (60a)$$

or equivalently

$$Y = \frac{R_0}{Z} \rightarrow 0 \quad (60b)$$

We stress that the analysis considers only the phase information, neglecting amplitude attenuation effects across the observing array.

We summarize here the main results.

$$M \sim \left(\frac{2\pi}{\lambda}\right)^2 \left[\begin{array}{c|c} \sin^2\theta + \cos\theta \cos\left(2\theta \frac{\pi}{2} Y\right) & \\ \hline R_0 \left(-\sin\theta + \frac{\pi}{2} \sin\left(2\theta Y\right)\right) & R_0^2 \left(1 - \frac{\cos 2\theta}{\cos\theta} \frac{\pi}{2} Y\right) \end{array} \right] \quad (61a)$$

$$\text{Det } M \sim \left(\frac{2\pi}{\lambda}\right)^4 R_0^2 \frac{\pi}{2} \frac{Y}{\cos\theta} \quad (61b)$$

$$M^{-1} \sim \left(\frac{\lambda}{2\pi}\right)^2 \left[\begin{array}{c|c} \frac{2}{\pi} \frac{\cos\theta}{Y} - \cos 2\theta & \frac{\sin 2\theta}{R_o} \left(\frac{1}{\pi Y} - \cos\theta\right) \\ \hline = & \frac{1}{R_o^2} \left(\frac{2}{\pi} \frac{\cos\theta \sin^2\theta}{Y} + \cos^2\theta \cos 2\theta\right) \end{array} \right] \quad (61c)$$

The Cramer-Rao bounds are obtained by scaling M with the signal energy to noise ratio gain G given by equation 57

$$G^{-1/2} = \frac{\alpha}{\sqrt{\text{SNR}_{\text{eff}}}} \frac{1}{\sqrt{LT}} \quad (62)$$

If the estimation problem reduces to a single parameter estimation, the other parameter being assumed known a priori, the standard deviations are given by

$$\sigma_{R_o} \sim G^{-1/2} \frac{1}{\sin^2\theta_o} \quad (\text{Bearing Known}) \quad (63a)$$

or

$$\sigma_{\sin\theta_o} \sim G^{-1/2} \frac{1}{R_o} \quad (\text{Range Known}) \quad (63b)$$

Because

$$G^{-1/2} \xrightarrow{L \rightarrow \infty} 0 \quad (64a)$$

we obtain

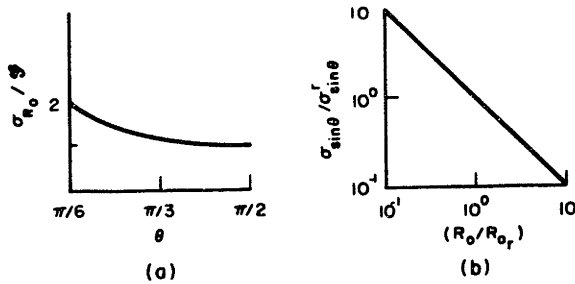
$$\sigma_{R_0} \xrightarrow{L \rightarrow \infty} 0 \quad (64b)$$

or

$$\sigma_{\sin\theta} \xrightarrow{L \rightarrow \infty} 0 \quad (64c)$$

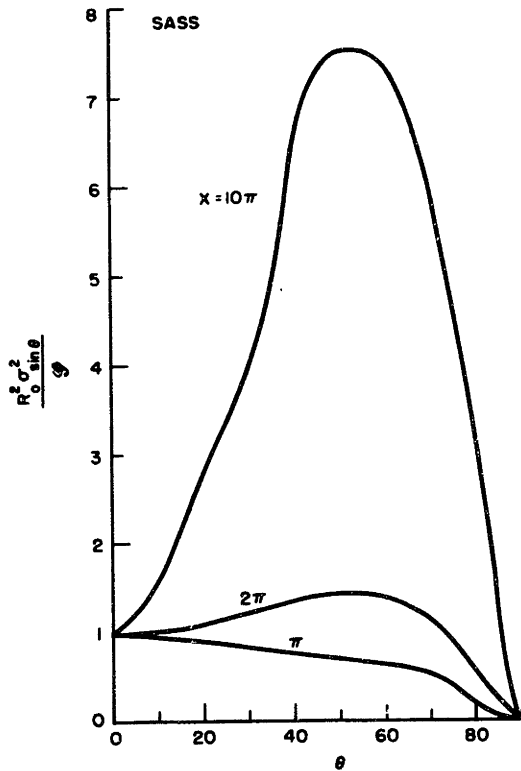
This reflects the unrealistic assumption of an array with infinite gain. For large, but finite array gain L , the individual parameter performances depend on the relative source/receiver geometry, as illustrated by figures 17a and 17b.

Both curves present an intuitively satisfying behavior. As the geometry progresses from broadside to end fire, and when the effective array length is larger than the source/array center separation R_0 , the source gets closer to the receiver, and the performance of the single range parameter estimation problem improves. Similarly, expression 63b or figure 17b, says that the single parameter angle performance for large arrays is determined by the source/receiver separation.

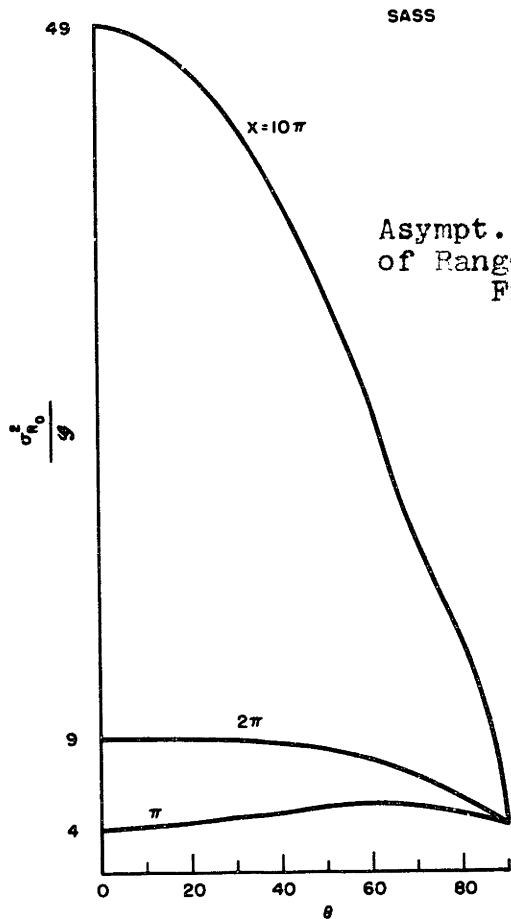


Asympt. Beh. of single MSSM, SASS param.

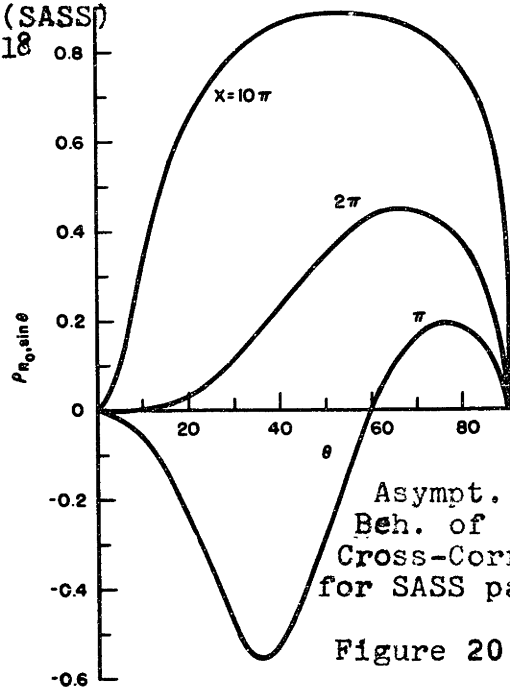
Figure 17



Asympt. Beh. of MSSM Angl. Par. SASS
Figure 19



Asympt. Beh. MSSM of Range Par. (SASS)
Figure 18



Asympt. Beh. of Cross-Corr. for SASS par.
Figure 20

Consider now the full SASS problem. The mean square range and bearing asymptotic spread functions

$$f_{R_0}(Y, \theta) = \frac{2}{\pi} \frac{\cos \theta}{Y} - \cos 2\theta \quad (65a)$$

$$f_{\theta}(Y, \theta) = \frac{1}{R_0^2} \left[\frac{2}{\pi} \frac{\cos \theta \sin^2 \theta}{Y} + \cos^2 \theta \cos 2\theta \right] \quad (65b)$$

are studied analytically in Appendix C. They are also displayed in figures 18 and 19.

These curves show that, for large effective array length, the receiver's behavior is highly sensitive to the relative geometry of the problem. This is due to the high correlation between the errors in the estimates. The cross correlation for $\theta \neq 0, \frac{\pi}{2}$.

$$\rho_{R_0, \sin \theta}^2 \sim \frac{\sin^2 \theta - 2 \frac{\pi}{2} Y \sin \theta \sin 2\theta}{\sin^2 \theta + \frac{\pi}{2} Y \frac{\cos^2 2\theta}{\cos \theta}} \cong 1 - \frac{\pi}{2} Y \frac{1}{\sin^2 \theta \cos \theta} \xrightarrow{Y \rightarrow 0} 1 \quad (66)$$

tends asymptotically to 1 (perfect correlation), and M becomes singular, as Y goes to zero. For small, nonzero Y , the behavior is highly dependent on the geometry as illustrated by figure 20.

The asymptotic behavior of the mean square performance bounds are obtained by scaling the diagonal elements of M^{-1} in equation 61c. We obtain

$$\sigma_{R_o}^2 \sim G^{-1} f_{R_o}(Y, \theta) = G^{-1} \left[\frac{2}{\pi} \frac{\cos \theta}{Y} - \cos 2\theta \right] \quad (67a)$$

$$\sigma_{\sin \theta}^2 \sim G^{-1} f_{\theta}(Y, \theta) = G^{-1} \frac{1}{R_o^2} \left[\frac{2}{\pi} \frac{\cos \theta \sin^2 \theta}{Y} + \cos^2 \theta \cos 2\theta \right] \quad (67b)$$

As the array length increases

$$\sigma_{R_o}^2 \longrightarrow \sigma_{R_{o\infty}}^2 = \frac{\alpha^2}{(\text{SNR}_{\text{eff}}^T)} \frac{2}{\pi} \frac{\cos \theta}{R_o} \quad (68a)$$

$$\sigma_{\sin \theta}^2 \longrightarrow \sigma_{\sin \theta_{\infty}}^2 = \frac{\alpha^2}{(\text{SNR}_{\text{eff}}^T)} \frac{2}{\pi} \frac{\cos \theta}{R_o} \frac{\sin^2 \theta}{R_o^2} \quad (68b)$$

with the relation

$$\left(\frac{\sigma_{R_{o\infty}}}{R_o} \right)^2 = \left(\frac{\sigma_{\sin \theta_{\infty}}}{\sin \theta} \right)^2 \quad (68c)$$

For large values of X the range and bearing performance approach the asymptotic values 68a and 68b. But the estimation problem is highly sensitive, since in the limit, as $X \rightarrow \infty$, the spread matrix becomes singular, as noted above. The asymptotic values 68a and 68b combine this highly sensitive behavior with the unrealistic assumption of an array with unbounded gain. In order to retain the simultaneous identifiability of both range and bearing we need at least the first order terms in Y .

An intuitive explanation for this apparently pathological behavior can be given, if we analyse the range phase history for the ∞ -observation interval. Rewrite the range phase as

$$R(\ell) = \{(\ell - R_0 \sin \theta)^2 + R_0^2 \cos^2 \theta\}^{1/2}, \ell \in [-\frac{L}{2}, \frac{L}{2}] \quad (69)$$

and define the range phase information content on the observations as the graph of the range phase

$$R_L = \{R(\ell) = \{(\ell - R_0 \sin \theta)^2 + R_0^2 \cos^2 \theta\}^{1/2}, \ell \in [-\frac{L}{2}, \frac{L}{2}]\} \quad (70a)$$

Set

$$R_Z = \{R(z) = \{z^2 + R_0^2 \cos^2 \theta\}^{1/2}, z \in [-Z, +Z]\} \quad (70b)$$

If

$$Z = \frac{L}{2} - R_0 \sin\theta \quad (71)$$

we have

$$R_L = R_Z ;$$

when

$$L \rightarrow \infty \implies Z \rightarrow \infty ,$$

and we obtain the isomorphism of the two information contents

$$\lim_{L \rightarrow \infty} R_L = R_{Z=\infty} \quad (72)$$

But $R_{Z=\infty}$ is completely determined by the single parameter

$$R_0 \cos\theta_0 = \text{distance from source to the linear observer,}$$

and so, for an infinitely large array, this is the identifiable parameter.

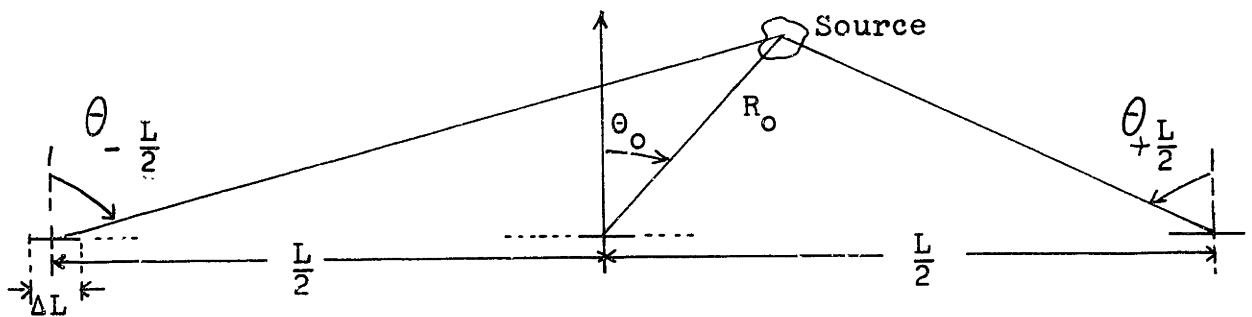
4.1.3 Very Long Baseline Staved Array

In radio and radar astronomy it is well known that Very Long Baseline Interferometry (VLBI) achieves high angular resolution by using two or more widely separated radio telescopes [IEEE Proceedings Special Issue on Radio And Radar Astronomy, vol. 61, no. 9, pp. 1164-1376, Sept. 1973]. The quantity which one measures on VLBI techniques is simply a differential delay--the difference between the times of propagation from the source to two or more separate receiving sites. A complete analysis of the techniques to estimate this differential delay from the data recorded simultaneously at the separate receiving stations, and the accuracy attained, has been given by [Hin 72] and [Rog70]. Essentially with natural radio sources, the attainable accuracy, within each fringe of ambiguity, is inversely proportional to the carrier frequency and the available signal to noise ratio. The VLBI concept has also been applied with coherent sources, i.e., sources whose emitted signals are slowly varying sinusoidals, as the artificial radio transmitters used with the Apollo Lunar Surface Experiment Package (ALSEP) [IEE73], [Con73], developed for tracking the Lunar Rover Vehicle.

With these VLBI techniques the source is assumed at infinity ("distant" observer). We study now performance bounds for a simple geometry, where a very long baseline

observer is generated by linear arrays located at distant sites, with simultaneous measurement of the angle and range source parameters. The essential distinction with the VLB interferometry is that now we analyse the possibility of measuring the source/receiver separation from the phase modulations, by assuming that the source is within the observer's finite geometry. This will be made precise subsequently.

Figure 21 illustrates a linear observer composed of three widely separated short colinear arrays placed far apart of each other. We derive the Cramer Rao performance bounds for the range and bearing parameters, under suitable assumptions made explicit below.



Long Baseline (3-element) Staved Linear Array

Figure 21

For $R_0 \gg \Delta L$ we linearize in Appendix C the range phase function across each individual stove, about its geometric center. Also for $R_0 \ll L$ we approximate $\sin(\theta_{\pm \frac{L}{2}})$ by the arc. With these simplifications the Cramer-Rao² bounds derived in Appendix C are

$$\sigma_{\sin} \approx \frac{\alpha}{\sqrt{\text{SNR}_{\text{eff}}}} \frac{1}{\sqrt{\Delta L T}} \sqrt{\frac{3}{2}} \frac{1}{\pi} \left(\frac{1}{\lambda} \right) \quad (73a)$$

and

$$\sigma_{R_0} \approx \sigma_{\sin} \tan^2 \theta_{\frac{L}{2}} R_0 \quad (73b)$$

These expressions illustrate the performance achieved by triangulation with a linear scheme, when the simplifications assumed hold. We conclude that the angle performance is determined from the central element, while the range observation is accomplished by triangulation with the end point elements. Finally from equations 73 we see that the performance deteriorates monotonically with the viewing angle $\theta_{\frac{L}{2}}$:

$$\sigma_{R_0} \xrightarrow{\theta_{\frac{L}{2}} \rightarrow \frac{\pi}{2}} \infty \quad (73c)$$

4.1.4 Graphical Representation of the Cramer-Rao Bounds

We evaluate in a digital computer the exact closed form expressions B-25 to B-38 of the elements of the inverse mean square spread matrix M^{-1} , and the Cramer-Rao bounds obtained after normalizing them by the gain G.

The nominal conditions assumed are:

$$R_o = R_o^r = 6 \times 10^4 \text{ feet}$$

$$\theta = 15^\circ$$

$$\lambda = 50 \text{ feet}$$

$$\beta = \frac{2\pi}{\lambda} = \text{modulation index}$$

$$\text{SNR} = P/N_o = -3\text{dB}$$

$$2\zeta_b^2 = 1$$

T=250 sec for the stationary array-stationary source

L=250 feet, v=30 feet/sec for the moving omnidirectional sensor with stationary source.

In figures 22, 23, and 24 we represent the diagonal elements of M^{-1} normalized by the square of the modulation index

$$\tilde{M}_{ii}^{-1} = \frac{M_{ii}^{-1}}{\left(\frac{\lambda}{2\pi}\right)^2}, i=R_o, \sin\theta$$

and the cross-correlation $\rho_{R_o, \sin\theta}$ as a function of the geometric parameter X.

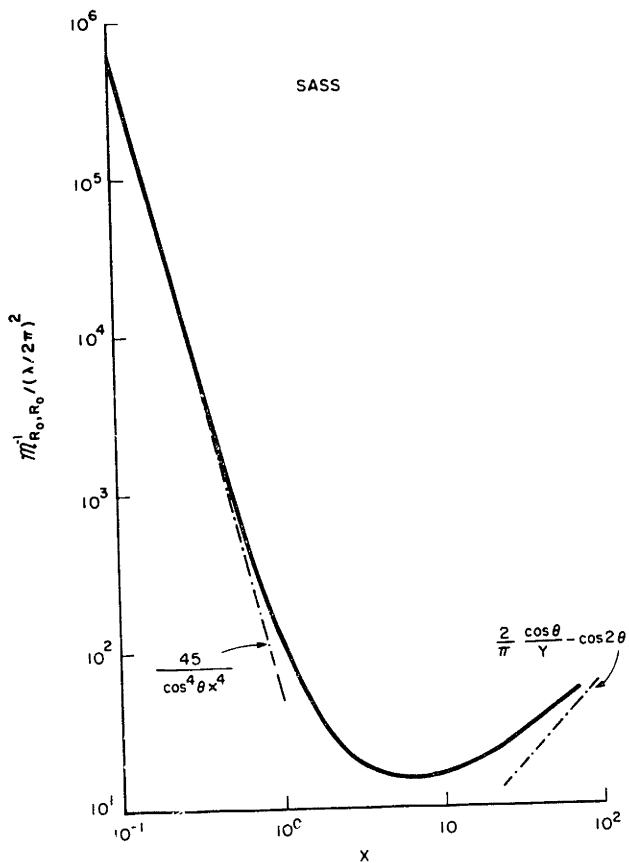


Fig. 22 Inv. Ran MSS versus X

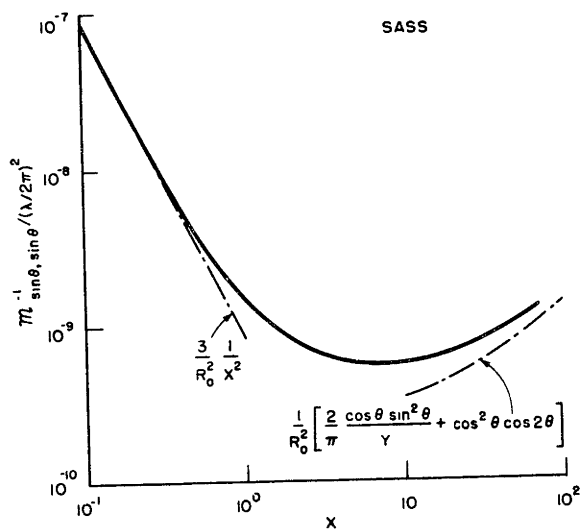


Fig. 23 Inv. angle MSS versus X

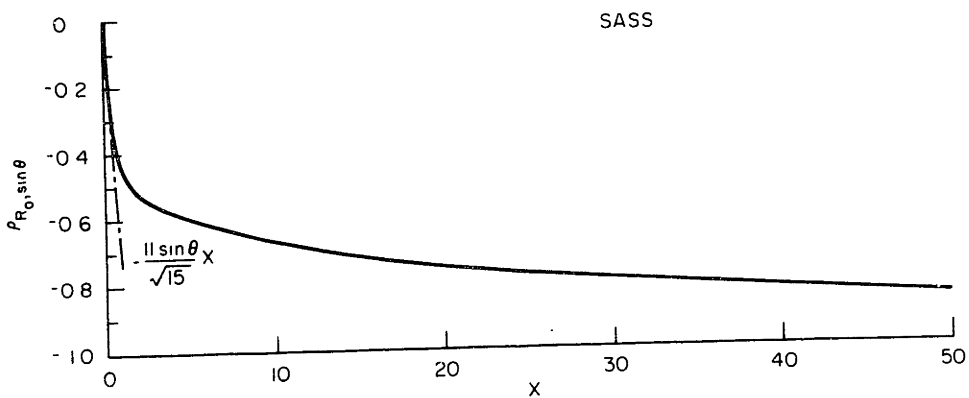


Figure 24 Range/angle Cross-Correlat. versus X

We observe the quadratic (convex cup) behavior of the range and bearing mean square spreads. This is the result of two different phenomena. For small X (distant observer) the main lobe is spreaded out and flat at the origin (source location), with corresponding large inverses of the second order derivatives of GAF; when X increases it gets sharper, but the cross correlation also decreases monotonically to -1 with a shearing of the main lobe. As a consequence, the spread functions bottom down at a value of X between 6 and 7 and then increase monotonically. These figures also display the local and asymptotic tangents to which the spread functions converge and which were derived in sections 4.1.1 and 4.1.2.

Figures 25, 26 show the range and bearing standard deviations predicted by the Cramer-Rao bounds, when the parameter X varies. These curves are a consequence of associating to the geometric effects displayed in figures 22 and 23 the energy to noise ratio gain, which increases with X , leading to an overall steady improvement in the predicted accuracy as we would expect. But we stress that, for large X , sensitivity problems arise since the estimation errors get highly correlated, as displayed by the right ends of figure 24, or predicted by the analytical results of the asymptotic analysis.

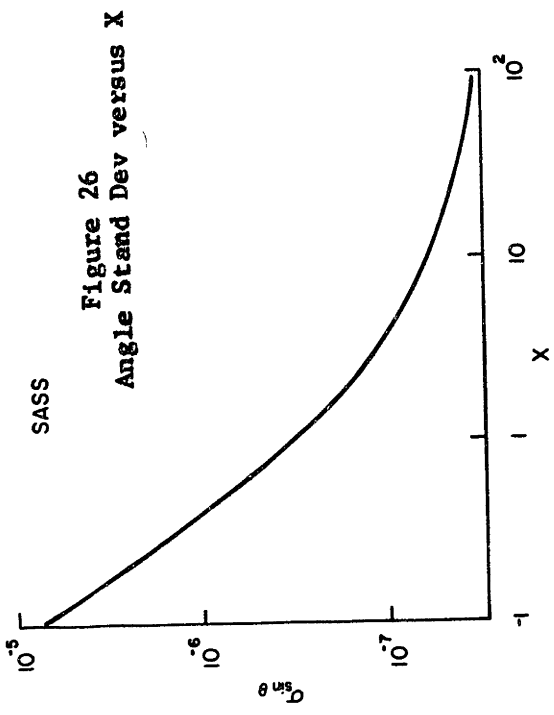
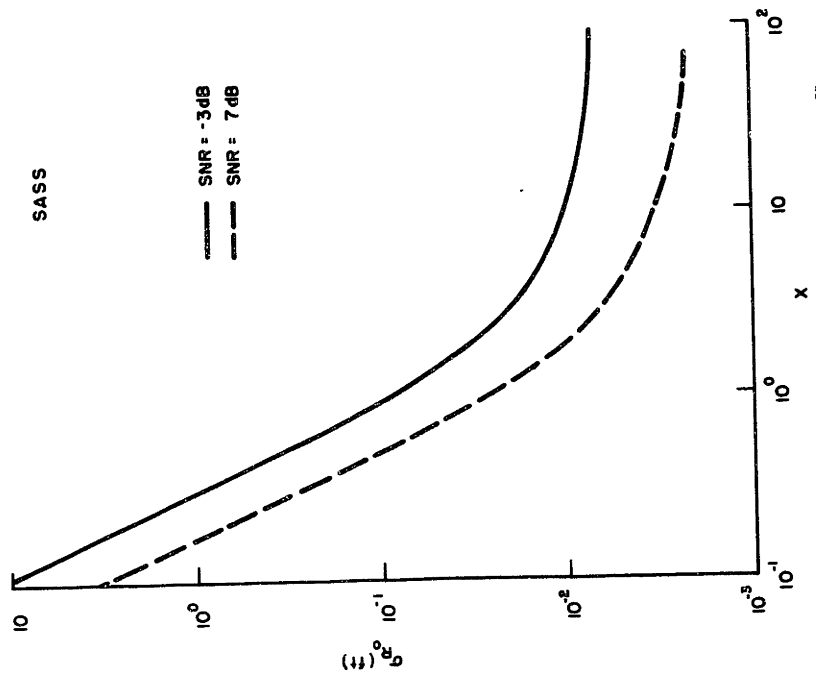
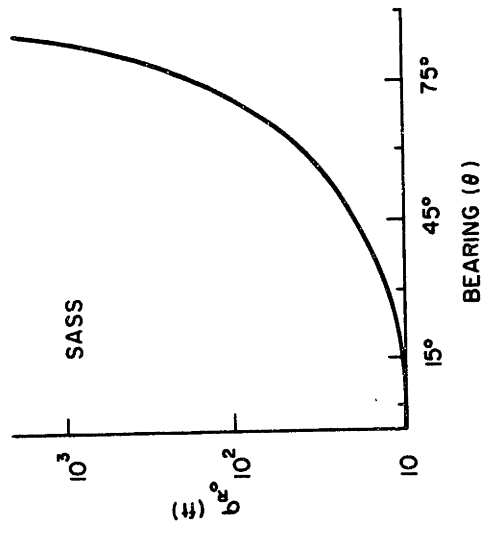


Fig. 27 Ran Stand Dev versus Bear. Ang.



Finally, in figure 27 is shown the behavior of σ_{R_0} as a function of the bearing angle θ , for a small value of X , namely

$$X = \frac{1}{2}$$

The performance deteriorates when the geometry progresses from a broadside to an end fire, as concluded from the local analysis.

4.2 Global Performance

The Cramer-Rao bounds studied in the previous paragraphs place theoretical limitations to the accuracy of the source parameter estimates. In the sequel, we analyze how these bounds compare to the mean square errors (MSE) in the algorithm implementing the ML-estimation, by working directly with equation 34 here in repeated

$$\begin{aligned} E(A_{j\epsilon}^2) &= E[(A_j - A_{j_{ml}})^2] \\ &= E(A_{j\epsilon}^2 | \epsilon) \Pr(\epsilon) + E(A_{j\epsilon}^2 | \bar{\epsilon}) [1 - P_r(\epsilon)] \end{aligned} \quad 74$$

From physical considerations, dependent upon the particular application, we delimit the region of interest Ω of the parameter space, to the 2-dimensional rectangle

$$\Omega = \sum_{i=1}^2 [A_{j_m}, A_{j_M}] = [R_{o_m}, R_{o_M}] x [\sin\theta_m, \sin\theta_M] \quad 75$$

Designing the elementary cell of the grid discretizing Ω on the coarse search step, as the ellipsoide defined by the quadratic form

$$Q(\Delta A) = (\Delta A)^T M(\Delta A) = 1$$

it follows, from the negligible side lobe structure of the ambiguity function (see section 3), that the signals evaluated at points in different cells are uncorrelated. These considerations justify, that we model the coarse search, as an M-ary hypothesis decision testing problem with orthogonal signals transmitted over a Rayleigh channel.

Under hypothesis H_n , $n=1, \dots, M$ the received waveform is

$$H_n = \tilde{r}_n(t) = \sqrt{2} \operatorname{Re} \left\{ \left[\sqrt{\frac{E_r}{LT}} \delta \exp \left(j \frac{2\pi}{\lambda} \sqrt{R_{o_n}^2 + x^2 + 2xR_{o_n} \sin\theta_n} \right) + \tilde{w}(x) \right] \exp(-j\omega_c x) \right\} \quad n \in M = \{1, \dots, M\}$$

with

M = total number of cells of Ω ;

$A_n = \begin{bmatrix} R_{o_n} \\ \sin\theta_n \end{bmatrix}$ = center coordinates of each cell;

$\tilde{w}(x)$ = complex "white" Gaussian noise with double spectral height of N_0 .

The hypotheses are a priori equally probable since, besides the overall dimensions of Ω , no further knowledge on the source parameters is assumed.

The first step of the estimation algorithm is then a "largest of" receiver choosing the largest ℓ_m of the sufficient statistics

$$\ell_n = |\tilde{L}_n|^2 = |\langle \tilde{r}(t), \tilde{s}(t, \ell, A_n) \rangle|^2, \quad n \in M$$

and identifying the ML-estimate

$$\tilde{A}_{m\ell} = A_m$$

We proceed with the computation of each quantity in equation 74.

$$4.2.1 \quad \underline{E(A_{j\epsilon}^2 | \epsilon)}$$

$$E(A_{j\epsilon}^2 | \epsilon) = E[(A_j - A_{jm\ell})^2 | \epsilon]$$

$$= E\{[(A_j - \bar{A}_j) - (A_{jm\ell} - \bar{A}_j)]^2 | \epsilon\}$$

$$= E[(A_j - \bar{A}_j)^2 | \epsilon] + E[(A_{jm\ell} - \bar{A}_j)^2 | \epsilon] - 2E[(A_j - \bar{A}_j)(A_{jm\ell} - \bar{A}_j) | \epsilon]$$

76a

where

$$\bar{A}_j = E(A_j | \epsilon) = E(A_{jm\ell} | \epsilon) = \frac{A_{jM} - A_{jm}}{2} \triangleq \frac{\Delta_M A_j}{2}$$

The second equality follows because if a diversion occurred, by the orthogonal signals assumption, it is equally likely to have been decided upon any one of the wrong cells. From this we also conclude that the last term in equation 76a is zero. The other two terms will be bounded by

$$E[(A_j - \bar{A}_j)^2 | \epsilon] = E[(A_{jm\ell} - \bar{A}_j)^2 | \epsilon] \leq \frac{(A_{jM} - A_{jm})^2}{12} = \frac{\Delta_M A_j^2}{12},$$

where we neglect the influence of diversions carrying no error on the A_j parameter. It follows then

$$E(A_j | \epsilon) \geq 2\sigma_{A_j}^2 = \frac{(A_{jM} - A_{jm})^2}{6} = \frac{\Delta_M A_j^2}{6} \quad 76b$$

4.2.2 Probability of a Diversion

The probability of a diversion is the probability of error on an M-ary decision with orthogonal signals transmitted over a Rayleigh channel. Several authors have studied this probability of error for M-ary signaling over fading channels,

*The ML-estimates have an MAP interpretation, namely that they coincide with the Maximum A Posteriori estimates, when the parameters a priori distribution is uniform in Ω . For the purpose of computing the MSE when a diversion occurs, we use this MAP interpretation, and model A_j as uniformly distributed in $[A_{jm}, A_{jM}]$, $j=1,2$.

conform [Pie 58], or for additional references see [Va 71b]. The exact expression is

$$\Pr(\epsilon) = \sum_{i=1}^M \binom{M-1}{n} \frac{(-1)^{n+1}}{n+1+n\beta} \quad 77a$$

where

$$\beta = \frac{\bar{E}_R}{N_0} = \frac{2G_b^2 E_t}{N_0} \quad 77b$$

Equation 77a is an alternating series of large terms posing numerical problems in a digital computer. [Sus 64]

has derived more convenient equivalent expressions and several approximations displaying the functional dependence of $\Pr(\epsilon)$ on the several parameters. In particular we have

$$\Pr(\epsilon) = 1 - \frac{\Gamma\left(1 + \frac{1}{\beta+1}\right) \Gamma(M)}{\Gamma\left(M + \frac{1}{\beta+1}\right)} \quad 78$$

where Γ is the gamma function.

For

$$\beta \gg 1 \quad 79$$

a truncated Taylor series expansion approximates the probability of a diversion by

$$\Pr(\epsilon) \approx \frac{1}{\beta} [\psi(M) + \gamma] \quad 80a$$

where $\psi(M)$ is the Digamma or Psi function, e.g. [Abr 65]
 defined by

$$\psi(z) = \frac{d}{dz} \ln \Gamma(z) = \frac{\Gamma'(z)}{\Gamma(z)}$$

and γ is the Euler constant

$$\gamma \cong .5772156649$$

From the asymptotic expansion for $\psi(z)$

$$\psi(z) \sim \ln z - \frac{1}{2z} - \frac{1}{12z^2} + \frac{1}{120z^4} - \frac{1}{252z^6} + \dots$$

We get approximately

$$\Pr(\epsilon) \approx \frac{1}{\beta} \left[\ln M - \frac{1}{2M} + \gamma \right] \quad 80b$$

With an error smaller than $\frac{1}{12M^2}$.

Another useful expression follows from

$$\psi(M) = -\gamma + \sum_{k=1}^{M-1} k^{-1}$$

leading to

$$\Pr(\epsilon) \approx \frac{1}{\beta} \sum_{k=1}^{M-1} k^{-1} \quad 80c$$

Figures 28 and 29 compare the probability of a diversion, as computed from the exact and the approximate expressions, and as a function of the energy to noise ratio β , having M as a parameter, and vice versa, respectively. The curves demonstrate the good agreement between both expressions for sufficiently large energy to noise ratio parameter values.

4.2.3 $E(A_j \epsilon^2 | \epsilon^c)$

This quantity represents the mean square error when no diversion occurs, and so the coarse search leads to the correct cell in the Ω region of the parameter space. The fine search proceeds within the main lobe, and this local mean square error will depend on the quantitative description of GAF near the origin.

We note that, for a rectangular grid aligned with the coordinate axis, we have

$$0 \leq E(A_j \epsilon^2 | \epsilon^c) \leq \frac{(A_{jM} - A_{jm})^2}{M_j} \quad 81$$

where M_j is the number of subintervals into which the A_j -axis is divided by the grid.

As the geometric parameter x increases, we noted a shearing effect on the main lobe, with the grid tilting over both axis, so that the high bound in eq. 81 does not hold.

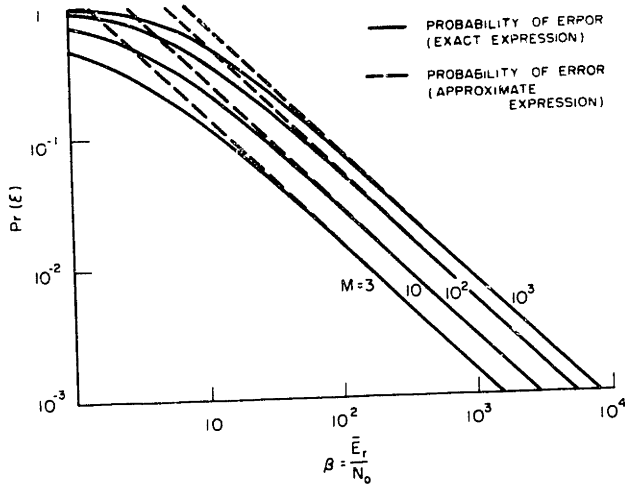


Fig 28 Prob. of Div. versus Sg.En/Nse Ratio

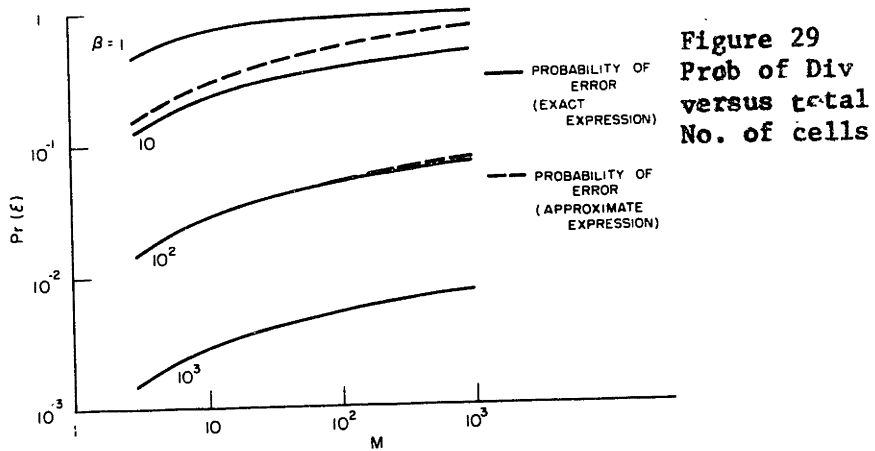
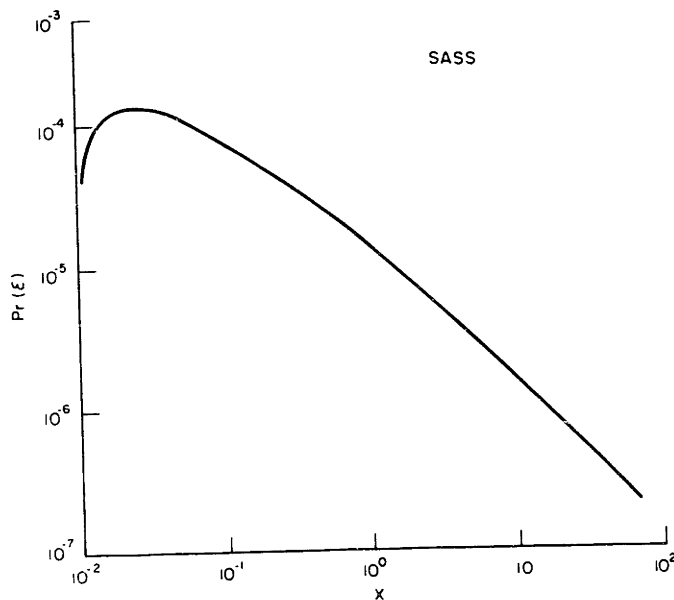


Figure 29
Prob of Div
versus total
No. of cells

Figure 31 Prob of Div versus X



Alternatively, working with a quadratic description for the main lobe, as given by equation 39, it is plausible to approximate the local m.s.e. by the Cramer-Rao bounds computed in paragraph 4.1, i.e., we assume that

$$E(A_j \epsilon^2 | \epsilon^c) \approx \sigma_{jj}^2 \quad 82$$

with σ_{jj} given by 54. In summary, the total mean square error is decomposed on a global and a local component

$$\sigma_{tot_j}^2 = E(A_j^2) \approx \sigma_{gl_j}^2 + \sigma_{loc_j}^2 \quad 83a$$

where

$$\sigma_{gl_j}^2 \approx \frac{\Delta_M A_j^2}{6} \Pr(\epsilon) \quad 83b$$

$$\sigma_{loc_j}^2 = \sigma_{jj}^2 [1 - \Pr(\epsilon)] \quad 83c$$

4.2.4 Performance Graphical Analysis

In the sequel the nominal values are the ones assumed when studying numerically the Cramer-Rao bounds at the beginning of section 4.1.2. Furthermore we take

$$V_\Omega = \Delta_M R_O \times \Delta_M \sin \theta$$

with $\Delta_M R = R_{O_M} - R_{O_m} = 10 R_O$, $\Delta_M \theta = \theta_M - \theta_m \approx 5^\circ$. We start by analyzing the dependence of the probability of error and the total number of grid cells on the geometric parameter X.

We have

$$M = \frac{V_\Omega}{V_a} \tag{84}$$

where

$$V_\Omega = \text{volume of } \Omega = \prod_{j=1}^3 \Delta_M A_j = \Delta_M R_O \times \Delta_M \sin \theta.$$

V_a = volume of elementary cell.

For a fixed V_Ω the total number M decreases with V_a . The volume of the elementary cell depends on the eigenvalues and eigenvectors of M^{-1} which determines the form and dimensions of the cell. In particular we have

$$V_a = k \prod_{i=1}^2 \lambda_i^{-1/2} = k (\text{Det } M)^{-1/2} \tag{85}$$

where

λ_i = eigenvalues of M given by equations 53a and 53b

Det M = determinant of M.

k = constant dependent on the specific form assumed for a.

For the elementary ellipsoide

$$Q(\Delta A) = \Delta A^T M \Delta A = \sum_{j=1}^3 \frac{(\Delta A_j)^2}{\left(\frac{1}{\sqrt{\lambda_j}}\right)^2} = 1$$

We have

$$k = k_\ell = \pi$$

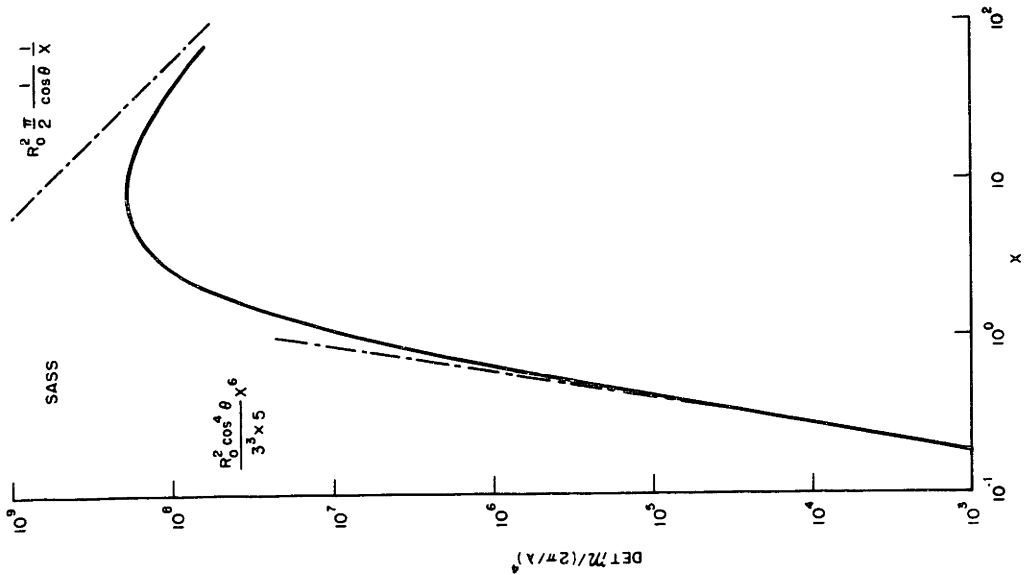
For the rectangular parallelepiped circumscribing this ellipsoide

$$k = k_\rho = 4$$

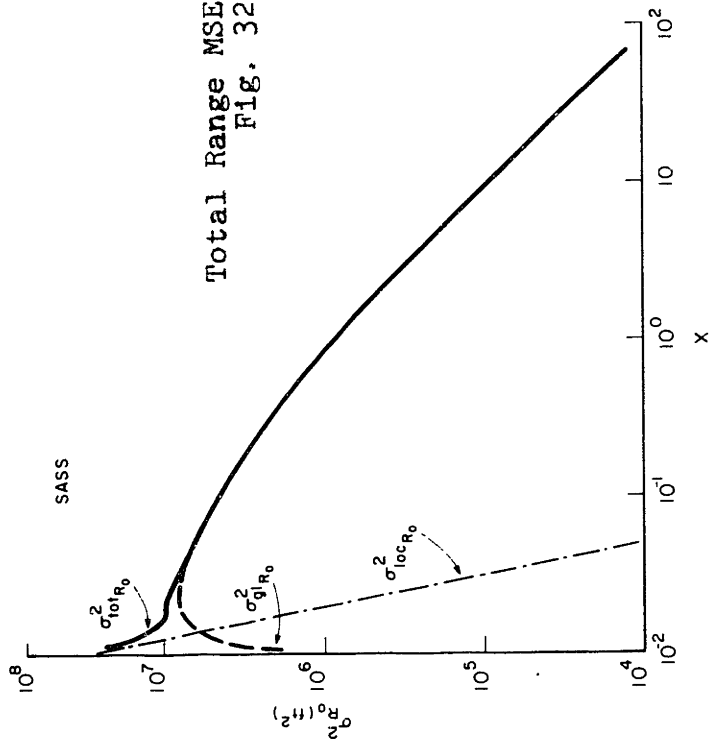
The total number of cells is then

$$M = \frac{V_\Omega}{k} (\text{Det } M)^{1/2} \quad 86$$

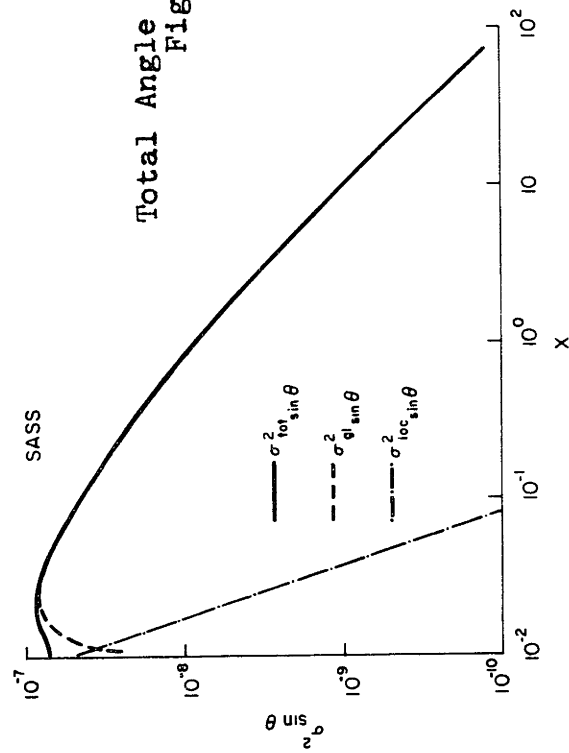
In figure 30 we show Det M as a function of X and the local and asymptotic approximations. The convex cap behavior has essentially the same physical interpretation already noted, namely that for small X the main lobe is flat at the origin and well spread out, while for large X it approaches a sheared rectangular type format.



Det M Versus X
Fig. 30



Total Range MSE Versus X
Fig. 32



Total Angle MSE Versus X
Fig. 33

The total number M presents a similar dependence on X . We observe the large computational work involved when actually implementing the ML-receiver, due to the large number of grid cells.

In figure 31* we show the evolution of the probability of error with X . As X increases, not only M changes accordingly to the cap behavior of figure 30, but the signal energy to noise ratio also increases. Since for very small X the main lobe spreads over all the Ω space, the grid reduces to one cell, and the probability of error vanishes. As X increases M eventually gets larger than 1. Initially this dominates the corresponding increase of $\beta = \bar{E}_r / N_0$, and the probability of error changes drastically to a maximum value, after which it decreases monotonically and in accordance with a $\ln X / X$ law. Estimates on the value of M can be obtained from the local and asymptotic expressions for Det M . Specifically we have for small X

$$M \sim M_{loc} \cong M_{\Omega} \frac{1}{3\sqrt{15}} R_0 \cos^2 \theta X^3 \quad 87a$$

and for large X

$$M \sim M_{asympt} \cong M_{\Omega} \sqrt{\frac{\pi}{2}} R_0 \frac{1}{\sqrt{X \cos \theta}} \quad 87b$$

* See page 110

where

$$M_{\Omega} = \frac{V_{\Omega}}{k} \left(\frac{2\pi}{\lambda}\right)^2 = \frac{\Delta_{M^R} \Delta_{M^{\text{sim}\theta}}}{k} \left(\frac{2\pi}{\lambda}\right)^2 \quad 87c$$

These expressions exhibit the rate of growth of M with the several parameters specifying the model and the geometry, and reflect the dependence of the volume of the elementary cell on the source parameters.

Figures 32 and 33 show the behavior, as a function of X, of the total, as well as the global and local components of the performance bounds. σ_{loc}^2 follows essentially the Cramer-Rao bounds, while σ_{gl}^2 reflects the behavior of $\text{Pr}(\epsilon)$ with X. We note that for small X, the local errors dominate the global ones, since the probability of error is practically zero, due to the wide spread of the main lobe. After a value of $X=X_{tr}$, in between .02 and .04, the algorithm mean square performance is essentially dominated by the global errors. These threshold effects are discussed in more detail on the next paragraph.

4.3 Limiting Behavior of the ML-Algorithm for Large Signal to Noise Ratio and with the Total Number of Independent Observations.

Figures 32 and 33 exhibited a well defined threshold on the processor's performance. For $X < X_{tr}$ the system

behaves as predicted by the Cramer-Rao. For $X < X_{tr}$ the global errors dominate the algorithm behavior, and the performance departs significantly from the one predicted by the Cramer-Rao. For the high signal energy to noise ratio situation, and for

$$\Pr(\epsilon) \ll 1$$

88

the ratio of the two m.s.e. components leads to

$$\delta = \frac{\sigma_{gl_j}^2}{\sigma_{loc_j}^2} \approx \frac{(\Delta_{MA_j})^2 [\text{Ln } M - \frac{1}{2M} + \gamma]}{6 \left(\frac{\lambda}{2\pi}\right)^2 f_j(A, X)}$$

89

where the f_j 's represent the dependence on A and X of the diagonal elements of M^{-1} . This expression shows that, for the high signal energy to noise ratio, δ is practically independent of the signal to noise ratio.

Depending on the several parameters, and as shown by figures 32 and 33, δ may be greater or smaller than 1, with the expected performance dominated by the global or local errors respectively. Where $\delta > 1$, no matter how large we make the signal to noise ratio, the mean square

error performance does not approach the Cramer-Rao bounds. This inherent suboptimality is characteristic of the way the ML-algorithm is implemented, namely the two step procedure.

As commented in section 4.5 of the next chapter, it is easy to prove that the ML-estimates are still asymptotically efficient in the signal to noise ratio sense.

In practice this is not a major issue, and can be circumvented by means of independent measurements. In actual applications the channel characteristics have a finite coherence time, and so multiple independent measurements are available.

It can be easily seen that, for N independent measurements with

$$\tilde{r}_i(t) = \sqrt{2} \operatorname{Re} \{ [\tilde{b}_i \tilde{s}(t) + \tilde{w}_i(t)] \exp(-j\omega_c t) \} \quad i=1, \dots, N$$

90

where the \tilde{b}_i are independent, identically distributed, complex Gaussian random variables, the first step of the algorithm can be modelled as a multiple hypothesis testing with diversity, i.e., an M-ary decision with orthogonal observations transmitted over N-Rayleigh channels. The probability of error can be approximated, for the high signal energy to noise ratio, see

[Van 68],[Va71b] by

$$\Pr(\epsilon) = M \sqrt{\frac{1}{\pi N}} \frac{(1 + \bar{E}_r/N_o)^N}{\frac{\bar{E}_r}{N_o} (1 + \frac{2\bar{E}_r}{N_o})^{2N-1}} \quad 91$$

The Cramer-Rao bounds are given by expressions equivalent to the ones derived before, provided we normalize the signal energy to noise ratio by a factor of N.

It follows for $N \geq 2$

$$\lim_{\text{SNR} \rightarrow \infty} \delta = 0 \quad 92a$$

or

$$\lim_{N \rightarrow \infty} \delta = 0 \quad 92b$$

i.e., that the estimates are asymptotically efficient in both the SNR and classical sense (large N).

Chapter III

Stationary (Omnidirectional) Array with Moving Sources

In chapter II we studied in detail the tracking of stationary sources by linear observers. The problem reduced to the estimation of two parameters - range and bearing - from narrowband passive signals.

In this chapter the class of passive tracking problem is enlarged to include nonstationary sources. In order to resolve for the fundamental issues we restrict the source dynamics to be deterministic and linear. For simplicity we assume a stationary and omnidirectional receiver. In the next chapter we lift this restriction and discuss what are the essential features on a general tracking problem. We will see there how these relate and include the ones dealt with herein.

As with the previous one, this chapter progresses by first establishing the model and discussing the constraints imposed on the problem. The receiver is designed next. Thirdly, we analyze the receiver structure, and finally we study its error performance. The essential aspects of the theory (maximum-likelihood) follow the details described in Chapter III, and we simply refer to the general results contained therein and proceed with their application to the problem at hand.

1. Model

The radiated signals are narrowband, and modeled by

$$s(t) = \sqrt{2} \operatorname{Re}\{\tilde{s}(t)\exp(j\omega_c t)\}$$

The received signal

$$r(t, \ell) = \sqrt{2} \operatorname{Re}\{\tilde{r}(t, \ell)\exp(+j\omega_c t)\}$$

has the complex envelope

$$\tilde{r}(t, \ell) = \tilde{s}(t - \mathcal{T}(t, \ell)) + \tilde{w}(t, \ell)$$

where the delay at time t and point ℓ of the receiving array is approximated by

$$\mathcal{T}(t, \ell) \cong \frac{R(t, \ell)}{c}$$

The signal envelope at the received aperture is

$$\tilde{s}(t - \mathcal{T}(t, \ell)) = \sqrt{\frac{E_r}{LT}} \tilde{b} \exp[-j \frac{2\pi}{\lambda} R(t, \ell)] \quad (1)$$

where, as before, E_r = total received energy during observation interval $[-\frac{T}{2}, \frac{T}{2}]$ by an array of dimension parameter L ;

$R(t, \ell)$ = distance (range) at time t from the source to the array element at location ℓ ; $\lambda = \frac{c}{f} = \text{wavelength}$;

\tilde{b} = zero mean, complex Gaussian random variable = $|\tilde{b}| \exp(-j\psi)$,

with $E|\tilde{b}|^2 = 2\sigma_b^2$. The parameter b accounts for fading in

the transmission path, phase jitter and other model

inaccuracies. As discussed earlier, its presence

is of fundamental importance, reflecting in the model the following equivalence. Define

$$\xi(t, \ell) = \frac{2\pi}{\lambda} [R(t, \ell) \bmod(\lambda)]$$

The observed signal, as given by equation 1 is then equivalent, from an information content, to

$$\tilde{s}(t - \tau(t, \ell)) = \sqrt{\frac{E_R}{LT}} \tilde{\delta} \exp \left[j \xi(t, \ell) \right],$$

in the sense that no information on the source/receiver separation, as measured by an integer number of wavelengths, is conveyed by the absolute phase reference.

$\tilde{\delta}$ is assumed independent of the wideband (white) Gaussian complex noise $\tilde{\omega}(t, \ell)$ with (double) spectral height of N_0 .

The functional form of the range depends on the class of motions and parametrization chosen. We assume a planar geometry, and that the source moves along a deterministic linear path with constant speed v as illustrated in Figure 2.

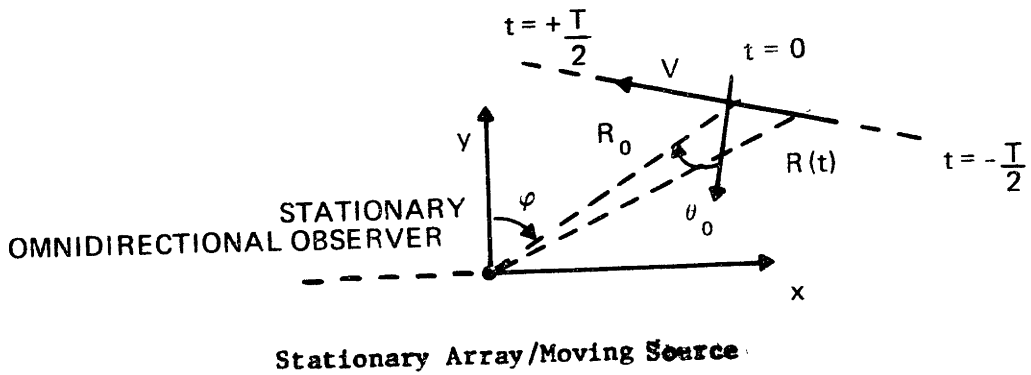


Figure 2

The observer is stationary and has no bearing discrimination capabilities of its own, i.e., is either a short baseline linear array, or an omnidirectional nonlinear array with dimension L . For this geometry the estimation problem is reduced to a 3-parameter estimation where

$$R(t, \ell) = \{R_0^2 + v^2 t^2 - 2vt R_0 \sin \theta_0\}^{1/2} \quad t \in [-\frac{T}{2}, \frac{T}{2}] \quad (2a)$$

with the parameter vector

$$A = \begin{bmatrix} R_0 \\ v \\ \sin \theta_0 \end{bmatrix} \quad (2b)$$

Comparing this problem with SASS we note that we have now, in addition to the range and angle parameter, the source speed v , as an unknown, to be estimated. We remark also that, the problem, as described, is unrealistic from a practical

point of view, since the angle ψ on Figure 2 is not uniquely specified, with the geometry rotating about the observer location on the plane defined by the source linear motion and the sensor. To solve this ambiguity one needs observer angle discrimination of its own. This will be considered on the next chapter.

The SAMS₀ configuration shows that the required information to describe the range function, in the entire observation interval, is conveyed by 3-parameters.

Conversely, SAMS₀ represents the problem where the range function (namely the 3 source parameters) is being solely reconstructed from the temporal modulations induced by the relative dynamics.

By a Taylor series (TS) expansion we approximate equation 2a

$$R(t, \ell) \approx R_0 - (v \sin \theta_0) t - \frac{v^2 \cos^2 \theta}{R_0} \frac{t^2}{2!} + 3 \frac{v^2 \cos^2 \theta}{R_0} \frac{v \sin \theta_0}{R_0} \frac{t^3}{3!} + \dots \quad (3)$$

Note that, since the signal model assumes no knowledge of the absolute phase, the information on the source parameters is on the modulations induced on the temporal signal structure.

In order to focus on the range, \quad on the source speed v and angle θ_0 , we need to be able to measure at least third order effects. This restricts the problem to high speed targets or to large observation intervals.

We remark that in equation 3 the Doppler shift (linear coefficient in t) gives the down range velocity at time $t=0$, while the 2nd order term coefficient $\frac{v^2 \cos^2 \theta_0}{R_0}$ is the radial acceleration at time $t=0$. Intuitively the system is required to measure these, as well as the 3rd order range time derivative, and use the model structure (namely the motion constraints) to locate the source in the (range, velocity, angle)-space. For small observation intervals a linearized approximation is valid, and the observer measures the source down range velocity component. This finds practical applications in navigation. Radio-location systems like Loran, Decca, Omega utilize phase information to measure velocity. This velocity determination has found increased use when tracking remote platforms such as dropsondes, balloons measuring wind, drifting buoys collecting oceanographic data (e.g. ocean currents). In all these techniques a receiver is installed on the moving platform and the radio-navigation information is retransmitted back to the base station, which determines the velocity

(down range) from the incremental motion recorded.

By further enlarging the observation interval one can measure the second (radial acceleration) and third order effects. Since the transformation of coordinates defined by

$$\dot{R}_0 = -v \sin\theta_0 \quad (4a)$$

$$\ddot{R}_0 = \frac{v^2 \cos^2\theta_0}{R_0} \quad (4b)$$

$$\dddot{R}_0 = 3 \frac{v^2 \cos^2\theta_0}{R_0} \frac{v \sin\theta_0}{R_0} \quad (4c)$$

has a nonzero Jacobian

$$\frac{\partial(\dot{R}_0, \ddot{R}_0, \dddot{R}_0)}{\partial(R_0, v, \sin\theta_0)} = \frac{6v^5}{R_0^4} \cos^2\theta_0 \sin\theta_0 \quad (4d)$$

except at broadside ($\theta=0$), endfire ($\theta=\frac{\pi}{2}$), or for stationary target/receiver configurations ($v=0$), we conclude that 3rd order effects are sufficient for local specification of the source position and dynamics (Implicit Function Theorem). That the Jacobian is zero for specific geometries, may serve as a warning to possible difficulties for these configurations. Whenever the Jacobian is nonzero, we have

$$R_o = - \frac{3 \ddot{R}_o \dot{R}_o}{\ddot{R}_o} = 3 \left| \frac{\dot{R} \ddot{R}}{\dot{R} \ddot{R}} \right| \quad (5a)$$

$$v = \dot{R}_o \left[1 - \frac{3 \ddot{R}^2}{\dot{R} \ddot{R}_o} \right]^{1/2} = \dot{R}_o \left[1 + \frac{3 \ddot{R}^2}{|\dot{R} \ddot{R}_o|} \right]^{1/2} \quad (5b)$$

$$\sin\theta = - \frac{1}{\left[1 + \frac{3 \ddot{R}^2}{|\dot{R} \ddot{R}|} \right]^{1/2}} \quad (5c)$$

and, besides an indetermination on the signal of v or $\sin\theta$, we have global parameters identifiability; we assume thereafter $v > 0$.

2. Receiver Design

We apply the maximum-likelihood techniques described in section 2 of chapter II. The receiver is a matched filter followed by an envelope detector. We repeat herein the more important expressions, and refer the reader either to chapter II or to reference [Va71b], for more discussion on the background and implementation of the receiver. The log ML-function is

$$\ln \Lambda_1(A) = \frac{1}{N_o} \frac{\bar{E}_r}{N_o + \bar{E}_r} \{ |\tilde{L}(\bar{A})|^2 \}$$

where now the parameter vector is

$$A = \begin{bmatrix} R_0 \\ v \\ \sin\theta \quad 0 \end{bmatrix}$$

The average received energy

$$\bar{E}_R = 2\sigma_b^2 E_R$$

Using the inner-product notation introduced in equation 3-10

$$|L(\bar{A})|^2 = |\langle \tilde{r}, \tilde{s}(\bar{A}) \rangle|^2$$

We have a 3-dimensional stochastic maximization which will be accomplished via the two step mechanization discussed in chapter II . The receiver is now equivalent to a 3-dimensional bank of matched filters followed by square envelope detectors. We look essentially for the network maximizing the signal to noise ratio. A local tune up on the source parameters follows the coarse search accomplished on the first step.

3. Generalized Ambiguity Function

As we have seen in chapter II the Generalized Ambiguity Function (GAF) as given by definition 3.1 is

$$\phi(A, \bar{A}) = |\psi(A, \bar{A})|^2 \quad (6a)$$

where $\psi(A, \bar{A})$ is the signal autocorrelation function

$$\psi(A, \bar{A}) = \frac{1}{LT} \int_{-\frac{T}{2}}^{\frac{T}{2}} dt \int_{-\frac{L}{2}}^{\frac{L}{2}} d\ell \exp\left[j \frac{2\pi}{\lambda} \Delta R(t, \ell, A, \bar{A})\right] \quad (6b)$$

For the SAMS₀ problem, and by direct substitution,

$$\psi(A, \bar{A}) = \frac{1}{T} \int_{-\frac{T}{2}}^{\frac{T}{2}} dt \exp[j \Delta R(t, A, \bar{A})] \quad (6c)$$

with the phase range difference

$$\Delta R(t, A, \bar{A}) = \frac{2\pi}{\lambda} \left\{ [R_0^2 + v^2 t^2 - 2v t R_0 \sin \theta_0]^{1/2} - [\bar{R}_0^2 + \bar{v}^2 t^2 - 2\bar{v} t \bar{R}_0 \overline{\sin \theta_0}]^{1/2} \right\} \quad (6d)$$

As discussed previously, the receiver's ability to locate the source is intrinsically connected to the structure of GAF. Two main points have to be investigated, namely 1) the form and dimensions of the main lobe, which designs the grid discretizing the parameter space; 2) the side lobe structure, i.e., we have to determine if GAF exhibits significant secondary maxima. Due to the complexity of the expression defining GAF this is done by first studying the rate of fall-off of GAF, as the errors on the parameters increase, and secondly by bounding the GAF behavior for large parameter errors.

The first issue-main lobe-is essentially a local analysis on the parameters space, i.e., GAF is expanded in a truncated Taylor series (TS). Graphical analysis confirms that a second order expansion on the parameter errors accurately describes the main lobe structure. The second point is made through an asymptotic analysis, i.e., by expanding GAF on a TS on the inverse of the parameter errors. We have then two descriptions of GAF, each one valid in a certain region of the parameter space. By graphical analysis one can conclude that they essentially account for all the significant structure of the ambiguity function.

Before we proceed, and in analogy with what was done in chapter II, we consider first, an approximate expression for GAF, obtained when we assume that the third order polynomial approximation equation 3 to the phase range function is valid.

3.1 Polynomial Approximations to the Range Phase Difference

We analyzed, in Appendix A, the ambiguity function when the range is approximated by a third order polynomial

$$\Delta R(t, A, \bar{A}) = \sum_{n=0}^3 \Delta R_0^{(n)} t^n \quad (7)$$

The results are naturally interpreted using the coefficients of equation 7 which represent the mismatch on the Doppler, radial acceleration, and third order time derivative of the range. Since the source parameters may be recovered from these, see equations 5a, 5b, and 5c, we concentrate the discussion herein in terms of the range time derivatives.

Given the form of GAF along the parameter axis we make the Definition 1 - The Squared Sinc function of nth order is given by

$$\text{Sinc}_n^2 = \left| \frac{1}{2\Sigma} \int_{-\Sigma}^{\Sigma} \exp j\tau^n d\tau \right|^2 \quad (8a)$$

It is easily seen that for

$$n = \text{odd} \quad \text{Sinc}_n^2 = \left| \frac{1}{\Sigma} \int_0^{\Sigma} \cos \tau^n d\tau \right|^2 \quad (8b)$$

$$n = \text{even} \quad \text{Sinc}_n^2 = \left| \frac{1}{\Sigma} \int_0^{\Sigma} \exp j\tau^n d\tau \right|^2 \quad (8c)$$

Along the parameter-axis the ambiguity function is given by these sinc_n^2 . Specifically, along the Doppler axis it is the usual sinc^2 function. For the radial-acceleration parameter, GAF is sinc_2^2 which relates to the Fresnel Integrals. Finally, along the third order time derivative parameter-axis GAF is

$$\text{Sinc}_3^2 = \left| \frac{1}{\Sigma} \int_0^{\Sigma} \cos \tau^3 d\tau \right|^2 \quad (9)$$

The integral in 9 is represented in figure 3, with the limit for large Σ being given in terms of the value at zero of an Airy function, i.e.,

$$\lim_{\Sigma \rightarrow \infty} \int_0^{\Sigma} \cos \tau^3 d\tau = \frac{\pi A_1(0)}{3^{1/3}} = \frac{\pi}{3\Gamma(\frac{2}{3})} \approx .765 \quad (10)$$

Figure 4 represents sinc_3^2 while figure 5 compares the first 3 squared sinc functions. We observe that for larger n , sinc_n^2 is flatter near the origin, as one would expect, with the main lobe approaching a rectangle window type. Outside this main lobe we observe ripples which are more significant, but also die out faster, as the order of the function increases. The rippling behavior is intuitively related to the overshooting of the integrals - Gibb's type

Fig. 3 Int. of $\cos x^3$ versus integrt. interv.

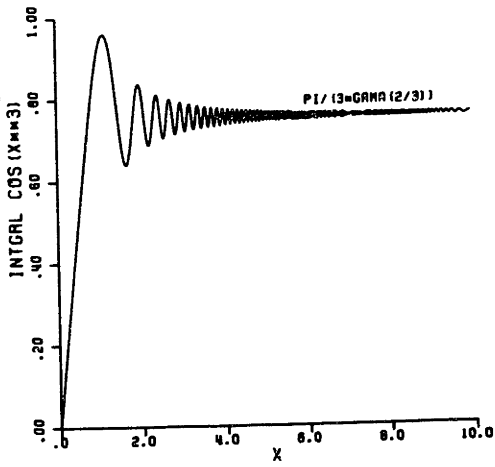


Fig. 4 Squar. General. 3th Sinc Fcn.

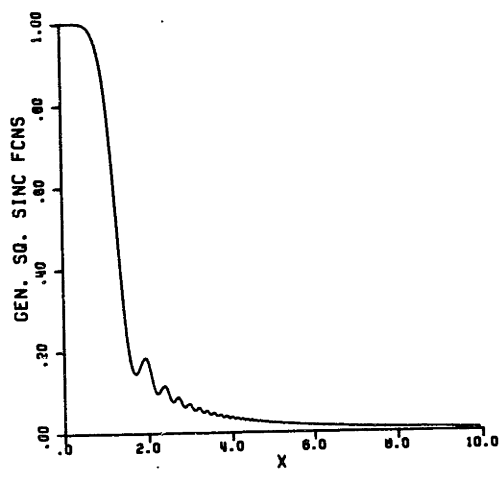
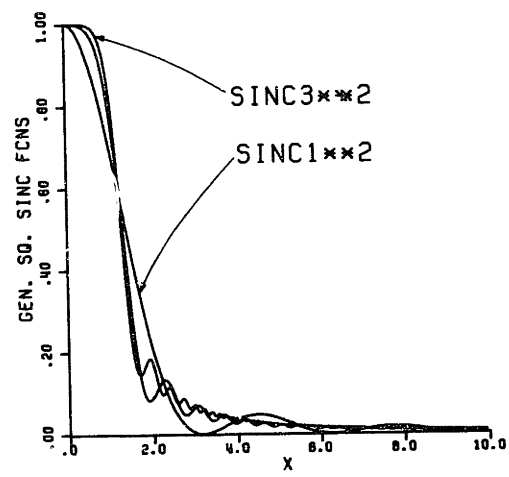


Fig. 5 Sq. Gen. Sinc Fcn up to 3th Order



phenomena, see figure 5. The smoother behavior for the higher order sinc_n^2 relates directly to the cancellation of the integral, due to the highly oscillatory character of the exponential function, and which is the naive reason to study these integrals by the Method of Stationary Phase (MSP), see Appendix A.

For sinc_3^2 the first minimum occurs approximately at

$$\Sigma_m \approx 1.72 \quad (11a)$$

with

$$\text{Sinc}_3^2(\Sigma_M) \approx .1449 \quad (11b)$$

and the largest secondary maxima is the first one outside the main lobe at

$$\Sigma_{M_2} \approx .196 \quad (12a)$$

with

$$\text{Sinc}_3^2(\Sigma_{M_2}) \approx .184 \quad (12b)$$

i.e., the function is reduced to approximately 18.4% of its maximum at the origin.

In Appendix A, and by a change of variable, we arrive at the signal autocorrelation function, for the general third order polynomial approximation to the range,

$$\psi(A, \bar{A}) = \frac{1}{\Delta \Sigma} \int_{\Sigma_1}^{\Sigma_f} \exp j\omega\tau \exp j\tau^3 d\tau \quad (13)$$

with

$$\omega = \frac{1}{\Delta_3^{1/3}} \left(\Delta_1 - \frac{\Delta_2^2}{3\Delta_3} \right) \quad (14a)$$

$$\Delta \Sigma = \Sigma_f - \Sigma_1 = \Delta_3^{1/3} \left[\frac{T}{2} + \frac{1}{3} \frac{\Delta_2}{\Delta_3} \right] - \Delta_3^{1/3} \left[-\frac{T}{2} + \frac{1}{3} \frac{\Delta_2}{\Delta_3} \right] = \Delta_3^{1/3} T \quad (14b)$$

We do not display graphically this function here, since we will present plots for the exact ambiguity structure later on. We turn instead to its asymptotic behavior. For large observation intervals the signal autocorrelation function may be written in terms of an Airy function (Appendix A). We have

$$\psi(A, \bar{A}) \sim \frac{\pi}{3^{1/3}} \frac{1}{\Sigma} A_1 \left(\pm \frac{\omega}{3^{1/3}} \right) \quad (15)$$

For large ω , and using the asymptotic expansions for the Airy functions shown in Appendix A, we have

$$\psi(A, \bar{A}) \sim \frac{\pi}{2 \cdot 3^{1/3}} \frac{1}{\Sigma} \left(\pi^2 \frac{\omega}{3^{1/3}} \right)^{-1/4} e^{-\xi} \left(1 - \frac{5}{72} \xi^{-1} \right)$$

if $\omega > 0$ (16a)

$$\psi(A, \bar{A}) \sim \frac{\pi}{2 \cdot 3^{1/3}} \frac{1}{\Sigma} \left(\pi^2 \frac{\omega}{3^{1/3}} \right)^{-1/4} \left[\sin\left(\xi + \frac{\pi}{4}\right) - \cos\left(\xi + \frac{\pi}{4}\right) \frac{5}{72} \xi^{-1} \right] \text{ if } \omega < 0$$

(16b)

where

$$\xi = \frac{2}{3} \left(\frac{\omega}{3^{1/3}} \right)^{3/2} \tag{16c}$$

$$\Sigma = \Delta_3^{1/3} \frac{T}{2} \tag{16d}$$

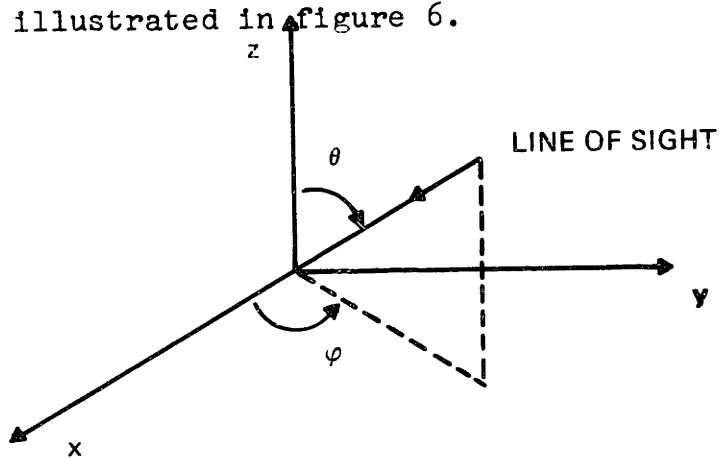
Equations 16 show that, for large parameter errors, the ambiguity function decreases with the inverse of a certain power of Σ and ω , and hence, of the mismatch on the range derivative parameters.

3.2 General Case

The generalized ambiguity function, given by equation 6, is studied graphically in figures 7 to 15. The source actual parameters are assumed fixed

$$A_a = \begin{bmatrix} R_{o_a} \\ v_a \\ \sin\theta_a \end{bmatrix} = \begin{bmatrix} .6 \times 10^5 \text{ feet} \\ 30 \text{ feet/sec} \\ \sin 15^\circ \end{bmatrix}$$

Figures 7, 9, 11 represent 3-dimensional plots of GAF on the coordinate planes. The line of sight is given by the angles θ and ϕ illustrated in figure 6.



Viewing Angles For 3-Dimensional Plots

Figure 6

In particular for these figures

$$\theta = 150^\circ$$

$$\phi = 210^\circ$$

*Figures 7 and 8 are not repeated here, since they correspond to figures II-7 and II-8.

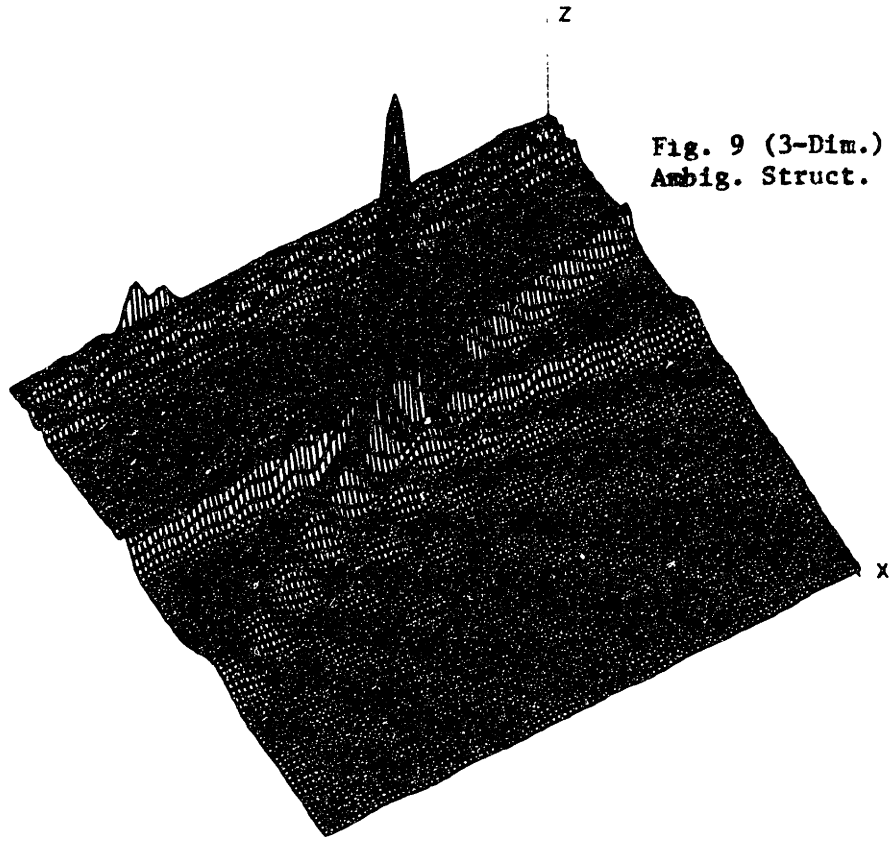


Fig. 9 (3-Dim.) Ran/Vel Ambig. Struct. ($x=1/4$)

Fig. 10 (Contour) Ran/Vel Ambig. Struct. ($x=1/4$)

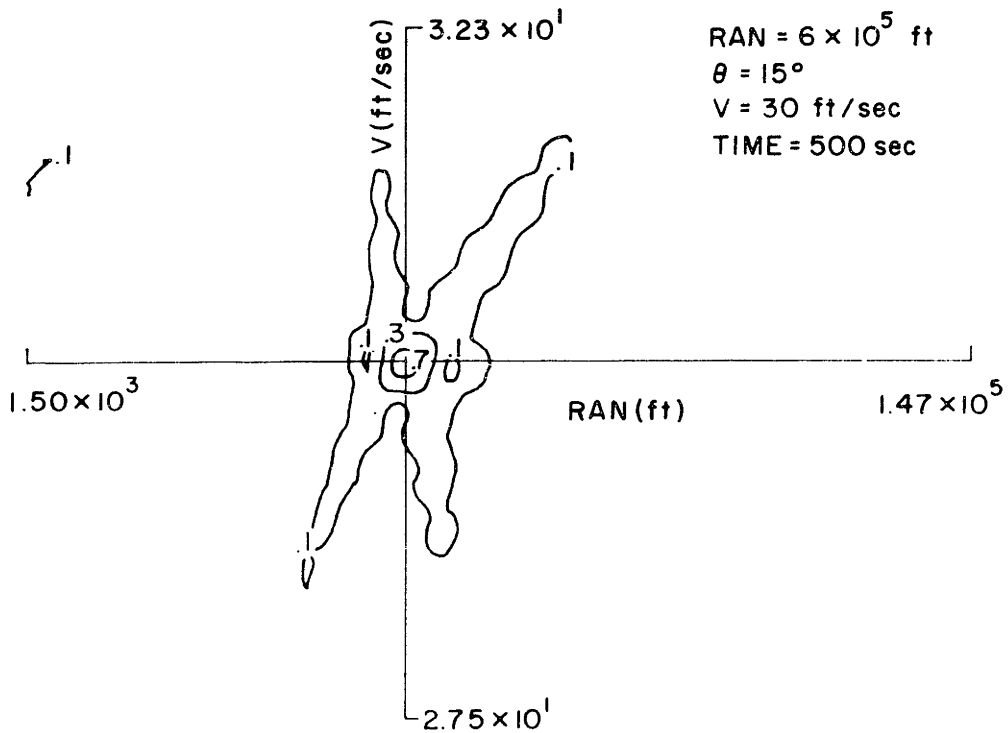


Fig. 11 (3-Dim.) Vel/Ang Ambig. Struct. ($x=1/4$)

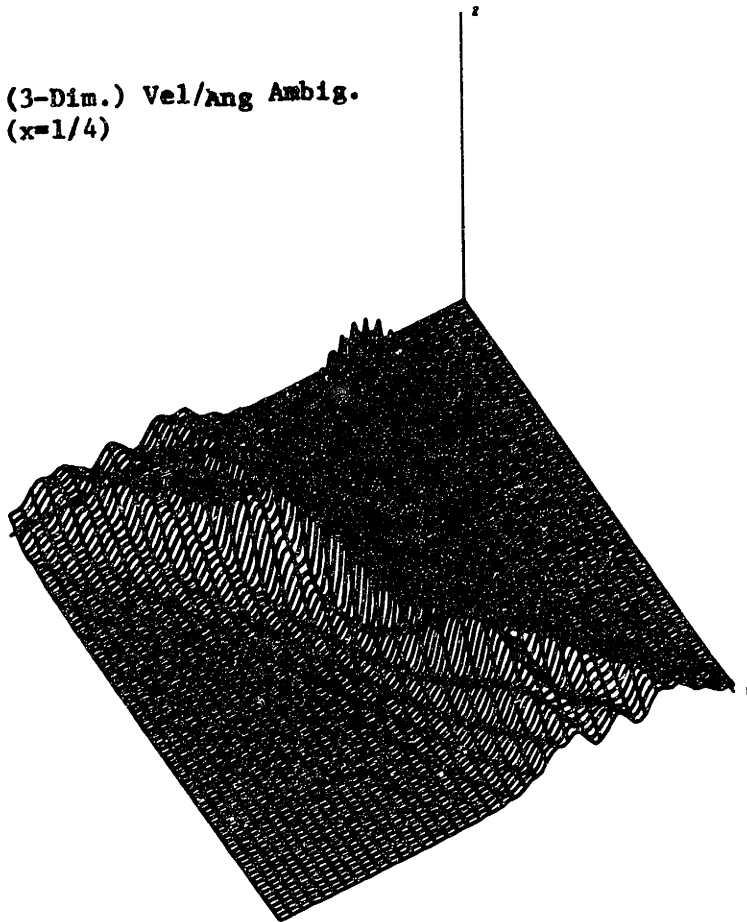
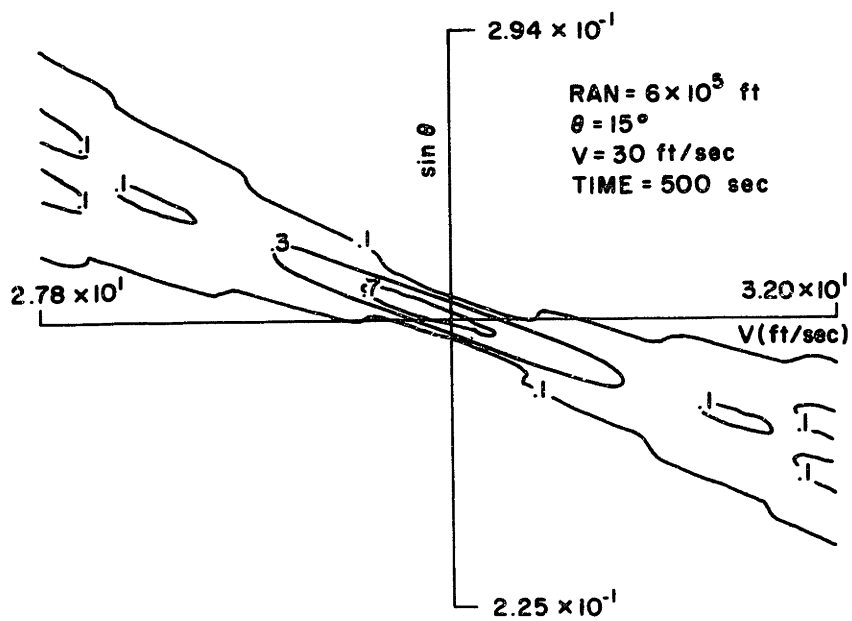


Fig. 12 (Contour) Vel/Ang Ambig Struct ($x=1/4$)



i.e., GAF is viewed from below and behind. Figures 8, 10, 12 show the corresponding contour plots. We note in figure 12 the shearing of the ambiguity function which, alike what happens with Chirp (linear frequency modulated) continuous waveform radars. The value of the geometric parameter x is

$$x = \frac{vT}{2R_0} = \frac{1}{8}$$

Figures 13, 14, show the ambiguity functions on the Ran/vel plane for a smaller value of x

$$x = \frac{1}{16}$$

as seen from two different viewing angles. Figure 15 is the corresponding contour plot. In chapter II we presented several 3-dimensional and contour plots of GAF on the Ran/sin θ plane, for different values of x . For the sake of brevity we do not repeat them here.

From these graph displays we conclude, qualitatively, that the ambiguity function has a main lobe, centered at the source geographical position at $t=0$ (middle point of the observations interval) and subsidiary negligible peaks which will be ignored in the subsequent error analysis. As we recall, the generalized ambiguity function is the output of the ML-receiver in the absence of noise. Its peaked

Fig. 13
(3D) Ran/Vel Amb. Str.

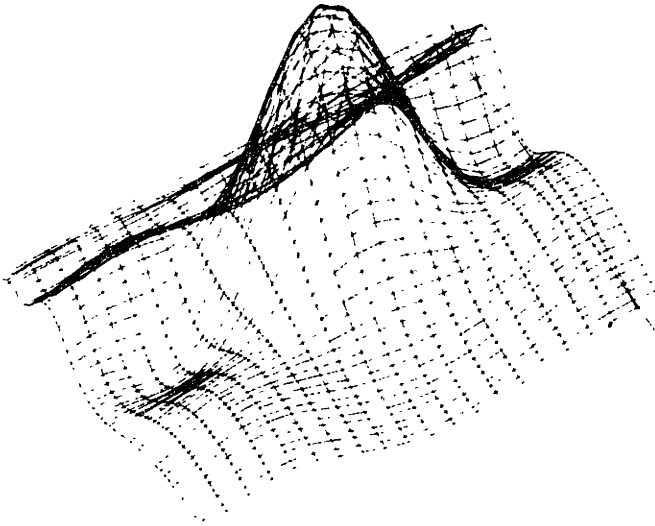
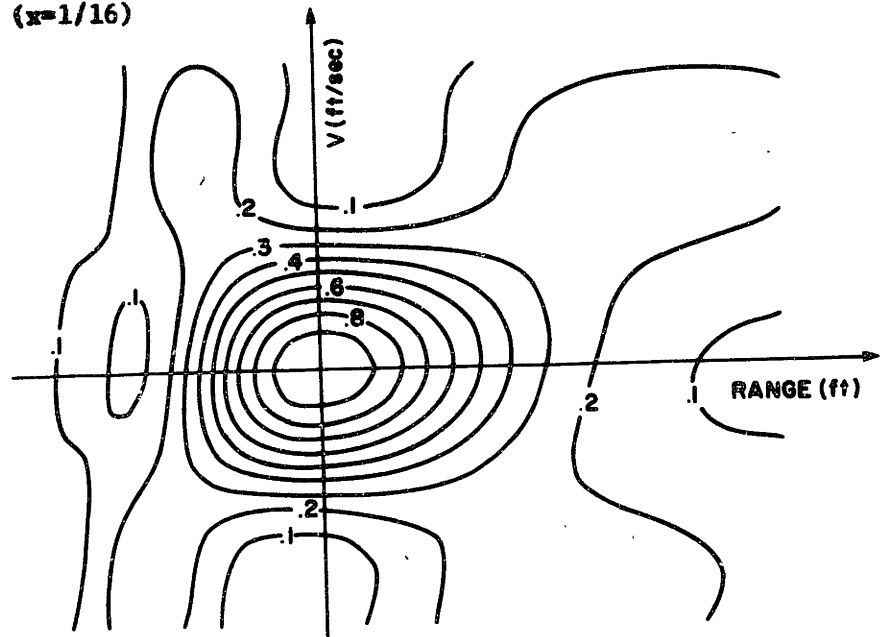


Fig. 14 (3D) Ran/Vel Amb. Str.

Fig. 15 (Contour) Ran/Vel
Amb. Str. ($x=1/16$)

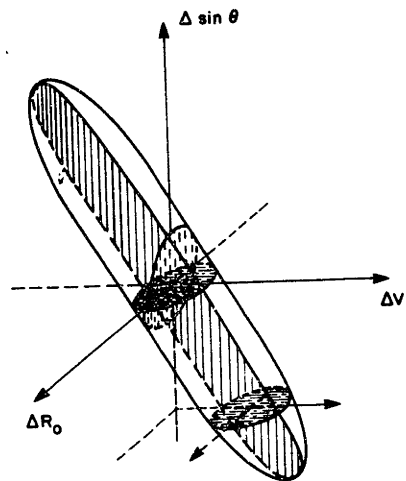


structure shows the model global identifiability, i.e., that it is possible to estimate globally and simultaneously all of the source parameters from the array measurements.

The contour plots of GAF, figures 8, 10, 12 show that the equal height contours of its main lobe on the 3 coordinate planes, approximate ellipses, suggesting that the 3-dimensional equal height-contours of the main lobe are roughly ellipsoids. This was confirmed by looking at the equal height contour plots of the main lobe of GAF on planes parallel to the coordinate axis planes. In figure 16 we show one of these ellipsoids generated from the corresponding intersections (ellipses) on the coordinate planes.

This main lobe configuration will be referred to as ellipsoidal structure. It will play an important role on the performance studies of the next section, since it determines the form and dimension of the elementary cells of the grid used on the first step of the algorithm implementing the ML-estimation.

Finally we want to comment on the rate of fall of the secondary GAF structure, i.e., how large are the secondary main lobes of GAF, and how do they fall off, as we get further away from the source location in the parameter space, and what is the asymptotic behavior of this secondary structure, as the observation interval is increased.



Main Lobe Ellipsoidal Struct.

Fig. 16

In Appendix A we resorted to the Method of Stationary Phase (MSP) to find the asymptotic behavior of GAF and bound its secondary structure. We found that, at each point of the parameter space Ω , these bounds depend on the value of the first nonzero range phase difference derivatives, on the observation interval. We report the reader to equations 65 and 67 of the Appendix A for the actual form of these bounds. They show that the ambiguity structure decreases hyperbolically with the square of the n th root of the n th range phase difference derivative (which is the first derivative evaluated at that point of the parameter space which does not vanish in the whole observation interval). This asymptotic structure also decreases with $(T/2)^{-2}$.

Because this structure of the ambiguity function plays an essential role on the global parameters observability, and on the mean square performance bounds, we keep referring back to it. We normalize then our nomenclature:

1) Main lobe ellipsoidal structure stands for a GAF exhibiting a main lobe which can be well approximated by a quadratic expansion on Ω ;

2) Secondary negligible structure means that GAF is negligible outside its main lobe;

3) Hyperbolic secondary structure refers to GAF decaying with the inverse of a certain power of the parameter errors, on Ω .

The evolution of the main lobe form, and dimensions, as we increase the observation interval, will be quantified later on, when studying the asymptotic performance of the mechanization of the ML-algorithm.

4. Performance Analysis

We analyse the mean square error performance of the two step algorithm mechanizing the ML-estimation of the source parameter vector

$$A = \begin{bmatrix} R_0 \\ v \\ \sin\theta \end{bmatrix}$$

The total mean square error (MSE) of the component A_j is decomposed in two terms. The first, referred to as the global MSE $\sigma_{gl_j}^2$, results from decision errors or diversions. The second, the local MSE $\sigma_{loc_j}^2$, depends on the flatness of the main lobe, and is estimated from the Cramer-Rao bounds.

Recalling equation 2-74 we have

$$\begin{aligned} E(A_j - \bar{A}_j)^2 &= E(A_{j\epsilon}^2) = \sigma_j^2 \\ &= \sigma_{j_{gl}}^2 + \sigma_{j_{loc}}^2 \\ &= E(A_{j\epsilon}^2 | \epsilon) \Pr(\epsilon) + E(A_{j\epsilon^c}^2 | \epsilon^c) (1 - \Pr(\epsilon)) \end{aligned} \quad (17)$$

Due to the main lobe ellipsoidal structure, and to the negligible secondary structure, the assumptions behind the derivation of the MSE expressions of chapter II still hold. In particular we have that 1) GAF can be approximated by a second order expansion about the actual source parameter values, with the result expressed in terms of the mean square spread matrix M ; and 2) the first step of the ML-algorithm can be modeled as an M -ary decision problem with orthogonal signals over a Rayleigh Channel. Once again the total number M of hypothesis depends on the a priori region of interest Ω in the parameter space and on the matrix M , namely its eigenvalues and eigenvectors.

These circumstances underline the importance of the mean square spread matrix M . In Appendix B we have computed this matrix and arrived at closed form expressions for its elements. Given its unappealing complexity we present first a local analysis based on truncated Taylor series (TS) when the geometric parameter

$$x = \frac{\sqrt{T}}{2R_0}$$

is small.

4.1 Short Observation Interval Analysis (Distant Observer)

4.1.1 Full SAMS_o Problem

In many situations of practical significance the geometric parameter

$$x = \frac{vT}{2R_o} < 1 \quad (18)$$

i.e., the geometry corresponds to a distant observer type. With this condition, a truncated Taylor series (TS) analysis can be pursued, leading to meaningful results. Accordingly we consider this type of approach.

The range phase is approximated by an nth order polynomial

$$R(t,A) = [R_o^2 + v^2 t^2 - 2vt R_o \sin\theta_o]^{1/2} \approx \sum_{i=0}^n R_o \frac{t^i}{i!} \quad (19a)$$

where

$$R_o^{(i)} = \left. \frac{d^i}{dt^i} R(t,A) \right|_{t=0} \quad (19b)$$

In the sequel we are interested on the matrix M , its inverse, its classical adjoint

$$\tilde{M} = (\det M) M^{-1}$$

and its determinant. As it turns out, the first nonzero coefficient of the Taylor series of $\det M$, is the coefficient of the 12th power in x . A priori this requires that we keep in the development of equation 19 up to 12th order terms, i.e.,

$$n \geq n_{\text{sams}_0} = 12$$

With some preliminary manipulation, and using all possible simplifications, one can see that we do not need to carry through such a large expansion of the range phase. Nevertheless we have to save in equation 19 terms up to 6th power in x , i.e.,

$$n_{\text{min}} = 6$$

in order to get the correct expression for the 12th order coefficient of $\text{Det } M$. This discussion has been intended only to illustrate the complicated algebra one has to go through to compute the TS local analysis for M . As will be analysed subsequently, these involved algebraic manipulations, and the necessity of saving higher order terms in the TS expansions of the range phase, reflect the fact that, for the purpose of getting a nonsingular estimation problem,

the higher order modulation effects have to be taken into account.

After much algebra,* which we spare to the reader, we present below the results of the local analysis. We note that, for the sake of brevity and intuition, we display only the leading term of the TS expansion for each element (i.e., its first nonzero term). As mentioned above higher order terms (h.o.t.) have to be included in actual computations (e.g., computing $\det M$ or M^{-1} from M) so that we preserve the nonsingular character of M .

$$M = \left(\frac{2\pi}{\lambda} \right)^2 \left[\begin{array}{c} \frac{\cos^4 \theta x^4}{3^2 x^5} \left| \frac{R_0}{v} \frac{(11 \sin^2 \theta - 2) \cos^2 \theta x^4}{3^2 x^5} \right| \frac{R_0}{3^2 x^5} \frac{11 \sin \theta \cos^2 \theta x^4}{3^2 x^5} \\ \\ = \left| \frac{R_0^2}{v^2} \frac{\sin^2 \theta x^2}{3} \right| \frac{R_0^2}{v} \frac{\sin^2 \theta x^2}{3} \\ \\ = \left| \quad \quad \quad \right| \frac{R_0^2}{3} x^2 \end{array} \right] \quad (20a)$$

* Part of the manipulations were carried out using Macsym, at Project MAC.

$$\tilde{M} = \text{Adj } M = \left(\frac{2\pi}{\lambda} \right)^4 \frac{\cos^2 \theta x^6}{3^3 x^5} \begin{bmatrix} \frac{R_o^4}{v^2} & \frac{4 R_o^3}{\cos^2 \theta v} & \frac{R_o^3}{v^2} 2 \sin \theta \\ \frac{R_o^2 \cos^2 \theta}{v} & \frac{R_o^2}{v} \sin \theta \cos^2 \theta \\ \frac{R_o^2}{v^2} \sin^2 \theta \cos^2 \theta & & \end{bmatrix} \quad (20b)$$

$$M^{-1} = \left(\frac{\lambda}{2\pi} \right)^2 \frac{5^2 x^7}{x^6} \begin{bmatrix} \frac{1}{\sin^2 \theta \cos^4 \theta} & \frac{v}{R} \frac{1}{2 \sin^2 \theta \cos^2 \theta} & -\frac{1}{R} \frac{1}{2 \sin \theta \cos^2 \theta} \\ \frac{v^2}{R^2} \frac{1}{4 \sin^2 \theta} & & -\frac{v}{R^2} \frac{1}{4 \sin \theta} \\ \frac{1}{R^2} & & \frac{1}{4} \end{bmatrix} \quad (20c)$$

$$\text{Det } M = \left(\frac{2\pi}{\lambda} \right)^6 \frac{R_o^4}{v^2} \frac{4 \sin^2 \theta \cos^4 \theta x^{12}}{3^3 x^5 3^3 x^7} \quad (20d)$$

The Cramer Rao bounds are obtained by normalizing the mean square spread matrix by the gain

$$G'^{-1} = \left[\begin{array}{cc} \frac{2\bar{E}_R}{N_o} & \frac{\bar{E}_R/N_o}{1 + \frac{\bar{E}_R}{N_o}} \end{array} \right]^{-1} \quad (21a)$$

with

$$\bar{E}_R = \text{average received energy} = 2P_n T L \sigma_b^2 \quad (21b)$$

where the received power due to the spherical spread has been normalized

$$P_n = \frac{P}{\left(\frac{R_o}{R_o^r} \right)^2} \quad (21c)$$

as discussed in chapter II , section 4. We define the normalizing signal energy to noise ratio dependent gain

$$G^{-1/2} = \left[1 + \frac{N_o}{2P_n \sigma_b^2} \frac{1}{LT} \right]^{1/2} \frac{1}{\sqrt{\frac{2P}{\left(\frac{R_o}{R_o^r} \right)^2} \frac{2\sigma_b^2}{N_o} \left(\frac{2\pi}{\lambda} \right)^2}} \frac{1}{\sqrt{LT}} \quad (21d)$$

$$= \alpha \frac{1}{\sqrt{\text{SNR}_{\text{eff}}}} \frac{1}{\sqrt{LT}} \quad (21e)$$

where the effective signal to noise ratio at the receiver level SNR_{eff} has been defined in equation II-56, and has taken into account the spherical geometry, the Rayleigh fading and the modulation index

$$\beta = \frac{2\pi}{\lambda} \quad (22)$$

The standard deviations for the error parameters and for the local analysis results are

$$\sigma_{R_0} = \frac{\alpha}{\sqrt{\text{SNR}_{\text{eff}} \text{LT}}} \frac{5\sqrt{7}}{\sin\theta \cos^2\theta} \frac{1}{x^3} \quad (23a)$$

$$\sigma_v = \frac{\alpha}{\sqrt{\text{SNR}_{\text{eff}} \text{LT}}} \frac{5\sqrt{7}}{2} \frac{v}{R_0 \sin\theta} \frac{1}{x^3} \quad (23b)$$

$$\sigma_{\sin\theta} = \frac{\alpha}{\sqrt{\text{SNR}_{\text{eff}} \text{LT}}} \frac{5\sqrt{7}}{2} \frac{1}{R_0} \frac{1}{x^3} \quad (23c)$$

where, we recall

$$x = \frac{vT}{2R_0}$$

The source/receiver geometry affects the performance in two distinct ways, which we have separated, in expressions 23a to 23c. On the one hand it renormalizes the received energy.

In particular for the same emitted power and quality of sensors the standard deviation performance deteriorates with the inverse of the source/receiver separation. On the other hand the performance bounds are directly affected by the actual source parameters and length of the observations, as they determine the spread out of the GAF main lobe, measured by the matrix M . We concentrate the discussion now on the latter effects.

We note the third order dependence of the standard deviations on the geometric parameter x . This relates intuitively to the fact that the simultaneous estimation of all 3 source parameters requires at least the observation of third order time modulation effects, as discussed at the end of section 1 of this chapter.

The range standard deviation bound, as given in equation 23a, has two stationary points at

$$\sin\theta = \pm \frac{1}{\sqrt{3}} \quad (24a)$$

for which

$$\theta = \theta_{\min} = 35.26^\circ \pmod{\frac{\pi}{2}} \quad (24b)$$

Its second derivative w.r.t. $\sin\theta$ is positive for $\sin\theta \in [-1,1]$, i.e., it is a convex cup function of $\sin\theta$. This cup behavior reflects the dependence of the range performance on both the down range and cross range velocity components given by

$$v_s = v \sin\theta \quad (25a)$$

$$v_c = v \cos\theta \quad (25b)$$

which vanish for broadside and end fire geometries, respectively. We conclude that the range performance standard deviation, for the distant observer geometry (or equivalently short observation interval analysis), presents a minimum at $\theta_{\min} \approx 35^\circ$ and deteriorates monotonically, as we approach both a broadside and an end fire geometry. While this last behavior just reflects the dependence of the range performance on the effective array length, which vanishes for end fire, the former is a new phenomenon, characteristic of the SAMS_o problem, and which did not appear with the SASS configurations. The monotonic range performance deterioration for broadside, brings about the coupling between the error in the other parameters, and is a direct consequence of the fact that, in the SAMS_o we jointly estimate speed and bearing.

The velocity standard deviation σ_v has an hyperbolic dependence on $\sin\theta$, increasing drastically for $\theta \approx 0^\circ$ (broadside or closest approach geometry). The bearing performance exhibits an hyperbolic dependence on the source/receiver separation and is practically independent of θ .

From equations 23a to 23c we obtain the relations

$$\left(\cos^2\theta \frac{\sigma_{R_0}}{R_0}\right) = \frac{\sigma_v}{v} = \frac{\sigma_{\sin\theta}}{\sin\theta} \quad (26)$$

which reflect the tradeoffs in the performance errors, as we vary the geometry parameters.

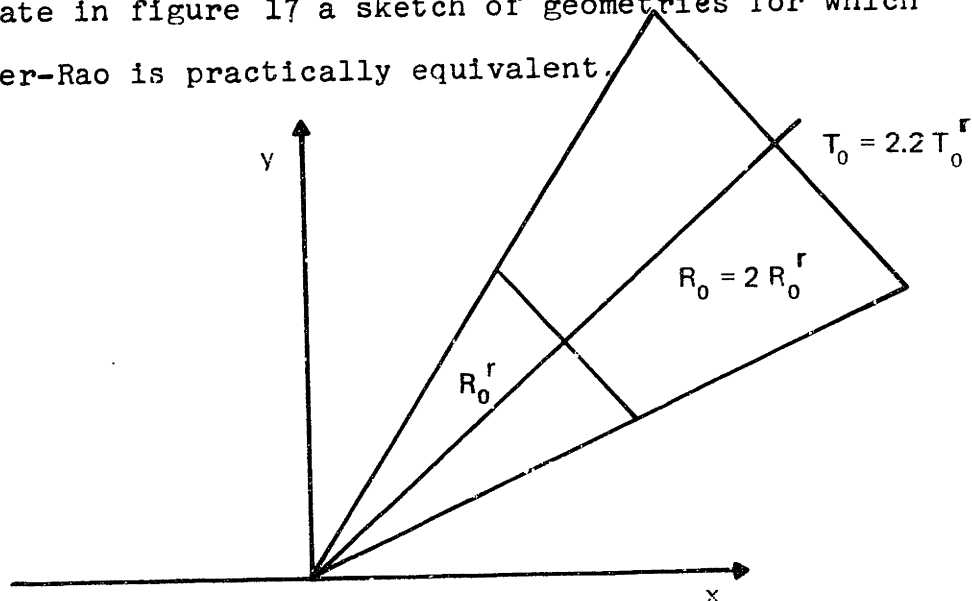
If we indicate by a superscript r the reference or nominal values assumed when designing the receiver to meet a prespecified performance, in actual system operation, when the source parameters are different from the one assumed at the design stage, the performance changes according to (for example, for the range parameter and when all other quantities are assumed equal).

$$\frac{\sigma_{R_0}}{\sigma_{R_0}^r} \approx \left(\frac{T^r}{T}\right)^{7/2} \left(\frac{R_0}{R_0^r}\right)^4 \quad (27a)$$

To match the desired Cramer-Rao nominal performance, the observation durations should be adjusted as

$$T \approx T^r \left(\frac{R_0}{R_0^r} \right)^{8/7} \quad (27b)$$

We indicate in figure 17 a sketch of geometries for which the Cramer-Rao is practically equivalent.



(Cramer-Rao Bound) Range Performance Geometries

The parameter errors cross correlations, defined as

$$\rho_{ij} = \frac{(M^{-1})_{ij}}{[(M^{-1})_{ii}(M^{-1})_{jj}]^{1/2}} \quad (28)$$

are, from equation 20c, given by

$$\rho_{R_0, v} \approx 1 - \alpha_{R_0, v}(\theta) x^2 \quad (29)$$

$$\rho_{R_0, \sin\theta} \approx 1 - \alpha_{R_0, \sin\theta}(\theta) x^2 \quad (30)$$

$$\rho_{\sin\theta, v} \approx -1 + \alpha_{v, \sin\theta}(\theta) x^2 \quad (31)$$

where $\alpha_{ij}(\theta)$, $i, j = R_0, v, \sin\theta$ are suitable expressions in $\sin\theta$. These results show that the parameter errors are highly correlated, up to second order effects. In order to have a nonsingular estimation problem, i.e.,

$$\rho_{ij} < 1 \quad , \quad i, j \in \{R_0, v, \sin\theta\} \quad (32)$$

we need a significant value for x . This point will be discussed further when we plot the Cramer-Rao bounds.

Before proceeding we analyze the spread matrix and the Cramer-Rao performance bounds when we assume that one of the source parameters is a priori known. This may be the case either because it has been determined by some other means, or it represents a higher order of complexity, as it happens with the velocity parameter in the MASS* context or simply because its incorporation into the estimation problem makes no physical sense, e.g., source speed in

* MASS = Moving (Omnidirectional) Array with Stat.Source

SASS. This analysis will shed light on the effects of the geometry, the higher order modulations, and the coupling between the parameter errors on the SAMS₀ receiver's performance. Besides this, each of the situations described below has a practical significance of its own which warrants an independent interest on the explicitation of their corresponding results.

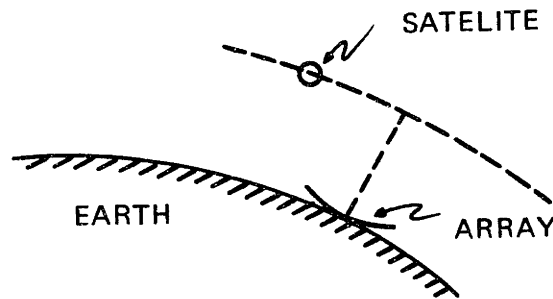
The spread matrix is obtained by deletion of the corresponding line and column in the 3-dimensional result. We also present the inverse M^{-1} and other useful parameters.

4.1.2 Range/Angle Estimation (SASS)

These applications have been considered in detail in the preceding chapter, and we refer the reader to the results reported therein. We comment that, knowledge of the own vehicle speed and/or the total array length, makes the range focusing and the angle measurement, to be essentially achieved from the linear and quadratic effects with a corresponding range performance gain of one order of magnitude of x . Furthermore, for broadside geometries and small x -parameter, the errors on the parameter estimates are essentially decoupled.

4.1.3 Range/Velocity Estimation - Applications to Navigation

In this problem the bearing angle is assumed to be known. This might occur on some navigational applications, or when tracking satellites transmitting narrowband signals. The latter is illustrated in figure 18



Satellite Tracking Geometry

Figure 18

The array on earth observes the satellite passing a beam. The duration of the observations is determined by the strength of the emitted signal and the receiving array gain. By physical reasons we assume that the observations are symmetric about the rising angle (closest approach), determined for example from the position and the orientation of the own stationary observer. The essence of the application is that the moving source follows a prescribed or a priori known path, the only unknowns being the source/receiver separation and the relative speed.

The results for this problem parallel the ones for the Range/Angle estimation (SASS or MASS) after a rescaling of the involved quantities.

The parameter vector is

$$A = \begin{bmatrix} R_0 \\ v \end{bmatrix}$$

and the (local) approximate expressions are

$$M_{R_0, v} = \left(\frac{2\pi}{\lambda} \right)^2 \left[\begin{array}{c} \frac{\cos^4 \theta x^4}{45} \left| \frac{R_0}{v} \frac{(11\sin^2 \theta - 2)\cos^2 \theta}{45} x^4 \right. \\ \hline \frac{R_0^2}{v^2} \frac{\sin^2 \theta}{3} x^2 \end{array} \right] \quad (33a)$$

$$M_{R_0, v}^{-1} \cong \left(\frac{\lambda}{2\pi} \right)^2 \left[\begin{array}{c} \frac{45}{\cos^4 \theta x^4} \left| - \frac{v}{R_0} \frac{3(11\sin^2 \theta - 2)}{\sin^2 \theta \cos^2 \theta x^2} \right. \\ \hline \frac{v^2}{R_0^2} \frac{3}{\sin^2 \theta x^2} \end{array} \right] \quad (33b)$$

$$\det M_{R_0, v} \cong \left(\frac{2\pi}{\lambda} \right)^6 \frac{R_0^2}{v^2} \frac{\sin^2 \theta \cos^4 \theta}{135} x^6 \quad (33c)$$

The degree of coupling is specified by the cross correlation which is

$$\rho_{R_0, v} \cong - \frac{(11\sin^2\theta - 2)x}{\sqrt{15} \sin\theta}, \quad (34)$$

and the eigenvalues and eigenvectors, up to truncation, are

$$\lambda_{R_0} \cong \left(\frac{2\pi}{\lambda}\right)^2 \frac{\cos^4\theta x^4}{45} \quad e_{R_0} \cong \begin{bmatrix} 1 \\ 0 \end{bmatrix} \quad (35a)$$

$$\lambda_v \cong \left(\frac{2\pi}{\lambda}\right)^2 \left(\frac{R_0}{v}\right)^2 \frac{\sin^2\theta x^2}{3} \quad e_v \cong \begin{bmatrix} 0 \\ 1 \end{bmatrix} \quad (35b)$$

As with the SASS and MASS the range is focussed by the Chirp (2nd order) effects, while the source's velocity is measured from the linear modulations on the signal structure. We note that the velocity standard deviation increases monotonically as the geometry approaches broadside. This is intuitively clear since for broadside the linear effects are minimum, and the velocity is measured from zero Doppler effects.

4.1.4 Velocity/Angle Estimates

In this application we assume that the range is known (e.g., by means of active range measurement). The analysis in this paragraph brings up one of the major difficulties underlining the $SAMS_0$ estimation problem namely, the high correlation between the errors on the velocity and angle estimates.

The parameter vector is

$$A = \begin{bmatrix} v \\ \sin\theta \end{bmatrix}$$

and the quantities of interest are approximately given by

$$M_{v, \sin\theta} \cong \left(\frac{2\pi}{\lambda}\right)^2 \left[\begin{array}{l} \frac{R_0^2}{v^2} \left(\frac{\sin^2\theta}{3} x^2 + \frac{\cos^2\theta(4-31\sin^2\theta)}{45} x^4 \right) + \frac{R_0^2}{v} \left(\frac{\sin\theta x^2}{3} \right. \\ \left. + \frac{x^4 \sin\theta(9\sin^2\theta - 22\cos^2\theta)}{45} \right) \\ \left. = \frac{R_0^2}{v^2} \left(\frac{x^2}{3} + \frac{(31\sin^2\theta - 9)}{45} x^4 \right) \right] \end{array} \right.$$

(36a)

$$M_{v, \sin \theta}^{-1} \approx \left(\frac{\lambda}{2\pi} \right)^2 \begin{bmatrix} \frac{v^2}{R_o^2} \frac{45}{4x^4} & - \frac{v}{R_o^2} \frac{45 \sin \theta}{4x^4} \\ \dots & \dots \\ \dots & \dots \\ \dots & \frac{1}{R_o^2} \frac{45 \sin^2 \theta}{4x^4} \end{bmatrix} \quad (36b)$$

$$\text{Det } M_{v, \sin \theta} \approx \left(\frac{2\pi}{\lambda} \right)^4 \frac{R_o^4}{v^2} \frac{4x^6}{135} \quad (36c)$$

We stress that the velocity and the angle mean square errors, calculated from the diagonal elements of M^{-1} depend on the 4th power of X^{-1} , as compared with SASS or the previous applications, where they were a function of X^{-2} . One of the eigenvalues is

$$\lambda_s = \left(\frac{2\pi}{\lambda} \right)^2 \frac{R_o^2 X^2}{3} \left(\frac{\sin^2 \theta}{v^2} + 1 \right) \quad (37a)$$

with eigenvector

$$l_s \approx \frac{1}{\sqrt{2}} \begin{bmatrix} 1 \\ 1 \end{bmatrix} \quad (37b)$$

oriented along the down range velocity component

$$v_s = v \sin \theta$$

The other eigenvalue, of order X^4 , corresponds to the eigenvector along the cross range velocity component

$$v_c = v \cos \theta$$

The cross-correlation between the parameter errors is

$$\rho_{v, \sin \theta} \sim -1 + \alpha_{v, \sin \theta}(\theta) x^2 \quad (38)$$

which underlines the coupling between the errors on the velocity and angle estimates.

4.2 Long Observation Interval Analysis (Close Observer)

We analyse briefly the asymptotic behavior of the Cramer-Rao bounds as the geometric parameter X is increased, or equivalently as

$$Y = X^{-1} = \frac{2R_o}{vT} \rightarrow 0 \quad (39)$$

The expressions for the asymptotic behavior of M^{-1} are presented in Appendix C. After normalizing by G^{-1} we obtain the asymptotic standard deviations predicted by the Cramer-Rao bounds:

$$\sigma_{R_o} \approx \sigma_{R_o \infty} = G^{-1/2} \sqrt{\frac{2 \cos \theta}{\pi Y}} = \frac{\alpha}{\sqrt{\pi \text{SNR}_{\text{eff}} L}} \sqrt{\frac{v \cos \theta}{R_o}} \quad (40a)$$

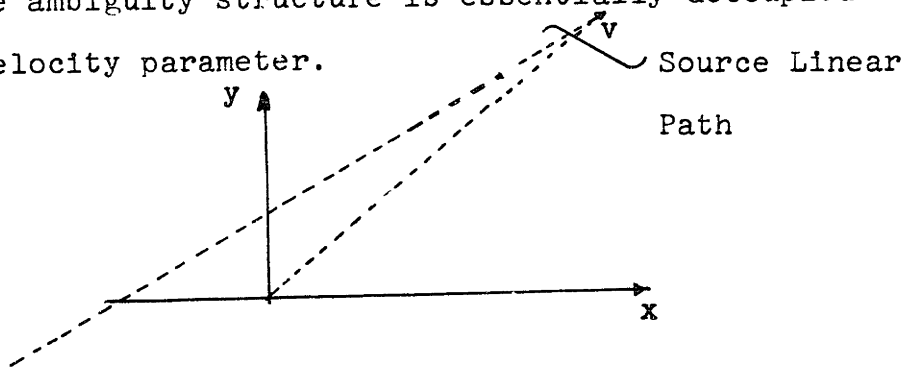
$$\sigma_{\tilde{v}} \sim \sigma_{v_{\infty}} = G^{-1/2} \sqrt{12} \frac{v}{R_c} Y = \frac{\alpha \sqrt{12}}{\sqrt{\pi \text{SNR}_{\text{eff}} L}} \frac{2R_o}{vT^{3/2}} \quad (40b)$$

$$\sigma_{\sin\theta} \sim \sigma_{\sin\theta_{\infty}} = \left(\frac{\sigma_{R_{o\infty}}}{R_o} \right) \sin\theta \quad (40c)$$

Like with SASS, the range and bearing performance decrease monotonically to nonzero lower bounds, while the velocity bound vanishes. The errors in the velocity estimates are asymptotically uncorrelated to the other parameter errors, i.e., for large ratio X the velocity estimation uncouples from the bearing and range estimation. This is intuitively clear, since for large observation interval, the problem tends to the Doppler configuration illustrated in figure 19, for which the ambiguity function is given by

$$\phi(A, \bar{A}) \sim \text{sinc}^2 \left[\frac{2\pi}{\lambda} \Delta V \frac{T}{2} \right] \tilde{\phi}(\Delta R, \Delta \sin\theta, A) \quad (41)$$

i.e., the ambiguity structure is essentially decoupled in the velocity parameter.



Doppler Configuration

Figure 19

Just as with SASS, the errors in the two other parameters are asymptotically perfectly correlated, which involves sensitivity problems, like the ones discussed in section 4.1.2 of chapter II .

4.3 Graphical Display of the Cramer-Rao Bounds

We return to the closed form expressions for M^{-1} , arrived at in Appendix B, and to the Cramer-Rao bounds obtained from the diagonal elements of M^{-1} , after normalization by the gain G^{-1} .

The nominal conditions, unless otherwise specified, are assumed to be

$$\text{SNR} = \text{emitted signal to noise ratio} = .5 = -3\text{dB}$$

$$R_0^r = 6 \times 10^4 \text{ feet}$$

$$\lambda = 50 \text{ feet}$$

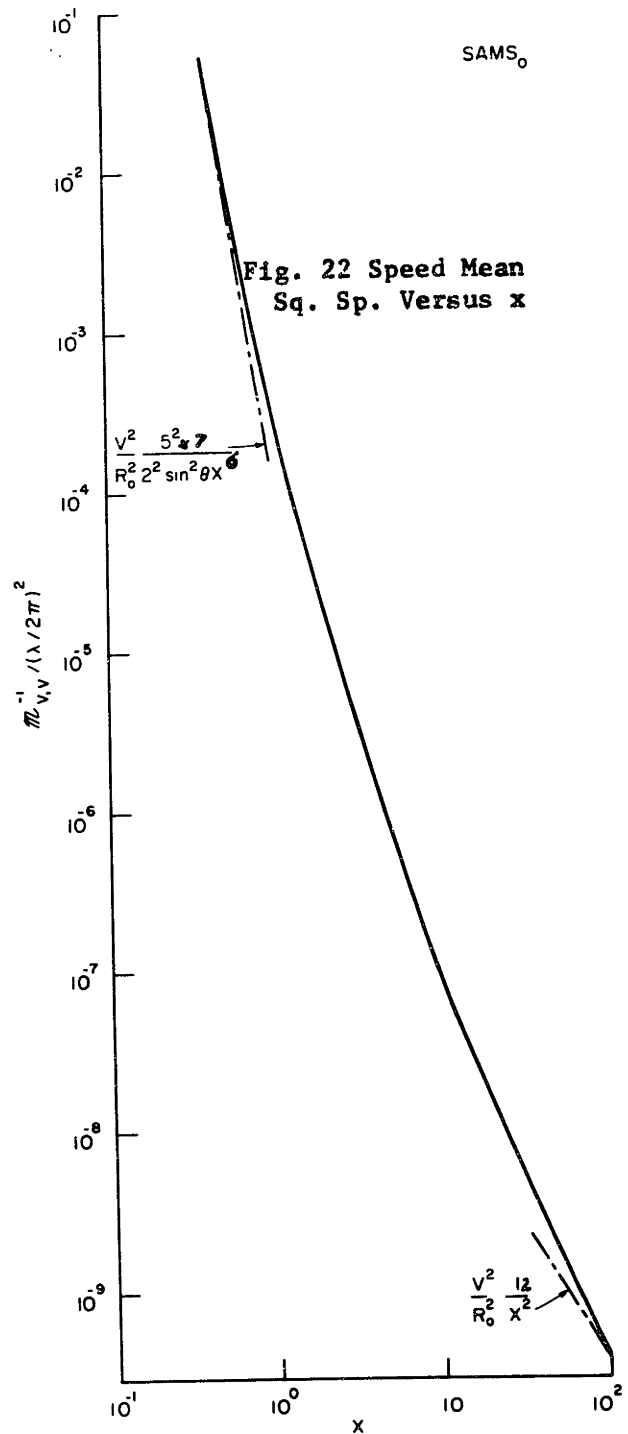
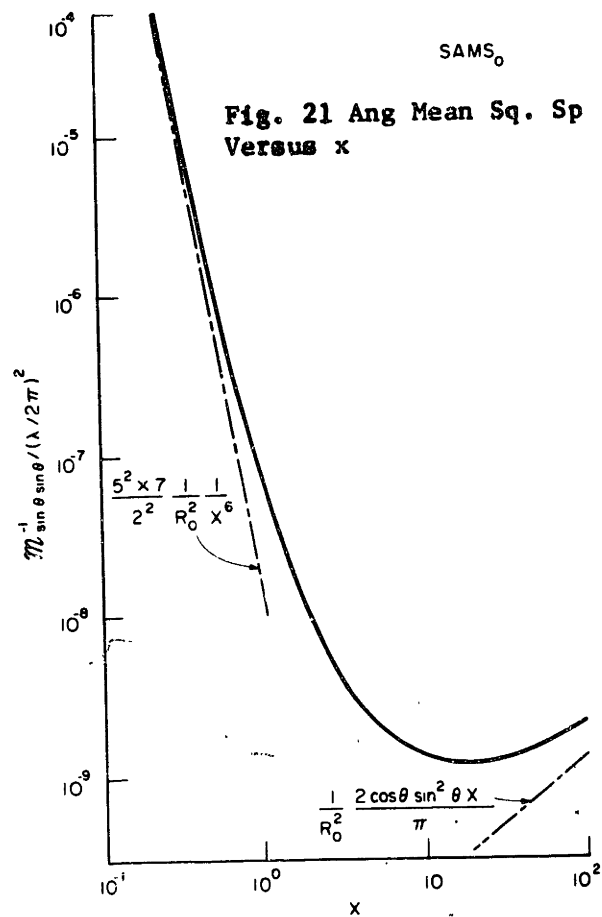
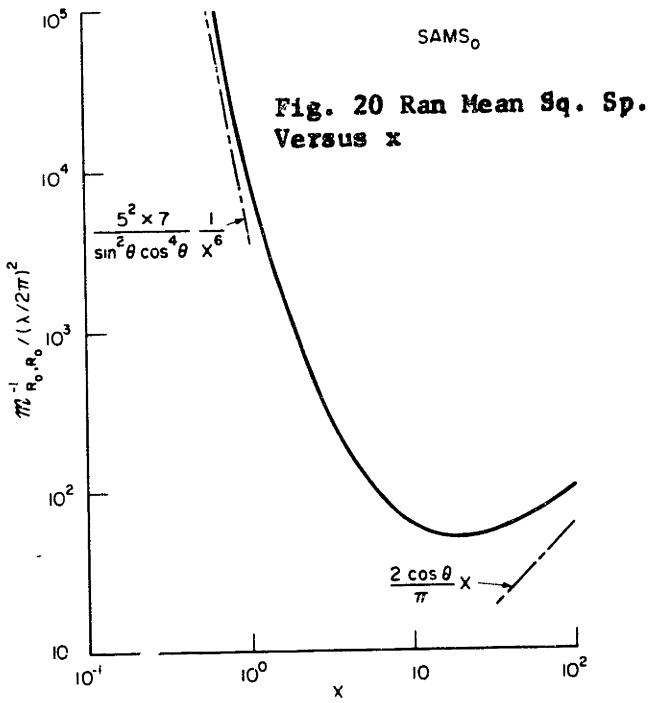
$$V = 30 \text{ feet/sec}$$

$$\theta = 15^\circ$$

$$L = 250 \text{ feet}$$

$$\sigma_b^2 = 1/2$$

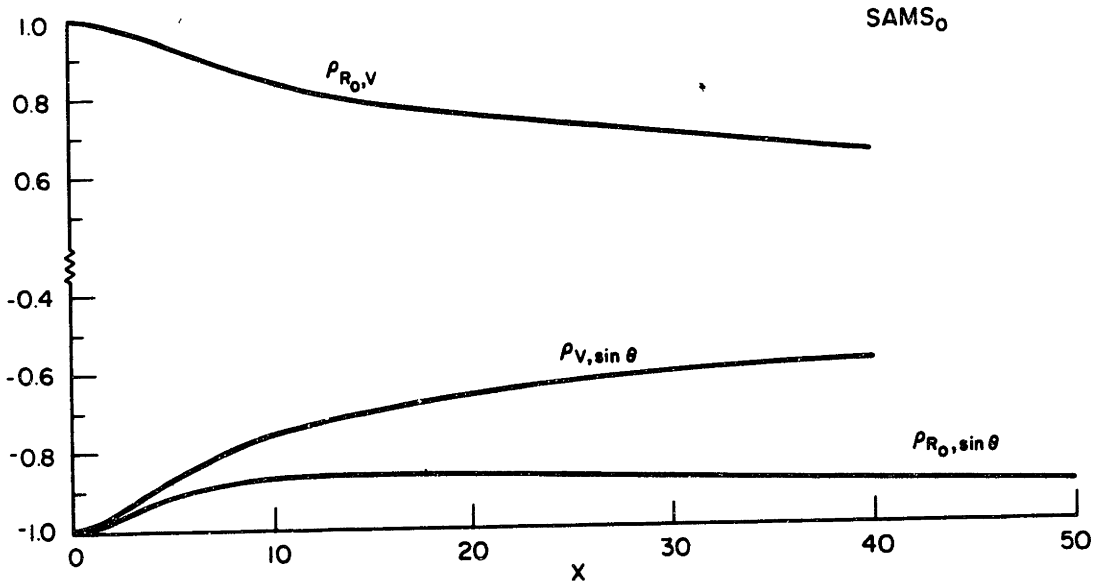
Figures 20, 21, 22 show, as functions of X , the diagonal elements of M^{-1} (normalized by the squared inverse of the modulation index $\beta = \frac{2\pi}{\lambda}$), with the local and asymptotic tangents arrived at, by the truncated Taylor series expansions. The convex cup behavior of $M^{-1}_{R_0}$ and $M^{-1}_{\sin\theta}$ is due to the



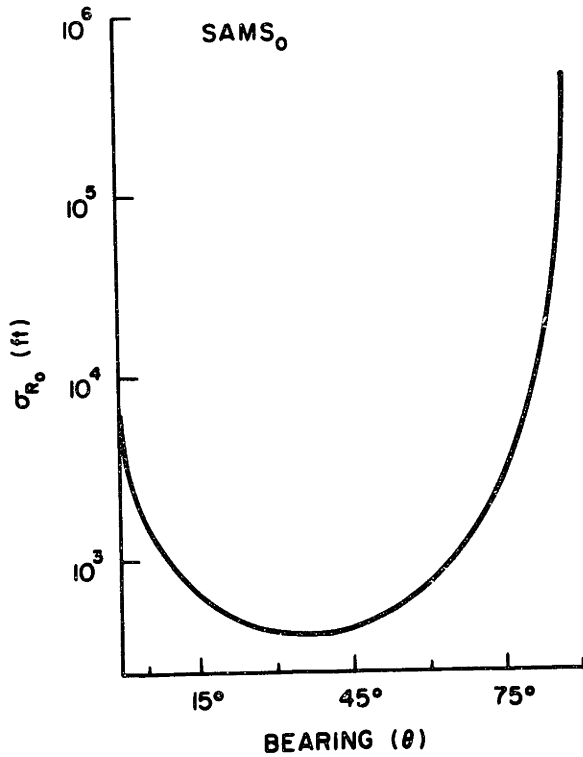
phenomena analysed in chapter II : 1) for small x , the lobe is well spread over Ω with consequent small second order derivatives of GAF at the source location; 2) for large X , the main lobe approaches a rectangular type window in the range/bearing subspace. The inverse velocity spread M_V^{-1} is monotonically decreasing, evolving from the local tangent to the asymptotic one.

Figure 23 shows, as a function of X , the cross-correlation between the errors in the estimates for the several parameters. For small X the errors are highly correlated. As X increases $\rho_{R_0, V}$ and $\rho_{V, \sin\theta}$ decrease monotonically (evolution to Doppler configuration see figure 19), while $\rho_{R_0, \sin\theta}$ decreases first (reflecting reduction in correlation, as higher order effects are measured) to increase again for large X (rectangular type ambiguity function in the $R_0/\sin\theta$ subspace, as referred to in section 4.2).

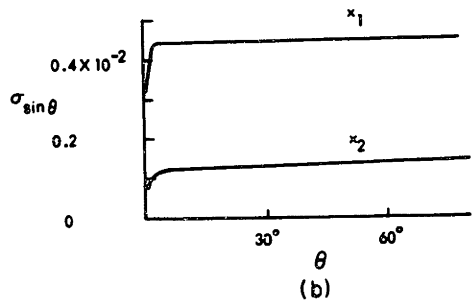
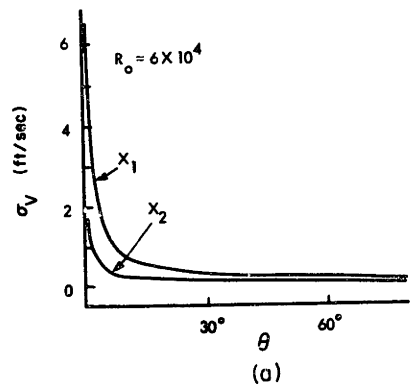
Figures 24 to 27 illustrate, for small values of the geometric parameter X (valid local analysis), the dependence of the Cramer-Rao bounds on the source parameters and the geometry. Figure 24 shows the behavior of σ_{R_0} as a function of θ . It displays the convex cup behavior referred to in the local analysis of the bound, reflecting the strong coupling between the errors in the angle and velocity estimates (skewed error ellipsoids) which get propagated to the range errors. A maximum range performance is obtained



Cross-Corr. Versus X
Fig. 23



Ran CR-Bd Versus Bear.
Fig. 24



Speed and Angle
CR-BD Versus Bear.
Fig. 25

for a geometry with

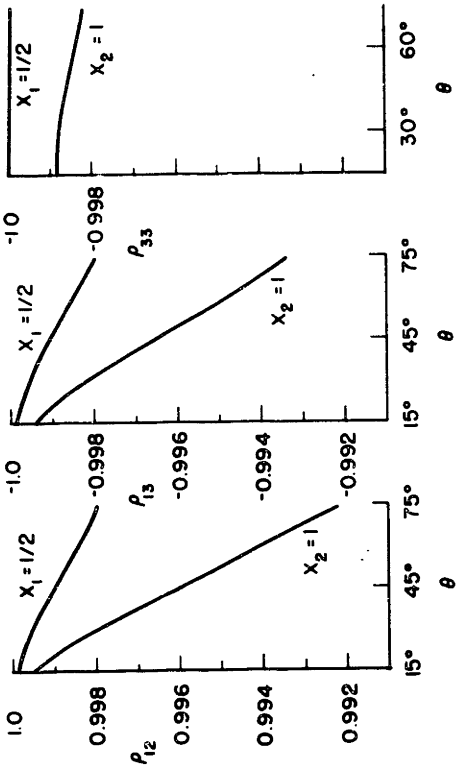
$$\theta \approx 35^\circ,$$

as predicted by the local analysis. This performance deteriorates monotonically, as we approach either Broadside (large errors in the velocity parameter) or end fire (reduction of effective array length).

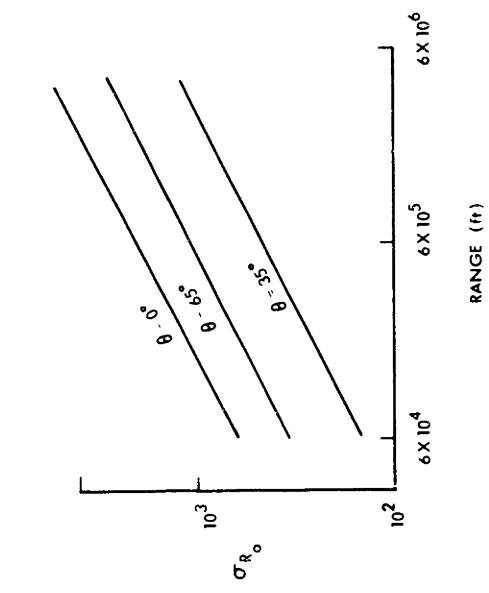
Figures 25a and 25b show the velocity and $\sin\theta$ performance as a function of bearing. The behavior predicted is confirmed. σ_v increases sharply at broadside (vanishing down range velocity) and decreases monotonically as we approach end fire, for which the down range velocity component is the source's speed. The bearing performance is practically invariant to the actual bearing angle.

Figure 26 shows the dependence of the range performance on the absolute value of R_0 , as we increase proportionately the observation interval, so that the geometric parameter X is kept constant. The deterioration in performance is essentially due to the signal power dependence on the normalized inverse of the range squared.

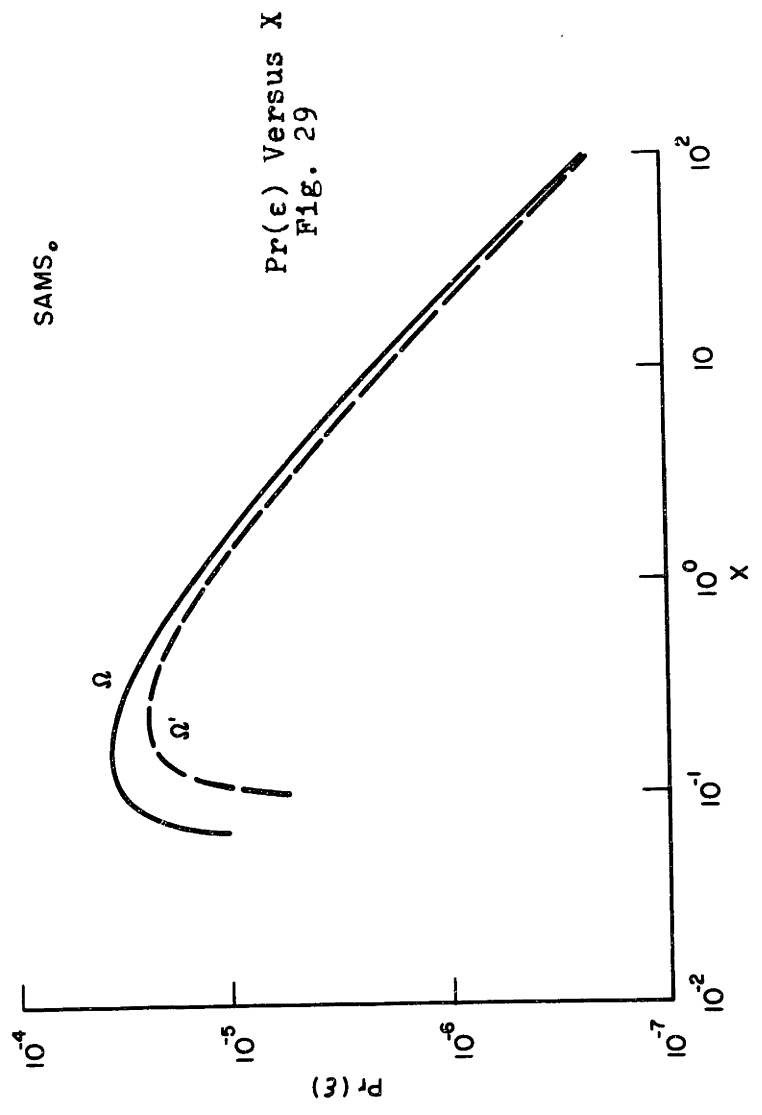
Figure 27 presents the cross correlation between the errors in the several parameters as a function of θ with X as a parameter. They display the strong coupling already noted, which for small x is one order of magnitude stronger



Cross-Corr. Versus Bearing
Fig. 27



Range CR-BD Versus Range ($X = cte$)
Fig. 26



Pr(ϵ) Versus X
Fig. 29

for $\rho_{v, \sin\theta}$. The curves for $\rho_{R_o v}$ and $\rho_{R_o \sin\theta}$ should be compared with the corresponding values obtained in the two parameter estimation problem (the third parameter either velocity or bearing being assumed known). It is immediately apparent that the presence of the third parameter in the full SAMS_o introduces a strong coupling between the errors.

4.4 Global Performance

As discussed in chapter II, section 4 the total mean square error (MSE) for the mechanization of the ML-algorithm in two stages, is approximately given by equation

$$\begin{aligned} \sigma_{\text{total } j}^2 &= E(A_j^2 | \epsilon) = \frac{\Delta_M A_j^2}{6} \text{Pr}(\epsilon) + \sigma_{jj}^2 [1 - \text{Pr}(\epsilon)] \\ &= \sigma_{gl_j}^2 + \sigma_{loc_j}^2 \end{aligned} \quad (42a)$$

where

$$\Delta_M A_j = A_{jM} - A_{jm} \quad (42b)$$

$$\sigma_{jj}^2 \approx \text{Cramer-Rao performance bound for } A_j \quad (42c)$$

$$\text{Pr}(\epsilon) = \text{Probability of a diversion (decision error)}. \quad (42d)$$

We analyze in the sequel the dependence of these quantities on the several parameters. We will assume in the graphical representations, unless stated otherwise, the nominal conditions given in the beginnings of section 4.3. We also assume that the a priori region Ω of interest in the parameter space is

$$\Omega = \begin{cases} \Delta_M R_o = R_o - R_o_m = 6 \times 10^5 \text{ feet} \\ \Delta_M v = v_M - v_m = 3 \text{ feet/sec} \\ \Delta_M \theta = \theta_M - \theta_m = 5^\circ \end{cases}$$

and that the signal to noise ratio is

$$\text{SNR} = 0 \text{ dB}$$

4.4.1 Probability of Error and Total Number of Grid Cells

We start by discussing $\text{Pr}(\epsilon)$ and M . In chapter II several expressions are presented for the probability of a diversion. For the high signal energy to noise ratio situation, i.e., whenever

$$\frac{\bar{E}_r}{N_o} \gg 1 \quad (43)$$

we have

$$\text{Pr}(\epsilon) \sim \frac{1}{\frac{E_r}{N_0}} \left[\text{Ln } M - \frac{1}{2M} + \gamma \right] \quad (44)$$

where γ is the Euler constant. The total number of grid cells is given by

$$M = \frac{V_\Omega}{V_a} \quad (45)$$

where the volume of the elementary cell is the product of the square root of the eigenvalues of M^{-1} after normalization by a factor, dependent on the specific form assumed for the elementary cell. An analytic expression for the eigenvalues of M^{-1} is difficult to obtain since it would involve the roots of a 3th order polynomial. We observe however that since all we need is the product of the eigenvalues, which is an invariant characteristic of a linear transformation we have

$$\text{Det } M^{-1} = \prod_{i=1}^3 \lambda_i M^{-1}$$

It follows then

$$M = \frac{V_\Omega}{k} (\text{Det } M)^{1/2} \quad (46a)$$

For the distant observer geometry (local analysis)

$$M_{loc} \sim \frac{V_{\Omega}}{k} \left(\frac{2\pi}{\lambda}\right)^3 \frac{R_o^2}{v} \frac{2\sin\theta\cos^2\theta x^6}{3 \times 5 \times \sqrt{3 \times 5 \times 7}} \quad (46b)$$

For the close observer geometry (asymptotic analysis)

$$M_{asympt} \sim \frac{V_{\Omega}}{k} \left(\frac{2\pi}{\lambda}\right)^3 \frac{R_o^2}{v} \frac{1}{2} \sqrt{\frac{\pi}{6 \cos\theta Y}} \quad (46c)$$

These expressions show analytically the rate of growth of the total number of grid cells with the several parameters, for the local and asymptotic geometries. In figure 28 we represent Det M as a function of X. We observe that it is monotonically increasing, evolving from a weak to an asymptotic tangent, implying a change on the rate of growth of M from X^6 to \sqrt{X} .

Figure 29* shows the evolution of $Pr(\epsilon)$ as we increase X, and for two regions of a priori interest in the parameter space. We took

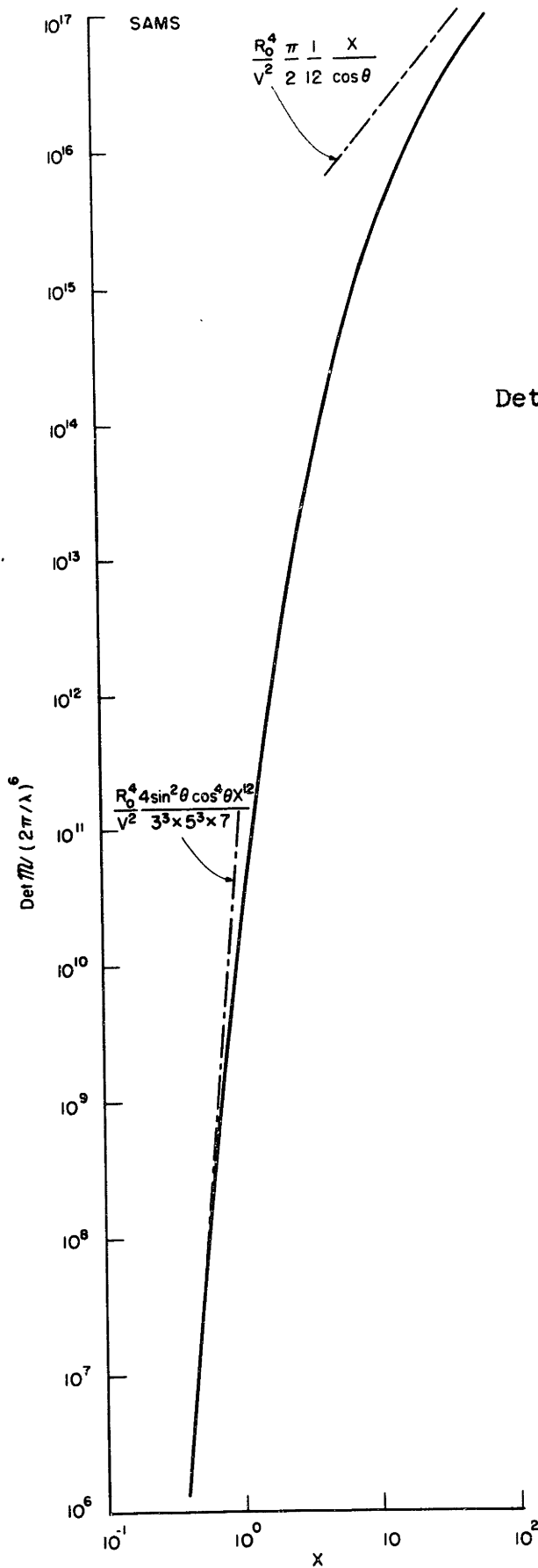
$$\Omega_1 = \Omega$$

and $\Omega_2 = \begin{cases} \Delta_M R_o = 6 \times 10^5 \text{ feet} \\ \Delta_M v = 1.5 \text{ feet/sec} \\ \Delta_M \theta = 1^\circ \end{cases}$

i.e.,

$$v_{\Omega_2} = \frac{v_{\Omega_1}}{10}$$

* See page 171



Det M Versus X
Fig. 28

We note first the concave behavior of $\text{Pr}(\epsilon)$ with X . For small x the GAF main lobe is spread all over Ω and so $M=1$, implying $\text{Pr}(\epsilon)=0$. As X increases, the variation in M dominates over the signal energy to noise ratio variation, till a maximum is reached which could be arrived at analytically. Afterwards $\text{Pr}(\epsilon)$ decreases monotonically following a $\frac{1}{T} \ln T$ type law. The effect of changing V_Ω is of course more marked for small x , essentially pushing to a larger value of X , the point for which the GAF main lobe is smaller than the a priori region of interest, and so leading to $M>1$. For large X , this has a vanishing effect due to the $\ln T/T$ type law.

Finally we note that when x is small, so that the local analysis holds, and whenever all the other parameters are kept identical

$$M = M^R \left(\frac{R_o}{R_o^r} \right)^2 \quad (47a)$$

where M^R corresponds to R_o^r (reference range). This expression says that the total number of grid cells increases with the square of the source/receiver separation, and it underlines the vast amount of computation time that may be required for very far away targets. When similar conditions hold

$$\Pr(\epsilon) = \frac{R_o}{R_o^r} \left[1 + 2 \frac{\ln(R_o/R_o^r)}{\ln M^r} \right] [\Pr(\epsilon)]^r \quad (47b)$$

where $[\Pr(\epsilon)]^r$ is the probability of error under reference conditions. This equation displays the rate of growth of $\Pr(\epsilon)$, as the source/receiver separation gets bigger. We note that the first factor

$$s = \frac{R_o}{R_o^r} \quad (47c)$$

accounts for the normalization of the received power (spherical propagation), while the bracketed factor reflects the change in the total number of grid points with the source/receiver separation.

4.4.2 Graphical Analysis of the Total Performance Bounds

In figures 30 to 32 we represent, as a function of X , the total mean square error σ_{tot}^2 , and its global and local components, for the two different a priori regions of interest Ω_1, Ω_2 . We first note that, for small x , the local component dominates the performance, since as seen, the $\Pr(\epsilon)$ is zero for small x . After a transition region, where both components are of the same order, the global errors essentially dominate the performance. For the record we observe that, for the numerical conditions and the a priori region assumed, this transitional region occurs first for

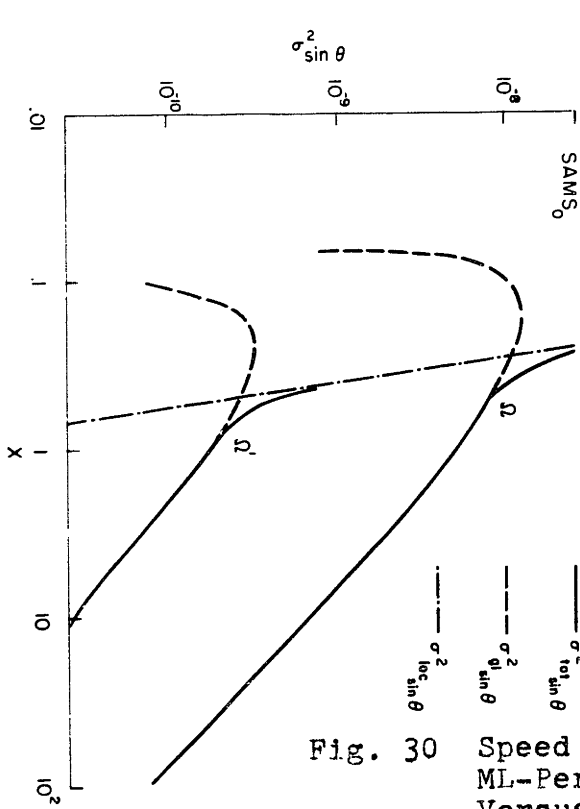
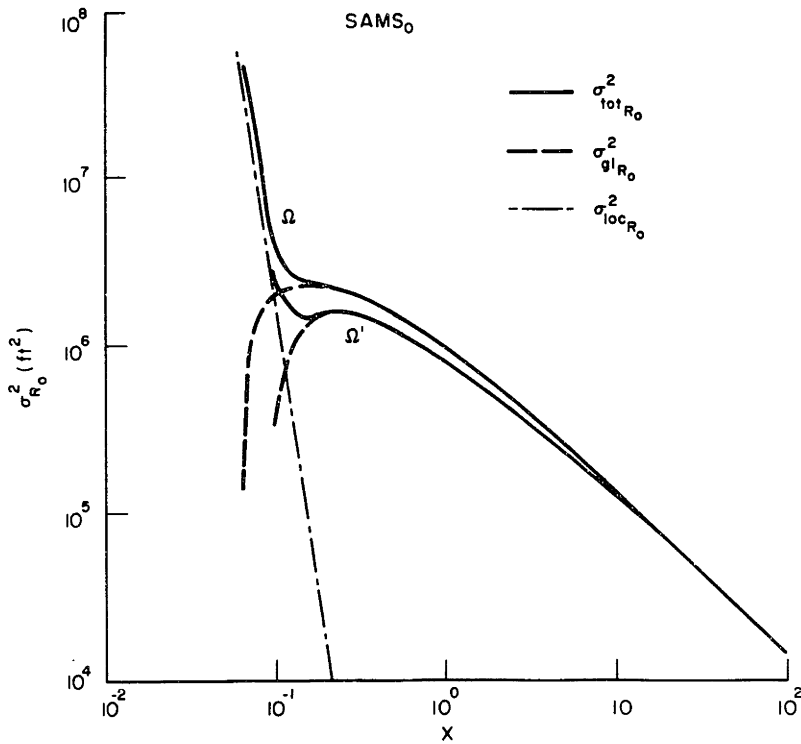


Fig. 30 Speed Tot. ML-Perf. Versus X



the range parameter, then the $\sin\Theta$ parameter, and finally for the velocity parameter. We also note that it occurs for values of $X \in [.1, 1]$ which is a region of interest in many applications.

The effect of reducing the a priori region of interest is two fold. One, noted, is the change of $\Pr(\epsilon)$ and gets purely reflected in figure 30. The second results from the change in the a priori uncertainty of the parameters. Since in Ω_2 we have reduced $\Delta_M v$ and $\Delta_M \theta$, the changes in figures 31 and 32 reflect the coupling of both effects.

4.5 Asymptotic Behavior of the ML-Algorithm

We analyzed how the performance of the estimation algorithm depends on the geometric parameter X . We have seen that for X smaller than a transitional value X_{tran} , the performance is well predicted by the Cramer-Rao bounds. Improvements can only be achieved by increasing the effective signal energy to noise ratio, e.g. by using better sensors. For X larger than the transitional value, a threshold phenomenon occurred with the receiver's performance departing from the Cramer-Rao bound, due to the dominance of the global (large) errors.

As in chapter II, the issues of asymptotic behavior, as SNR and/or N (total number of independent measurements) get large, can be pursued. The conclusions are essentially equivalent to the ones encountered there. By comparing the

$\sigma_{gl\ j}^2$ and $\sigma_{loc\ j}^2$, one finds a relation that when $N=1$, and for the high signal energy to noise ratio, is essentially independent of SNR. This says that, in these conditions, for a given geometry, we cannot make the m.s.e. term due to diversions, arbitrarily small w.r.t. the local m.s.e. just by increasing SNR; the receiver presents threshold effects, with its performance departing significantly from the one predicted by the Cramer-Rao.

We note that this suboptimal behavior is inherent to the two step implementation of the ML-receiver, and not intrinsic to the ML-parameter estimation with signals propagating through a Rayleigh channel. In fact one can prove that, the ML-parameter estimation problem with signals over a Rayleigh channel is asymptotically efficient in the signal to noise ratio sense, i.e., as we let $SNR \rightarrow \infty$. The proof follows essentially the arguments in Kelly, Reed, and Root [Kel60] for the equivalent problem, of asymptotic efficiency in the SNR sense, of ML-estimation of parameters imbedded in signals multiplied by a channel characteristic of constant unknown, but nonrandom, amplitude b and uniform phase ψ . We only have to be careful to further restrict their bounding argument to the sample functions with unknown nonzero amplitude b . But since the set of sample functions for which $b=0$ is a set of measure zero, this introduces no essential modification of the Kelly et. al argument, leading to the

efficiency of the ML-estimate in the SNR sense in the more general context of signals over Rayleigh channels.

Finally, if we assume that we have N independent measurements, and if we let

$$\Delta_j^N = \frac{\sigma_{g1j}^2}{\sigma_{locj}^2}, \quad (48)$$

we can prove the asymptotic efficiency in the classical sense

$$\lim_{N \rightarrow \infty} \Delta_j^N = 0 \quad (49a)$$

and also

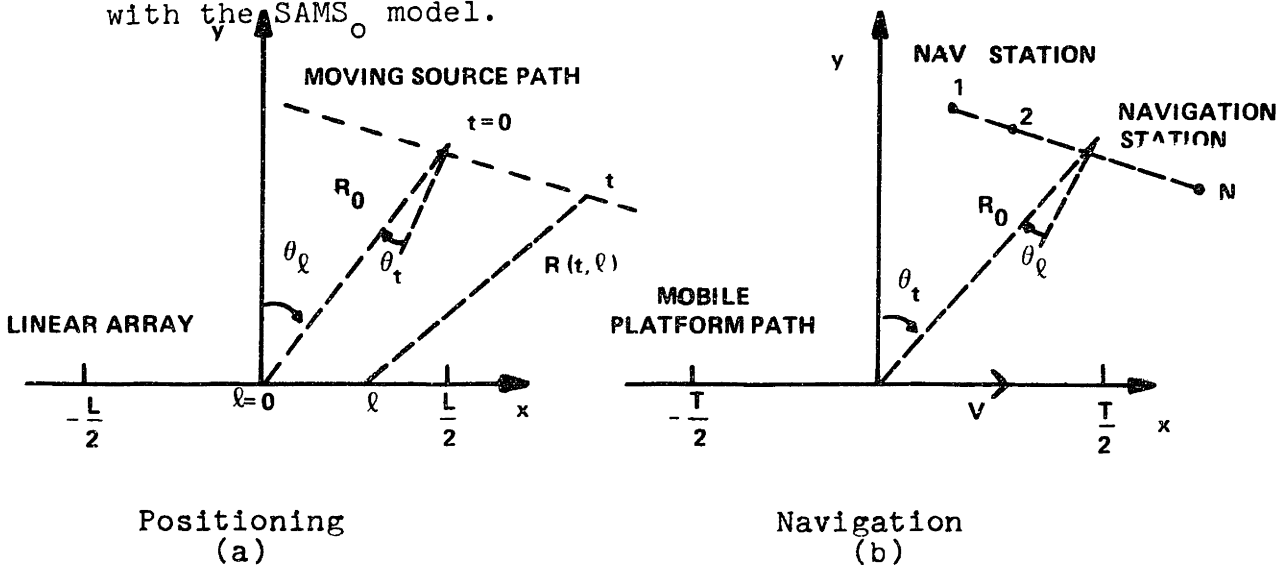
$$\lim_{SNR \rightarrow \infty} \Delta_j^N = 0 \quad \text{if } N \geq 2 \quad (49b)$$

i.e., that the suboptimality of the two step mechanization disappears, and that the estimates are also efficient in the SNR sense.

Chapter IV

Synthetic Array with Moving Sources

In the last chapter we carried out the analysis for the equivalent positioning and navigation problems for moving platforms, when either the receiving aperture is omnidirectional (e.g. short baseline), or the navigational station reduces to a fixed point source. These twin applications were cast in terms of a Stationary Array/Moving Source Model with Omnidirectional Sensor (SAMS_o), reducing the passive position/navigation to the estimation of three parameters, namely the source/receiver separation R_0 , the relative speed, and a suitably defined angle θ_t , see figure 1. The temporal modulations induced by the relative dynamics conveyed no information on the bearing angle θ_ℓ , see figure 1, which is unidentifiable with the SAMS_o model.



Stationary Array/Moving Source

Figure 1

In this chapter we consider the class of position/ navigation problems illustrated in figure 1, where a spatial and temporal nonnegligible baseline is generated, inducing both spatial and temporal diversity on the signal structure. Keeping, as usual, the tracking or positioning terminology, we refer to this class as a Stationary Array/Moving Source (SAMS) problem. We put the analysis of SAMS in the perspective of the results contained in the two preceding chapters, and pursue the study of the optimal ML-receiver structure, and of the processor performance, for two configurations arising in most applications of practical significance. We discuss in detail the space/time factorability of the ambiguity function, and the fundamental implications, in terms of parameters identifiability, introduced by the spatial/temporal coupling.

1. Model

We make the planar geometry, the narrowband radiated signals, and the constant speed linear path assumptions of the previous chapters.

The received signal is

$$r(t, \ell) = \sqrt{2} \operatorname{Re} \{ \tilde{r}(t, \ell) \exp j \omega_c t \}, \quad t \in [-\frac{T}{2}, \frac{T}{2}], \ell \in [-\frac{L}{2}, \frac{L}{2}]$$

(1a)

with

$$\tilde{r}(t, \ell) = \tilde{s}(t, \ell) + \tilde{w}(t, \ell) \quad (1b)$$

$$\tilde{s}(t, \ell) = \sqrt{\frac{E_R}{LT}} \tilde{b} \exp[j \frac{2\pi}{\lambda} R(t, \ell)] \quad (1c)$$

where E_R = received energy = $2 PLT$

λ = wavelength = $\frac{c}{f}$

\tilde{b} = Rayleigh parameter = complex Gaussian r.v. with statistics

$$E \tilde{b} = 0$$

$$E |\tilde{b}|^2 = 2\sigma_b^2$$

L = total array length

T = total observation interval duration.

$\tilde{w}(t, \ell)$ = complex zero mean homogeneous, 2-dimensional, white Gaussian noise with spectral height $\frac{N_0}{2}$.

We will make use in the sequel of the two following geometric parameters,

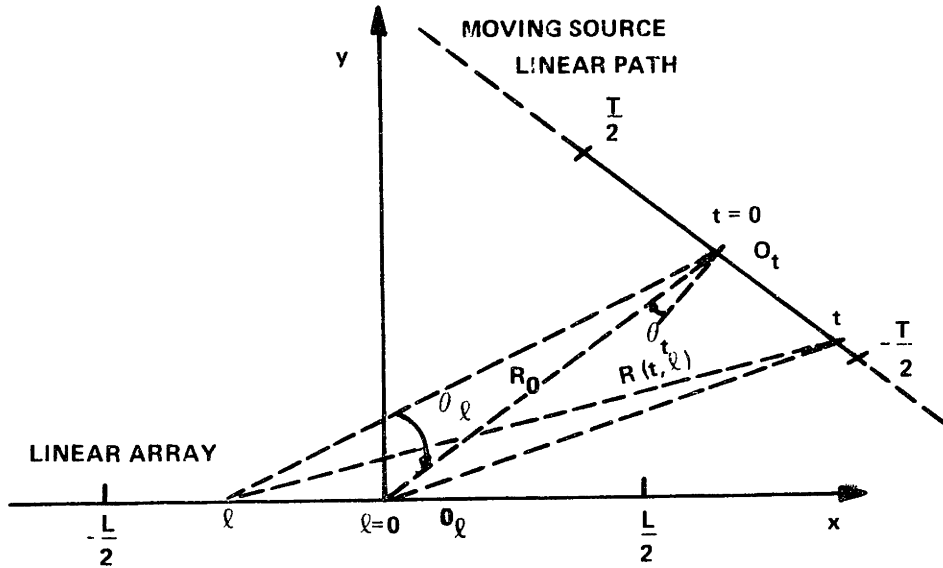
$$\text{spatial geom. para. } X_\ell = \frac{L}{2R_0} \quad (2a)$$

$$\text{Temporal geom. par. } X_t = \frac{VT}{2R_0} \quad (2b)$$

which normalize the linear dimensions (half of the array length, or half the travel of the moving source during the observation interval) with respect to the source/receiver

separation.

The range function $R(t, \ell)$ is the distance between the source at time t and the point at location ℓ in the linear array, which, due to the deterministic assumption on the



SAMS-Planar Geometry

Figure 2

motions, may be completely described by four parameters. Centering with respect to the array geometric center and the midpoint of the observation interval, we define the parameter vector

$$A = \begin{bmatrix} R_0 \\ v \\ \sin\theta_t \\ \sin\theta_\ell \end{bmatrix}$$

where R_0 is the source/receiver separation at $t=0$, $\ell=0$, the angles $\sin\theta_i$, $i=\ell,t$, are indicated in figure 2, and v is the source speed. By solving successively the triangles $\ell-0_\ell-t$ and 0_t-t-0_ℓ we obtain

$$R(t,\ell,A) \triangleq R(t,\ell) = \{R_0^2 + \ell^2 + (vt)^2 - 2R_0(\ell\sin\theta_\ell + vt\sin\theta_t) + 2\ell vt \cos(\theta_\ell - \theta_t)\}^{1/2} \quad (3a)$$

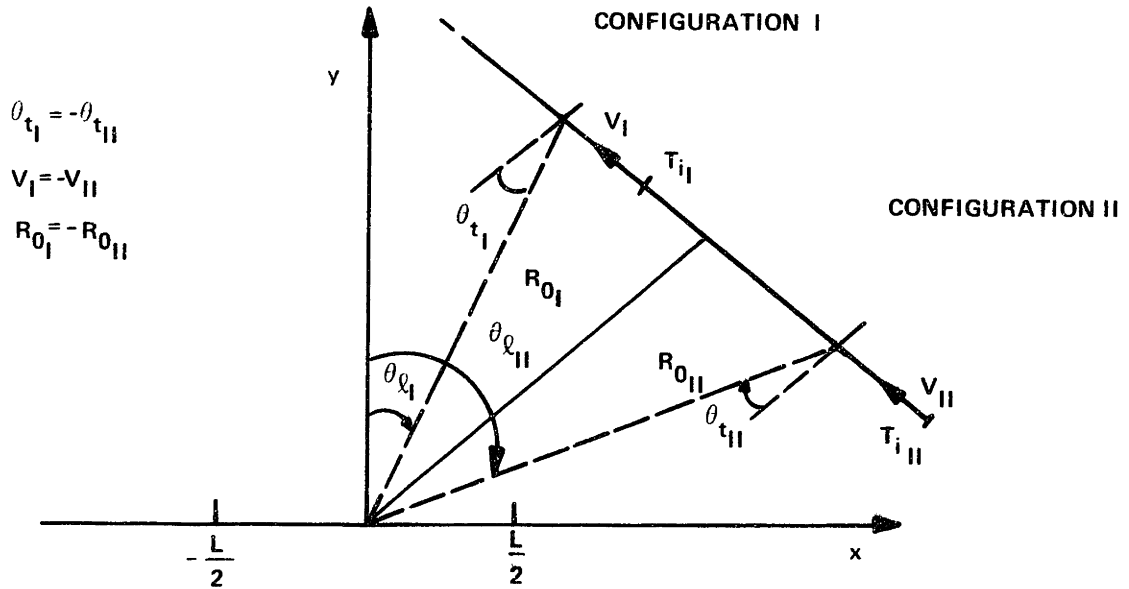
which can equivalently be expressed as

$$R(t,\ell,A) = \{[R_0 - \ell\sin\theta_\ell - vt \sin\theta_t]^2 + [\ell\cos\theta_\ell + vt \cos\theta_t]^2\}^{1/2} \quad (3b)$$

As discussed in previous chapters, we work with $\sin\theta_i$, $i=\ell,t$ and not with the angles themselves. This wavenumber type dependence does not uniquely specify the relative source/receiver geometry, but removes from the model the known ambiguity introduced by the linear constraints. To illustrate the point, consider a ship navigation problem; then, we either know the side where the source center is, e.g. on port, or the experiment is repeated a second time with a different line course.

The measurement of the bearing angle θ_ℓ resolves the indetermination of the signs of each individual factor in the product $v\sin\theta_t$ that was observed in the previous

chapter, for, as seen from Figure 3, the two geometric configurations I and II are now clearly distinguishable.



Ambiguity Resolution of Signs of V and $\sin \theta_f$ in SAMS

Figure 3

2. Receiver Structure

The positioning/navigation problem with spatial and temporal diversity has been cast in the context of an estimation problem with a finite number of nonrandom,

unknown parameters imbedded nonlinearly on signals corrupted by additive (temporally-) white, (spatially-) homogeneous Gaussian noise. As discussed in earlier chapters, the maximum-likelihood receiver is asymptotically efficient, and consists of a matched filter followed by a square law envelope detector. The receiver structure is determined by the signal correlation function and by the Generalized Ambiguity Function (GAF) introduced in chapter II and given by

$$\psi(A, \bar{A}) = \frac{1}{T} \int_{-\frac{T}{2}}^{\frac{T}{2}} dt \frac{1}{L} \int_{-\frac{L}{2}}^{\frac{L}{2}} d\ell \exp[j\frac{2\pi}{\lambda} \Delta R(t, \ell, A, \bar{A})] \quad (4a)$$

and

$$\phi(A, \bar{A}) = |\psi(A, \bar{A})|^2 \quad (4b)$$

with

$$\Delta R(t, \ell, A, \bar{A}) = R(t, \ell, A) - R(t, \ell, \bar{A}) \quad (4c)$$

and $R(t, \ell, A)$ given by equation 3a or equation 3b.

The ML-receiver specified by equations 4 represents a processing over two dimensions, space and time. With the SASS and SAMS₀ of chapters II and III, the homogeneity introduced in one of these domains, namely the time stationarity of the relative dynamics in SASS, or the omnidirectional sensor with SAMS₀, lead to a simpler one dimensional processor. This can be viewed as a special case of a more general situation, where the receiver's two-dimensional structure is decoupled on its spatial and temporal dimensions, i.e., the signal autocorrelation function factors as the product of a time integral and a space integral

$$\psi(A, \bar{A}) = \psi(A, \bar{A}, T) \psi(A, \bar{A}, L) \quad (5a)$$

where

$$\psi(A, \bar{A}, Z) = \frac{1}{Z} \int_{-\frac{Z}{2}}^{\frac{Z}{2}} dz \exp j \Delta R(z, A, \bar{A}), \quad z=l \text{ or } t \quad (5b)$$

The importance of this factorability or separability is two fold. First, it expresses the processor in terms of two independent blocks, each one representing a processing in one of the domains. If there are changes in one of these, not affecting the underlying assumptions leading to the factorability of equation 5a, they only affect the design

of one of the blocks, having the other unaltered. Second, this factorability may lead to a separability of the signal autocorrelation, and hence of the Generalized Ambiguity Function, over the parameter space, giving rise to considerable savings in the processing load work.

In the detection context, a different concept of factorization of the optimal processor's structure has been considered by [Mid65] where conditions are found for the factorability of the optimal detector in two operations. The first depends only on the geometry of the array, the second on the statistics of the noise processes. It is pointed out there that, in general, factorability in this sense is not possible in optimal systems. For active systems, and for detection and estimation problems, some conditions on the signal structure, ensuring the factorability of the processor, are present in [Urk62], and generalized to the case of reverberation and colored noise in [Pa746].

With the SAMS model of this chapter, the received random form exhibits a nonhomogeneous spatial and nonstationary temporal structure, leading to a complex receiver whose analysis is not conducive to intuitive closed form expressions.

To understand the structure of SAMS and the theoretical limitations of the performance, we pursue, in the subsequent sections of the chapter, the questions of factorability (in the sense defined by equation 5a), and spatial/temporal coupling, by developing the analysis of SAMS for two specific configurations. The first, assumes that the temporal diversity dominates the spatial diversity. This leads to a decoupling of the spatial and temporal operations of the receiver, which are reflected on a separability of the ambiguity function as the product of two reduced dimension (on the parameter space Ω) ambiguity structures. It is shown that, for this configuration, the passive ranging is essentially accomplished using the temporal modulations. SAMS is put in the perspective of the previous chapters, decoupling into a SAMS and a passive bearing problem with a Rayleigh model. The second configuration considers the problem where the spatial and temporal baselines are comparable, and investigates the effects induced on the receiver structure and performance by the coupling.

For both we pursue a least order type analysis, based on truncated Taylor series approximations to the range function, and compute the ambiguity function, and bounds on the mean square performance.

3. Decoupled Spatial/Temporal SAMS Structure

We make two hypothesis on the geometric configuration of SAMS:

$$H1: X_{\ell} = \frac{L}{2R_0} \ll 1$$

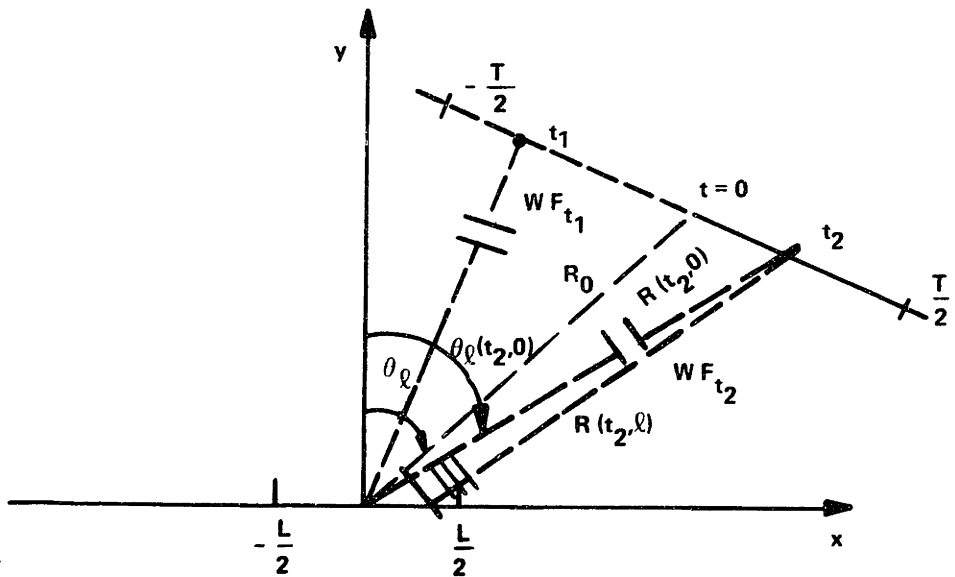
$$H2: X_{\ell} \ll X_t = \frac{vT}{2R_0}$$

These assumptions justify a linearized Taylor series analysis on the spatial variable. The range function becomes

$$R(t, \ell) \approx R(t, 0) + \frac{\cos(\theta_t - \theta_{\ell})vt - R_0 \sin\theta_{\ell}}{R(t, 0)} \ell \quad (6a)$$

$$= R(t, 0) - \sin\theta_{\ell}(t, 0)\ell \quad (6b)$$

where $\theta_{\ell}(t, 0)$ is the bearing angle at time t with respect to the center of the reference frame, see figure 4. This linearized structure in the space variable, simply states that, at each particular instant of time, the wavefield across the receiver's array is planar, and that, as the source moves along its linear track, the spatial structure of the received signals changes, see figure 4.



Time Varying Spatial Structure

Figure 4

We note that

$$R(t,0) = \{R_0^2 + (vt)^2 - 2(vt)R_0 \sin\theta_t\}^{1/2} \quad (7)$$

depends only on the reduced dimension vector

$$A_0 = \begin{bmatrix} R_0 \\ v \\ \sin\theta_t \end{bmatrix} \quad (8)$$

of the source parameters associated with the SAMS₀ model of the last chapter, while $\theta_{\ell}(t, o)$ depends on the full parameter vector A .

3.1 Ambiguity Structure

The signal autocorrelation function can be rewritten as

$$\psi(A, \bar{A}) \approx \frac{1}{T} \int_{-\frac{T}{2}}^{\frac{T}{2}} dt \exp\left[j\frac{2\pi}{\lambda}\Delta R(t, o, A_o, \bar{A}_o)\right] \left\{ \frac{1}{L} \int_{-\frac{L}{2}}^{\frac{L}{2}} d\ell \exp\left[-j\frac{2\pi}{\lambda}\Delta \sin\theta_{\ell}(t, o, A, \bar{A})\right] \right\} \quad (9a)$$

or

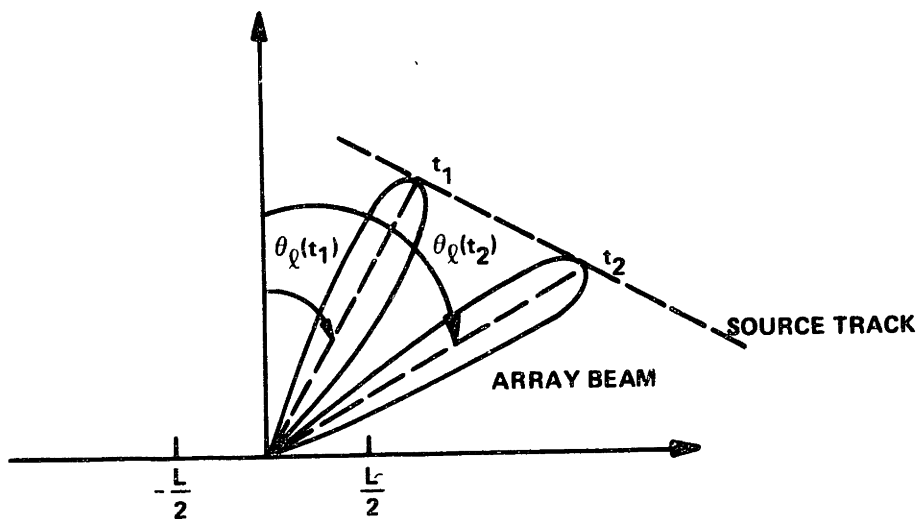
$$\psi(A, \bar{A}) \approx \frac{1}{T} \int_{-\frac{T}{2}}^{\frac{T}{2}} dt \exp\left[j\frac{2\pi}{\lambda}\Delta R(t, o, A_o, \bar{A}_o)\right] \psi_{\ell}(\Delta \sin\theta_{\ell}(t, o, A, \bar{A})) \quad (9b)$$

where

$$\psi_{\ell}(\Delta \sin\theta_{\ell}(t, o, A, \bar{A})) = \text{sinc}\left[\frac{2\pi}{\lambda}\Delta \sin\theta_{\ell}(t, o, A, \bar{A})\frac{L}{2}\right] \quad (9c)$$

Since the wavefronts are planar across the array, we assume that spatial diversity techniques are used, (array processing with beam forming) to match the bearing angle, so that, as the source sweeps the horizon, the receiver updates the bearing estimate. The function

$\psi_{\ell}(\Delta \sin \theta_{\ell}(t, o, A, \bar{A}))$ is kept practically constant across the source travel (approximately tuned to 1), with the array sequentially steered to the source varying bearing, as illustrated in figure 5.



Sequential Beam Steering

Figure 5

To compute the number of updates we define in the usual way [Bag73] the array bearing resolution by

$$\psi_{\ell}(\sin \theta_{\ell}(t_1, o) - \sin \theta_{\ell}(t_2, o)) > \frac{1}{\sqrt{2}} \quad (10)$$

i.e., assuming the aperture steered at $\theta_{\ell}(t_1, o)$, the

resolution is given by the bearing interval over which the (spatial) aperture response does not drop below the 3 dB cutoff. Since ψ_ℓ is the sinc function of equation 9c we obtain

$$\sin\theta_\ell(t_1,0) - \sin\theta_\ell(t_2,0) < \frac{2.78}{\frac{2\pi}{\lambda} L} \quad (11a)$$

Taking $t_1=0$ the resolution is given by

$$\Delta\sin\theta_\ell = \sin\theta_\ell - \sin\theta_\ell(t_2,0) < \frac{2.78}{\frac{2\pi}{\lambda} L} \quad (11b)$$

The total bearing variation across the source travel is approximately

$$\sin\theta_\ell\left(\frac{T}{2},0\right) - \sin\theta_\ell\left(-\frac{T}{2},0\right) = \cos(\theta_\ell - \theta_t) X_t \left[1 + \left(1 - \frac{4\frac{vT}{2} R_o \sin\theta_t}{R\left(-\frac{T}{2},0\right)} \right)^{1/2} \right] \quad (11c)$$

$$\approx 2\cos(\theta_\ell - \theta_t) X_t \quad (11d)$$

so that the number of updates is

$$N_u \approx \left\lceil 4.5 \cos(\theta_\ell - \theta_t) \frac{LX_t}{\lambda} \right\rceil \quad (12a)$$

where $\lfloor (\cdot) \rfloor$ stands for the largest integer contained in (\cdot) . In the sequel we omit the bars.

For

$$\begin{aligned} \theta_\ell &= \theta_t \\ N_u &\cong 4.5 \frac{LX_t}{\lambda} \\ &= 2.25 \frac{L}{\lambda} \frac{(vT)}{R_o} \end{aligned} \quad (12b)$$

Returning to the ambiguity structure, if

$$N_u = 1$$

$$\psi_\ell(\Delta \sin \theta_\ell(t, o, A, \bar{A})) \cong \text{sinc} \left[\frac{2\pi}{\lambda} (\Delta \sin \theta_\ell) \frac{L}{2} \right] \quad (13a)$$

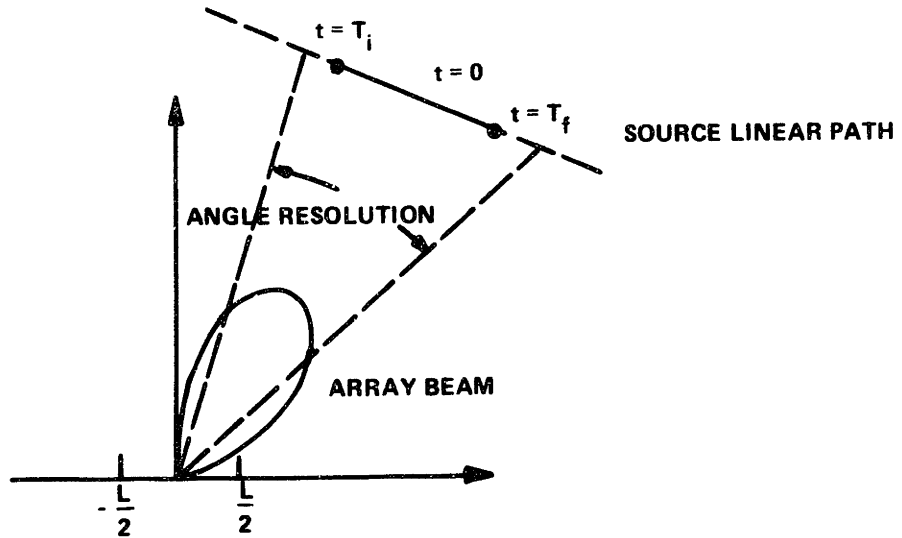
and

$$\psi(A, \bar{A}) = \psi_o(A_o, \bar{A}_o) \text{sinc} \left[\frac{2\pi}{\lambda} (\Delta \sin \theta_\ell) \frac{L}{2} \right] \quad (13b)$$

where $\psi_o(A_o, \bar{A}_o)$ is the signal autocorrelation function associated with the SAMS_o model.

This says that, when the angle spanned by the source travel is smaller than the receiver's aperture beamwidth, see figure 6, the SAMS signal autocorrelation decouples in its spatial and temporal aspects, with a correspondent factorization over the parameter space Ω : the range,

speed, and angle $\sin\theta_t$ being estimated from the temporal diversity, and the bearing from the spatial diversity.



Source Dynamics Within a Resolution Cell of the Linear Array

Figure 6

When

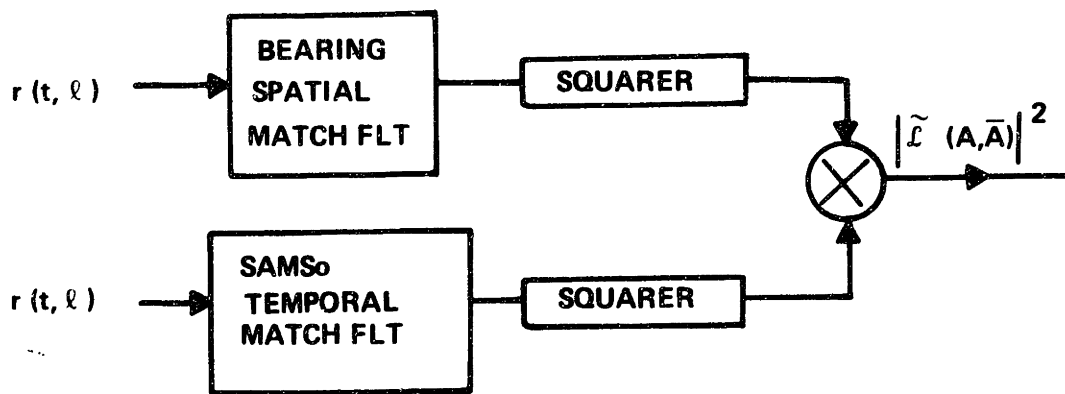
$$N_u > 1,$$

and assuming the sequential beam steering discussed above, shown in figure 5, the receiver's structure is still practically decoupled

$$\psi(A, \bar{A}) \cong \psi_o(A_o, \bar{A}_o) \psi_\ell(\Delta \sin\theta_\ell(t, o, A, \bar{A})) \quad (14)$$

The important difference between this and equation 13b lies on the time updating of the latter, which yields a

sequence of bearing measurements, instead of a single bearing. The receiver structure is mathematically equivalent to the block diagram displayed in figure 7.



Decoupled Receiver Structure

Figure 7

We study now the mean square performance of the decoupled structure. We concentrate on the analysis of the mean square spread matrix M and its inverse.

3.2 Computation of the Inverse of the Mean Square Spread Matrix

The Mean Square Spread Matrix (MSSM) given by equations 14,15 in Appendix B, requires the computation of the gradient of the range phase with respect to the source parameters. The (spatially-) linearized range function is (see equations 6)

$$R(t, \ell, A) \approx R(t, o, A_o) - \sin \theta_\ell(t, o, A) \ell \quad (15)$$

where we explicitly exhibited as arguments the vectors A_o , and A , to show on which source parameters does each term depend on. The gradient is

$$\nabla_A R(t, \ell, A) = \begin{bmatrix} \nabla_{A_o} R(t, o, A_o) \\ 0 \end{bmatrix} - \nabla_A \sin \theta_\ell(t, o, A) \ell \quad (16)$$

Noting that i) the first term does not depend on ℓ , ii) on the second term this dependence is linear, and iii) using the assumed symmetry of the array geometry, it follows that the MSSM can be written as

$$M \approx M_R + M_{\theta_\ell} \frac{\ell^2}{3} \quad (17a)$$

where

$$M_R = \begin{bmatrix} M_o & \text{---} \\ \text{---} & \underline{o} \\ \underline{o} & \text{---} \\ \text{---} & \underline{o} \end{bmatrix} \quad (17b)$$

$$M_{\theta_\ell} = \begin{bmatrix} M_{\theta_\ell}^3 & \text{---} & m \\ \text{---} & \text{---} & \text{---} \\ m^T & \text{---} & M_{44\theta_\ell} \end{bmatrix} \quad (17c)$$

M_o = MSSM associated with SAMS_o model of chapter III

$$M_{44\theta_\ell} = \left(\frac{2\pi}{\lambda}\right)^2 \left[\frac{\sin^2(\theta_t - \theta_\ell)}{\cos^2 \theta_\ell} H_2 + H_0 \right] R_o^2 \quad (17d)$$

$H_2 = \ell$ equation B-30; $H_0 =$ equation B-28

and where the exact expression for the matrix $M_{\theta_\ell}^3$ and the vector m are of no special interest at this moment.

In order to compute the inversion of M we rearrange the terms in equation 17a. We define

$$\tilde{M}_R = \begin{bmatrix} M_o & \text{---} & \underline{o} \\ \text{---} & \text{---} & \text{---} \\ \underline{o} & \text{---} & M_{44\theta_\ell} \frac{x_\ell^2}{3} \end{bmatrix} \quad (18a)$$

$$\tilde{M}_{\theta_\ell} = \begin{bmatrix} M_{\theta_\ell}^3 & \text{---} & m \\ \text{---} & \text{---} & \text{---} \\ m & \text{---} & \underline{o} \end{bmatrix} \frac{x_\ell^2}{3} \quad (18b)$$

Since

$$\tilde{M}_R > 0 ,$$

we can define a suitable unique square root matrix such that

$$\tilde{M}_R = \tilde{M}_R^{1/2} \tilde{M}_R^{1/2} \quad (19a)$$

where

$$\tilde{M}_R^{1/2} = \begin{bmatrix} M_0^{1/2} & \underline{0} \\ \underline{0} & [M_{44} \theta_\ell \frac{x_\ell^2}{3}]^{1/2} \end{bmatrix} \quad (19b)$$

The inverse of M leads to

$$\tilde{M}^{-1} = \tilde{M}_R^{-1/2} [I + \tilde{M}_R^{-1/2} M_{\theta_\ell} \tilde{M}_R^{-1/2} \frac{x_\ell^2}{3}]^{-1} \tilde{M}_R^{-1/2} \quad (20)$$

For a valid mean square expansion of the inverse of the bracketed matrix in equation 20, we need to satisfy

[Mid65]

$$\max \lambda_i(\Delta) < 1 \quad (21)$$

where $\lambda_i(\Delta)$ are the eigenvalues of

$$\Delta = \tilde{M}_R^{-1/2} \tilde{M}_{\theta_\ell}^{-1/2} \tilde{M}_R^{-1/2} \frac{X_\ell^2}{3} = \left[\begin{array}{ccc|c} \tilde{M}_O^{-1/2} & \tilde{M}_{\theta_\ell}^3 & \tilde{M}_O^{-1/2} & X_\ell \\ \hline & & & m_\Delta \\ \hline & m_\Delta^T & & o \end{array} \right] \quad (22a)$$

$$m_\Delta = \left[\begin{array}{c} M_{44} \theta_\ell \\ \hline 3 \end{array} \right]^{-1/2} M_O^{-1/2} m \quad (22b)$$

By a continuity argument, or by analysing the trace and the determinant of Δ , we can show that

$$\lambda_1(\Delta) \sim o(X_\ell) \quad (23)$$

i.e., is at least of the order X_ℓ , or is zero and of $o(X_\ell^2)$. For sufficiently short baseline arrays, condition 21 will be satisfied. It follows then

$$M^{-1} \approx \tilde{M}_R^{-1/2} \left\{ I + \sum_{n=1}^{\infty} (-1)^{n_\Delta n} \right\} \tilde{M}_R^{-1/2} \quad (24)$$

which up to the least nonzero order in Δ is

$$M^{-1} \approx \tilde{M}_R^{-1/2} (I - \Delta) \tilde{M}_R^{-1/2} \quad (25a)$$

$$= \begin{bmatrix} M_o^{-1} & & \tilde{m} \\ \hline \tilde{m}^T & (M_{44} \theta_\ell \frac{X_\ell^2}{3})^{-1} & \end{bmatrix} - \begin{bmatrix} M_o^{-1} M_{\theta_\ell}^3 M_o^{-1} \frac{X_\ell^2}{3} & \hline \hline \underline{o} & \underline{o} \end{bmatrix} \quad (25b)$$

where

$$\tilde{m} = -M_o^{-1} M_{\theta_\ell} M_o^{-1} m \quad (25c)$$

A sufficient condition for equation 25a to be a reasonable approximation to equation 24 is that (see [Mid65])

$$\max \frac{X^T \Delta X}{X^T X} \ll 1 \quad (26)$$

which will certainly be the case for sufficiently small array baseline, i.e., whenever

$$X_\ell \ll 1.$$

Equation 25a represents the inverse of MSSM for SAMS when, due to the overall geometry, the signal wavefield presents instantaneously a planar wavefront across the array. The second term of the right hand side of equation 25b represents the first order correction, when the sequence

of bearing measurements, obtained by processing the time varying spatial signal structure, is coupled to the information conveyed in the temporal modulations, to lead the estimates of the remaining source parameters, namely the reduced parameter vector A_0 .

When this coupling is neglected as suggested by the decoupled receiver in figure 7, the inverse MSSM is given by the first term of equation 25, leading to a deterioration in the mean square performance as seen from the oscillant character of the geometric series in equation 24.

The 3×3 minor M_0^{-1} in equation 25b is equivalent to the inverse of MSSM for the $SAMS_0$ model, as given in the previous chapter. The global and local results on the mean square performance of the parameters in A_0 are then equivalent to the ones derived for $SAMS_0$.

The cross correlations between the parameter errors, as computed from the inverse of MSSM are

$$\rho_{ij} = \rho_{ij_0} \text{ for } i, j \leq 3 \quad (27a)$$

and

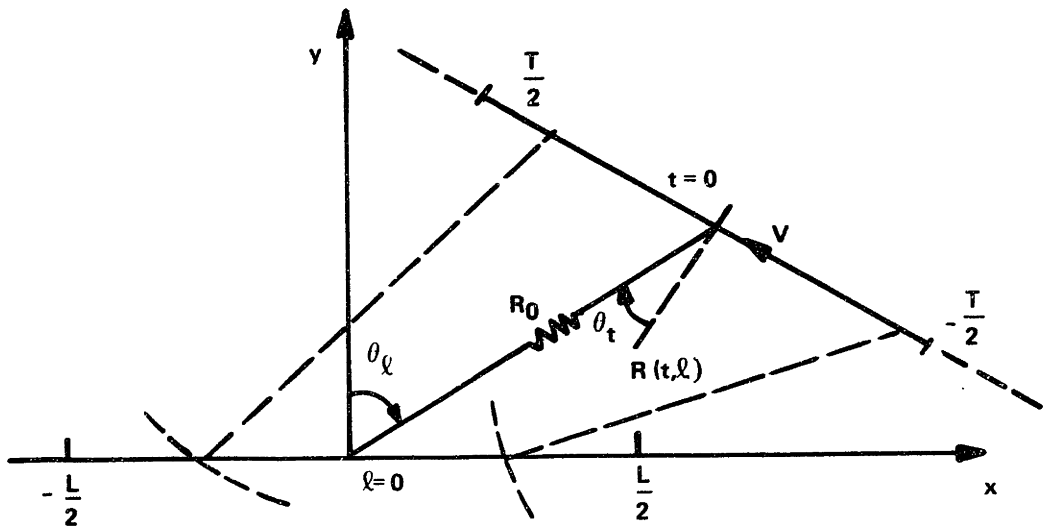
$$\rho_{i4} = \frac{(M^{-1})_{i4}}{[(M^{-1})_{ii}(M^{-1})_{44}]^{1/2}} \quad (27b)$$

$$= \rho_{i4}(A, X_t) X_\ell$$

i.e., the cross correlation between the components of A_0 are as in $SAMS_0$; but we note that a cross correlation of the order of X_ℓ is introduced by the weak coupling between the errors on the parameter estimates of A_0 and the bearing angle θ_ℓ .

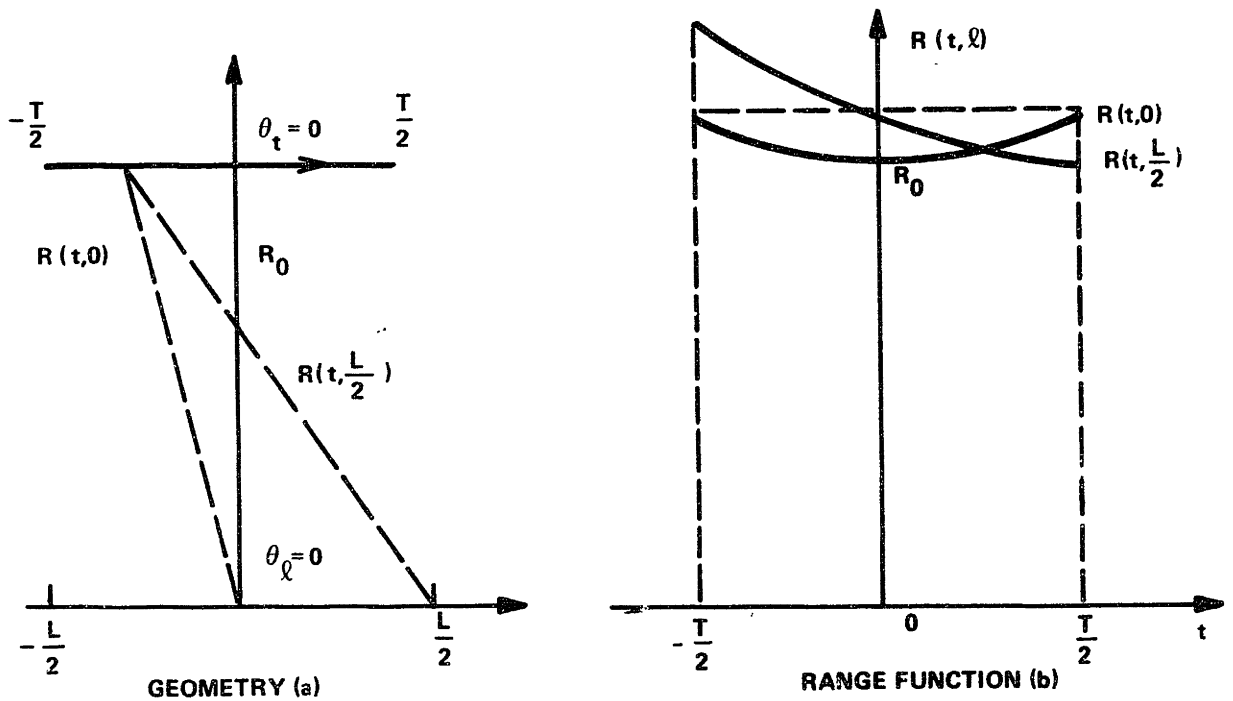
4. Coupled Spatial/Temporal SAMS Structure

We consider in this section the problem where, due to the overall geometry and relative dimensions, the spatial/temporal structures are coupled. The source travels in the near field of the array, and is observed by the receiver for a sufficiently large time interval. Consequently, significant (spatial-) curvature and higher order (temporal-) modulation effects are available, as illustrated in figure 8, to be jointly processed, and to yield the estimation of the four source parameters. The range function $R(t, \ell)$ exhibits a significant variation at each instant across the linear array, and at each array point across the source travel, as illustrated in figure 9 for a broadside ($\theta_\ell=0$) and closest approach ($\theta_t=0$) geometry, and for the special case where the array length equals the source travel.



Spatial / Temporal Coupled Curvature Geometry

Figure 8



Spatial / Temporal Cross-Coupling ($X_1 = X_t$)

Figure 9

To obtain closed form expressions and an intuitive understanding of the coupling issues, we pursue in detail the analysis for the case:

$$H1: X_l = \frac{L}{2R_0} < 1$$

and

$$H2: X_t = \frac{vT}{2R_0} < 1$$

where the range is H1) larger than half the array length and H2) larger than half the source travel. These conditions justify a higher order truncated Taylor series study, in both the space and time variables, about the geometry center $t=0, l=0$.

In operator form, the truncated Taylor series is given by

$$R(t, l) \cong \sum_{n=0}^N \frac{1}{n!} \left(t \frac{\partial}{\partial t} + l \frac{\partial}{\partial l} \right)^n R(t, l) \Big|_{\substack{t=0 \\ l=0}} \quad (28)$$

The lower order terms lead to

$$\begin{aligned} R(t, l) \approx R_0 & - \\ & - \sin\theta_t(vt) + \frac{\cos^2\theta_t(vt)^2}{R_0^2} + \dots \quad (29) \\ & - \sin\theta_l l + \frac{\cos^2\theta_l l^2}{R_0^2} + \dots \\ & + \frac{\cos\theta_l \cos\theta_t(vt)l}{R_0} + \dots \end{aligned}$$

Let, in compact notation,

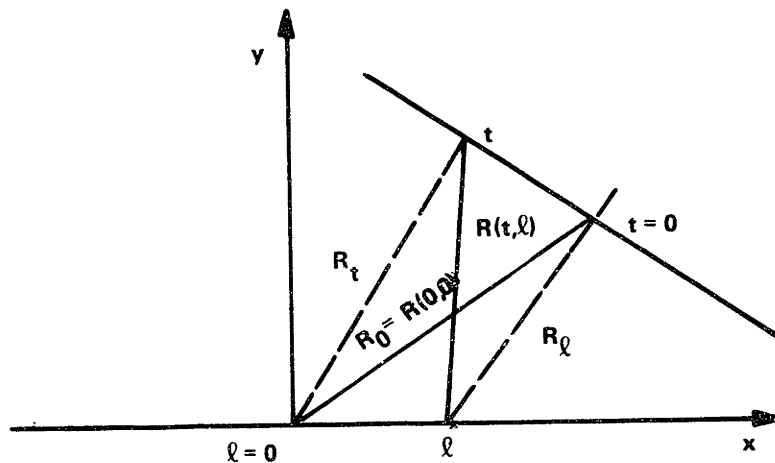
$$R_t \triangleq R(t, 0) \quad (30a)$$

$$R_\ell \triangleq R(0, \ell) \quad (30b)$$

and recalling their Taylor series expansion, we have

$$R(t, \ell) + R(0, 0) \approx R_t + R_\ell + \frac{\cos\theta_\ell \cos\theta_t}{R_0} (vt)\ell + \text{h.o.t.} \quad (30c)$$

Equation 30c represents the decomposition of the range function in terms of uncoupled terms (R_t and R_ℓ), and the cross coupling, which is approximated by a polynomial expression. Figure 10 illustrates several terms of the decomposition. We note that due to the incoherent model, the $R_0 = R(0, 0)$ term in equation 30c, plays no essential



Range Function Decomposition

Figure 10

role on the phase estimation process, and can be absorbed in the uniformly distributed random signal phase. Accordingly, it will be ignored in the subsequent discussions.

We consider first the structure of the ambiguity function on the parameter space Ω , and secondly the mean square matrix M , from which the performance bounds can be obtained.

4.1 Ambiguity Structure

In general, the signal autocorrelation and the ambiguity functions will be too complex to lend themselves to exact analysis, since they involve the double integration in time and space of a highly nonlinear function. We obtain a qualitative, as well as quantitative, description of their structure for SAMS, by exploiting the harmonic nature of the integrand, applying the Method of Stationary Phase (MSP), and coupling the results for the SAMS₀ and SASS models.

First, we analyse the secondary structure by discussing the asymptotic behavior of the exact autocorrelation function for large parameter deviations in the parameter space Ω . Secondly, we use the Taylor series approximation to the range phase, and investigate analytically the effects of the cross coupling on the ambiguity structure.

4.1.1 Asymptotic Behavior and Rate of Fall Off of the Ambiguity Structure

The signal autocorrelation function is, as before,

$$\psi(A, \bar{A}) = \frac{1}{LT} \int_{-\frac{T}{2}}^{\frac{T}{2}} dt \int_{-\frac{L}{2}}^{\frac{L}{2}} d\ell \exp[j\frac{2\pi}{\lambda} \Delta R(t, \ell, A, \bar{A})] \quad (31)$$

If large errors in one or more of the source parameters occur, we can apply the MSP to obtain the dominant term on the right hand side (r.h.s.) of equation 31. It requires an extension to two dimensions of MSP, which reduces to a sequential application of the MSP results for one dimension to each one of the integrals on the r.h.s. of equation 31, see for example [Pap67].

For a phase stationary point (t^*, ℓ^*) in the domain of integration, i.e., if

$$\left. \begin{aligned} \frac{\partial \Delta R_*}{\partial t} &\stackrel{\Delta}{=} \frac{\partial \Delta R(t, \ell, A, \bar{A})}{\partial t} \Bigg|_{\substack{t=t^* \\ \ell=\ell^*}} = 0 \end{aligned} \right\} \quad (32a)$$

and

$$\frac{\partial \Delta R_*}{\partial \ell} = 0 \quad (32b)$$

for some $(t^*, \ell^*) \in [-\frac{T}{2}, \frac{T}{2}] \times [-\frac{L}{2}, \frac{L}{2}]$, the signal autocorrelation

function behaves asymptotically ($\|A-\bar{A}\|$ gets large in Ω),
as

$$\psi(A, \bar{A}) \sim \frac{1}{\frac{2\pi}{\lambda} LT} \frac{2\pi j}{\left[\frac{\partial^2 \Delta R_*}{\partial \ell^2} \frac{\partial^2 \Delta R_*}{\partial t^2} - \left(\frac{\partial^2 \Delta R_*}{\partial \ell \partial t} \right)^2 \right]^{1/2}} \exp\left[j \frac{2\pi}{\lambda} \Delta R_*\right]$$

(33)

where

$$\Delta R_*, \frac{\partial^2 \Delta R_*}{\partial \ell^2}, \text{ etc.}$$

stand for the evaluation of

$$\Delta R, \frac{\partial^2 \Delta R}{\partial \ell^2}, \text{ etc.,}$$

at the point of stationary phase (t^*, ℓ^*). The denominator in equation 33 is assumed to be nonzero. If it vanishes, one obtains a bound involving higher order derivatives. Substituting in equation 33 the expression for the range phase $\Delta R(t, \ell, A, \bar{A})$, and computing the several derivatives, evaluated at the stationary phase, we obtain the asymptotic behavior of $\psi(A, \bar{A})$, and hence, the rate of fall off of the ambiguity function, for large parameter errors. These bounds are essentially inversely proportional to a certain combination of powers of the errors on the parameters. We refer to this, as we did in previous chapters, as the

hyperbolic decay of the secondary ambiguity structure. We can obtain similar bounds, in case only one or neither of equations 32 are satisfied. They express the dominant behavior of the signal autocorrelation, for large parameter deviations, in terms of the first order partial derivatives of the phase range difference evaluated at the extremes of the integration intervals.

Due to the unappealing analytical nature of these bounds we do not write them explicitly, but note that they can be computed in a straightforward way. They lead, as remarked above, to a hyperbolic decay of the secondary ambiguity structure. Our previous experience has shown that these type of bounds are tight, see figure 10 in chapter II, and so we conclude that, for large parameter errors, the ambiguity function is negligible in Ω .

4.1.2 Analytical Expression for the Coupled Ambiguity Structure

We proceed with the evaluation of the double integral defining the signal autocorrelation function $\psi(A, \bar{A})$ in equation 31. We use the polynomial approximation to the range function given in equations 29 and 30. The range phase difference function is written as

$$\frac{2\pi}{\lambda} \Delta R(t, \ell) \sim \Delta R_\ell + \Delta R_t + \Delta_{\ell t} \ell t \quad (34a)$$

where

$$\Delta R_{\ell} \triangleq \alpha_1 \ell + \alpha_2 \ell^2 + \dots = \frac{2\pi}{\lambda} \left[-\Delta(\sin \theta_{\ell}) + \Delta\left(\frac{\cos^2 \theta_{\ell}}{R_0^2}\right) \ell^2 + \dots \right] \quad (34b)$$

$$\Delta R_t \triangleq \beta_1 t + \beta_2 t^2 + \dots = \frac{2\pi}{\lambda} \left[-\Delta(\sin \theta_t) t + \Delta\left(\frac{\cos^2 \theta_t}{R_0^2}\right) t^2 + \dots \right] \quad (34c)$$

$$\Delta_{\ell t} = \frac{2\pi}{\lambda} \Delta\left(\frac{\cos \theta_1 \cos \theta_2 v}{R_0}\right) = \frac{2\pi}{\lambda} \left(\frac{\cos \theta_1 \cos \theta_2 v}{R_0} - \frac{\overline{\cos \theta_1 \cos \theta_2 v}}{\bar{R}_0} \right) \quad (34d)$$

We make several remarks:

- i) The $\Delta(\cdot)$ notation is explained in equation 34d, and represents the difference of the argument evaluated at the source parameter vector A and at the scanning value \bar{A} .
- ii) As noted below equation 30c, due to the incoherent model, the constant phase factor R_0 that should appear in equations 34a, 34b, 34c contribute nothing to GAF, and so can be ignored.
- iii) ΔR_{ℓ} depends only on the bearing angle $\sin \theta_{\ell}$ and the range R_0 . We let in the sequel the two dimensional parameter vector associated with the SASS model be

$$A_s = \begin{bmatrix} R_o \\ \sin\theta_\ell \end{bmatrix} \quad (35a)$$

ΔR_t depends only on the reduced 3 dimensional vector

$$A_o = \begin{bmatrix} R_o \\ v \\ \sin\theta_t \end{bmatrix} \quad (35b)$$

associated with $SAMS_o$. Only the cross coupling, reduced in equation 34a to its lowest order term $\Delta_{\ell t}$, does depend on the full parameter vector A. Below, when a specific dependence is to be underlined, we exhibit explicitly as argument A_s , A_o or A, as might be the case.

The signal autocorrelation becomes

$$\psi(A, \bar{A}) \sim \frac{1}{L^2} \int_{-\frac{T}{2}}^{\frac{T}{2}} dt \int_{-\frac{L}{2}}^{\frac{L}{2}} d\ell \exp[j(\Delta R_t + \Delta R_\ell + \Delta_{\ell t} \ell t)] \quad (36)$$

Integrating first, for example, over the space dimension, after some algebraic manipulations

$$\psi(A, \bar{A}) = \psi_s(A_s, \bar{A}_s) \psi_o(A_o, \bar{A}_o) + j_{\ell t} \quad (37a)$$

where

$$\psi_o(A_o, \bar{A}_o) = \frac{1}{T} \int_{-\frac{T}{2}}^{\frac{T}{2}} dt \exp[j\Delta R_t] \quad (37b)$$

is the signal autocorrelation associated with SAMS_o;

$$\psi_s(A_s, \bar{A}_s) = \frac{1}{L} \int_{-\frac{L}{2}}^{\frac{L}{2}} d\ell \exp[j\Delta R_\ell] \quad (37c)$$

is the signal autocorrelation associated with SASS;

$$J_{\ell t} = \frac{1}{T} \int_{-\frac{T}{2}}^{\frac{T}{2}} dt \exp[j\Delta R_t] \left\{ \frac{1}{\Delta L_o} \int_0^{\gamma_t} d\sigma [\exp j(\sigma + L_{f_o})^2 - \exp j(\sigma + L_{i_o})^2] \right\} \quad (37d)$$

is the term exhibiting the coupled nature of the processor. For the definitions of ΔL_o , L_{f_o} , etc. see table I. For a quadratic

$\Delta L_o = L_{f_o} - L_{i_o} = \sqrt{\frac{2}{\pi} \alpha_2} L$ $L_{f_o} = \sqrt{\frac{2}{\pi} \alpha_2} \left(\frac{L}{2} - \frac{\alpha_1}{2\alpha_2} \right)$ $L_{i_o} = \sqrt{\frac{2}{\pi} \alpha_2} \left(-\frac{L}{2} - \frac{\alpha_1}{2\alpha_2} \right)$ $\gamma_t = \frac{\Delta \ell t}{2\alpha_2^{1/2}}$ $F(\Sigma) = (\text{exp.}) \text{Fresnel Integ.} = \int_0^\Sigma \exp j\sigma^2 d\sigma$

Table I

range phase expansion we recall that we can rewrite, for example

$$\psi_s(A_s, \bar{A}_s) = \frac{1}{\Delta L_o} [F(L_{f_o}) - F(L_{i_o})] \quad (38)$$

The quantities defined in table I have the physical interpretation presented in Appendix A below equations 24.

Equation 37a presents the coupled signal autocorrelation as given by two terms. The first represents the product of the ambiguity structures associated with each individual dimension of the problem (space and time). The second introduces the correction due to the coupling. We see that the ambiguity structure is not separable, unless $\gamma_t = 0$, or, as will be shown in the sequel, $\gamma_t T$ is large.

In order to interpret the cross coupling term we rewrite its expression. Let

$$f(t, \Sigma) = \frac{1}{\Delta \Sigma} \int_0^{\gamma_t t} d\sigma \exp j(\sigma + \Sigma)^2 \quad (39a)$$

$$\begin{aligned} F(t, \Sigma) &= \frac{1}{T} \int_0^t f(t, \Sigma) dt \\ &= \frac{t}{T} f(t, \Sigma) - \int_0^t t \frac{df(t, \Sigma)}{dt} dt \\ &= \frac{1}{\gamma_t T} \frac{1}{\Delta \Sigma} \{ (\gamma_t t + \Sigma) [F(\gamma_t t + \Sigma) - F(\Sigma)] - \frac{1}{2j} [\exp j(\gamma_t t + \Sigma)^2 \\ &\quad - \exp(j\Sigma^2)] \} \quad (39b) \end{aligned}$$

We have then

$$J_{\Delta t} = J(T, L_{f_0}) - J(T, L_{i_0}) \quad (40a)$$

where

$$J(T, \Sigma) = F\left(\frac{T}{2}, \Sigma\right) \exp\left[j\Delta R\left(\frac{T}{2}\right)\right] - F\left(-\frac{T}{2}, \Sigma\right) \exp\left[j\Delta R\left(-\frac{T}{2}\right)\right] - j \int_{-\frac{T}{2}}^{\frac{T}{2}} F(t, \Sigma) \frac{d\Delta R(t)}{dt} \exp[j\Delta R_t] dt \quad (40b)$$

For the quadratic expansion of ΔR_t

$$\left. \frac{d\Delta R(t)}{dt} \right|_{t=t_*} = \beta_1 + 2\beta_2 t_* = 0$$

$$\Rightarrow t_* = -\frac{\beta_1}{2\beta_2}, \quad \beta_2 \neq 0 \quad (41)$$

For T sufficiently large, $t_* \in \left[-\frac{T}{2}, \frac{T}{2}\right]$, and by MSP

$$j \int_{-\frac{T}{2}}^{\frac{T}{2}} F(t, \Sigma) \frac{d\Delta R(t)}{dt} \exp[j\Delta R_t] dt \approx 0 \quad (42)$$

For a large cross coupling parameter γ_t , when the coupling is more evident, and for sufficiently large T

$$F\left(\pm\frac{T}{2}, \Sigma\right) \xrightarrow[\text{large } \gamma_t T]{\sim} \frac{1}{2} \frac{1}{\Delta \Sigma} \left[\frac{1}{2} \mp F(\Sigma) \right] \quad (43)$$

which leads to

$$J(T, L_{f_0}) - J(T, L_{i_0}) \xrightarrow[\text{large } \gamma_t T]{\sim} -\exp[j\beta_2(\frac{T}{2})^2] \cos(\beta_1 \frac{T}{2}) \psi_S(A_S, \bar{A}_S) \quad (44)$$

where we used equation 43 in equation 40b, and assumed a quadratic range approximation.

Finally

$$\begin{aligned} \psi(A, \bar{A}) \approx \psi_S(A_S, \bar{A}_S) \{ [\psi_0^r(A_0, \bar{A}_0) - \cos(\beta_1 \frac{T}{2}) \cos[\beta_2(\frac{T}{2})^2]] + \\ + j[\psi_0^i(A_0, \bar{A}_0) - \cos(\beta_1 \frac{T}{2}) \sin[\beta_2(\frac{T}{2})^2]] \} \quad (45) \end{aligned}$$

where

$$\psi_0 = \psi_0^r + j\psi_0^i \quad (46)$$

Equation 45 shows that whenever T and $\gamma_t T$ are large, the signal autocorrelation is still separable in two parts, one dependent on the space and the other on the time domain, but with the latter factor not simply being the $SAMS_0$ signal autocorrelation. Similarly we obtain equivalent results, if we start by integrating first over time, and assume a large L and $\gamma_l L$, where γ_l has a

definition equivalent to γ_t .

We now look at the coupled ambiguity structure along specific subspaces in Ω , namely the coordinate axes or planes.

$(\Delta v, \Delta \sin \theta_t)$ - Plane

Let $\pi_{v\theta_t}$ be the subspace (plane) in Ω given by

$$\Delta R_o = 0 \quad (47a)$$

$$\Delta \sin \theta_{\ell} = 0 \quad (47b)$$

The signal autocorrelation function in $\pi_{v\theta_t}$ becomes

$$\psi(A, \bar{A}) \approx \frac{1}{T} \int dt \exp[j\Delta R_t] \text{sinc}(\Delta_{\ell t} t \frac{L}{2}) \quad (48)$$

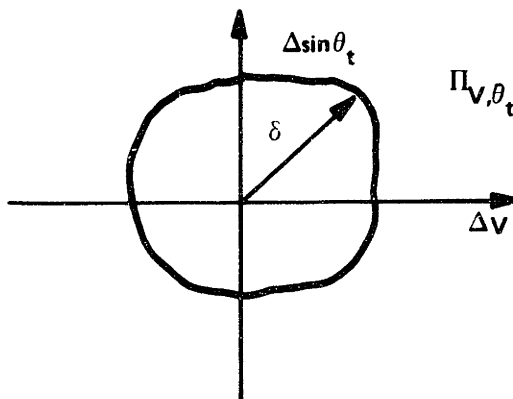
Consider on $\pi_{v\theta_t}$ the locus L where

$$\Delta_{\ell t} < \Delta_* = \frac{\pi}{\frac{L}{2} \frac{T}{2}} \quad (49a)$$

or equivalently

$$\Delta(v \cos \theta_t) < \delta = \frac{R}{\cos \theta_{\ell}} \frac{\pi}{\frac{L}{2} \frac{T}{2}} \quad (49b)$$

shown in figure 11.



Locus on $\Pi_{V\theta_t}$

Figure 11

For points in L

$$0 < \text{sinc}[\Delta_{\lambda t} t \frac{L}{2}] < 1 \quad \text{for } vt \in [-\frac{T}{2}, \frac{T}{2}] \quad (50)$$

leading to

$$\psi(A, \bar{A}) \sim \psi_0(A_0, \bar{A}_0) \text{sinc}(\Delta_{\lambda t} t^* \frac{L}{2}) \quad (51)$$

where $\text{sinc}(\Delta_{\lambda t} t^* \frac{L}{2})$ is either computed at the stationary phase, if $t^* \in [-\frac{T}{2}, \frac{T}{2}]$, or is an average value.

Outside L the sinc is negligible whenever

$$t > |t_0| \quad (52a)$$

where

$$t_o = \frac{\pi}{\frac{L}{2} |\Delta_{\ell t}|}, \quad (52b)$$

and so

$$\psi(A, \bar{A}) \sim \frac{2t_o}{T} \left[\frac{1}{2t_o} \int_{-t_o}^{t_o} dt \exp[j\Delta R_t] \text{sinc}(\Delta_{\ell t} t \frac{L}{2}) \right] \quad (53)$$

But, by the same argument as above,

$$\psi(A, \bar{A}) \sim \frac{2t_o}{T} \psi_{2t_o}(A_o, \bar{A}_o) \text{sinc}(\Delta_{\ell t} t * \frac{L}{2}) \quad (54)$$

In equation 54 the index $2t_o$ makes explicit the "modified" total observation interval.

The effect of coupling is to sharpen the ambiguity structure, maintaining its fundamental aspects, namely a main lobe and a secondary negligible structure. The quantitative analysis, in terms of the dimensions of the main lobe, will be pursued when we study the MSSM.

$\Delta \sin \theta_1$ -Subspace

The analysis parallels the preceding one. We find

$$\psi(A, \bar{A}) \approx \frac{1}{L} \int_{-\frac{L}{2}}^{\frac{L}{2}} d\ell \exp[j\Delta R_\ell] \text{sinc}(\Delta_{\ell t} \ell \frac{T}{2}) \quad (55)$$

Similarly, we define the locus L by equation 49a, which now implies

$$\Delta(\cos\theta_\ell) < \delta = \frac{R_o}{v \cos\theta_t} \frac{\pi}{\frac{L}{2} \frac{T}{2}} \quad (56)$$

For points in the locus

$$\psi(A, \bar{A}) \sim \psi_s(A_s, \bar{A}_s) \text{sinc}(\Delta_{\ell t} \ell * \frac{T}{2}) \quad (57)$$

Outside L we define

$$\ell_o = \frac{R \pi}{\frac{vT}{2} \cos\theta_t |\Delta(\cos\theta_\ell)|} \quad (58)$$

and obtain

$$\psi(A, \bar{A}) \sim \frac{2\ell_o}{L} \psi_{2\ell_o}(A_s, \bar{A}_s) \text{sinc}(\Delta_{\ell t} \ell * \frac{T}{2}) \quad (59)$$

The conclusions are equivalent to the previous ones.

Radial Parameter

Along the radial parameter subspace

$$\psi(A, \bar{A}) \approx \frac{1}{LT} \int_{-\frac{T}{2}}^{\frac{T}{2}} dt \int_{-\frac{L}{2}}^{\frac{L}{2}} d\ell \exp\left[j \frac{2\pi}{\lambda} \frac{1}{2} (\cos\theta_{\ell} \ell + \cos\theta_t vt)^2 \Delta\left(\frac{1}{R_o}\right)\right] \quad (60)$$

Define the change of variables

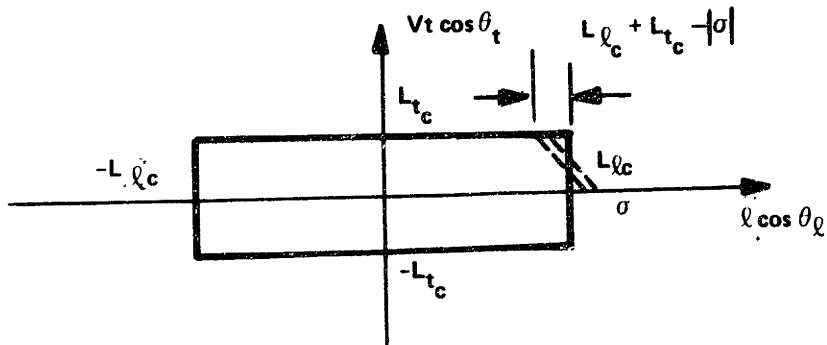
$$\sigma = \cos\theta_{\ell} \ell + \cos\theta_t vt \quad (61a)$$

and recall the definitions

$$x_{\ell c} = \frac{L}{2R_o} \cos\theta_{\ell} = \frac{L_{\ell c}}{R_o} \quad (62b)$$

$$x_{t c} = \frac{vT}{2R_o} \cos\theta_t = \frac{L_{t c}}{R_o} \quad (62c)$$

Performing the double integration in equation 60 along the dashed lines illustrated in figure 12, where the integrand is constant, we obtain



Reduction of Double to Single Integration

Figure 12

$$\psi(A, \bar{A}) = \frac{(X_{lc} + X_{tc})^2}{X_{lc} X_{tc}} \psi'(A, \bar{A}) \quad (63a)$$

with

$$\psi'(A, \bar{A}) = \frac{1}{X_{ltc}} \int_0^{X_{ltc}} \left(1 - \frac{2\sigma}{X_{ltc}}\right) \exp[j(\Delta K)\sigma^2] d\sigma \quad (63b)$$

where we defined the wavenumber type parameter

$$\Delta K = \frac{\pi}{\lambda} \Delta\left(\frac{1}{R}\right) \quad (63c)$$

and the equivalent total geometric parameter

$$X_{ltc} = 2(X_{lc} + X_{tc}) \quad (63d)$$

Performing the integral in equation 63b

$$\psi'(A, \bar{A}) = \frac{F(\Delta K_{\ell t})}{\Delta K_{\ell t}} + \frac{1 - \exp[j\Delta K_{\ell t}^2]}{j(\Delta K_{\ell t})} \quad (64a)$$

with

$$\Delta K_{\ell t} = \sqrt{\Delta K} X_{\ell t c} \quad (64b)$$

Equation 63b shows that the spatial/temporal coupled signal autocorrelation along the radial parameter subspace, apart from a normalizing factor, corresponds to the signal autocorrelation for a one-dimensional problem, with the source at broadside, where the equivalent total linear dimension is, see figure 13a,

$$L_{\text{tot}} = L \cos\theta_{\ell} + vt \cos\theta_t \quad (65)$$

and where the array shading is of triangular type, and not uniform, as illustrated in figure 13b.

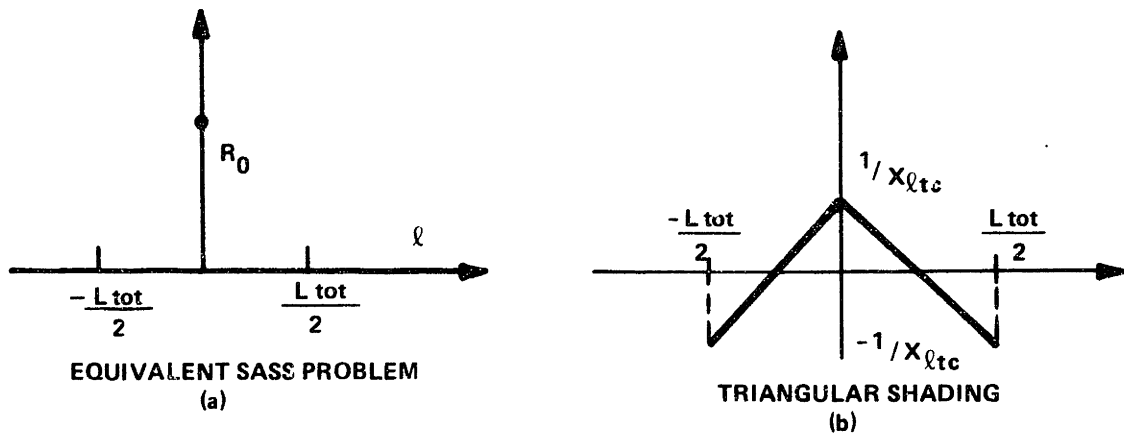


Figure 13

We finally comment that equation 63b generalizes the usual one dimensional distribution of the (Fresnel zone) diffracted field for a plane wave in optics, to the case where the line source (equivalent in our problem to the temporal baseline) and the receiving aperture (spatial baseline) are not parallel ($\theta_l \neq \theta_t$), and there is a wide angle ($\theta_l \neq 0$) and oblique incidence ($\theta_t \neq 0$).

4.2 Mean Square Spread Matrix

We study the Mean Square Spread Matrix (MSSM) M which exhibits the essential geometric aspects of the problem, and how they are reflected on the mean square performance of the ML-estimator.

In order to obtain intuitive closed form expressions we pursue a Taylor series analysis in terms of the geometric parameters

$$X = \frac{L}{2R_0} \quad (66a)$$

and

$$X_t = \frac{vT}{2R_0} \quad (66b)$$

We first consider a Taylor series expansion of the range function, which, in operator form, is given by

$$R(t, \ell) \cong \sum_{n=1}^N \frac{1}{n!} \left(t \frac{\partial}{\partial t} + \ell \frac{\partial}{\partial \ell} \right)^n R(t, \ell) \Bigg|_{\substack{t=0 \\ \ell=0}} \quad (67)$$

Although we restrict our attention to the lowest order term of $\text{Det } M$ (needed to compute M^{-1} , and the volume of the elementary grid cell), the dimensionality of M requires that we keep a relatively large number N of terms in expansion 67. The consequence is an extensive burden

of algebraic manipulations, leading to a not less extensive list of expressions. We concentrate in Appendix D. the results for the least order terms of M , its classical adjoint M , the inverse M^{-1} , and $\det M$. In the text we limit the analysis to $\det M$, the diagonal elements of M^{-1} (from which the performance bounds can be obtained), and to the parameter error cross correlations, defined from the elements of M^{-1} .

4.2.1 Det M

The determinant is given by

$$\det M = \left(\frac{2\pi}{\lambda}\right)^8 \frac{1}{3^6 \cdot 5} \frac{\cos^2 \theta_l}{\cos^2 \theta_t} X_l^4 X_t^4 (X_{l_c}^4 + \frac{4}{5} X_{l_c}^2 X_{t_c}^2 + X_{t_c}^4) \frac{R_o^6}{v^2} \quad (68a)$$

where

$$X_{l_c} = X_l \cos \theta_l = \frac{L \cos \theta_l}{2R_o} \quad (68b)$$

$$X_{t_c} = X_t \cos \theta_t = \frac{vT \cos \theta_t}{2R_o} \quad (68c)$$

We make the following remarks:

i) The lowest order term in Det M contains terms in

$$X_l^8 X_t^4, X_l^6 X_t^6, X_l^4 X_t^8$$

and is of order

$$n_{\text{SAMS}} = \text{order of least order term of } \det M = 12$$

In chapter IV we concluded that for the SAMS_0 problem

$$n_{\text{SAMS}_0} = 12$$

On the other hand the single parameter bearing estimation leads to

$$n_{\sin\theta_\ell} = 2$$

We see that, due to the coupling

$$n_{\text{SAMS}} < n_{\text{SAMS}_0} + n_{\sin\theta}, \quad (69)$$

while for the decoupled structure of the previous section, equality held. The spatial/temporal cross coupling improves, in a nontrivial way, the joint estimation of all source parameters, reducing the overall order of the problem. Intuitively speaking, with the decoupled problem,

at least third order effects had to be measured from the temporal diversity, while only the linear delays could be estimated from the spatial curvature (bearing). The cross coupling reduces to second, the lowest order effects that have to be measured, but now from both spatial and temporal diversity. We refer the reader to figure 9, pg.208 showing that, for the coupled geometry, the range function depends significantly on both time and space, and so intuitively suggesting an improvement of performance.

ii) The terms in

$$X_\ell^{12}, X_t^{12}, X_\ell^{10} X_t^2, X_\ell^2 X_t^{10}$$

are absent. This follows from the fact that M_{22} and M_{33} depend on at least X_t^2 , and M_{44} on X_ℓ^2 . Finally the last term has to be absent, since it would correspond to a decoupled type structure, for which

$$n_{\text{SAMS}} = n_{\text{SAMS}_0} + n_{\text{sin}\theta} = 14$$

corresponding to lowest order terms $X_\ell^2 X_t^{12}$.

iii) The matrix M is positive definite, as can be concluded by direct application of Sylvester's rule.

iv) We observed in the last section 4.1 that on the parameter subspace $\pi_{v\theta_t}$, the ambiguity structure, although separable, lead to a sharper lobe. Comparing the determinant for the $v, \sin\theta_t$ parameters for the SAMS

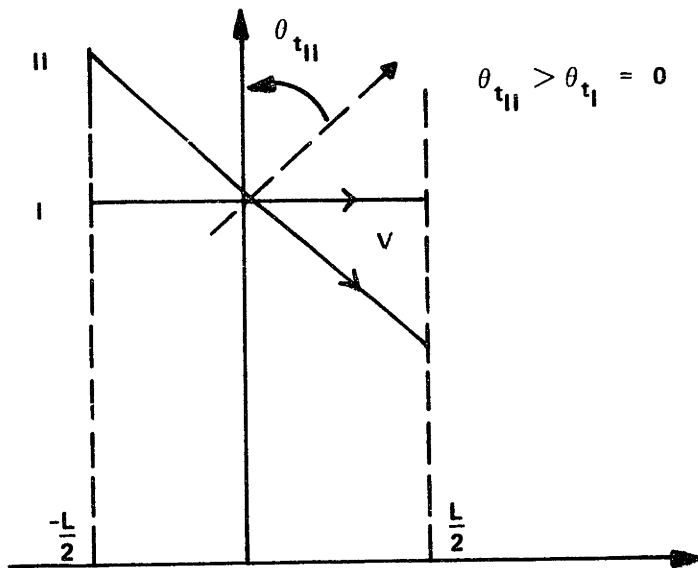
$$\begin{aligned} \text{Det } M_{v\sin\theta_t} &= M_{22}M_{33} - M_{23}^2 \\ &= \left(\frac{2\pi}{\lambda}\right)^4 \frac{R_0^4}{v^2} \frac{X_t^4}{3^3} \left[\frac{4}{5} X_t^2 + \frac{\cos^2\theta_\ell}{\cos^2\theta_t} X_\ell^2 \right] \quad (70) \end{aligned}$$

with equation 3-36-c, we conclude that, the last term in equation 70, reflecting the cross coupling, quantifies the correction to the main lobe dimensions on $\pi_{v\theta_t}$.

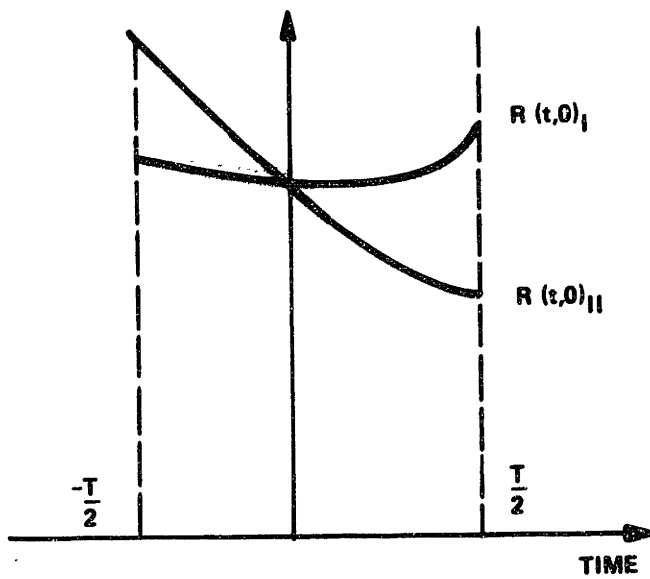
v) If we let

$$X_\ell, \cos\theta_\ell, X_{t_c} = X_t \cos\theta_t$$

to remain constant, while increasing θ_t from 0° (closest approach) to $\frac{\pi}{2}$, see figure 14(a), $\text{det } M$ increases. This is a result of the cross coupling observed in figure 14(b). As θ_t increases, but X_{t_c} is kept constant, the total source travel increases, with a larger variation of $R(t, \ell)$ over the total observation interval, and across the array.



(a)



(b)

Cross-Coupling. Dependence on θ_t - angle

Figure 14

4.2.2 Mean Square Parameters Spread

We discuss briefly the diagonal elements of the inverse matrix M^{-1} , which measure the spread of the ambiguity structure along the different parameter axes.

Range Spread: from Appendix D we obtain

$$M^{-1}_{R_0} = (M^{-1})_{11} = \left(\frac{\lambda}{2\pi}\right)^2 \frac{3^2 \cdot 5}{X_{c_\ell}^4} \frac{1 + \frac{4}{5} \gamma^2}{1 + \frac{4}{5} \gamma^2 + \gamma^4} \quad (71)$$

where γ defines the relation between the temporal and spatial effective baselines

$$\gamma = \frac{X_{c_t}}{X_{c_\ell}} = \frac{vT \cos\theta_t}{L \cos\theta_\ell} \quad (72)$$

i.e., as seen from the oblique angle θ_t and bearing θ_ℓ .

We consider three cases:

(i) Spatial baseline much larger than temporal baseline:

If

$$\gamma \ll 1$$

we obtain

$$(M^{-1}_{R_o})_I \approx \left(\frac{\lambda}{2\pi}\right)^2 \frac{3^2 \times 5}{X^4 c_\ell} \approx (M^{-1}_{R_o})_{\text{SASS}} \quad (73)$$

This equation 73 shows the range performance approaching the SASS result, of chapter III; the range parameter is essentially estimated from the spatial curvature effects observed across the array.

(ii) Comparable spatial and temporal baselines:

If

$$\gamma \approx 1$$

we have

$$(M^{-1}_{R_o})_{II} \approx \left(\frac{\lambda}{2\pi}\right)^2 \frac{3^2 \times 5}{X^4 c_\ell} \frac{1}{4} \left[\frac{9}{2} - 5(\gamma - 1) \right] \quad (74)$$

Comparing this with the previous one, at $\gamma = 1$

$$\frac{(M^{-1}_{R_o})_{II}}{(M^{-1}_{R_o})_I} \approx \frac{9}{14} \quad (75)$$

Equation 75 shows that the cross coupling reduces the range standard deviation to about 80%.

(iii) Temporal baseline much larger than spatial baseline:

If

$$\gamma \gg 1$$

we get

$$(M^{-1}_{R_o})_{III} \approx \left(\frac{\lambda}{2\pi}\right)^2 \frac{2^2 \times 3^2}{X_{c_t}^2 X_{c_l}^2} \quad (76)$$

Comparing with the correspondent expression for the SAMS_o problem of chapter IV

$$\frac{(M^{-1}_{R_o})_{III}}{(M^{-1}_{R_o})_{SAMS_o}} \approx \frac{X_{t_s}^2 \gamma^2}{5} \quad (77)$$

where

$$X_{t_s} = X_t \sin\theta_t = \frac{vT}{2R_o} \sin\theta_t \quad (78)$$

We recall that with the SAMS_o model the range performance deteriorated sharply for

$$\theta_t \approx 0$$

i.e., for broadside type geometries. Equation 77 says that, when there is a small, but nonzero, cross coupling, as long as

$$\frac{X_t^2 + \gamma^2}{5} < 1, \quad (79)$$

the range performance is sharply improved.

Velocity and $\sin\theta_t$ Spread

We obtain from Appendix D

$$M_{v,22}^{-1} = (M^{-1})_{22} = \left(\frac{\lambda}{2\pi}\right)^2 \frac{v^2}{R_0^2} \frac{3^2 x_5 \cos^2 \theta_t}{\cos^2 \theta_t X_\ell^2 X_t^2} \frac{1+5\gamma^2+\gamma^4}{1+4\gamma^2+5\gamma^4} \quad (80)$$

and

$$M_{\sin\theta_t}^{-1} = (M^{-1})_{33} = M_{v,22}^{-1} \left(\frac{\sin\theta_t}{v}\right)^2 \quad (81)$$

These lowest order terms are in $X_t^{-2} X_\ell^{-2}$, representing an improvement of order two over the decoupled problem performance (recall that for the decoupled structure of section 3 the speed and angle performance is essentially given by the SAMS₀ results, whose first nonzero term is of order X_t^{-6}). As in the discussion of point (i) for Det M, this represents the reduction on the order of the estimation problem introduced by the cross coupling.

We note that the relation in equation 81 is only for the coefficients of the lowest order terms.

From equation 80 we can consider, as we did for

the range spread, the three cases:

(i) Spatial baseline larger than the temporal baseline:

We have

$$\gamma \ll 1$$

and

$$(M_v^{-1})_I \approx \left(\frac{\lambda}{2\pi}\right)^2 \frac{v^2}{R_o^2} \frac{3^2 \times 5 \cos^2 \theta_t}{\cos^2 \theta_\ell X_\ell^2 X_t^2}$$

(ii) Comparable spatial and temporal baselines:

For

$$\gamma \approx 1$$

we obtain

$$\frac{(M_v^{-1})_{II}}{(M_v^{-1})_I} \approx \frac{7}{10} \approx .83^2 \quad (83)$$

(iii) Temporal baseline much larger than the spatial baseline: When

$$\gamma \gg 1$$

we get

$$\frac{(M_v^{-1})_{III}}{(M_v^{-1})_I} \approx \frac{1}{5} \approx .43^2 \quad (84)$$

These results exhibit the improvement on the speed performance, when the geometry changes from a spatially dominant (case I) to a temporally dominant (case II).

We can obtain similar relations for $M^{-1}_{\sin\theta_t}$.

Bearing Spread

The lowest order term for the bearing mean square spread is, from Appendix D,

$$M^{-1}_{\sin\theta_\ell} = (M^{-1})_{44} \approx \left(\frac{\lambda}{2\pi}\right)^2 \frac{1}{R_o^2} \frac{3}{X_\ell^2} = \left(\frac{\lambda}{2\pi}\right)^2 \frac{12}{L^2} \quad (85)$$

which is exactly the expression obtained for the decoupled problem.

4.2.3 Parameter-Errors Cross Correlations

The cross correlation between the several parameter errors, and as computed from the elements of M^{-1} , are algebraically complex expressions. We present below approximations obtained by Taylor series expansions on both geometric parameters X_t^2 and X_ℓ^2 , about $X_t=0$ and $X_\ell=0$.

Range-Speed Cross Correlation

The first terms of the Taylor series of the range speed cross correlation, lead to

$$\rho^2_{R_o, v} = \frac{(M^{-1}_{R_o, v})^2}{(M^{-1}_{R_o})^2 (M^{-1}_v)^2} \approx 1 - \frac{5}{4} \frac{1}{\gamma^2} + \dots \quad (\text{Taylor series in } X_\ell^2) \quad (86)$$

$$\rho^2_{R_o, v} = 5\gamma^2 - 25\gamma^4 + \dots \quad (\text{Taylor series in } X_t^2) \quad (87)$$

where γ is as before

$$\gamma = \frac{vT \cos\theta_t}{L \cos\theta_\ell} \quad (88)$$

We note that in equation 86, for very large γ , the range and the velocity parameters are perfectly correlated. This is in accordance with our previous results since, for large γ , the temporal diversity dominates the spatial diversity. Furthermore for X_ℓ small the spatial curvature is negligible, and the SAMS problem is decoupled on its spatial and temporal aspects, having as net effect that the lowest order term in Det M becomes of order 14 and not 12.

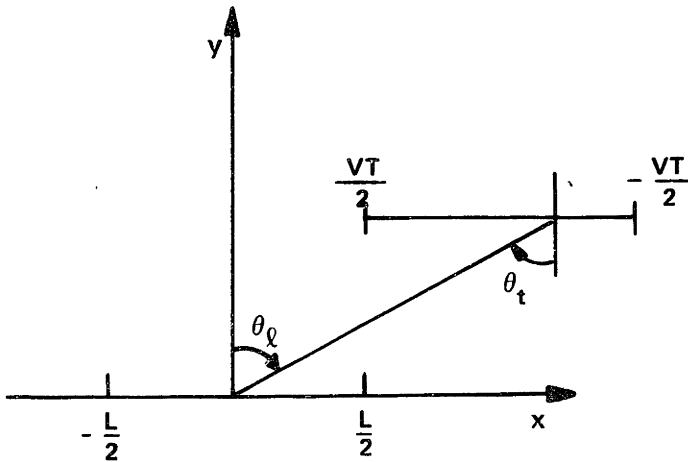
Equation 87 states that for a significant spatial diversity ($\gamma \ll 1$) the range and velocity parameter errors are relatively uncoupled, the range being estimated from the spatial diversity and the speed from the temporal modulations.

We study now the range/speed cross correlation for special configurations of practical interest.

(i) Let the spatial/temporal geometry be symmetric and parallel as illustrated in figure 15. Then

$$\cos\theta_l = \cos\theta_t \quad (89a)$$

$$X_l = X_t \quad (89b)$$



Spatial / Temporal Symmetric and Parallel Configuration

Figure 15

and the range/speed cross correlation becomes

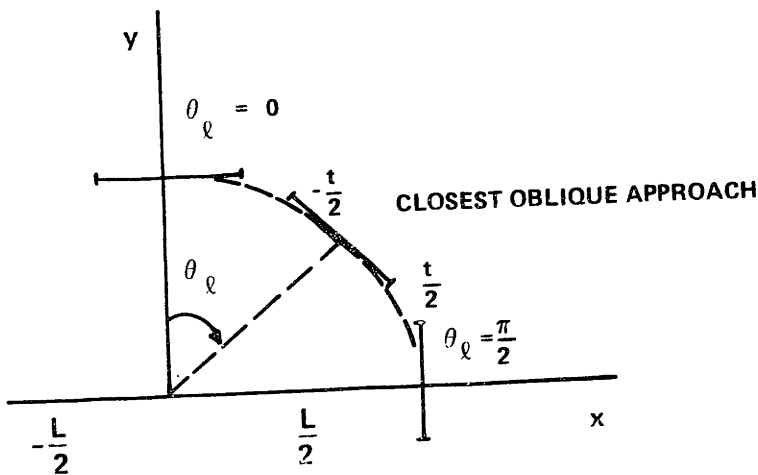
$$\rho_{R_o, v}^2 = \frac{7}{9} \quad (90)$$

(ii) We study the cross correlation $\rho_{R_o, v}$ as a function of the bearing angle. We consider a specific geometric configuration, namely the symmetric closest approach

$$\cos \theta_t = 1 \quad (91a)$$

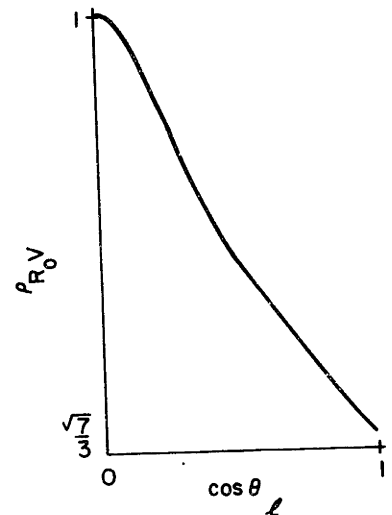
$$X_t = X_\ell \quad (91b)$$

displayed in figure 16, as it changes from broadside ($\theta_\ell = 0$)



(Closest Approach) Geometry

Figure 16



Range Velocity Cross-Corr. Versus $\cos \theta_\ell$
(closest app. geometry)
Figure 17

to endfire ($\theta_t = \frac{\pi}{2}$).

$$\rho_{R_o, v}(\cos\theta_\ell) \Big|_{\substack{\cos\theta_t=1 \\ X_\ell = X_t}} = \frac{4+20 \cos\theta_\ell^2 + 25 \cos\theta_\ell^4}{4+25 \cos\theta_\ell^2 + 29 \cos\theta_\ell^4 + 5\cos\theta_\ell^6} \quad (92)$$

We represent graphically this function in figure 17. We note that at endfire ($\cos\theta_\ell = 0$) the errors on the range and the speed parameters are perfectly correlated, and that this correlation decreases monotonically to the minimum

$$\frac{\sqrt{7}}{3} \approx .88347583 \quad (93)$$

at the broadside ($\cos\theta_\ell = 0$).

(iii) In figure 19 we study $\rho_{R_o, v}$ as a function of the spatial geometric parameter

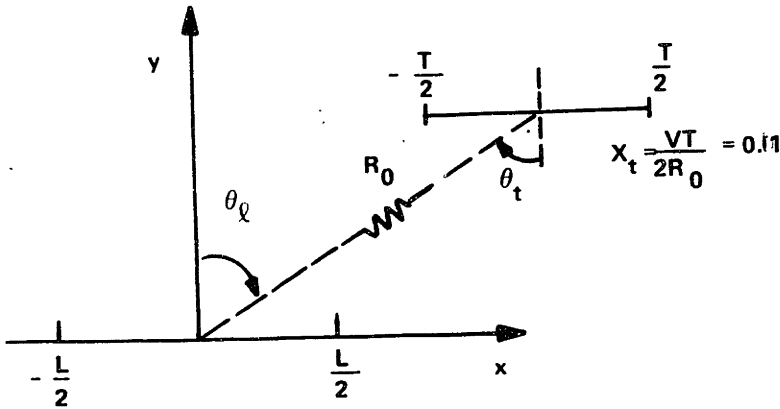
$$X_\ell = \frac{L}{2R_o} = \frac{L}{2R_o}$$

for the parallel geometry

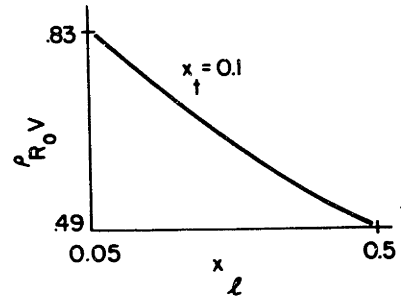
$$\cos\theta_\ell = \cos\theta_t \quad (94a)$$

displayed in figure 18, when

$$X_t = .1 \quad (94b)$$



SAMS Parallel Geometry
Figure 18



Ran/Vel Cross-Corr Versus X_l
(Parallel Geometry)
Figure 19

Under the above conditions

$$\rho_{R_0, V} \cong \frac{2+100X_l^2+1250X_l^4}{2+125X_l^2+1450X_l^4+2500X_l^6} \quad (95)$$

We note that this expression is valid for all θ_l or θ_t , as long as the geometry remains parallel. From figure 18 we see that as X_l increases the errors cross correlation decreases monotonically.

Range-Sin θ_t Cross Correlation

Remarks and results equivalent to the preceding ones.

Range, Velocity, or $\sin\theta_t$, and $\sin\theta_\ell$ - Cross-Correlation

For the cross-correlation between R_o , v or $\sin\theta_t$, and $\sin\theta_\ell$ we obtain essentially

$$\rho_{i \sin\theta_\ell} \approx f(X_t) X_\ell^2 \quad (96)$$

where $f(X_t)$ is a certain function of X_t , $\cos\theta_t$, $\cos\theta_\ell$. The important thing to note, in equation 96, is the homogeneous behavior on X_ℓ^2 , expressing the fact that, for small X_ℓ , the errors between $\sin\theta_t$ and the remaining parameters are practically uncorrelated.

Velocity- $\sin\theta_t$ Cross-Correlation

We have

$$\rho_{v, \sin\theta_t} \approx -1 + \alpha X_t^2 \quad (97)$$

i.e., in order to uncouple the estimates we require some finite, nonzero, observation interval (conversely and more intuitively in order to estimate speed v and $\sin\theta_t$, one needs to observe these motions).

For the special case of a symmetric and parallel geometry, i.e., for

$$X_t = X_\ell \quad (98a)$$

$$\cos\theta_t = \cos\theta_\ell \quad (98b)$$

A Taylor series leads to

$$\rho_{v, \sin\theta_t} \approx -1 + \left[\frac{\sin^2\theta_\ell + 28}{5} + 891 \sin^4\theta_\ell - 465 \cos^2\theta_\ell \sin^2\theta_\ell \right] X_\ell^2 \quad (98c)$$

We present this expression, just as an illustration of the complicated algebraic form that these cross correlations take.

Summary of the Chapter

This chapter considered the Positioning/Navigation problems, when both spatial and temporal diversity are present. After a brief description of the model and the receiver, we pursued two main class of problems. The first was characterized by the dominance of the temporal over the spatial baseline. It was shown that it leads to a decoupled processing structure, with the receiver estimating the bearing angle from the spatial delays, and the remaining source/receiver parameters from the temporal diversity. The SAMS reduced to the "direct sum" of a SAMS₀, and a (time-varying) bearing angle estimation. We derived an expression for the required number of beam steering updates, and expressed the mean square error performance in terms of the SAMS₀ results. The second

class assumed a balanced geometry, i.e., that the spatial and temporal diversity parameters X_ℓ and X_t were of comparable size. This leads to a coupled receiving structure. The cross-coupling term was isolated and an expression derived. Its effects were analyzed for several limiting geometries and along special subspaces of the parameter space Ω . We concluded that the cross-coupling represented a non-trivial improvement, with a decrease of 2 on the order of the overall problem. Recall that this order is twice the sum of the lowest orders of the modulation effects that have to be measured, in order to obtain a globally identifiable parameter estimation problem, and that it is also given by the order of the lowest order nonzero term of $\det M$.

For both problems we derived expressions for the ambiguity structure and for the mean square spread matrix, from which the local and global performance bounds can be computed.

PART II

APPLICATIONS TO POSITIONING
AND NAVIGATION

Chapter V	THE HYBRID ALGORITHM: A PRACTICAL SOLUTION TO THE PASSIVE TRACKING
Chapter VI	APPLICATIONS TO NAVIGATION AND POSITIONING. SIMULATION
Chapter VII	CONCLUSIONS . EXTENSIONS BIBLIOGRAPHY
Appendix A	GENERALIZED AMBIGUITY FUNCTION
Appendix B	MEAN SQUARE SPREAD MATRIX COMPUTATION
Appendix C	ASYMPTOTIC BEHAVIOR OF THE MEAN SQUARE SPREAD MATRIX
Appendix D	TAYLOR SERIES APPROXIMATION TO 4-DIMEN- SIONAL SAMS-MEAN SQUARE SPREAD MATRIX

Chapter V

The Hybrid Algorithm: A Practical Solution to the Passive Tracking

This chapter explores important issues arising in the design of practical systems for passive tracking. In summary they relate to:

- (i) Global identifiability of the source/receiver relative parameters;
- (ii) Minimization of the involved computational effort;
- (iii) Sensitivity of the actual processing to model perturbations.

As will be seen, the first and second points motivate a practical integrated solution, referred to as Hybrid Algorithm, consisting of three steps:

- (i) Global acquisition via ML-techniques;
- (ii) Tracking of the local dynamics by a recursive linearized structure;
- (iii) Reacquisition every T_1 seconds.

The details of this technique are expanded upon in the next section. Sections 2 and 3 discuss the design and expected performance of each block of the Hybrid Algorithm. Section 4 studies the sensitivity of the ML-global acquisition to modelling assumptions. Section 5 obtains the overall receiver mean square performance. Finally, section 6 integrates the analysis carried out in the previous sections in terms of four characteristic regions of behavior for the Hybrid Algorithm.

1. Hybrid Algorithm

The proposed procedure is illustrated in the context of the decoupled SAMS of chapter IV, where the available spatial baseline is much smaller than the one synthesized by the source travel. The bearing angle is estimated from the spatial diversity and the remaining parameters are observed from the temporal diversity, with SAMS being equivalent to a passive bearing measurement decoupled from a SAMS₀ problem. We concentrate on the latter, where only the time dependence arises.

Under the narrowband and linear constraints, passive tracking reduces to a phase demodulation. The phase of the signal component of the received waveform is

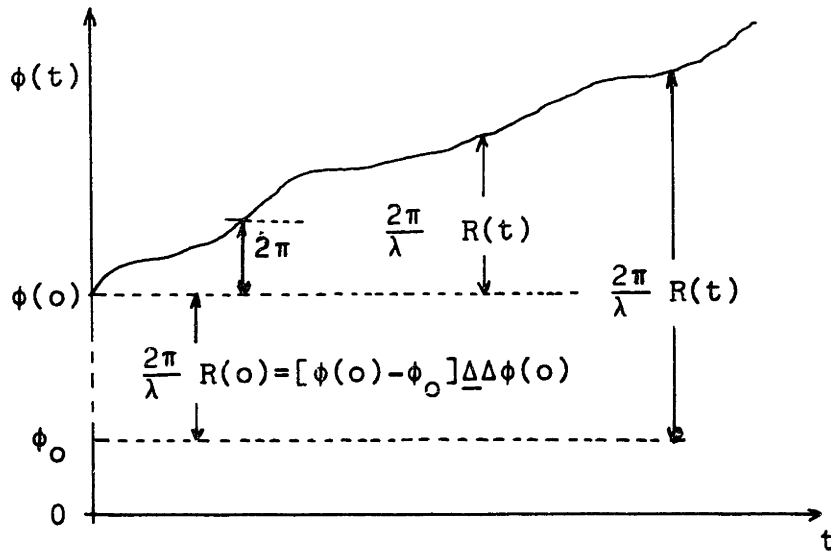
$$2\pi ft + \phi(t) \cong 2\pi ft + \phi_0 + 2\pi f \tau(t) \quad (1a)$$

where

$$\tau(t) \approx \frac{R(t)}{c} = \text{observed delay} \quad (1b)$$

$$\phi_0 = \text{absolute phase reference for incoherent model} \quad (1c)$$

We note that $\phi(t)$, as given in equation 1a, represents the total phase modulation shown in figure 1, and not its modulo 2π version.



Absolute Phase Evolution

Figure 1

From equation 1 or Figure 1 we obtain

$$R(t) \approx \frac{\lambda}{2\pi} \Delta\phi(t) = \frac{\lambda}{2\pi} [\phi(t) - \phi_0] \quad (2)$$

with $\lambda f = c$, and where $\Delta\phi(t)$ represents the total, integrated, absolute phase variation. From Figure 1, we also write

$$R(t) = R(o) + \Delta R(t) \quad (3)$$

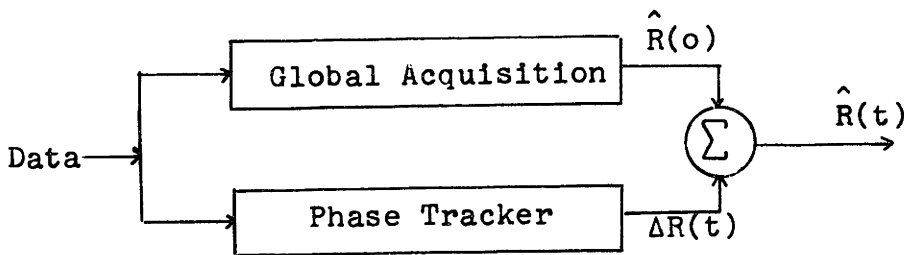
with

$$R(o) \cong \frac{\lambda}{2\pi} \Delta\phi(o) \quad (4)$$

and

$$\Delta R(t) = \int_0^t \dot{R}(u) du = \frac{\lambda}{2\pi} [\Delta\phi(t) - \Delta\phi(o)] = \frac{\lambda}{2\pi} [\phi(t) - \phi(o)] \quad (5)$$

Equations 4 and 5 suggest that the range estimation be performed in two steps. The first, acquires globally the source/receiver separation $R(o)$ at a particular time reference $t=0$; the second tracks the instantaneous phase variation, in order to obtain the range increment. The corresponding receiver structure is presented in Figure 2, and will be referred to as the Hybrid Algorithm.



Global Acquisition/Tracking Hybrid Algorithm

Figure 2

The Hybrid Algorithm represents a compromise between two conflicting requirements, namely parameters observability and computational effort. The upper block of figure 2 accomplishes the global identifiability, but is nonrecursive; the lower one is recursive, but tracks only the local dynamics.

We explore subsequently the design of both blocks, their sensitivity to the geometry, to the statistical parameters and to the model assumptions.

2. Global Acquisition

In active radar and in certain coherent and synchronized passive navigation systems ($\phi_0 \approx 0$ in equation 4) the global ranging is achieved from a direct measurement of travel times. From equation 4

$$\hat{R}(o) = \frac{\lambda}{2\pi} \hat{\phi}(o) = \hat{\tau}(o)c \quad (6)$$

where $\hat{\tau}(o)$ is the delay estimate. Equation 6 shows that ranging with coherent and synchronized clocks is based on absolute phase measurements. However, they may require sophisticated and expensive equipment; and more importantly, from a conceptual view point, they assume an unrealistic model for many practical situations.

In this thesis we introduced an incoherent and asynchronous phase model. The absence of receiver/transmitter synchronism precludes global range estimation techniques, based on absolute travel time measurements. By imposing motion constraints, we were able to develop an inherently nonlinear receiver structure, which basically achieves the global acquisition, by estimating the higher order spatial/temporal modulations induced on the signal.

In this context the upper block of figure 2 is the nonlinear ML-processor derived in the preceding chapters, where the influence of the geometry and other statistical

parameters on the receiver structure and performance have been analysed.

There are two remaining points demanding further study.

(i) The ML-receiver requires a nonrecursive multi-dimensional stochastic maximization, making impractical its use for tracking continuously the changing geometry. To alleviate the associated computational effort we investigate, as mentioned earlier, recursive structures for the phase tracker block of the Hybrid Algorithm;

(ii) The sensitivity of the ML-receiver to variations of the source travel, from the deterministic constant speed path. To quantify it, we assume that the path perturbations are random accelerations. Because this more general model is used to design the phase tracker, we postpone the sensitivity issue till section 4.

3. Phase Tracker

Once the ML-receiver has acquired the source, the range time update can be accomplished, as given by equation 5, by measuring the range differences from the Doppler effects. This may be achieved, for example, with a digital Doppler counter [Spi74], or with any other phase estimation structure. In [Mo73a] we used linearizing type arguments to derive recursive filters based on Extended Kalman Bucy (EKB)

techniques. We recall briefly the analysis and results of [Mo73a], and [Mo73b].

3.1 Random Accelerations Motion Model

The model in the above references [Mo73a], [Mo73b] incorporates more realistic assumptions on the relative dynamics, than we have assumed so far. Specifically, they are described by a set of finite dimensional, nonlinear stochastic differential equations, modeling a nominal constant speed linear path, perturbed by random accelerations. In the state variable framework

Dynamical System

$$dx(t) = f(x(t))dt + g(x(t))du(t) \quad (7a)$$

$$= \begin{bmatrix} \underline{F}_R & \underline{0} \\ \underline{0} & \underline{F}_\theta \end{bmatrix} x(t)dt + \begin{bmatrix} \underline{g}_R \\ \underline{g}_\theta \end{bmatrix} du(t) \quad (7b)$$

with

$$X = \begin{bmatrix} X_1 \\ \dots \\ X_4 \end{bmatrix} = \begin{bmatrix} R \\ \dot{R} \\ \theta \\ \dot{\theta} \end{bmatrix}; \quad \underline{F}_R = \begin{bmatrix} 0 & 1 \\ \theta^2 & 0 \end{bmatrix}; \quad \underline{F}_\theta = \begin{bmatrix} 0 & 1 \\ 0 & -\frac{2\dot{R}}{R} \end{bmatrix}; \quad (7c)$$

$$\underline{g}_R = \begin{bmatrix} 0 & 0 \\ \sin\theta & \cos\theta \end{bmatrix}; \quad \underline{g}_\theta = \frac{1}{R} \begin{bmatrix} 0 & 0 \\ \cos\theta & -\sin\theta \end{bmatrix}; \quad du(t) = \begin{bmatrix} du_x(t) \\ du_y(t) \end{bmatrix}$$

(7d)

Equations 7 are to be interpreted in the Ito integral sense. We note however that the Wong Zakai correction term is zero for the specific $g(x(t))$ of equation 7d, [Mo73a].

The observations are narrowband and corrupted by an additive white Gaussian noise

$$dr(t) = h(X(t))dt + dw(t) \quad (8a)$$

with

$$h(X(t)) = \sqrt{2P} \begin{bmatrix} \sin\gamma(t, \ell) \\ \cos\gamma(t, \ell) \end{bmatrix}, \quad \ell \in [-\frac{L}{2}, \frac{L}{2}] \quad (8b)$$

$$\gamma(t, \ell) = \frac{2\pi}{\lambda} [R(t) - \ell \sin\theta(t)] + \xi(t) \quad (8c)$$

The phase drift process $\xi(t)$ is generated by a finite dimensional system, uncoupled from the state process, and is independent of $u(t)$ and $w(t)$. The driving $du(t)$ and the disturbance $dw(t)$ are stochastic independent, Gaussian, white with spectral matrices

$$Q \quad I \quad (9a)$$

and

$$\frac{N_0}{2} \quad I \quad (9b)$$

respectively, where I is the 2×2 identity matrix. We assume in the sequel that the power level associated with the process $\xi(t)$ is much smaller than Q and $\frac{N_0}{2}$.

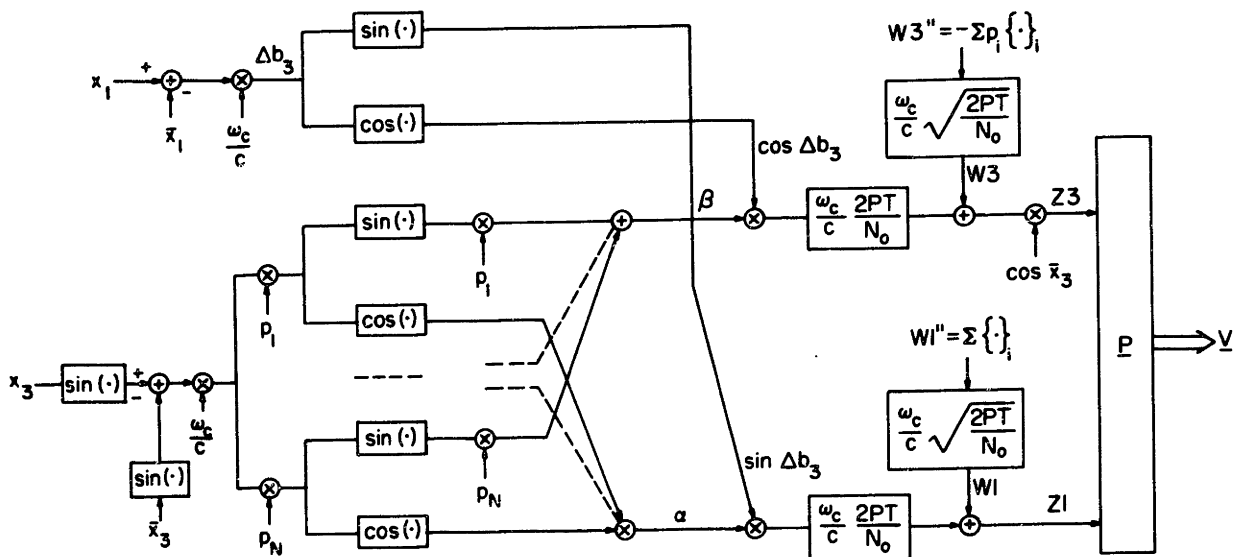
3.2 Linearized Mathematical Equivalent to the Extended Kalman Bucy Filter

Several linear approximations to the ∞ -dimensional optimal filter were studied in [Mo73a]. Since, under the above assumptions on $\xi(t)$, the portion of the linearized receiver associated with the phase drift $\xi(t)$ decouples from the remaining part of the filter, we ignore it in the sequel.

We limit our attention to a brief discussion of the EKB. It can be shown [Mo73a], that the EKB is mathematically equivalent to two beam form operations, which are the inputs to phase lock loops (PLL) tracking respectively the bearing and range waveforms. Under linearizing assumptions on the receiver behavior, and for a centered geometry, these loops are decoupled. The resulting receiver has the structure of figure 3a, which is further rearranged in figure 3b.

Remark: Figures 3a, 3b are taken from [Mo73a], where we implemented the discrete time, discrete array version of the above described continuous time, continuous array waveform tracking problem. The quantity T in the figures, associated with the (continuous time, discrete array) signal to noise ratio $\frac{2P}{N_0}$, is a normalizing factor relating it to the (discrete time, discrete array) signal to noise ratio. Other quantities in figure 3 are:

Fig. 3a EKB - Math. Model (Polar Coord.)



$$\alpha = \sum \cos(p_i \Delta b_i)$$

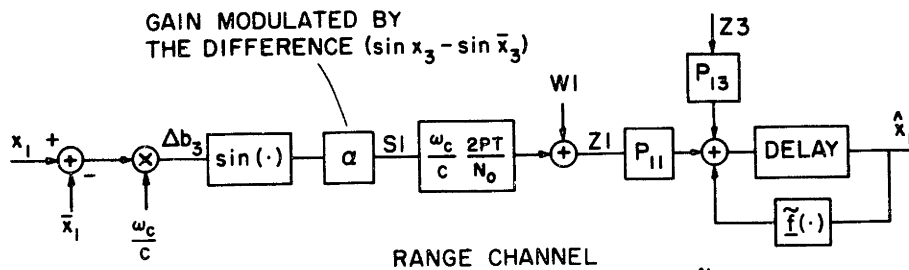
$$\beta = \sum p_i \sin(p_i \Delta b_i)$$

$$\Delta b_1 = \frac{\omega_c}{c} (\sin x_3 - \sin \bar{x}_3)$$

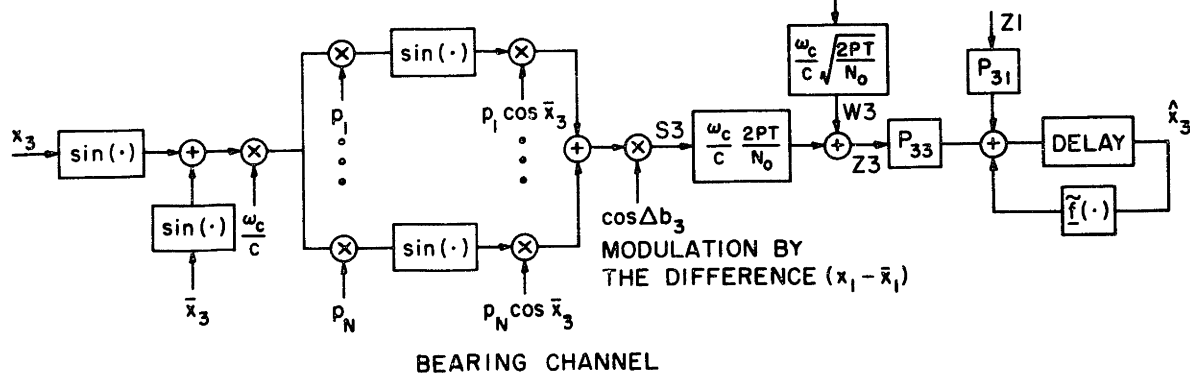
$$\Delta b_3 = \frac{\omega_c}{c} (x_1 - \bar{x}_1)$$

$$\{ \cdot \}_i = \cos \bar{a}_i \omega_{ci} - \sin \bar{a}_i \omega_{si}$$

GAIN MODULATED BY THE DIFFERENCE $(\sin x_3 - \sin \bar{x}_3)$



RANGE CHANNEL $\sum (p_i \cos \bar{x}_3) \{ \cdot \}$



BEARING CHANNEL MODULATION BY THE DIFFERENCE $(x_1 - \bar{x}_1)$

Fig. 3b EKB - Decoupled Structure

P_{ij} = error cov. elements, given by EKB Riccati Equation;
 p_i , $i=1, \dots, N$, gives the array elements location;
 $W1, W3$ = equivalent noise terms;
 $Z1, Z3$ = range and bearing beams.

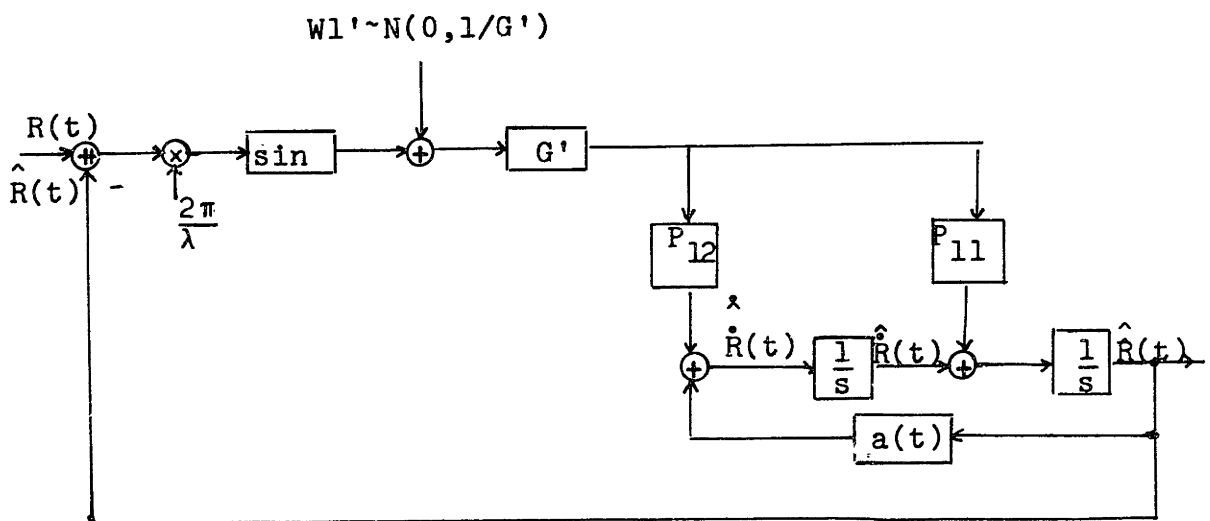
Under a small errors assumption, such that

$$\cos\left[\frac{2\pi}{\lambda}l(\sin\theta(t) - \sin\hat{\theta}(t))\right] \approx 1, \quad (10)$$

and neglecting P_{13} , compared to P_{11} and P_{12} (see [Mo73a]), the range channel of figure 3b can be further rearranged in the decoupled loop shown in figure 4, where the gains

$$G' = \frac{2\pi}{\lambda} \text{SNRL} \quad (11a)$$

$$a(t) = (\hat{\theta}(t))^2 \quad (11b)$$



Mathematical Equivalent for Signal Source Channel and EKB Range Loop

Figure 4

3.3 Linearized Decoupled Range Loop

In summary, under linearizing assumptions, the range phase tracking can be described by the following decoupled problem:

Dynamical System

$$dx(t) = F_R X(t)dt + g_R(X(t)) du(t) \quad (12a)$$

with

$$F_R = \begin{bmatrix} 0 & 1 \\ a(t) & 0 \end{bmatrix}; \quad X(t) = \begin{bmatrix} R(t) \\ \dot{R}(t) \end{bmatrix}; \quad a(t) = \dot{\theta}^2(t) \quad (12b)$$

Observation Process

$$dr(t) = h(X(t))dt + dw(t) \quad (12c)$$

with

$$h(X(t)) = \sqrt{2PL} \begin{bmatrix} \sin\left[\frac{2\pi}{\lambda}R(t)\right] \\ \cos\left[\frac{2\pi}{\lambda}R(t)\right] \end{bmatrix} \quad (12d)$$

The "steady state" solution for the covariance Riccati equation of the EKB, applied to the decoupled problem given by equations 12, leads to

$$P_{11} \cong \left(\frac{2P_{12}}{H_1}\right)^{1/2} \quad (13a)$$

$$P_{22} \cong (H_1 P_{12} - a) \sqrt{\frac{2P_{12}}{H_1}} \quad (13b)$$

$$P_{12} \cong \frac{a}{H_1} \left[1 + \sqrt{1 + \frac{QH_1}{a^2}}\right] \quad (13c)$$

where H_1 is an equivalent signal energy to noise ratio

$$H_1 = \left(\frac{2\pi}{\lambda}\right)^2 \frac{2P}{N_0} L \quad (13d)$$

Note in equation 13d the "modulation index"

$$\beta = \left(\frac{2\pi}{\lambda}\right)^2 \quad (13e)$$

Since

$$a(t) = \dot{\theta}^2(t) \lesssim \left| \frac{v}{R(T_0)} \right|^2 \ll 1 \quad (14a)$$

where v is the source nominal speed, and $R(T_0)$ the source/receiver separation at the point of closest approach, for a strong signal energy to noise ratio assumption

$$\frac{QH_1}{a^2} \gg 1 \quad (14b)$$

and equations 13 can be approximated by

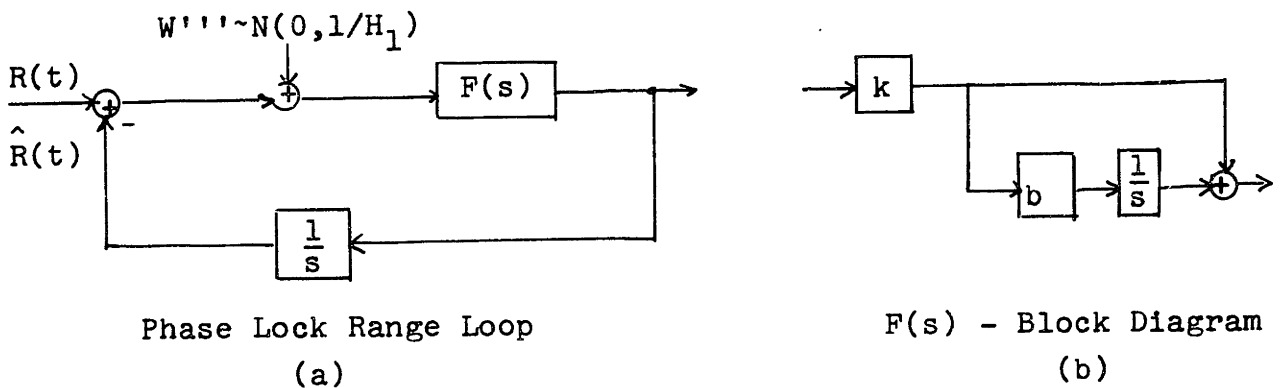
$$P_{12} \approx \frac{1}{H_1} (QH_1)^{1/2} \quad (14c)$$

$$P_{11} \approx \frac{1}{H_1} (4QH_1)^{1/4} \quad (14d)$$

$$P_{22} = \frac{2Q}{(4QH_1)^{1/4}} \quad (14e)$$

Equations 13 and 14 express the filter gains of figure 4 in terms of the nominal geometry and statistical parameters, and can be precomputed. In the subsequent analysis, and just for economy of notation, we work with equations 14. If condition 14b is not satisfied, the results remain valid, as long as we use the more correct equations 13.

Figure 5 represents a rearrangement of figure 4 and shows the block diagram for the steady state configuration of the EKB decoupled range loop.



EKB-Decoupled Range Loop

Figure 5

Steady State Loop Parameters

The block diagram of figure 5 has the structure of a second order phase lock loop (PLL) with filter

$$F(s) = k(1 + \frac{b}{s}) \tag{15a}$$

where

$$k = \left(\frac{2\pi}{\lambda}\right)^2 \text{SNR}_L P_{11} \quad (15b)$$

$$b = \frac{P_{12}}{P_{11}} \quad (15c)$$

In other words the EKB range channel performs like a second order PLL tracking the waveform

$$\phi(t) = \frac{2\pi}{\lambda} R(t)$$

Using the steady state error covariance values, equation 14, the filter's gain is

$$k = (4QH_1)^{1/4} \quad (16a)$$

and the zero

$$b = \left(\frac{QH_1}{4}\right)^{1/4} \quad (16b)$$

Important parameters are the noise bandwidth B_L and the signal to noise ratio α in the bandwidth loop e.g. [Va71b]. For the second order filter under considerations

$$B_L = \frac{k+b}{4} = \frac{3}{8}(4QH_1)^{1/4} \quad (16c)$$

$$\alpha = \frac{(\text{SNR})_{\text{eq}}}{B_L} = \frac{8}{3} \frac{H_1}{(4QH_1)^{1/4}} \quad (16d)$$

In terms of the noise bandwidth loop we can rewrite equations
14

$$P_{11} \approx \frac{8}{3} \frac{B_L}{H_1} \quad (16e)$$

$$P_{22} \approx \frac{3}{4} \frac{Q}{B_L} \quad (16f)$$

Equations 16e and 16f are intuitively satisfying expressions. They say that in steady state, the mean square error on the range increment increases with the loop bandwidth (more noise allowed in the system), and decreases with the equivalent signal energy to noise ratio H_1 ; and that the mean square error on the range phase rate decreases with the loop bandwidth B_L (for larger B_L the loop inertia decreases) and increases with the driving noise power level Q .

3.4 EKB Linearized Performance Versus ML-Performance

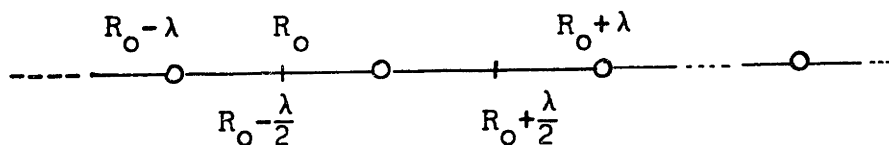
Equation 16e contrasts with the Cramer-Rao performance bound derived in chapter III, for the incoherent parametrized model

$$\sigma_{R_{o_{loc}}}^2 \approx \frac{1}{H_1 T} \frac{5^2 \times 7}{2 \sin^2 \theta_t \cos^4 \theta_t} \frac{1}{X_t^6} \quad (17a)$$

where the geometric parameter

$$X_t = \frac{vT}{2R_o} \quad (17b)$$

The conceptual difference is that the ML-algorithm acquires the range estimation from the modulations induced on the signal structure, while the EKB, achieves only the local tuning of the range. The EKB is not globally observable, exhibiting "lock in" points separated by the wavelength λ on the range parameter axis, as observed experimentally in [Mo73a], and illustrated by figure 6.



EKB Range "Lock in" Points

Figure 6

The EKB assumes that its a priori range estimate $R(o)$ satisfies

$$R(o) - \frac{\lambda}{2} \leq \hat{R}(o) < R(o) + \frac{\lambda}{2}. \quad (18)$$

When

$$(N - \frac{1}{2})\lambda \leq \hat{R}(o) - R(o) \leq (N + \frac{1}{2})\lambda \quad (19)$$

for $N=0$, the original global offset ($\approx N\lambda$) is not resolved by the EKB, which simply integrates the linear effects.

As remarked in paragraph 2, the global acquisition sensitivity to the random modulations, and in particular the validity of equation 17a, has to be analyzed. This will be done in section 4.

EKB Simulation Results

Simulation results in [Mo73a] showed that the error covariance propagated by the EKB's Riccati equation predicts correctly, in the linear region, the filter's performance. Figure 7, taken from [Mo73b], shows representative runs for the four-dimensional problem of equations 7. In particular figure 7b illustrates the range and range rate standard deviations (indicated respectively by $s(1)$ and $s(2)$) computed via Monte Carlo simulations. The curve for $s(1)$ indicates that, as long as the filter is started within the right range λ -cell, the filter range error standard deviation converges to the filter's predicted value. The curve for $s(2)$ illustrates the filter's insensitivity to large initial errors on the range rate parameter.

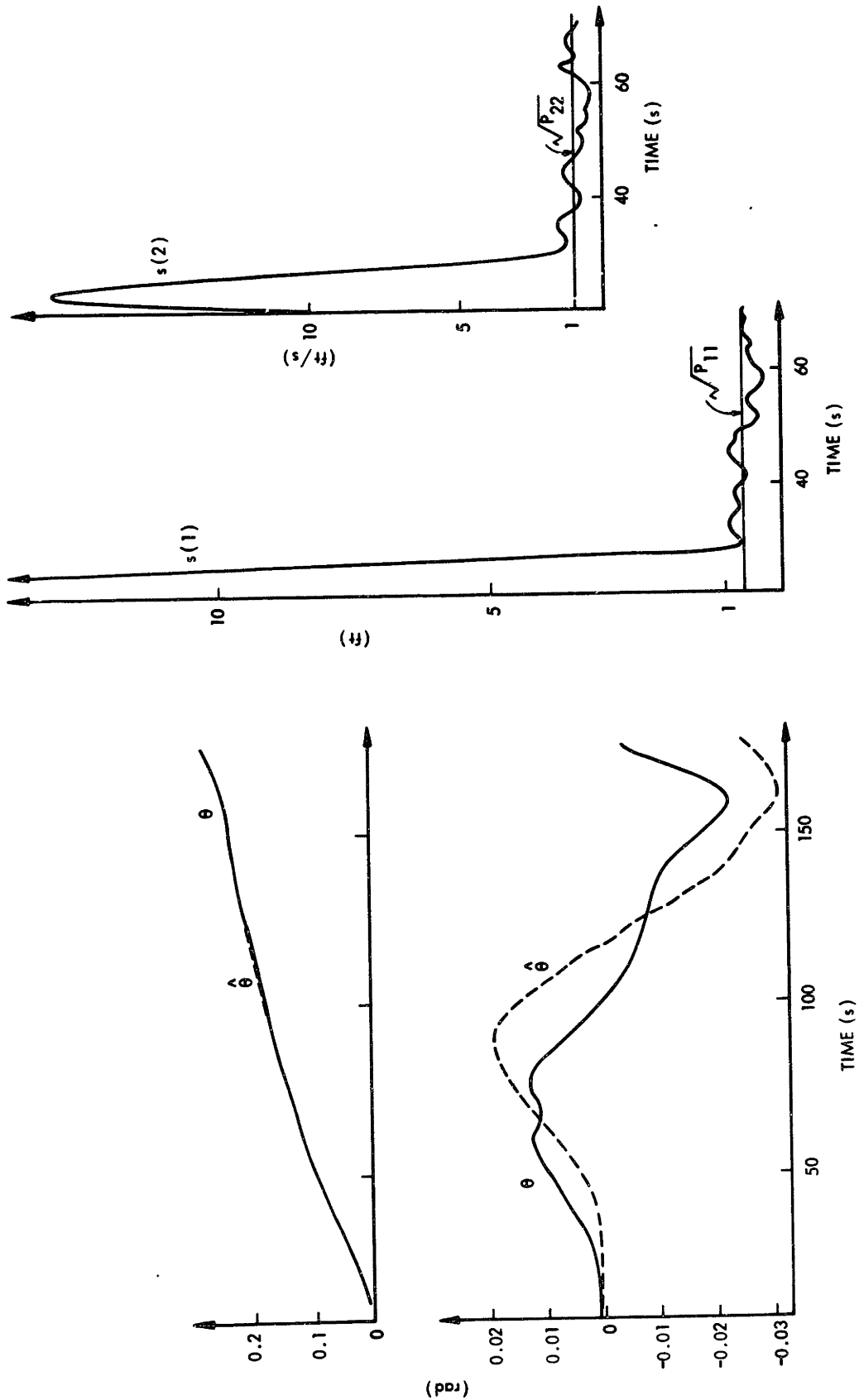
3.5 EKB Nonlinear Behavior

Due to the presence of noise, the actual range phase error at the output of the phase lock loop of figure 5, undergoes diffusion, resulting in the so called cycle slipping phenomena studied in conjunction with the nonlinear behavior of PLL's.

Basically the range increment error process at the EKB output can be decomposed as

$$E_{R}^{EKB}(t) \approx \tilde{E}_R(t) + \lambda J_R(t) \quad (20)$$

Fig. 7 Ext. Kalman-Bucy Filt. Simulation Results

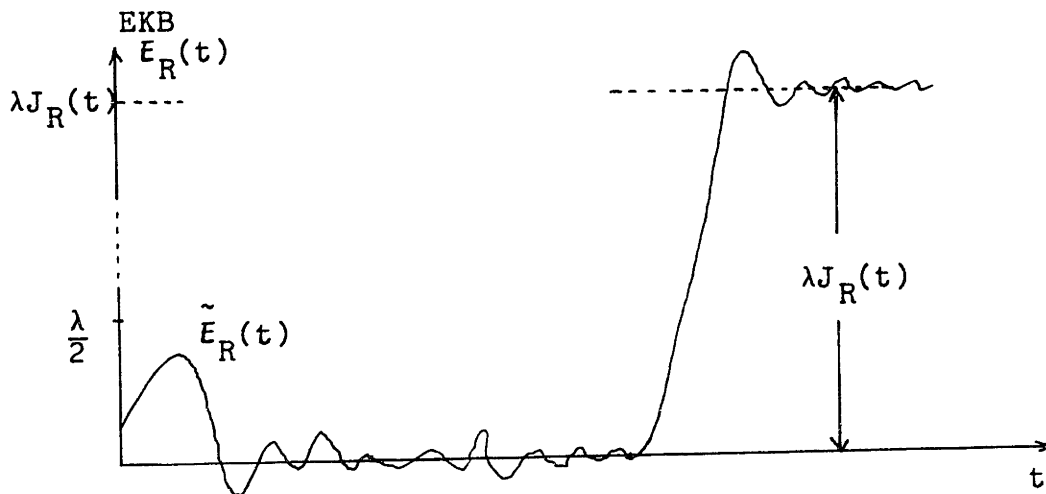


where

$\tilde{E}_R(t) \sim (E_R^{EKB}(t)) \pmod{\lambda}$ = error associated with the EKB range loop, whenever the loop performs in its linear region;

$J_R(t)$ = counting process, accumulating the number of cycles skipped by the loop in $[0,t]$.

This error decomposition is illustrated in figure 8, where we assumed that the filter was originally started within the right λ -cell.



Cycle Skipping Phenomena

Figure 8

$J_R(t)$ has been described by some authors [Lin73], on the basis of experimental evidence presented in [Cha66] and [Row67], as a Poisson process, with the resulting approximate probabilistic structure for the range phase jumping

$$\Pr\{J_R(t)=j\} = \frac{(\bar{J}_R t)^j \exp(-\bar{J}_R t)}{j!} . \quad (21)$$

\bar{J}_R represents the total average number of phase jumps per unit time, and is usually referred to, in the PLL literature, as the frequency of skipping cycles. Exact analytical results for \bar{J}_R are extremely hard to obtain for higher order loops, with or without modulation. A good approximation for the high SNR case, however can be worked out [Vit66]. The resulting expression is equivalent to the one for the first order loop, with the parameters depending on the system dynamics, being obtained with sufficient accuracy, from the linearized model of the PLL structure. The analysis [Vit66] has received good experimental confirmation for a second order loop [Cha66].

For the loop shown in figure 5 we obtain

$$\bar{J}_R = \text{frequency of cycle skipping} \approx \frac{2B_L}{\pi^2 \alpha I_0^2(\alpha)} \quad (22a)$$

which for $\alpha \gg 1$ can be approximated by

$$\bar{J}_R \approx \frac{4B_L}{\pi} e^{-2\alpha} \quad (22b)$$

In these equations $I_0(\alpha)$ is a modified Bessel function of the first kind. Substituting equations 16c and 16d in 22a and 22b yields

$$\bar{J}_R = \frac{3}{16\pi^2} \sqrt{\frac{Q}{H_1}} (I_0(\alpha))^{-2} \underset{\alpha \text{ large}}{\approx} \frac{3}{\pi\sqrt{2}} (QH_1)^{1/4} \exp(-2\alpha) \quad (23a)$$

The average time between cycle skips is given by the inverse of the frequency to skip a cycle

$$T_{\text{skp}} = (\bar{J}_R)^{-1} \quad (23b)$$

We represent, for the EKB range PLL, with bandwidth and signal to noise ratio in the bandwidth loop given by equations 16, the average time between cycle skips T_{skp} in figure 9, as a function of SNR at the receiver site, for several values of the spectral driving noise power level Q , and for a wavelength λ and an array length L

$$\lambda = 50 \text{ feet}$$

$$L = 250 \text{ feet}$$

We note that for large SNR, the curves approach an exponential behavior, and the cycle skip phenomena will not be an issue in most applications. For smaller SNR, and as Q increases, the larger bandwidth causes the loop to slip cycles at a much higher rate, with the curves approaching zero as $\text{SNR} \rightarrow 0$ or $Q \rightarrow \infty$.

The mean square of the error associated with the EKB phase tracker can be computed from equation 20.

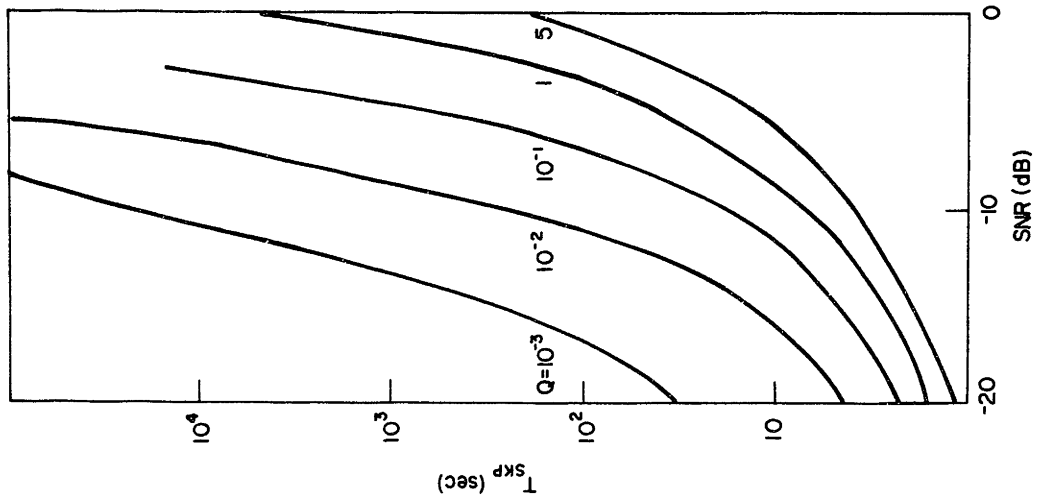


FIG. 9 Average Time for Cycle Skipp versus SNR (Q as a Parameter)

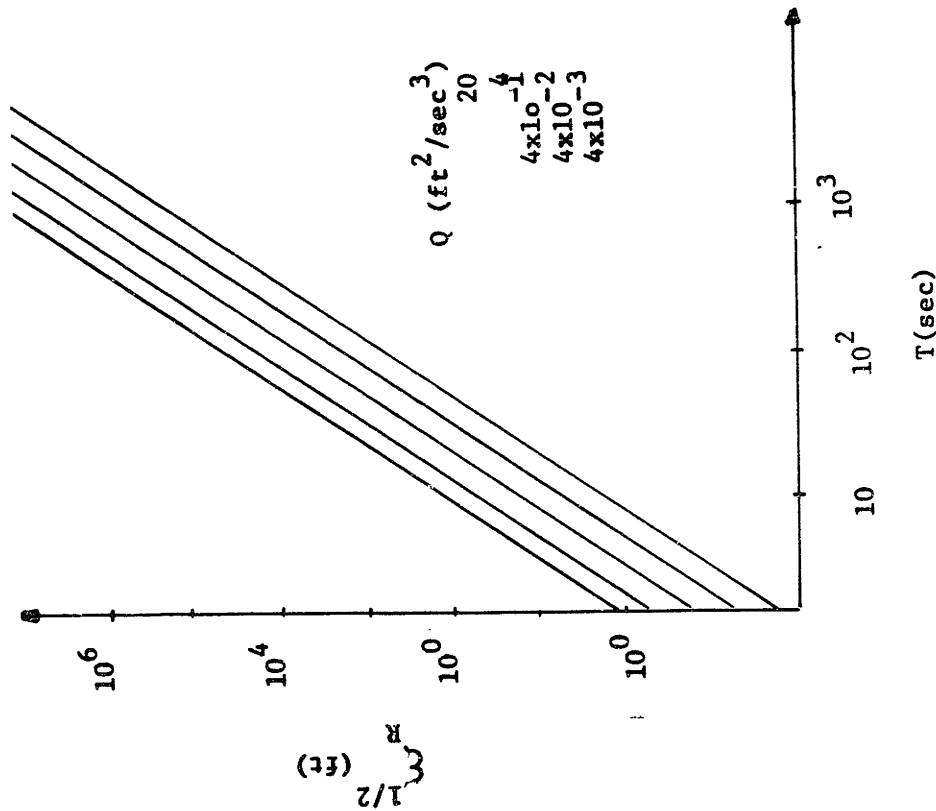


Figure 10: RMS Path Variation versus Acq. Time (var Q)

Assume

H1: In steady state, the two types of errors \tilde{E}_R and $\lambda J_R(t)$, in equation 20, are statistically independent. (A common assumption in the PLL literature, e.g. [Lin73].)

We have then, in steady state

$$E(E_R^{EKB}(t))^2 \approx P_{11} + \lambda^2(\bar{J}_R t) \quad (24)$$

This equation shows that the EKB error variance grows without bound with t . It justifies the third step of the Hybrid Algorithm (see end of section 6), namely reacquisition every T_1 sec.

Finally the probability P_{skp} of the loop losing lock in the interval $[0, t]$ is

$$P_{skp} \triangleq \Pr(J_R(t) \geq 1) \approx 1 - \exp(-\bar{J}_R t) \quad (25a)$$

For large signal to noise ratio and reasonable t , using equation 22b, we obtain

$$\ln P_{skp} \approx -2\alpha + \left[\ln \frac{4B_L t}{\pi} - \bar{J}_R t \right] \quad (25b)$$

$$\approx -2\alpha \quad (25c)$$

4. Sensitivity of ML-Global Acquisition to Path Perturbation

The error performance analysis of the ML-global acquisition algorithm assumed a deterministic constant speed linear path. We investigate now the sensitivity of this analysis to random path perturbations, by using the state variable model presented in the last section.

The range function is decomposed as

$$R(t) = R_d(t) + R_n(t) \quad (26)$$

where

$R_d(t)$ = deterministic component, parametrized by the source parameter vector;

$R_n(t)$ = noisy component, due to random perturbations of the nominal source course.

Working with the decoupled description of equation 12 we have

$$\ddot{R}_d(t) \cong a(t)R_d(t) + gu_d(t) \quad (27a)$$

$$\ddot{R}_n(t) \cong a(t)R_n(t) + gu_n(t) \quad (27b)$$

and

$$\ddot{R}(t) \cong a(t)R(t) + gu(t) \quad (27c)$$

with

$$u(t) = u_d(t) + u_n(t) = u_n(t) \quad (27d)$$

Assuming that at the starting point T_1 the noisy component is zero, the second order statistics of $R(t)$ are

$$E R(t) = R_d(t) \quad (28a)$$

$$\text{Cov}(R(t)) = \Sigma_{11_R}(t) \quad (28b)$$

Defining

$$\Sigma_R(t) = \text{Cov}([\dot{R}(t)]) \quad (28c)$$

we obtain the usual propagation equation

$$\frac{d}{dt} \Sigma_R(t) = \dot{\Sigma}_R(t) = F_R \Sigma_R(t) + \Sigma_R(t) F_R^T + g_R Q g_R^T \quad (28d)$$

where, from equation 12

$$F_R = \begin{bmatrix} 0 & 1 \\ a(t) & 0 \end{bmatrix}; \quad a(t) = \dot{\theta}^2(t); \quad g_R Q g_R^T = \begin{bmatrix} 0 & 0 \\ 0 & Q \end{bmatrix} \quad (28e)$$

Equation 28d can be integrated. Neglecting higher order terms in $a^2(t)$, which is consistent with a second order type approximation in X_t , we obtain

$$\Sigma_{11_R}(T) \cong \frac{T^3 Q}{3} [1 + \frac{aT^2}{5}] \quad (29a)$$

where, for simplification we assumed that at the starting point $t=T_1$

$$\Sigma_R(T_1) = \underline{0} \quad (29b)$$

Using the nominal bound on $a(t)$ given by equation 14a

$$\sum_{11R}(T) \cong \frac{T^3 Q}{3} \left[1 + \frac{4X_t^2}{5} \right] \quad (29c)$$

where, as before

$$X_t = \frac{vT}{2R_0} \quad (29d)$$

We make the

Definition: Root Mean Square Range Error due to Path Variations

$$\sum_R^{1/2} = \left\{ \frac{1}{T} \int_0^T \sum_{11R}(t) dt \right\}^{1/2} \quad (30a)$$

To shorten the notation we refer to $\sum_R^{1/2}$ more simply as the RMS range path variation. After substitution

$$\sum_R^{1/2} \approx \sqrt{\frac{QT^3}{12}} \left(1 + \frac{4^2 X_t^2}{30} \right) \quad (30b)$$

which for small X_t leads to

$$\sum_R^{1/2} \approx \sqrt{\frac{QT}{3}} \frac{T}{2} \quad (30c)$$

This quantity is represented in figure 10^{*} as a function of the acquisition time T and for several values of Q .

* See page 272

Notation: We let in the sequel

$$\sigma_R^2 = \left(\sum_R^{1/2} \right)^2 \approx \frac{QT^3}{12} \quad (30d)$$

and refer to it as the mean square range path variation (ms range path variation).

The total range error at the output of the ML-processor can be written as

$$E_R^{ML} \approx E_R^d + E_R^n \quad (31)$$

where

$E_R^d \approx$ error induced on the ML-algorithm by the additive measurement noise, after an acquisition time T_{acq} ;

$E_R^n \approx$ error induced on ML-receiver by the path random perturbations.

Assume

H2: The additive measurement noise and the path random accelerations are uncorrelated.

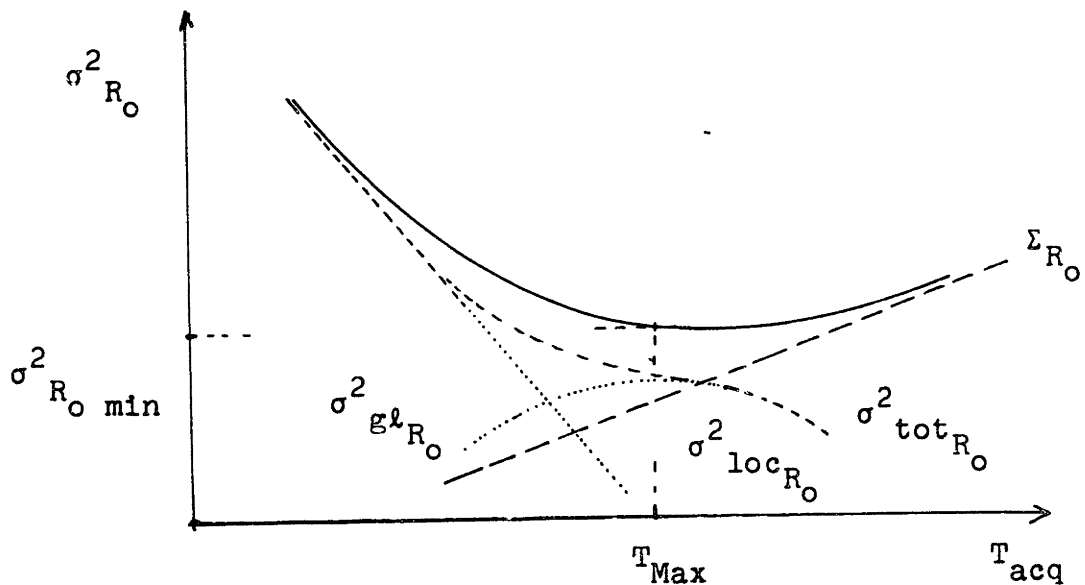
We have, under H2

$$\sigma_{R_0}^2 = E(E_R^{ML})^2 \approx E(E_R^d)^2 + E(E_R^n)^2 \quad (32a)$$

$$\approx \sigma^2_{R_{o\text{tot}}} + \sum_R \quad (32b)$$

where $\sigma^2_{R_{o\text{tot}}}$ is the mean square error (mse) associated with the ML-deterministic linear path analysis of the preceding chapters, and \sum_R is the MS range path variation given by equations 30d.

In figure 11 we represent schematically the range mse performance $\sigma^2_{R_o}$ at the output of the ML-processor, as a function of the total acquisition time T_{acq} .



Decomposition of the Mean Square Error at the ML-Processor Output

Figure 11

The main consequence of the path perturbations, as illustrated by figure 11, is the existence of a maximum acquisition time T_{max} , or equivalently of a minimum mse

$\sigma_{R_{O \min}}^2$; beyond T_{\max} the path random acceleration effects dominate, and the ML-performance deteriorates. We should note that $\sigma_{R_{O \min}}^2$ decreases as the signal to noise ratio SNR increases, while T_{\max} decreases when either the SNR or the driving noise level Q increase.

5. Hybrid Algorithm Error Analysis

Synthesizing the error analysis of the two last sections, we decompose the range error at the output of the Hybrid Algorithm as

$$E_R(t) \approx R(t) - \hat{R}(t) \approx N_{R}^{ML\lambda} + E_{R}^{EKB}(t) \quad (33)$$

where

$N_{R}^{ML\lambda} = \left[E_{R}^{ML} \right]$ = total error offset, in integer number of wavelengths, resulting from the global acquisition step of the Hybrid Algorithm;

$E_{R}^{EKB}(t)$ = error associated with the EKB phase tracker.

Besides hypotheses H1 and H2 of sections 3.5 and 4 respectively, we further assume.

H3: The steady state behavior of the EKB phase tracker is independent of the ML-estimator output.

Hypothesis H3 formalizes in the model the insensitivity of the phase lock loop structure to the absolute phase reference.

Under H1, H2, and H3 the mean square error at the output of the Hybrid Algorithm is, from equation 33

$$E(E_R^2(t)) \sim P_{11} + \lambda^2(\bar{J}_R t) \quad \text{if } E(E_R^{ML})^2 < \left(\frac{\lambda}{2}\right)^2 \quad (34a)$$

$$E(E_R^2(t)) \sim (N^{\overline{ML}} \lambda)^2 + P_{11} + \lambda^2(\bar{J}_R t) \quad \text{if } E(E_R^{ML})^2 > \left(\frac{\lambda}{2}\right)^2 \quad (34b)$$

$$E(E_R^2(t)) \sim \sigma_{R_{o_{tot}}}^2 + \lambda^2(\bar{J}_R t) \quad \text{if } E(E_R^{ML})^2 \gg \left(\frac{\lambda}{2}\right)^2 \quad (34c)$$

6. Regions of Behavior for the Hybrid Algorithm

In the last three sections we carried out in detail the analysis of the errors at the output of the two blocks of the Hybrid Algorithm. Besides the error analysis associated independently with each one, the hybrid structure raised additional points:

- 1) A maximum acquisition time T_{max} , determining the minimum attainable ML-mean square error performance, as illustrated in figure 11, and which is imposed by the errors induced on the global acquisition by the path variations;
- 2) A maximum usable time for the EKB recursive structure, determined by the average time T_{skp} for a cycle skip to occur;

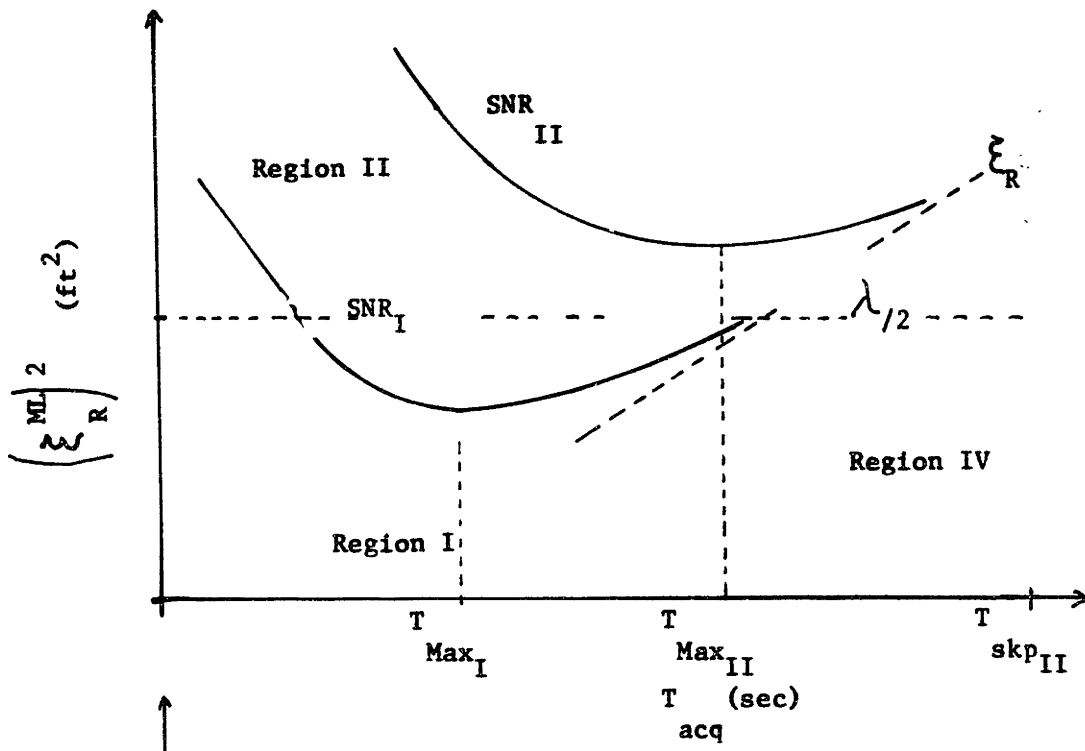
3) Suitable statistical independence assumptions H1, H2, H3 on the errors, which lead to the mean square error approximation given by equations 34.

Integrating these considerations, we distinguish four regions of behavior for the Hybrid Algorithm, as summarized in table I. Figure 12 illustrates them, in a sketch of the range mean square error performance as a function of the acquisition time, for three signal to noise ratio parameter values. In Chapter VI we will quantify them exactly in the context of specific applications.

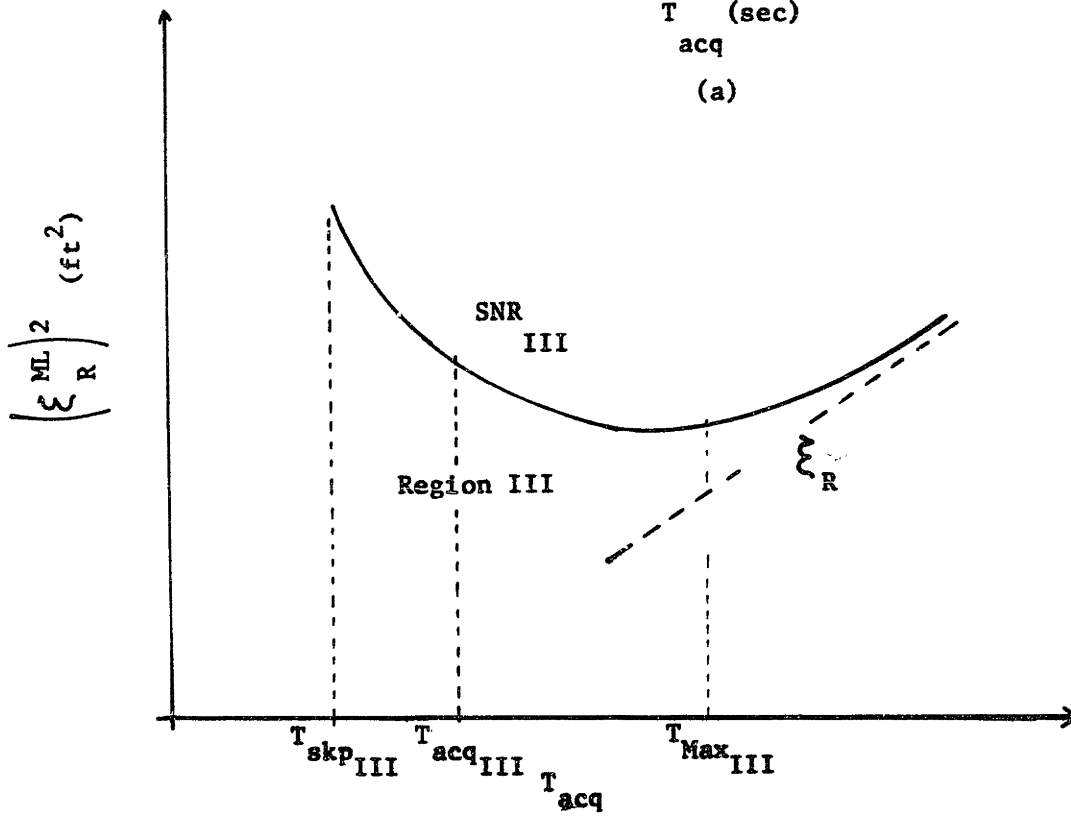
Region	T_{acq}	T_{skp}	$E(E_{R}^{ML 2})$	HA MSE	Remarks
I. Tracking within Phase	$< T_{Max}$	$> T_{acq}$	$< (\frac{\lambda}{2})^2$	Eq. 34a	EKB saves comput. eff. and determines final HA MSE
II. Tracking within Geometry			$> (\frac{\lambda}{2})^2$	Eq. 34b or 34c	EKB saves comput. eff.; ML-determines final HA MSE
III. Acquisition		$\sim T_{acq}$		Eq. 34c	EKB not used for significant time
IV. Large Errors	$> T_{Max}$				System has to be redesigned (e.g. larger SNR)

Regions of Behavior for Hybrid Algorithm

Table I



(a)



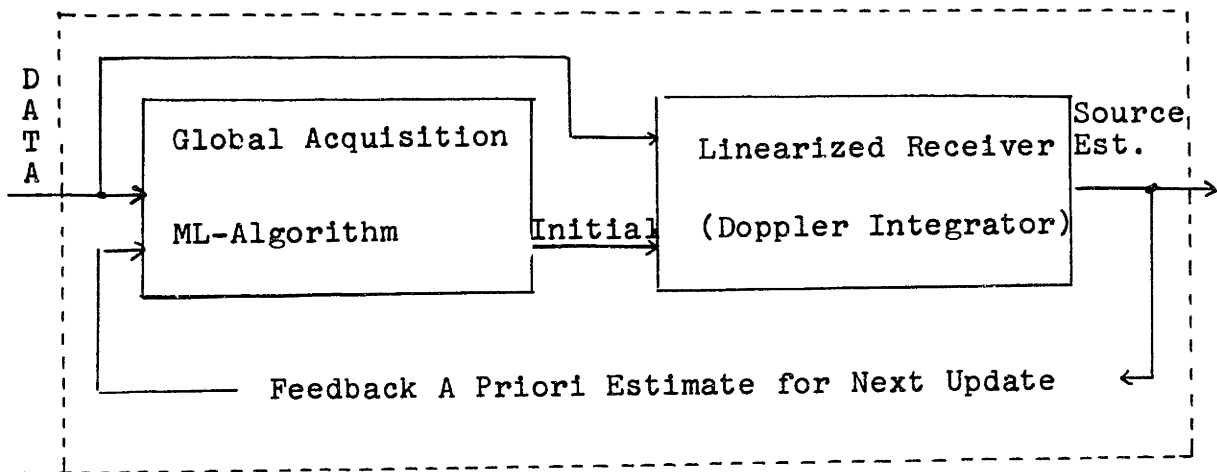
(b)

Figure 12: Typical Regions of Behavior for Hybrid Algorithm

Region IV, "Large Errors" see figure 12a, represents an underdesigned system, with the acquisition errors exceeding the required accuracy. In the other three regions, the path variations are not a fundamental constraint. In region III, "acquisition" see figure 12b, the average time for cycle skip is smaller or of the order of the required acquisition time, so that no recursive tracking is accomplished, and the Hybrid Algorithm just achieves the global acquisition step. In regions I and II, the phase, and so the range increments, may be recursively tracked via the EKB, with a corresponding savings in the associated computational effort. But only in region I, "Tracking within the Phase" curve SNR_I in figure 12a, does the Hybrid Algorithm performance attain the EKB accuracy. In region II, "Tracking within the Geometry" curve SNR_{II} in figure 12a, the acquisition errors are larger than half the wavelength, so that the original offset in wavelengths remains as a bias at the output of the EKB, and of the Hybrid Algorithm.

Since one does not want to accumulate range errors due to cycle skipping phenomena, a practical strategy for the Hybrid algorithm in regions I and II is indicated in Figure 13 and consists of:

- 1) Acquire globally with the ML-processor;
 - ii) Initialize the linearized recursive structure with the estimates resulting from the preceding step;
 - iii) Reacquire every T_{skp} sec with the nonlinear ML-filter.
- At this stage, the current EKB estimates, and the variance errors associated with it are used to determine the parameter region of interest to be scanned.



Hybrid Algorithm

Figure 13

For region III the Hybrid Algorithm simply reduces to the global acquisition step with the nonlinear ML-algorithm.

Chapter VI

APPLICATIONS TO NAVIGATION AND POSITIONING. SIMULATION

We now apply the passive tracking theory developed in the preceding chapters to problems drawn from actual practical situations. We consider distinct underlying physical environments (underwater and free space), and illustrate the applicability of the theory to very different geometric and statistical conditions.

We extract, for each application, the fundamental phenomena, casting it in the framework of one of the passive tracking classes considered in the previous chapters. Based on physical considerations we choose nominal range of values, and discuss the tradeoffs between the geometry, the statistical parameters and the desirable accuracies.

In sections 1 and 2 we study passive positioning problems. In section 3 we show how navigation can be cast in the context of passive tracking by exploiting its dualism to positioning. A significant novel issue arising in the navigation context results from discretization. This is explored and illustrated with an application involving geostationary satellites. In section 4 we present Monte Carlo simulation results for the ML-acquisition step of the hybrid Algorithm.

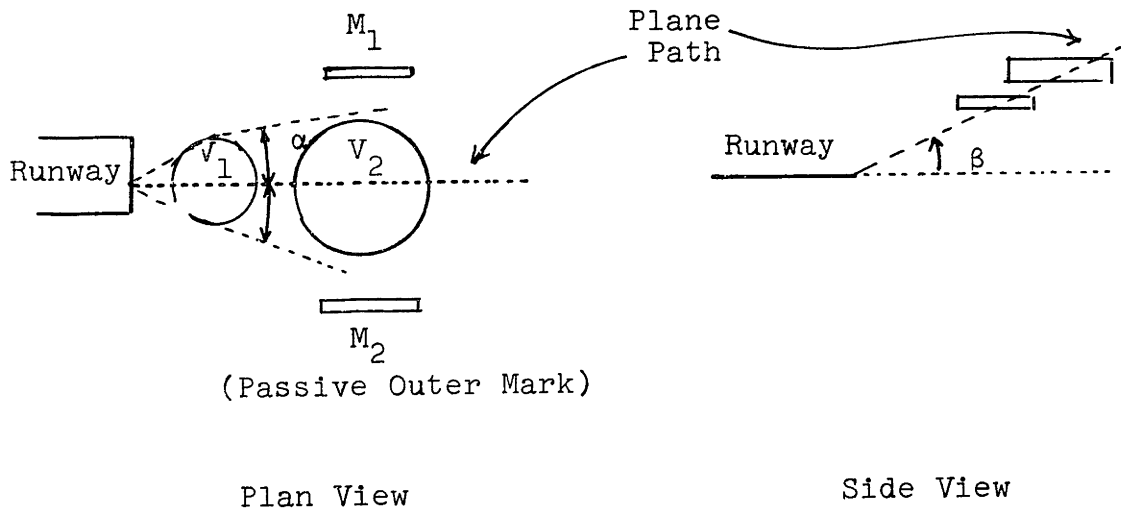
1. Air Traffic Control Precision Landing

1.1 Problem Description

There is a need for improving the accuracy of locating in 3-dimensional space a plane, as it approaches for landing. The airport control tower must decide if the plane is following a nominal path leading to a safe landing. If not, it declares a missed approach, and the plane is directed to circle the airport to prepare for a new approach. An important source of location errors derives from the altitude and speed measurements, which may be affected by large inaccuracies. One is required not to use very high structures, on the airport surface, and active systems may produce unacceptable interference problems. We investigate here the feasibility of a precision landing monitor involving passive measurements of aircraft position by ground sensors.

We show in Figure 1 the plan view and a side view for the ideal landing geometry. At the left of both views is the runway, which is approached by the plane from the right. The aircraft's course may be given by an azimuth α and an elevation angle β , both usually between 3° and 6° . A safe landing requires that the plane follow a certain nominal path, defined at the different ranges, by shrinking cylindrical volumes V_1, V_2, \dots (see circular sections on the plan view and vertical sections on the side view), which measure the allowable error on the aircraft position. At the threshold of the run-

way, the plane's position should be known with a very small residual error.



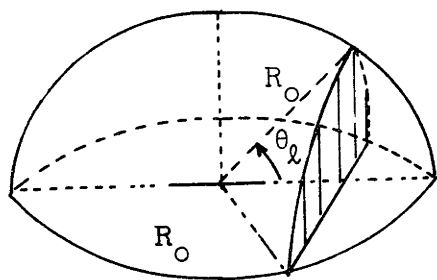
Landing Geometry

Figure 1

We assume that the system, has placed along the landing path, passive antennas monitoring narrowband signals transmitted from the aircraft (e.g. a single tone modulated by some coding for identification purposes). In order to avoid endfire type configurations, which lead to a considerable loss of performance, the passive structures are not placed at the end of the runway, but are mounted along the approach path, before the threshold of the runway, as indicated by M_1 and M_2 in the plan view of Figure 1. The passive location problem consists of positioning the plane with respect to these outriggers. On a particular application it may be

necessary to have several pairs of marks, placed along the landing path.

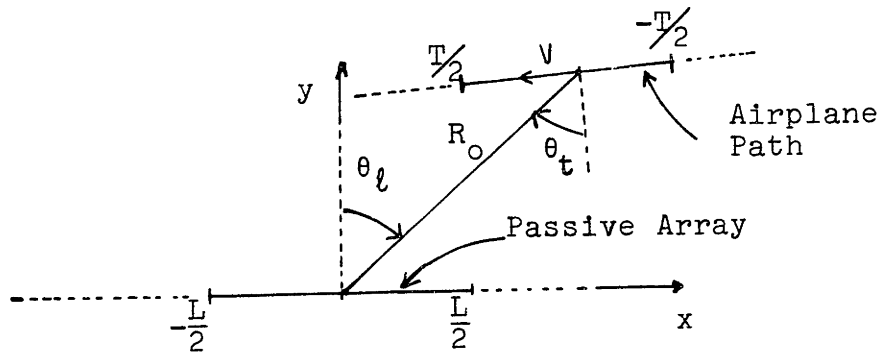
Although in (half-) 3-dimensional (3-D) space a single passive receiving element, e.g. the outermark M_1 in Figure 1, locates the airplane only up to the intersection of a half cone and a half sphere, see Figure 2, we consider here only the simpler problem of a planar geometry.



3-Dimensional Ambiguity Associated with Single Linear Array

Figure 2

The idealized version of this precision landing problem is sketched in Figure 3. The aircraft position and dynamics are parametrized by the range R_0 , the speed v with respect to the ground, and the two viewing angles θ_l and θ_t .



Precision Landing Geometry

Figure 3

1.2 Hybrid Algorithm

1.2.1 Model

As discussed in the preceding chapter, the Hybrid Algorithm achieves two main tasks, i) the global acquisition, followed by ii) the local tracking and integration of the dynamics. For the global acquisition step we model the vector

$$A = \begin{bmatrix} R_0 \\ V \\ \theta_t \\ \theta_l \end{bmatrix} \quad (1)$$

as unknown, nonrandom. For the linearized part of the Hybrid algorithm, the dynamics are assumed to be described by a finite dimensional system of stochastic differential equations, see Equations V-7.

Inside the plane, a crystal radiates a single tone at

frequency f which is observed, corrupted by additive, white, Gaussian noise. Due to the lack of synchronization, the phase of the received signal has a uniformly distributed random variable component. With these assumptions on the radiated signal and the above on vector A , the global acquisition step of the Hybrid algorithm fits the Stationary Array/Moving Source (SAMS) general model of Chapter IV. Accordingly, we use in the sequel the appropriate results on the ML-receiver's structure and performance.

1.2.2 Nominal Parameter Values

For a jet plane, in an airport traffic area, the altitude is below 10^4 feet, and the speed is required to be below a maximum, here taken approximately equal to 200 knots. The speed measurement with respect to the ground may have a large error (dependent on air circulation, wind speed, etc.); the knowledge of the altitude may also be considerably inaccurate. In air traffic control the frequencies used are in the VHF or L-Band. These considerations lead to the choice of numerical values indicated in Table I.

$$f = 1 \text{ GHz}, \lambda = 1 \text{ foot}$$

$$R_c \leq 10^4 \text{ feet, (typically = 6000 feet)}$$

$$V < 200 \text{ knots} = 337 \text{ feet/sec (typically = 300 ft/sec)}$$

$$\theta_t = 15^\circ; \theta_l \approx 15^\circ$$

$$\Delta_M V \leq 80 \text{ feet/sec}$$

$$\Delta_M \sin \theta_t = 1$$

$$\Delta_M R_o \leq \frac{R_o}{5}$$

$$L = 30 \text{ feet}; T = 8 \text{ sec (Typical value)}, X_t = .2$$

Numerical Values for Precision Landing

Table I

We used in Table I the notation of Chapters II to IV. In particular, we recall that

$$\Delta_M A_i$$

stands for the a priori uncertainty on the parameter A_i .

1.2.3 Review of ML-Performance Results

For a craft speed of 300 feet/sec and an observation interval larger than 1 sec, the temporal baseline is much larger than the spatial baseline, i.e.

$$\gamma = \frac{VT}{L} > 10 \gg 1 \quad (2)$$

In accordance with Chapter IV, the spatial/temporal ML-receiver is practically decoupled, with the reduced parameter

$$A_o = \begin{bmatrix} R_o \\ v \\ \sin\theta_t \end{bmatrix} \quad (3)$$

being estimated from the temporal diversity, and the bearing $\sin\theta_\rho$ from the spatial diversity. The performance analysis reduces to the corresponding one for SAMS_o and bearing estimation.

In order to concentrate on the basic problem aspects, we restrict the discussion mainly to the tradeoffs and demands imposed by the range accuracy requirements on the geometric and statistical parameters. In particular, for the resulting signal to noise ratio values, the attainable accuracies on the speed v , the bearing θ_ρ , and the inclination θ_t are well within the desirable limits.

The mean square performance at the output of the ML-processing block of the Hybrid Algorithm is, as seen previously, for parameter A_j

$$\sigma_{tot A_j}^2 = \sigma_{loc A_j}^2 + \sigma_{gl A_j}^2 \quad (4a)$$

with

$$\sigma_{loc A_j}^2 = \sigma_{CR A_j}^2 [1 - \Pr(\epsilon)] \quad (4b)$$

$$\sigma_{g1_{A_j}}^2 = \frac{(\Delta_M A_j)^2}{6} \Pr(\epsilon) \quad (4c)$$

where σ_{CR}^2 is the Cramer Rao (C-R) bound, and $\Pr(\epsilon)$ is the probability of a decision error. For the large signal energy to noise ratio case (see Equation II-80)

$$\Pr(\epsilon) \approx \frac{1}{\frac{E_r}{N_0}} \left[\ln M - \frac{1}{2M} + \gamma \right] \quad (4d)$$

with M = total number of grid cells in the first step of the ML-algorithm.

For the decoupled SAMS problem, and whenever

$$X_t = \frac{VT}{2R_0} < 1 \quad (5a)$$

we have the analytical expressions (Chapter III)

$$M = \frac{V_\Omega}{k} (\det M)^{1/2} \cong \frac{\Delta_M R_0 \Delta_M V \Delta_M \sin \theta_t}{8} \left(\frac{2\pi}{\lambda} \right)^3 \frac{R_0^2}{V} \frac{2 \sin \theta_t \cos^2 \theta_t X_t^6}{3 \times 5 \times \sqrt{105}} \quad (5b)$$

$$\sigma_{R_0_{CR}} = \text{Gain} \frac{\lambda}{2\pi} \frac{5\sqrt{7}}{\sin \theta_t \cos^2 \theta_t} \frac{1}{X^3} \quad (5c)$$

$$\sigma_{V_{CR}} = \text{Gain} \frac{\lambda}{2\pi} \frac{5\sqrt{7}}{2} \frac{V}{R_0 \sin \theta_t} \frac{1}{X^3} \quad (5d)$$

$$\sigma_{\sin\theta_{t_{CR}}} = \text{Gain} \frac{\lambda}{2\pi} \frac{5\sqrt{7}}{2} \frac{1}{R_o} \frac{1}{X^3} \quad (5e)$$

where

$$\text{Gain} = \left[1 + \frac{N_o}{2P_n \sigma_b^2} \frac{1}{LT} \right]^{1/2} \frac{1}{\sqrt{\frac{2P_n 2\sigma_b^2}{N_o} LT}} \quad (5f)$$

For the high signal energy to noise ratio

$$\text{Gain} \approx \frac{1}{\sqrt{2 \text{SNR} LT}} \quad (5g)$$

where SNR represents the effective signal to noise ratio (SNR) at the receiver site, i.e.

$$\text{SNR} = \frac{P_n}{N_o} 2\sigma_b^2 \quad (5h)$$

1.3 ML-System Curves

Unless otherwise stated, in the subsequent set of figures, we assume the nominal values in Table I.

Figure 4: Study of range accuracy versus SNR for two values of the geometric parameter

$$X_t = \frac{VT}{2R_0} = .1; .2$$

and the a priori range uncertainty

$$\Delta_M R_0 = 500 \text{ ft}; 10^3 \text{ ft}$$

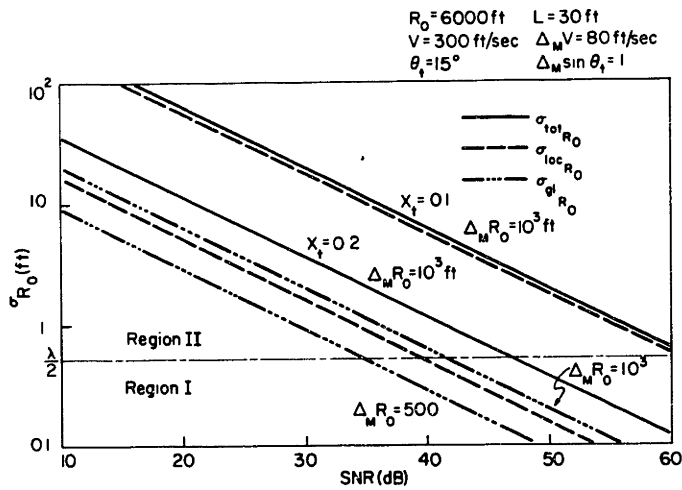
Note:

1) The curves for the local (Cramer-Rao bounds) $\sigma_{loc R_0}$, global $\sigma_{gl R_0}$, and total errors $\sigma_{tot R_0}$ are linear, reflecting the modelling assumptions on the SNR dependence;

2) For $X_t = .1$ and $\Delta_M R_0 \leq 10^3$ ft, the performance is well predicted by the Cramer-Rao bound (CR);

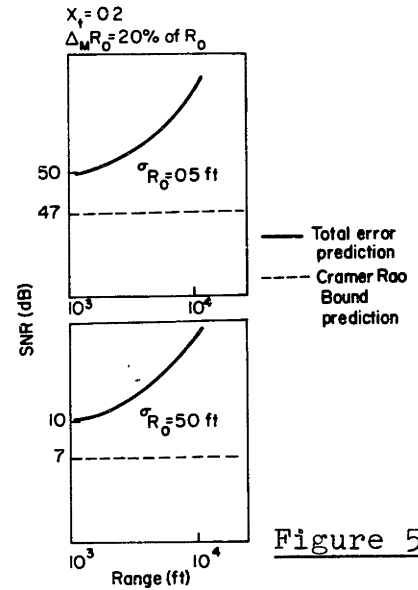
3) For $X_t = .2$ and for $\Delta_M R_0$ in the range of values indicated, both the local and global errors contribute significantly to the mean square performance (transitional region, referred to in Chapter III, section 4.4.2);

4) We indicate in Figure 4 the $\frac{\lambda}{2}$ threshold separating the tracking within the phase (Region I) from the tracking within the geometry (Region II) (see discussion on Section 6, Chapter V). The tracking within the phase requires about 50 dB for $X_t = .2$, and 60 dB for $X_t = .1$.



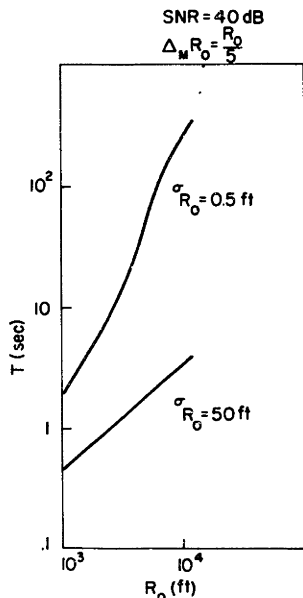
Range Acc. Versus SNR

Figure 4



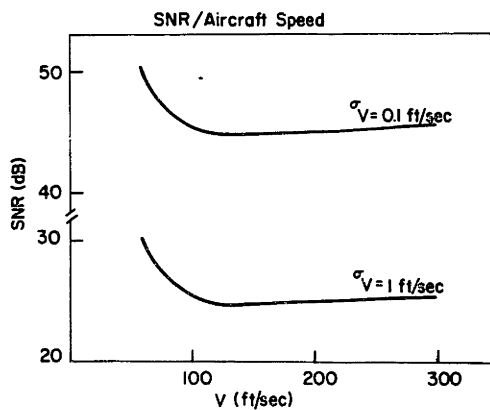
SNR Versus R_0

Figure 5



T_{acq} Versus R_0

Figure 6



Speed Acc. Versus SNR

Figure 7

Figure 5: Tradeoff between required SNR and actual aircraft/passive receiver separation, for two typical accuracy requirements

$$\begin{aligned}\sigma_{R_0} &= \frac{\lambda}{2} \text{ ft (Region I, upper curve)} \\ &= 50 \text{ ft (Region II, bottom curve)}\end{aligned}$$

Note:

- 1) The extra 40 dB required to go from Region II (tracking within geometry) to Region I (tracking within the phase);
- 2) The additional SNR required with respect to the value predicted by the CR bound, which is due to the global errors induced by the large a priori uncertainty.

Figure 5 suggests an iterative global acquisition scheme, where several (pairs of) receiving elements are placed along the airplane landing path, with increasingly greater accuracy requirements. This strategy is in accordance with the vanishing sequence of uncertainty cylinders of Figure 1. As the plane travels through, $\Delta_M R_0$ is reduced from one iteration to the next, with the net effect of diminishing σ_{glR_0} , and of the performance approaching the CR bounds.

Figure 6: Study of total acquisition time T_{acq} required by the ML-receiver, as the actual range changes, for an SNR = 40dB , and two accuracy requirements

$$\sigma_{R_0} = \frac{\lambda}{2} \text{ ft (Region I) , } \sigma_{R_0} = 50 \text{ ft (Region II)}$$

Note:

1) The tracking within the geometry (lower) curve is linear, reflecting the Cramer-Rao dependence on T_{acq} ;

2) The tracking within phase (upper) curve changes from the CR-dependence to a global type dependence, with a sharper slope.

Since we cannot increase arbitrarily the acquisition interval, due to the limitations imposed by the path random perturbations (recall Figure V-11, see also Section 1.4.1 below), Figure 6 says that if the overall geometry does not lead to a CR type dependence, it is unrealistic to expect to improve significantly the estimation accuracy by increasing the acquisition time; any significantly higher performance standard has to be met with enough SNR.

Figure 7: Speed accuracy versus SNR, for two different mean square speed accuracies.

Note:

1) For slower avionics the total temporal baseline is shorter, leading to a deterioration of performance (left end of both curves). This can be partly compensated by increasing T_{acq} , depending on the path perturbation (see Section 1.4.1).

2) The change in the curve slope, as the speed increases, from the CR-type to a global ($\ln v$) type

3) Even for $\sigma_v = .1$ ft/sec, which may be thought of as an upper bound on the desired speed accuracy in most practical situations, the necessary SNR is less than 50 dB which is below the SNR demanded by the tracking within the phase acquisition mode.

1.4 Related Hybrid Algorithm Issues

We consider, in the context of the precision landing scheme, the issues of i) sensitivity of the ML-algorithm to path disturbances, ii) Linear performance of the extended Kalman Bucy (EKB) filter, and iii) average time to skip a cycle.

1.4.1 Sensitivity of the ML-Receiver to Path Perturbations

As a function of the acquisition time the mean square range path variation is given by Equations V-30

$$\Sigma_R (T) \approx \frac{QT^3}{12} \left[1 + \frac{4^2 X_t^2}{30} \right]$$

Table II summarizes the values of $\Sigma_R^{1/2}$ for several Q and T, extracted from Figure V-10. It shows that the effects of the path variation may be a limiting factor on the final attainable range accuracy (see Section 5 below).

$\Sigma_R^{1/2}$ (ft)	4	8	T_{acq} (sec)
4×10^{-3}	.15	.35	
4×10^{-2}	.46	1.3	
4×10^{-1}	1.45	4.12	
4	4.6	13	
20	10	30	
$Q(\text{ft}^2/\text{sec}^3)$			

Root Mean Square Path Variation

Table II

1.4.2 Extended Kalman Bucy Linearized Performance

The source parameter estimates returned by the ML-processor initialize an Extended Kalman Bucy (EKB) filter as discussed in Chapter V. A simple calculation with equations V-13 and V-14 shows that, for the SNR values required by the global range acquisition, the EKB linearized mean square performance is well within most actual practical requirements. In particular, for a low SNR (in terms of the precision landing application), SNR = 10dB and $Q=1$, we have from Equation V-14c

$$P_{11} \approx \left(\frac{4Q}{H_1}\right)^{1/4} \approx .367 \text{ ft}^2$$

and for the steady state range rate mean square performance

$$P_{22} \approx \frac{2Q}{(4QH_1)^{1/4}} \approx .365^2 \text{ (ft/sec)}^2$$

1.4.3 Average Time for Cycle Skipping

We have from Equation V-23

$$T_{\text{skp}} = \bar{J}_R^{-1} \approx \frac{\pi\sqrt{2}}{3} (QH_1)^{-1/4} \exp 2\alpha$$

for an SNR ≈ 10 dB we obtain

$$\alpha \approx 12 \times 10^3$$

which leads to

$$\ln T_{\text{skp}} \approx 12 \times 10^3$$

The probability of a cycle skip is, from Equation V-26b

$$\ln P_{\text{skp}} \approx -2\alpha$$

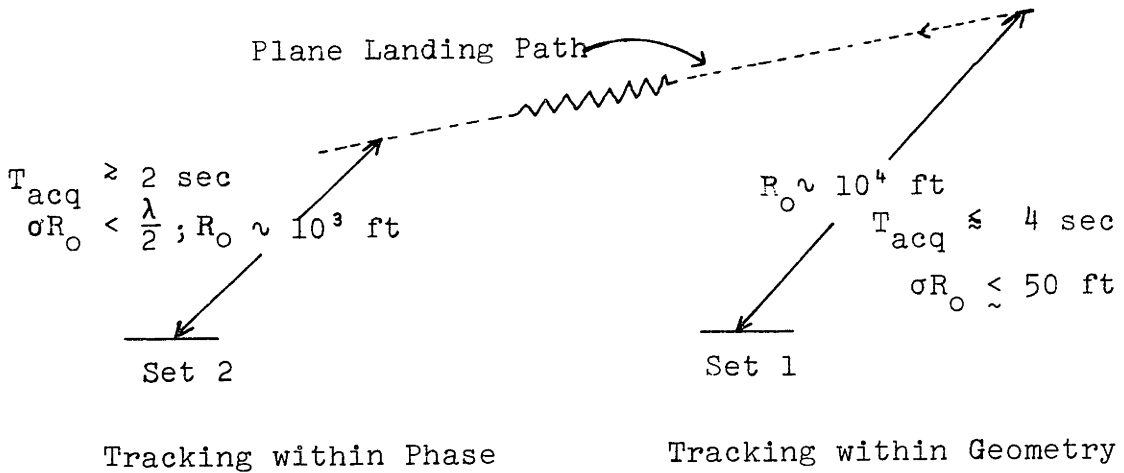
extremely low.

1.5 Conclusion

The preceding analysis showed that the range global acquisition is the determining factor of the Hybrid Algorithm performance in the passive precision landing. There are two main sources of inaccuracies. Errors incurred by the ML-receiver, due to the additive noise disturbances and errors

induced by flight turbulence.

We discuss briefly a practical solution to the passive precision landing. It consists of two sets of passive outriggers as illustrated by Figure 8. Relatively early in the approaching path we place the passive receiving element set 1 designed for tracking planes at ranges of 10^4 feet, with speeds of 300 ft/sec. Between set 1 and set 2 the plane is recursively tracked by the EKB. Set 2 is placed deeper in

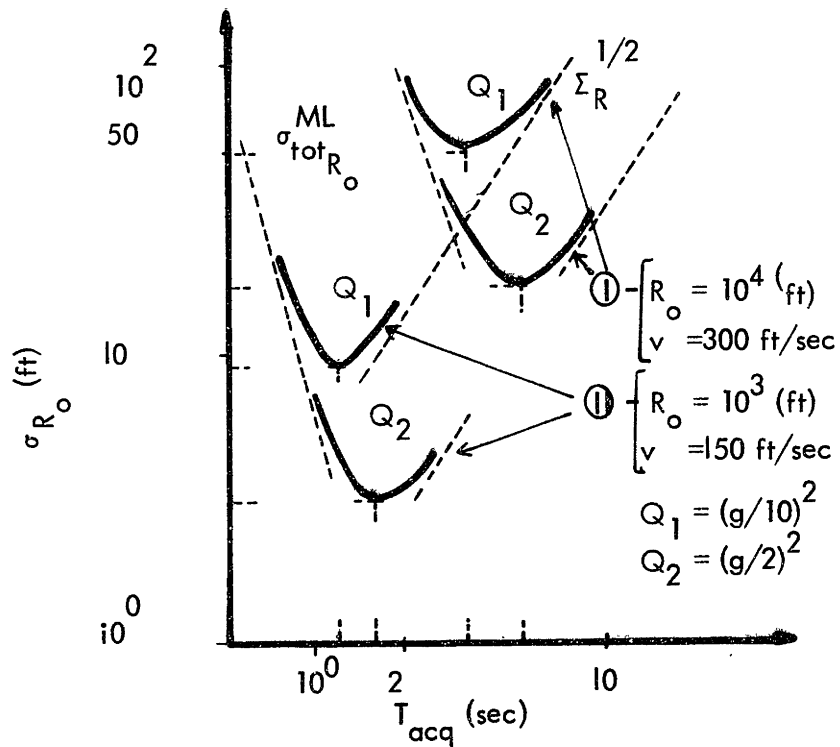


Practical Solution to Passive Landing

Figure 8

the landing path, and is designed for tracking planes at 10^3 feet ranges, with nominal speeds of 150 ft/sec. From then on the plane is tracked by the EKB. We assume that the passive receiver elements in each set have

$$L = 50 \text{ ft}$$



Range Accuracy (Two Different Flight Turbulence Conditions)

Figure 9

and the SNR level at the receiver site is

$$\text{SNR} = 50\text{dB}$$

The remaining nominal values are the ones in Table I. With this choice for the parameters, we study in Figure 9 the attainable range accuracies for light ($\sqrt{Q_2} = \frac{g}{10}$) and medium ($\sqrt{Q_1} = \frac{g}{2}$) turbulence flight conditions, where

$$g \cong 32 \text{ ft/sec}^2$$

is the gravitational constant.

The two upper curves I of Figure 9 correspond to the expected performance at the set 1 of outriggers of Figure 8, and the lower curves II to set 2. For the indicated turbulence conditions, the range acquisition accuracy depends on both the ML-receiver performance $\sigma_{\text{tot}_{R_0}}^{\text{ML}}$ and on the RMS path variance, which limits the maximum acquisition time and attainable accuracy.

As a final remark we note that range accuracy improvements can be obtained, by working with higher carrier frequencies.

2. Passive Positioning via Underwater Acoustics

We analyze the problem of locating an undersea platform in time and space, via passive acoustic techniques. These utilize the radiated signature of the platform source to determine a collection of parameters, called a fix, from which the source/receiver geometry can be reconstructed.

We explore two different configurations of important practical implications. One studies the issues involved with passive ranging by measuring curvature with a large array; the other concentrates on the tradeoffs and limitations of passive tracking the modulations induced by the relative source/receiver dynamics on the temporal signal structure.

We assume a planar geometry and linear structures. As before, we work with the narrowband assumption on the radiated signals (single tone type). For generalizations of this model, to which the analysis can be straightforwardly extended, see Chapter VII.

2.1 Underwater Acoustic Model

We consider two nominal geometries, sketched in Figure 10.

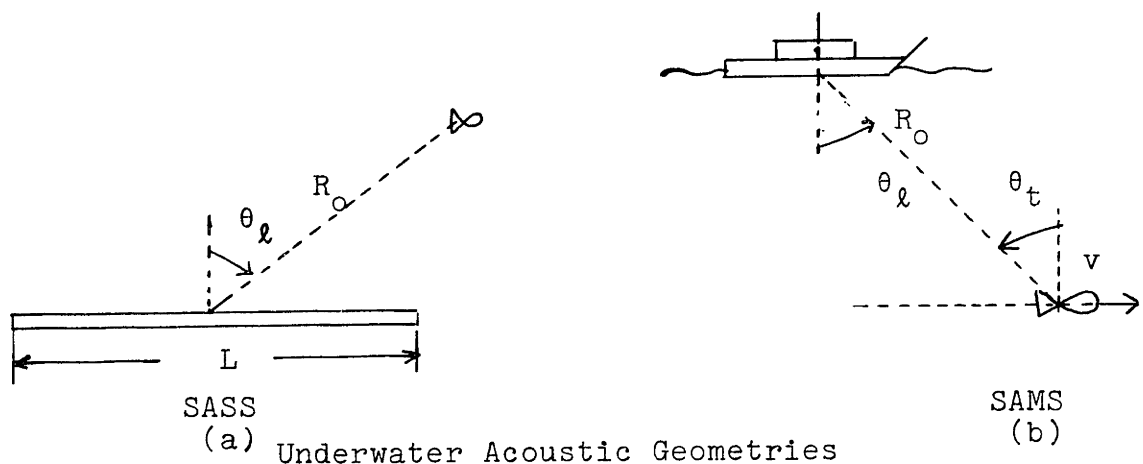


Figure 10

In Figure 10(a) a large array observes the spatial diversity of the source signature, with the source considered practically at rest during each observation interval. In Figure 10(b) a short array observes the temporal modulations induced on the signal structure, and tracks the source motion. We model the platform relative dynamics as a nominal constant speed linear path.

We study the applicability of the Hybrid Algorithm to both problems. For the global acquisition step we assume:

H1: The problem of Figure 10-a fits the SASS model of Chapter II, namely

$$A_s = \begin{bmatrix} R_0 \\ \sin\theta_l \end{bmatrix}$$

is a nonrandom, unknown parameter vector. Furthermore the source is at rest and the measurement noise is temporally

white and spatially homogeneous.

H2: The problem of Figure 10(b) fits the decoupled SAMS model of Chapter IV, namely

$$A = \begin{bmatrix} A_o \\ \text{-----} \\ \sin\theta_\ell \end{bmatrix} \quad \text{with} \quad A_o = \begin{bmatrix} R_o \\ v \\ \sin\theta_t \end{bmatrix} ,$$

is a nonrandom, unknown parameter vector. Also, the source follows a deterministic constant speed linear path, and the measurement noise is temporally white and spatially homogeneous.

For the phase tracker of the Hybrid Algorithm we assume that the nominal dynamics are disturbed by random accelerations, as described by the finite dimensional stochastic differential equation V-7.

We explore subsequently the tradeoffs between the geometry, the statistical parameters and the attainable accuracies for the global acquisition and the linearized tracking, the issues of global step sensitivity to path variations, and of linearized Kalman Bucy filter cycle skipping.

Because of the dualism between the two problems illustrated in Figure 10, and in order to avoid repetitions, we discuss both in parallel.

2.2 Nominal Parameter Values

Table III summarizes typical values for the several parameters. Unless otherwise stated these are the assumed conditions. We recall the notation

$\Delta_M A_i = A_{iMax} - A_{iMin}$ = a priori region of uncertainty for parameter A_i , in the parameter space Ω .

$\lambda = 50 \text{ ft}$	$\Delta_M R_O = 2 \times R_O = 12 \times 10^4 \text{ ft}$
$\sigma_b^2 = 1$	$\Delta_M \theta_\ell = 5^\circ$
$R_O = 6 \times 10^4 \text{ ft}$	
SASS	SAMS
$\theta_\ell = 0^\circ; T = 250 \text{ s.}$	$\theta_\ell = 0^\circ; \theta_t = 15^\circ$
$L = 12 \times 10^3 \text{ ft}; X_\ell = \frac{L}{2R_O} = .1$	$V = 30 \text{ ft/s}; \Delta_M V = 3 \text{ ft/s}$
	$L = 250 \text{ ft}; T = 400 \text{ s}; X_t = \frac{VT}{2R_O} = .1$

Nominal Values for Passive Acoustic Positioning

Table III

For the values in the right column of Table III the ratio between the spatial and temporal geometric parameter

$$\gamma = \frac{X_\ell}{X_t} = \frac{L}{VT} = \frac{1}{48} \ll 1,$$

and according to the analysis of Chapter IV, SAMS decouples in SAMS_o and a bearing angle estimation problem. In the sequel, we concentrate on the novel SAMS_o aspects, since the passive bearing estimation has been widely documented in the literature.

2.3 Review of ML-Mean Square Performance Results

Below, the subscripts s and o refer to SASS and SAMS_o respectively. The global acquisition ML-mean square performance is given by (Chapters II, III)

$$\sigma_{\text{tot}A_j}^2 \cong \sigma_{\text{loc}A_j}^2 + \sigma_{\text{gl}A_j}^2 \quad (6)$$

where $\sigma_{\text{loc}A_j}^2$, $\sigma_{\text{gl}A_j}^2$ and $\text{Pr}(\epsilon)$ have been reviewed by Eq.(4) of the last section. For SASS we recall from Chapter II the Taylor series results

$$M_s \approx \frac{V\Omega_s}{k_s} (\det M_s)^{1/2} \cong \frac{(\Delta M^R_o)(\Delta M^{\sin\theta})}{4} \left(\frac{2\pi}{\lambda}\right)^2 \frac{R_o \cos^2\theta X^3}{3\sqrt{15}} \quad (7a)$$

$$\sigma_{R_o CR_s} \approx G_s \frac{3\sqrt{5}}{\cos^2\theta X^2} \quad (7b)$$

$$\sigma_{\sin\theta CR_s} \approx G_s \frac{\sqrt{3}}{R_o X} \quad (7c)$$

$$G_s = \left[\frac{2\bar{E}_r}{N_o} \quad \frac{\bar{E}_r}{N_o + \bar{E}_r} \left(\frac{2\pi}{\lambda}\right)^2 \right]^{1/2} \approx \left[\frac{2\bar{E}_r}{N_o} \left(\frac{2\pi}{\lambda}\right)^2 \right]^{-1/2} \quad (7d)$$

$$\bar{E}_r = (\text{SNR}) (2\sigma_b^2) LT \quad (7e)$$

where SNR represents the signal to noise ratio at the receiver site.

For SAMS_o, the corresponding results have been quoted in the precision landing , Equations 5 of Section 1, and we direct the reader back to them.

Remark:

Since the discussion here is intended as an exploration of the fundamental design aspects, we concentrate, as we did with the previous application, on the range. With respect to the other parameters, the reader is referred to the performance curves in Chapters II and III, where they are drawn for a 50 ft. wavelength. As with section 1, the higher SNR demands are placed upon the system by the range accuracy requirements.

2.4 ML-System Curves

In this paragraph we present several system curves for the global acquisition step of the Hybrid Algorithm. We discuss first the SAMS_o aspects of the problem illustrated in

Figure 10b, and then the SASS problem of Figure 10a. The sensitivity issues of $SAMS_O$ to path variations will be dealt with in Section 2.6.

SAMS_O

Figure 11: Mean Square Range Performance versus available SNR at the receiver site, for several regions of a priori undetermination

$$\Delta_M R_O = R_O (6 \times 10^4 \text{ft}); 2R_O; 5R_O; 10R_O; 20R_O (=12 \times 10^5 \text{ft})$$

indicated as parameters along the curves.

Note:

1) We have only one curve for $\sigma_{loc R_O}^2$, since the Cramer-Rao bound depends only on the actual source/receiver separation but not on the a priori length $\Delta_M R_O$ of the associated region of undetermination;

2) We observe that for an a priori undetermination

$$\Delta_M R_O \leq 2R_O = 12 \times 10^4 \text{ft}$$

the global errors $\sigma_{gl R_O}^2$ are negligible compared with the $\sigma_{loc R_O}^2$ and the Cramer-Rao(CR) predicts well the system performance (local region). For

$$\Delta_M R_O \geq 20R_O = 12 \times 10^5 \text{ft}$$

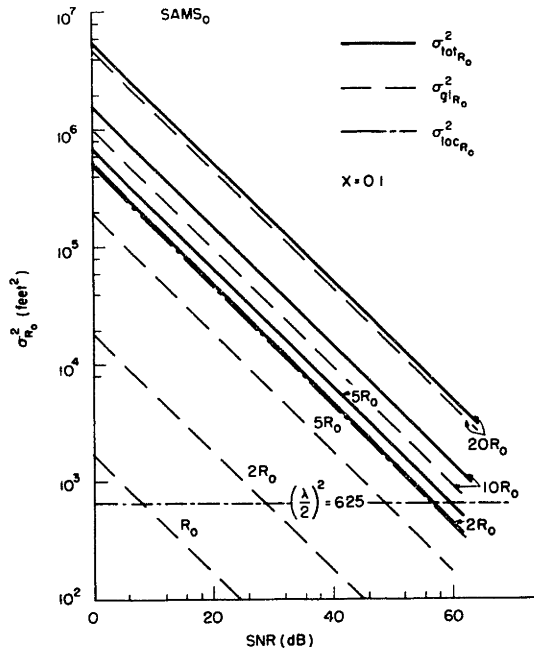
exactly the opposite is true (global region). For

$$12 \times 10^4 \text{ft} = 2R_O \leq \Delta_M R_O \leq 20R_O = 12 \times 10^5 \text{ft}$$

both errors affect significantly the total performance

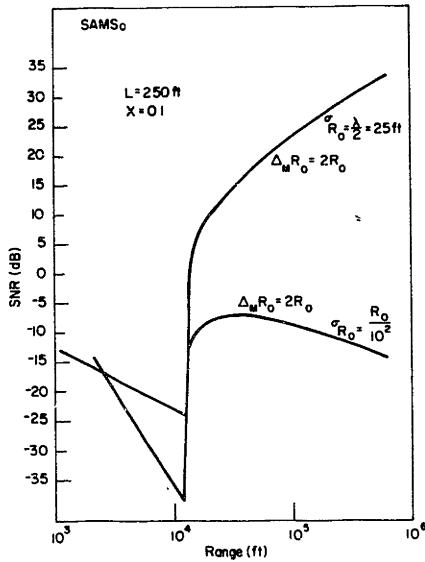
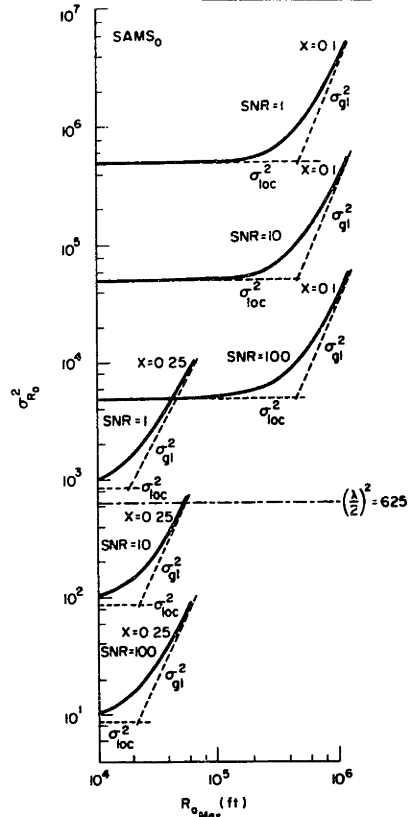
Mean Square Perf. Versus SNR

Figure 11



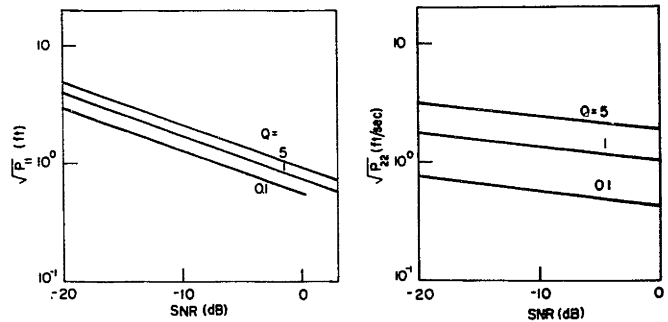
Mean Square Range Perf. vs. R_{0Max}

Figure 12



SNR Versus Range

Figure 13



EKB Mean Sq. Perf. Versus SNR

Figure 18

(transitional region). As observed in earlier chapters this transitional region is determined by the problem geometry $(X_t, \Delta_M R_o)$, but is independent of the statistical parameters (SNR).

3) The tracking within the phase requires SNR above 60dB which is unavailable in most practical situations. This can be improved by either enlarging X_t (increasing the observation interval), or by having a larger receiving array (larger array gain).

Figure 12: Mean Square Range Performance versus the length of the range region $\Delta_M R_o = R_{oMax}$ of a priori uncertainty. The figure has two sets of three curves each. The three upper ones correspond to

$$X_t = \frac{VT}{2R_o} = .1$$

and the three lower ones to

$$X_t = .25$$

For each value of X_t we considered three distinct SNR values

$$\text{SNR}=1 (0 \text{ dB}); 10(10 \text{ dB}); 100 (20 \text{ dB}).$$

The curves are essentially translations of each other. The σ_{loc}^2 are practically horizontal (independent of $\Delta_M R_o = R_{oMax}$). The transitional region, as observed before, is independent of SNR but does depend on the diversity geometric parameter X .

Figure 13 : SNR versus actual range of operation, for two values of the desired root mean square performance σ_{R_o}

$$\sigma_{R_0} = \frac{1}{2} = 25 \text{ ft (Tracking within Phase)}$$

$$\sigma_{R_0} = \frac{R_0}{10} \text{ ft (Tracking within the geometry).}$$

Note:

1) The sharp threshold exhibited by both curves at $R_0 = R_{0th} = 12.5 \times 10^3 \text{ ft}$, which is practically determined by the geometric parameter $X_t = .1$ and the a priori uncertainty $\Delta_M R_0 = 2R_0$. This threshold corresponds to the sudden transition from a local to a global region. For $R_0 < R_{0th}$, $\Delta_M R_0$ is small, and the main lobe of the ambiguity function structure spreads all over the region of interest in the parameter space Ω . As R_0 increases, so does $\Delta_M R_0 (=R_0)$, and at R_{0th} one has $M=2$, and so a nonzero probability of decision errors, which coupled to $\Delta_M R_0$ leads to a nonzero, large σ_{glR_0} .

2) Because the curves are drawn for a constant diversity geometric parameter $X_t = \frac{VT}{2R_0} = .1$, for larger range, the acquisition time is increased, having as a consequence the decreasing of the curves at their right ends.

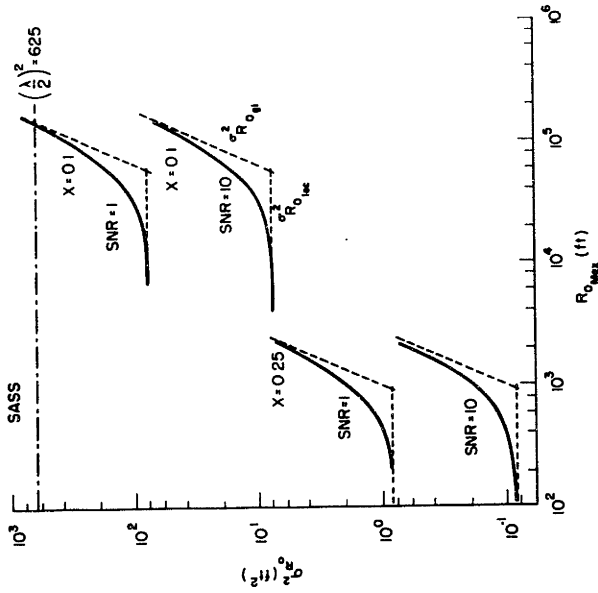
SASS

Figure 14: $\sigma_{R_0}^2$ versus SNR

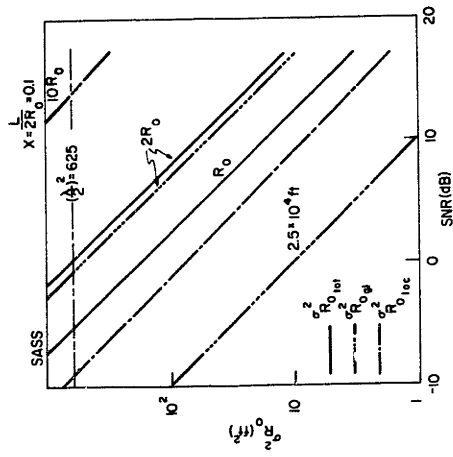
Discussion similar to the one carried for Figure 11. Note that the transitional region occurs for $\frac{R_0}{5} \leq \Delta_M R_0 \leq 2R_0$.

Figure 15: $\sigma_{R_0}^2$ as a function of $\Delta_M R_0 = R_{0Max}$ for two values of the diversity parameter $X_\ell = .1, .25$, and for two values of

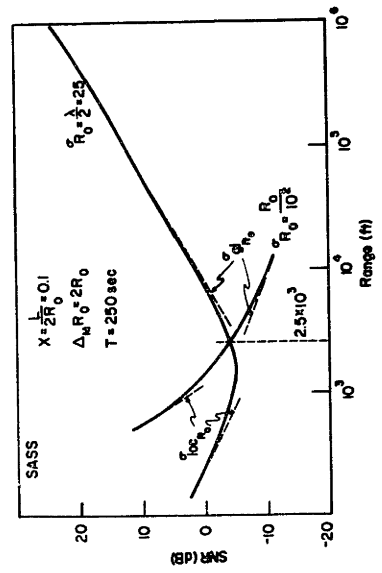
Range Perf. Versus SNR
 Figure 14



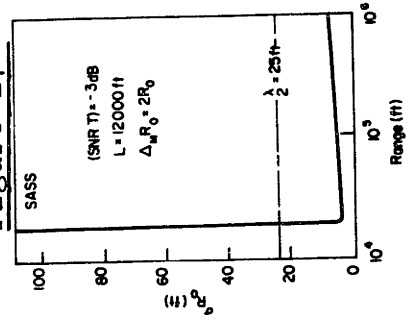
Range Perf. Versus SNR
 Figure 15



SNR Versus Range
 Figure 16



Range Perf. versus Range
 Figure 17



SNR. The discussion follows the one for Figure 12. Note that the curves shown are below the $\frac{\lambda}{2}$ threshold line. Comparing with Figure 11, we see that, for equivalent SASS and SAMS_o geometries, the same range performance requires an excess of about 40dB in SAMS_o. The alternative for an equivalent performance, at the same SNR levels, is to increase the SAMS_o diversity parameter X_t to about three times the SASS diversity parameter X_o . In practice, however, there exists an upper bound T_{Max} on the acquisition time due to path variations, as we will see in Section 2.6.

Figure 16: SNR versus actual range for two different range accuracy requirements

$$\begin{aligned}\sigma_{R_o} &= \frac{\lambda}{2} \text{ ft} \\ &= \frac{R_o}{10^2} \text{ ft}\end{aligned}$$

Discussion similar to the one for Figure 13. Note however the much smoother transition.

Figure 17: Explores the performance deterioration experienced by a fixed system ($L = 12 \times 10^3 \text{ ft}$) as the actual range increases.

We adjust the observation interval so that

$$(\text{SNR})T = -3\text{dB} = \text{constant}$$

After a sudden transition from a global region (left end of curve) to a local one (right part), the receiver's range performance changes very slowly over a wide range interval. It suggests, as a practical rule, that we overdimension slightly

the system, by increasing the SNR level at the receiver (e.g. improved sensor quality), to achieve the required accuracy at the nominal source/receiver separation. For further away platforms the system accuracy can be re-adjusted by augmenting the duration of the observation interval.

2.5 Linearized Performance of Extended Kalman Bucy Filter

The linearized block (phase tracker) of the Hybrid Algorithm has been analyzed and simulated in the context of the undersea water acoustics, in [Mo 73a], and the results reported in [Mo 73b]. The motions are modelled by a finite dimensional, stochastic, dynamical system, see Eq. V-7. For representative runs, see Figure V-7. Here we limit ourselves to a brief discussion of the EKB linearized range and range rate performance. We obtain for

$$\lambda = 50 \text{ ft}$$

$$L = 250 \text{ ft}$$

from Eq. V-14, in steady state

$$P_{11} \approx \frac{1}{2\text{SNR}} (Q \text{ SNR})^{1/4}$$

$$P_{22} \approx \frac{Q}{(Q \text{ SNR})^{1/4}}$$

Figure 18: shows the expected EKB steady state linearized mean square performance as a function of SNR, for several values of Q. Comparing these curves with the range performance curves for the ML-acquisition step we conclude that for the underwater acoustic tracking the linearized performance of the EKB filter is well within the required accuracies.

2.6 RMS Range Phase Variation and Cycle Skipping

The EKB loop cycle skipping phenomena and the effects of the RMS phase variations on the ML-receiver may introduce important limitations on the hybrid algorithm performance.

The average time for the loop to slip a cycle is, from Eq. V-23,

$$T_{\text{skp}} \approx \bar{J}_R^{-1} \approx \frac{32\pi^2}{3} \sqrt{\frac{\text{SNR}}{Q}} I_0(\alpha)^2 \approx \frac{\pi}{3} \frac{\exp 2\alpha}{\sqrt{Q} \text{SNR}}$$

As the driving noise power level Q increases, the larger loop bandwidth required for tracking the dynamics causes the loop to cycle skip at a higher rate. For large values of SNR, T_{skp} grows exponentially. But for SNR equal or smaller than 0dB the cycle skip phenomena may cause the loop behavior to depart significantly from the linearized prediction.

The RMS range phase variation is given by equation V-30

$$\Sigma_R^{1/2} \approx \sqrt{\frac{QT^3}{12}}$$

We show in Figure 19 the effects on σ_{R_0} of the path variations, for two different random acceleration levels. Figure 19a assumes an SNR = 0dB and Figure 19b an SNR = -10dB. The remaining nominal parameter values are the ones indicated in Table III. For small acquisition times T_{acq} , $\Sigma_R^{1/2}$ has a negligible contribution. But for larger ones it may become the limiting factor on the attainable accuracy, determining the maximum acquisition time T_{Max} and the maximum range performance $\sigma_{R_{0min}}$.

In both figures we have indicated the corresponding T_{skp} values. For an undisturbed path ($Q_2 = 4 \times 10^{-3} \text{ (ft}^2/\text{sec}^3)$) the cycle skipping phenomena is not a problem, even for SNR = -10dB. For larger $Q_1 = 4 \text{ ft}^2/\text{sec}^3$, T_{skp} may significantly determine the hybrid algorithm performance. In Figure 19a, for SNR = 0 dB, $Q=Q_1$ we have

$$T_{skp} \approx 32 \text{ minutes}$$

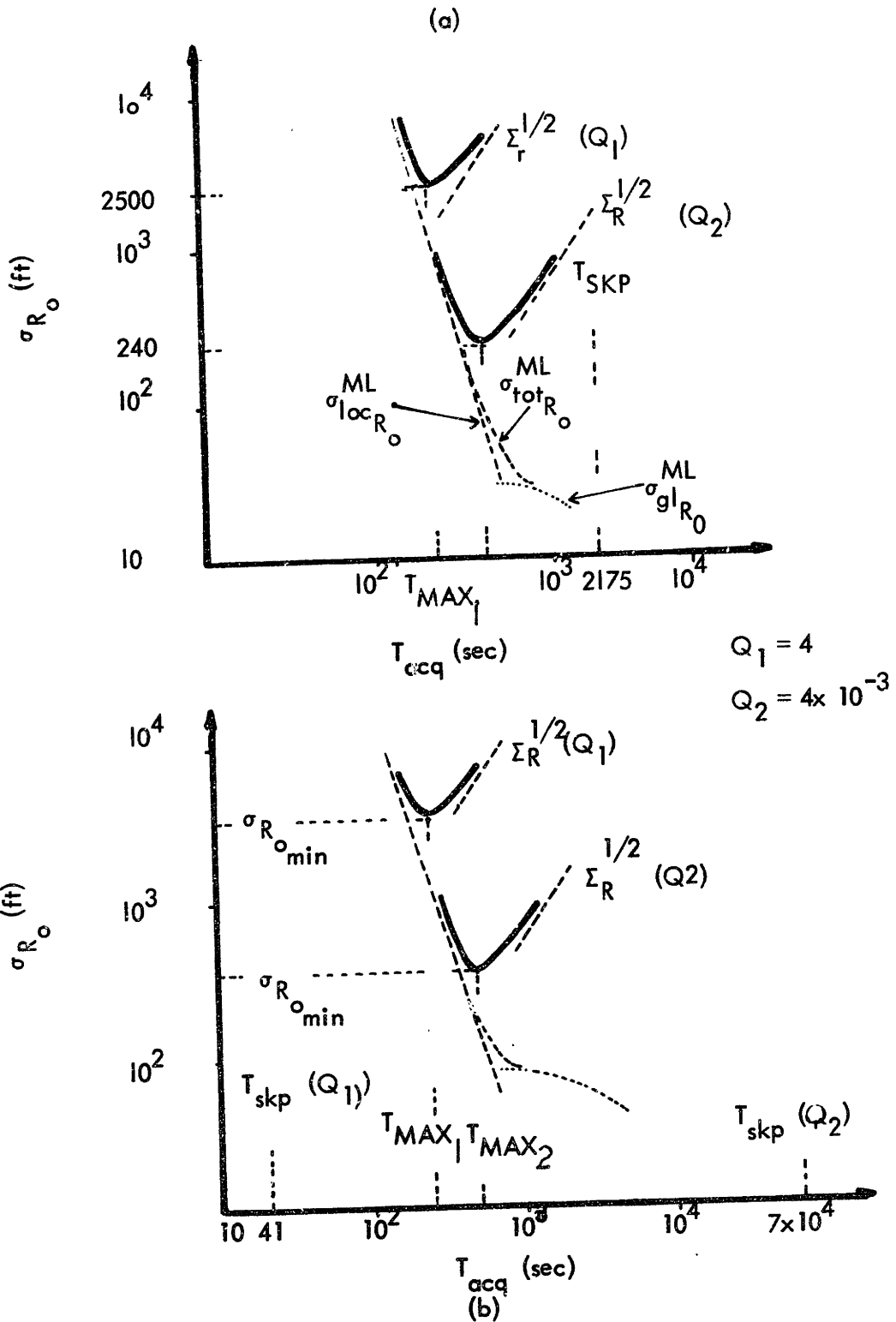
$$T_{max} \approx 3 \text{ min}$$

and the EKB has to be reacquired every half hour. In Figure 19b, SNR = -10dB, $Q=Q_1$

$$T_{skp} = 21 \text{ sec}$$

$$T_{Max} \approx 4 \text{ min}$$

and the hybrid algorithm is in the acquisition mode, with no



Underwater Acoustics Positioning Modes of Behavior
 Figure 19

tracking by the EKB being possible for a practically significant time interval.

2.7 Summary

We have analyzed the Hybrid Algorithm mean square performance and operation modes for the passive underwater acoustic position problem, both for a SASS and a SAMS_o configurations.

Due to the small geometry diversity synthesized, the problems usually fall near the boundary of transition and threshold regions, where the predicted performance changes from a local to a global bound; due to the low SNR available at the receiver site, and to the path disturbances, the RMS range phase variation and the cycle skipping phenomena determine significantly the performance and the behavior mode of the Hybrid Algorithm.

3. Precision Navigation via Satellites and Other Navigational Aids

There are presently available many radio navigation aids serving a wide variety of purposes, e.g. guidance of ships on high seas, surveillance of the intercontinental commercial air traffic, radio tracking of ocean drifting buoys or of free sounding balloons, location of a speeding truck on a highway, etc..

These navigation aids (Nav aids) are based on measurements of frequency Doppler shifts and/or of travel time delays of i) signals transmitted from a station (passive navigation), or ii) signals initiated or transponded at the user's platforms (active navigation). The measurements are converted to platform geometric parameters (e.g. range) and coupled to the known geographical location of the navigational station to provide for a platform fix.

Basically we group the navigational systems into i) earth based, and ii) satellites. The first class includes the low and very low frequency nav aids, usually consisting of several chains of a master, and two or three slave stations (e.g. Omega, Soran-C, Decca). Surveys on these include [Beu74], [Kay69].

In the second group, there is only presently available for general use the Navy Navigational Satellite System (NNSS)

also referred to as TRANSIT, [Eas72], [Ehr72]. For restricted purposes, and integrated in specific missions, several programs have been implemented, e.g. EOLE (monitoring meteorological collecting data balloons) [IEE75], TWERLE (Tropical Wind, Energy Conversion and Reference Level Experiment)[IEE75], etc. Numerous experiments have been proposed for navigation, collision avoidance, traffic control, e.g. the NASA Position Location and Communication Equipment (PLACE), the Department of Transportation's (DOT) Advanced Air Traffic Management Systems concepts, the Federal Aeronautics Administration (FAA) Astro-Dabs, the DOT/FAA Aerosat experiment, etc.[McD73].

Two important desirable characteristics are accuracy and global coverage. Omega with eight sparsed stations is worldwide, but has accuracies, e.g. for ship navigation, of 1 mile at 1500 mile ranges, while Decca is a coastal type navaid with 200-300 m accuracies at 100 miles range [Beu74]. The satellites represent the basic trend for future navigation systems, since they may provide global worldwide coverage with very significant accuracy improvements.

In the sequel we concentrate on satellites. They are either orbiting (low altitude, e.g. 1000km on NNSS, or medium altitude, up to 20×10^3 km) or geostationary (at about 40×10^3 km). Table IV summarizes pertinent data.

Sat.	Altitude(km)	Trans.Time	Coverage	Car. Freq.
Orbiting	Low $\sim 10^3$ -7000	15 min.	Pract.Glob.	VHF(150,400)
Orbiting	Med. $\sim 20 \times 10^3$	$2\frac{1}{2}$ -4 hrs.	Pract.Glob.	VHF,L-Bd
Geostat.	High $\sim 40 \times 10^3$	Permanent	$\frac{1}{3}$ of Earth	VHF,L-Bd

Data on Navigational Satellites

Table IV

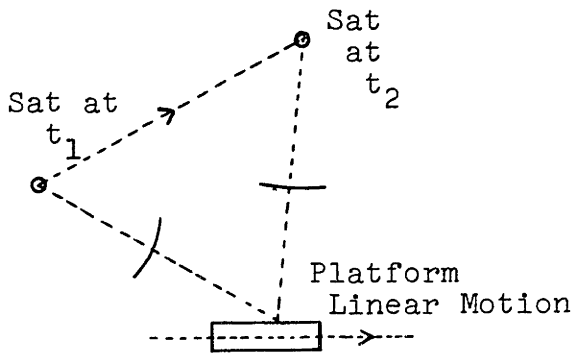
We discuss first orbiting satellites by applying straightforwardly the theory developed in the preceding chapters. The navigation with geostationary (also called geosynchronous) satellites is discussed next, after we extend to the case of a discrete space domain, the continuous space passive tracking results of Chapters II and IV.

3.1 Orbiting Satellites

Figure 20a illustrates a navigation configuration with an orbiting satellite. The moving platform monitors the signals radiated by the satellite as it passes overhead. Figure 20b casts this navigation problem in the SAMS₀ context of Chapter III.

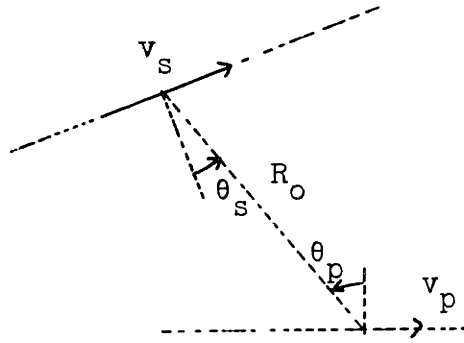
The identifiable source/receiver parameter vector is

$$A = \begin{bmatrix} R_o \\ y \\ \sin\theta_t \end{bmatrix} \quad (8a)$$



Moving Platform/Orbiting Satellite

(a)



SAMS_o

(b)

Figure 20

where

$$v = \{ v_s^2 + v_p^2 + 2v_s v_p \cos(\theta_s - \theta_p) \}^{1/2} \quad (8b)$$

$$\tan \theta_t = \frac{v_s \sin \theta_s + v_p \sin \theta_p}{v_s \cos \theta_s + v_p \cos \theta_p} \quad (8c)$$

The satellite speed v_s is usually accurately predicted and radioed to the passive user, and the satellite bearing $\sin \theta_s$ can be measured by auxiliary means, e.g. optically, so that, from equations 8b and 8c, we determine the platform speed v_p and bearing $\sin \theta_p$. In any case, we work with vector A of Eq. 8a.

To illustrate the application of the results of Chapter III and Chapter V we consider a ship navigating on high seas. A reasonable choice of parameters is

$$v = 7\text{km/s } (\approx v_s, \text{ since } v_p \ll v_s); \quad R_o = 5000\text{km}; \quad \theta_t = 30^\circ$$

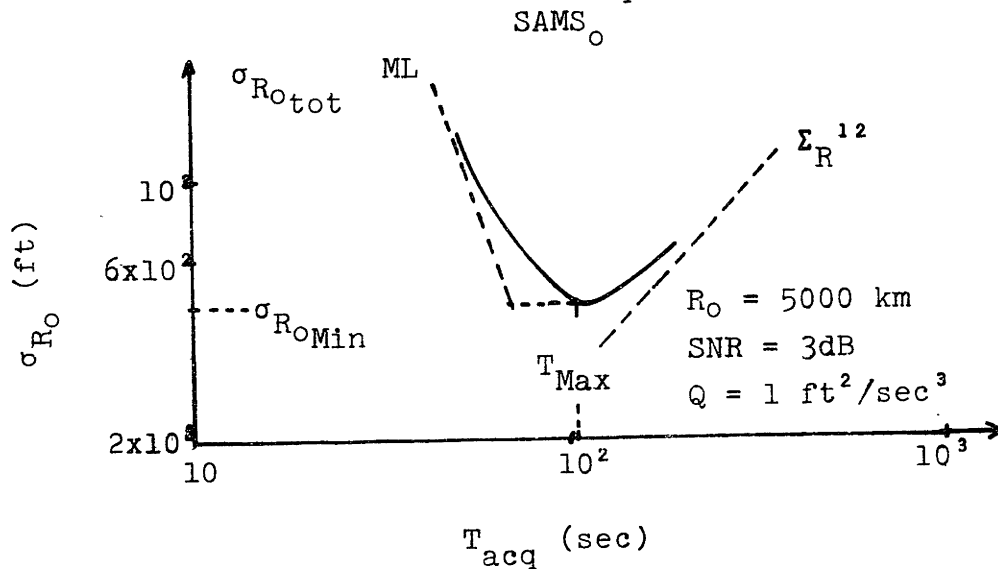
$$\text{SNR} = 3\text{dB (at the users site)}; \quad L = 250 \text{ ft}; \quad f = 400 \text{ MHz}$$

$$(\lambda \approx 2.46 \text{ ft})$$

We further assume a path disturbance level

$$Q = 1 \text{ ft}^2/\text{sec}^3$$

and an a priori range uncertainty of about 20 miles. Figure 21 studies the range accuracy as a function of the acquisition time. For smaller T_{acq} the performance is



Range Accuracy Versus Acquisit. Time for Ship Navig. Sat. Prbl.

Figure 21

essentially predicted by the Cramer-Rao bound (Eq.III-23a)

$$\sigma_{R_{\text{otot}}} \approx \sigma_{R_{\text{oloc}}} = \frac{1}{\sqrt{2 \text{ SNR } L T}} \frac{5\sqrt{7}}{\sin\theta_t \cos^2\theta_t} \frac{\lambda}{2\pi} \frac{1}{X^3} \quad (9a)$$

For large T_{acq} the RMS range phase variations dominate

(Eq. V-30c)

$$\sigma_{R_0}^{1/2} \approx \sqrt{\frac{QT^3}{12}} \quad (9b)$$

For the maximum T_{acq}

$$T_{max} \approx 120 \text{ sec}$$

the minimum root mean square error is approximately

$$\sigma_{R_0} \approx 450 \text{ ft}$$

which is below the .1 to .5 mile accuracy set as a goal for merchant ship high seas navigation, for the post 1985 year period [McD73].

For the choice of parameters given above the EKB exhibits a linearized performance well within the required accuracies, and leads to a very large value for T_{skp} . We conclude that the basic limitations are imposed by the global acquisition step, as discussed in Figure 21.

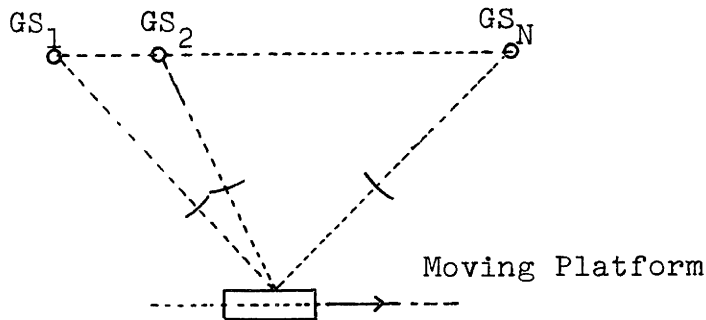
3.2 Geostationary Satellites

Figure 22 illustrates a navigational problem with geosynchronous satellites. We assume that the passive user recognizes the signals originating at N different satellites (e.g. by coding a common subcarrier on distinct carrier frequencies). The navigational problem with N spatial point sources is then the equivalent dual of a positioning problem with N sensors. Accordingly, we do not distinguish them,

and in particular we keep the positioning nomenclature (SASS, SAMS, etc.).

The satellite constellation can be viewed as an ensemble resulting from the spatial sampling of a continuous source. Two questions arise as to the applicability of the passive tracking theory developed in Chapters II to IV, namely:

- i) what are the effects of sampling on the side lobe structure of the ambiguity function;
- ii) how does the discretization affect the ML-receiver resolution, i.e. the mean square error performance.



Moving Platform/Geostationary Satellites

Figure 22

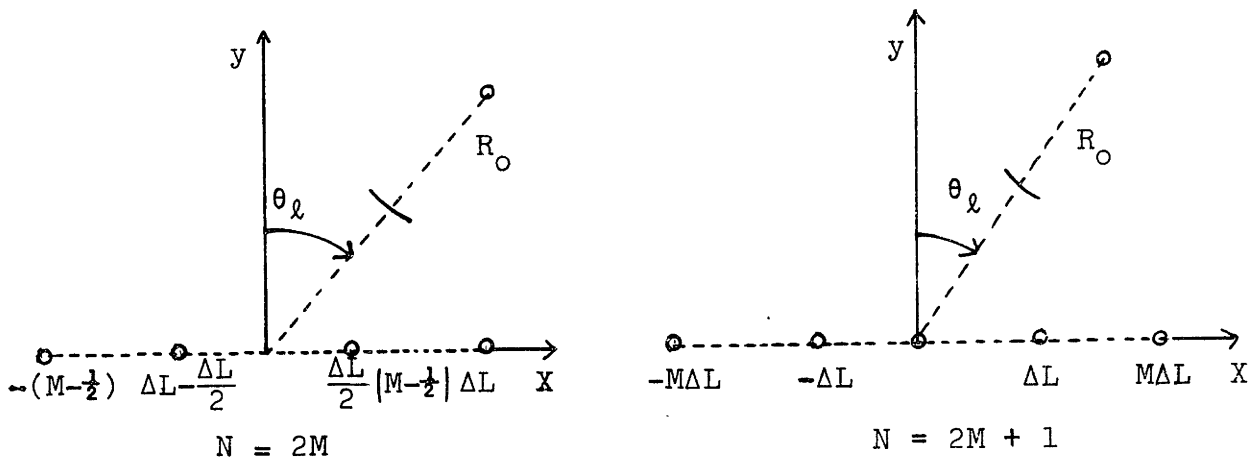
The modulation nonlinearities of the passive tracking make the answers to both problems nontrivial. We consider them briefly for a Stationary Array/Stationary Source configuration, and for a second order approximation (Fresnel zone) to the range phase function.

3.2.1 Discrete Ambiguity Function in the Fresnel Zone

Figure 23 illustrates a centered geometry with an array of N equally spaced elements. The range phase difference for the Fresnel zone is

$$\frac{2\pi}{\lambda} [\Delta R(t, \ell, A, \bar{A}) - \Delta R_0] \cong \frac{2\pi}{\lambda} [-(\Delta \sin \theta) \ell + \Delta \left(\frac{\cos^2 \theta}{2R_0} \right) \ell^2] \quad (10a)$$

$$\underline{\Delta} = k_1 \ell + k_2 \ell^2 \quad (10b)$$



Discrete SASS

Figure 23

The Discrete Generalized Ambiguity Function (DGAF)

$$\phi(k_1, k_2) = \left| \frac{1}{N} \sum_{i=1}^N \exp j (k_1 \ell_i + k_2 \ell_i^2) \right|^2 \quad (11a)$$

becomes, for the equally spaced geometries of Figure 23

1) $N = 2M+1 = \text{odd}$

$$\phi(k_1, k_2) = \frac{1}{N^2} \left\{ N + \frac{2 \cos [(M+1)k_1 \Delta L] \sin [Mk_1 \Delta L]}{\sin (k_1 \Delta L)} + \right.$$

$$\left. \begin{aligned} & 4 \sum_{l=1}^M \cos (k_1 m \Delta L) \cos (k_2 m^2 \Delta L^2) + \\ & 8 \sum_{m>n}^M \sum_{n=1}^{M-1} \cos (k_1 m \Delta L) \cos (k_1 n \Delta L) \cos [k_2 (m^2 - n^2) \Delta L^2] \end{aligned} \right\} \quad (11b)$$

2) $N = 2M = \text{even}$

$$\phi(k_1, k_2) = \left(\frac{2}{N} \right)^2 \left\{ \sum_{l=1}^M \cos^2 [k_1 (m - \frac{1}{2}) \Delta L] + \right.$$

$$+ 2 \sum_{m>n}^M \sum_{n=1}^{M-1} \cos [k_1 (m - \frac{1}{2}) \Delta L] \cos [k_1 (n - \frac{1}{2}) \Delta L]$$

$$\left. \cos [k_2 \Delta L^2 ((m^2 - m) - (n^2 - n))] \right\} \quad (11c)$$

we see that for

$$k_{1s} = m_1 \frac{2\pi}{\Delta L} \quad (\Delta \sin \theta_{\ell} = -\Delta \dot{R}_0 = m_1 \frac{\lambda}{\Delta L}) \quad (12a)$$

$$k_{2s} = m_2 \frac{2\pi}{\Delta L^2} \quad \text{for } N=\text{odd} \quad (\Delta \ddot{R}_0 = m_2 \frac{2\lambda}{\Delta L^2}) \quad (12b)$$

$$= m_2 \frac{\pi}{\Delta L^2} \quad \text{for } N=\text{even} \quad (\Delta \ddot{R}_0 = m_2 \frac{\lambda}{\Delta L^2}) \quad (12c)$$

the discrete ambiguity is

$$\phi(k_1, k_2) = 1 \quad (12d)$$

Let in the (k_1, k_2) space

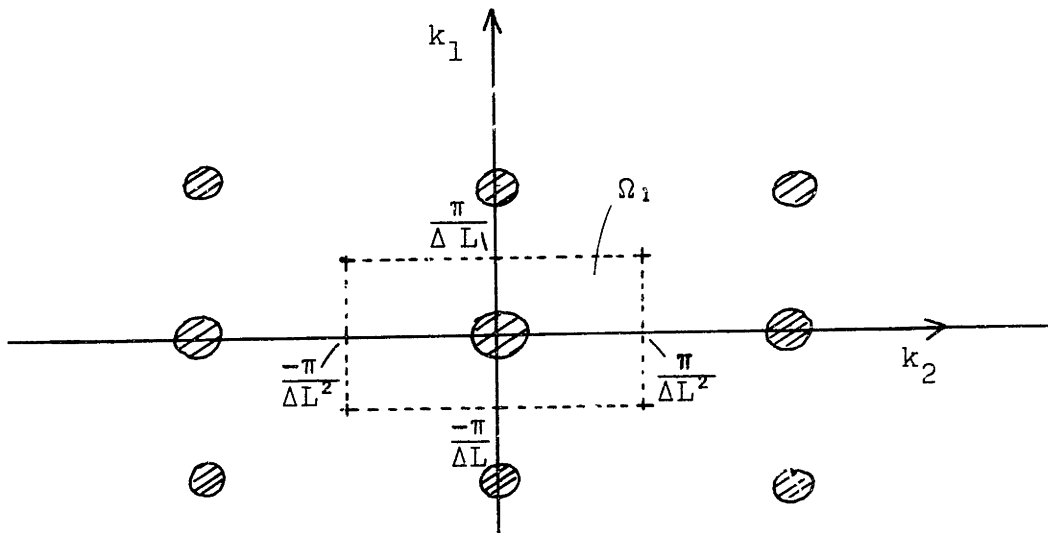
$$\Omega_1 = \left[\frac{\pi}{\Delta L}, \frac{\pi}{\Delta L} \right] \times \left[\frac{\pi}{\Delta L^2}, \frac{\pi}{\Delta L^2} \right] \quad \text{for } N=\text{odd} \quad (13a)$$

$$= \left[-\frac{\pi}{\Delta L}, \frac{\pi}{\Delta L} \right] \times \left[-\frac{\pi}{2\Delta L^2}, \frac{\pi}{2\Delta L^2} \right] \quad \text{for } N=\text{even} \quad (13b)$$

The structure of DGAF within Ω_1 , referred to as primary cell, depends on the sampling rate, and as in the linear theory, important distortion may result. For an over-sampled array

$$\frac{\Delta L}{\lambda} \ll 1, \quad \frac{\Delta L^2}{\lambda} \ll 1 \quad (14a)$$

we expect that DGAF approaches the continuous GAF. The intuitive reason is remnant of the Method of Stationary Phase, since a large number of sinusoidals with large and slightly different frequencies will tend to cancel their mutual effects. In Ω_1 DGAF will present then a quadratic main lobe and a negligible secondary structure, see the Siebert [Va71b] type plot in Figure 24, with the dashed areas indicating the regions where DGAF is significant (main lobe and, its equally spaced repetitions), and the unshaded ones, where DGAF is negligible (secondary structure).



DGAF Structure for an Over-Sampled Array

Figure 24

For an undersampled array

$$\frac{\Delta L}{\lambda} \gg 1 \quad \text{or} \quad \frac{\Delta L^2}{\lambda} \gg 1 \quad (14b)$$

aliasing results, and DGAF exhibits important secondary structure within Ω_1 , requiring a detailed study for each application.

3.2.2 Discrete Mean Square (Local) Performance in the Fresnel Zone

For the Rayleigh signal model the discrete mean square spread matrix (DMSSM) M_d is obtained by substituting sums for the integrals in Equations B-9 and B-10.

We define the n_{th} geometric moment associated with the

linear array of N sensors

$$L_n = \frac{1}{N} \sum_{i=1}^N \ell_i^n \quad (15)$$

where ℓ_i is the i th array element location.

In the Fresnel zone and for a centered geometry

$$M_d = \left(\frac{2\pi^2}{\lambda} \right) \begin{bmatrix} \frac{\cos^4 \theta}{4R_o^4} (L_4 - L_2^2) & \underline{0} \\ \underline{0} & L_2 \end{bmatrix} \quad (16)$$

The Cramer Rao bounds are obtained by normalizing the elements of M_d^{-1} by

$$G_d^{-1} = \frac{1}{\frac{2\bar{E}_r}{N_o}} \left[1 + \frac{N_o}{E_r} \right] \quad (17a)$$

where

$$\bar{E}_r = \left(\frac{2P}{N_o} \right)_d (2\sigma_b^2) NT \quad (17b)$$

$$\left(\frac{2P}{N_o} \right)_d = (\text{spatially-discrete}) \text{ SNR level at the receiver site} \quad (17c)$$

3.3. Discrete Ambiguity and Performance for Geostationary Satellites

For economic reasons the number of satellites simultaneously available at each location is usually ≤ 4 [McD73]. It is easy to see that a centered geometry (i.e. source parameters defined with respect to the array geometric center) requires at least three satellites to measure the apparent curvature, from which range is inferred. We present below explicitly the results for a four satellite constellation.

DGAF is

$$\phi(k_1, k_2) = \sin^2(k_1 \Delta L) \sin^2\left(\frac{k_1}{2} \Delta L\right) + \cos\left(\frac{3}{2} \Delta L k_1\right) \cos\left(\frac{k_1}{2} \Delta L\right) \cos(k_2 \Delta L^2) \quad (18a)$$

with the primary cell

$$\Omega_1 = \left[-\frac{\pi}{\Delta L}, \frac{\pi}{\Delta L}\right] \times \left[-\frac{\pi}{2\Delta L^2}, \frac{\pi}{2\Delta L^2}\right] \quad (18b)$$

Study of Eq. 18a shows that the main lobe is limited to

$$\Delta\Omega = \left[-\frac{\pi}{3\Delta L}, \frac{\pi}{3\Delta L}\right] \times \left[-\frac{\pi}{2\Delta L^2}, \frac{\pi}{2\Delta L^2}\right] \quad (19)$$

and that important secondary maxima exist in Ω_1 , e.g.

$$\phi\left(\pm \frac{2}{3} \frac{\pi}{\Delta L}, \pm \frac{\pi}{2\Delta L^2}\right) = \left(\frac{3}{4}\right)^2 \quad (20)$$

In the sequel we refer to $\Delta\Omega$ as the discrete resolution cell for the four satellite constellation problem.

The spread of DGAF's main lobe may also be quantified using the quadratic local approximation in terms of M_d and its inverse. For the four satellite problem, and from Eq. 16

$$M_d^{-1} = \left(\frac{\lambda}{2\pi}\right)^2 \begin{bmatrix} \frac{4R_o^4}{\cos^4\theta} & \frac{1}{L_4 - L_2^2} & 0 \\ \dots & \dots & \dots \\ 0 & \dots & \frac{1}{L_2} \end{bmatrix} \quad (21a)$$

where

$$L_2 = \frac{5}{4}\Delta L^2; \quad L_4 = \frac{41}{16}\Delta L^4; \quad L_4 - L_2 = \frac{21}{16}\Delta L^4 \quad (21b)$$

Substituting equation 21b into 21a and normalizing by the signal energy to noise ratio leads to the Cramer-Rao performance bounds for the discrete SASS with a 4 satellite constellation

$$\sigma_{R_o} \approx G_d^{-1/2} (M_d^{-1})_{R_o}^{1/2} \approx G_d^{-1/2} \frac{\lambda}{2\pi} \frac{\sqrt{73}}{6} \frac{1}{(x \cos\theta)^2} \quad (22a)$$

$$\sigma_{\sin\theta} \approx G_d^{-1/2} (M_d^{-1})_{\sin\theta}^{1/2} \approx G_d^{-1/2} \frac{3}{\pi\sqrt{5}} \frac{1}{L\lambda} \quad (22b)$$

where x = geometric spatial diversity parameter =

$$\frac{L}{2R_o} = \frac{3\Delta L}{2R_o} \quad (22c)$$

$$L_{\lambda} = \frac{L}{\lambda} = \frac{3\Delta L}{\lambda} \quad (22d)$$

3.4 Global Acquisition Strategy for a Constellation of Geostationary Satellites

The discrete ambiguity function exhibits a structure, reproduced in the parameter space Ω at equally spaced intervals. To avoid global ambiguities, the important sidelobes (peaks in Ω_1) must be shifted beyond the a priori region of uncertainty $\Delta_M \Omega$. In (k_1, k_2) space

$$\Delta_M \Omega = [k_{1 \min}, k_{1 \max}] \times [k_{2 \min}, k_{2 \max}] ; \quad (23a)$$

In the passive user parameter space

$$\Delta_M \Omega = \prod_i [A_{i \min}, A_{i \max}] \quad (23b)$$

which for the discrete SASS simply reduces to

$$\Delta_M \Omega = [\sin \theta_{\min}, \sin \theta_{\max}] \times [R_{o \min}, R_{o \max}] \quad (23c)$$

This may be achieved by matching the resolution cell $\Delta \Omega$ to $\Delta_M \Omega$ through, for example, proper choice of the wavelength. For the 4 satellite constellation, we have from Eq. 19 and 23a

$$\lambda > \max ((\Delta_M \sin\theta)\Delta L, (\Delta_M \ddot{R}_O)\Delta L^2) \quad (24a)$$

where

$$\begin{aligned} \Delta_M \sin\theta &= \frac{\lambda}{2\pi} \Delta_M k_1 = \frac{\lambda}{2\pi} (k_{1_{\max}} - k_{1_{\min}}) \\ &= \sin\theta_{\max} - \sin\theta_{\min} \end{aligned} \quad (24b)$$

$$\Delta_M \ddot{R}_O = \frac{\lambda}{2\pi} \Delta_M k_2 = \frac{\lambda}{\pi} (k_{2_{\max}} - k_{2_{\min}}) \quad (24c)$$

Alternatively, and using the quadratic representation for the main lobe, given by the mean square spread matrix, we want the diagonal elements of the inverse discrete spread matrix to satisfy

$$\left(M_d^{-1} \right)_{A_i}^{1/2} \geq \Delta_M A_i = A_{i_{\max}} - A_{i_{\min}} \quad \text{for every } i \quad (25)$$

which leads to the condition for λ

$$\lambda \geq \max_i \left(\left(M_d^{-1} \right)_{A_i}^{-1/2} \Delta_M A_i \right) \quad (26a)$$

where

$$\left(M_d^{-1} \right)_{A_i} = \frac{\left(M_d^{-1} \right)_{A_i}}{\lambda} \quad (26b)$$

Equations 24 or 26 however may lead to unacceptable resolution, i.e. to large Cramer Rao bounds. A practical strategy, which can be implemented whenever

$$G_d = 2 \frac{(\bar{E}_r/N_o)^2}{1 + \frac{\bar{E}_r}{N_o}} > 1, \quad (27a)$$

consists of a sequential procedure where the global ML-acquisition is repeated with decreasing wavelengths

$$\lambda_{j+1} \cong \frac{\lambda_j}{G_d^{1/2}} = \frac{\lambda_1}{(G_d^{1/2})^j} \quad (27b)$$

with λ_1 given by equations 24 or 26. Since the approach behind equation 26 generalizes in a straightforward way to arbitrary N and to other class of problems, e.g. discrete space, continuous time SAMS, and it is also consistent with the quadratic (local) analysis to GAF and DGAF, we assume in the sequel that λ_1 has been determined by Eq. 26.

The sequential procedure stops with the smallest order step $j = J$ (28a)

for which the corresponding mean square performance

$$\sigma_{A_i}^J < \sigma_{A_i} \quad \text{for every } i, \quad (28b)$$

where σ_{A_i} is the desired root mean square performance.

The corresponding wavelength is

$$\lambda_J = \frac{\max_i (\Delta_{M A_i} (M_d^{-1})_{A_i}^{-1/2})}{(G_d^{1/2})^{J-1}} \quad (29a)$$

and

$$\sigma_{A_i}^J = \frac{\max_m (\Delta_{M A_m} (M_d^{-1})_{A_m}^{-1/2})}{(G_d^{1/2})^J} (M_d^{-1})_{A_i} \quad (29b)$$

Let

$$(\Delta_{M A_{m_{\max}}} (M_d^{-1})_{A_{m_{\max}}}^{-1/2}) = \max_m (\Delta_{M A_m} (M_d^{-1})_{A_m}^{-1/2}) \quad (30a)$$

If

$m_{\max} = i$ in equation 29a, we obtain

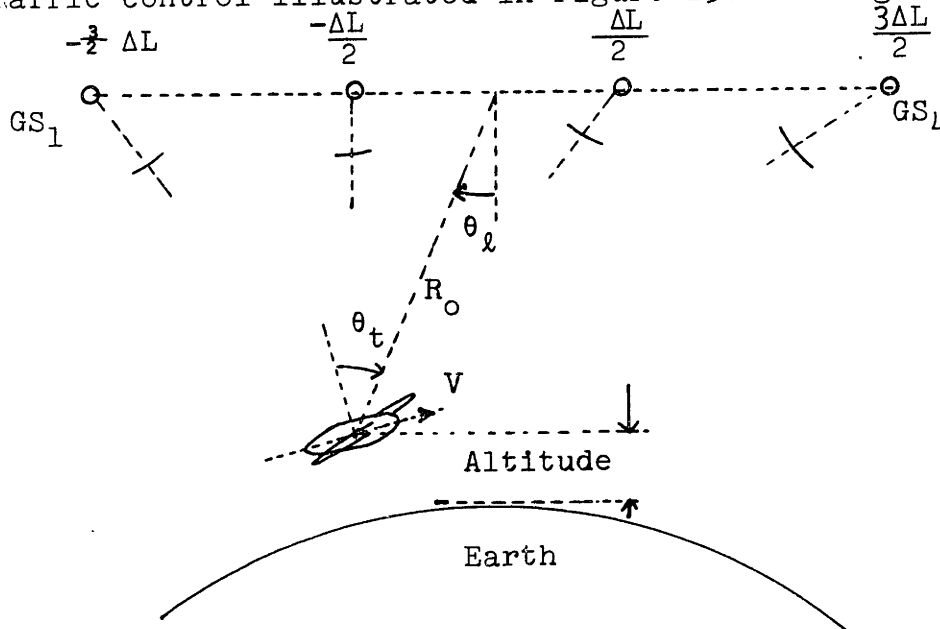
$$\sigma_{A_{m_{\max}}}^J = \frac{(\Delta_{M A_{m_{\max}}} (M_d^{-1})_{A_{m_{\max}}}^{-1/2})}{(G_d^{1/2})^J} \quad (30b)$$

Finally the number J is the smallest integer containing all J^i , where

$$J^i = \frac{\ln \{ [(\Delta_{M A_{m_{\max}}} (M_d^{-1})_{A_{m_{\max}}}^{-1/2}) (M_d^{-1})_{A_i}^{1/2}] \} - \ln \sigma_{A_i}}{\ln(G_d^{1/2})} \quad (30c)$$

3.5 Commercial Avionics Surveillance with Geostationary Satellites

The preceding considerations are applied to the air traffic control illustrated in Figure 25. As argued before



Commercial Avionics Surveillance with Geostationary Satellites
Figure 25

the signals radiated by each geosynchronous satellite are coded for identification purposes and for relaying to the passive users the satellites' ephemeris, necessary for their ultimate geographic position determination. The signals are also modulated by a common set of subcarriers available for refinement of the relative position estimates.

We summarize in Table V the nominal relative parameter values, for the configuration of Figure 25.

Once again we stress that equations 26 to 30 apply not only to the SASS context, but also to SAMS₀ or SAMS.

Remarks:

1) For $N \neq 4$ the rationale behind this sequential global acquisition procedure remains, but the values of λ and λ_{i+1} are not simply determined by equations 26a and 27. If the problem geometry leads to a local type configuration, where the global errors are negligible and the mean square performance is correctly predicted by the Cramer-Rao bounds, Eq. 27 is still valid. When

$$\sigma_{\text{tot}_{A_i}} > \sigma_{\text{CR}_{A_i}}$$

the sequence of λ_j is determined from both, the local and global error components, which can be easily done by graphic means. For large N , when no significant secondary lobes arise in the primary cell Ω_1 , λ_1 should be determined from the dimensions of Ω_1 , see Eq. 13.

2) To avoid ionosphere propagation losses and simplify the implementation, we assume that each satellite radiates a carrier modulated by a set of common subcarriers, with decreasing wavelengths. The passive user refines its resolution, by sequentially processing these subcarriers.

$$R_o \approx 4 \times 10^4 \text{ km}$$

$$\theta_t \approx 30^\circ$$

$$\theta_\ell \approx 15^\circ$$

$$v \approx 2000 \text{ knots} = 10^3 \text{ m/sec (SST)}$$

$$\text{Elementary Observation Time} = \Delta T \approx \frac{1}{2} \text{ sec}$$

$$\text{Surveillance Update Cycle } T \approx 30 \text{ sec for SST;}$$

$$T \approx 90 \text{ sec for subsonic}$$

$$\sigma_v \approx 5 \text{ ft/sec}, \sigma_{R_o} \approx 250 \text{ ft}$$

$$\text{Carrier Frequency} \approx f \approx 1.5 \text{ GHz (L-Band)}$$

$$\text{Satellites interspacing } \Delta L \approx \frac{6000}{3} \text{ km}$$

Nominal Values for Commercial Avionics Surveillance

Table V

3.5.1 Model Considerations

In order to apply the Hybrid Algorithm concept to this navigation problem we assume for the global acquisition step that

H ML 1: The problem fits a discrete space, continuous time SAMS model, i.e.:

i) the source/receiver parameter vector, see Fig. 25,

$$A = \begin{bmatrix} R_o \\ v \\ \sin\theta_t \\ \sin\theta_\ell \end{bmatrix} \quad (31)$$

is unknown, nonrandom,

- ii) the plane follows a constant speed linear path;
- iii) the additive measurement noise is white;
- iv) the narrowband signals originated at the point sources (discrete space) are continuously available in time.

For the linearized phase tracker this model is generalized by substituting the two first points by

H EKB 1:

- 1) The plane follows a nominal constant speed linear path disturbed by random accelerations (Eq. V-7).

3.5.2 ML - Mean Square Performance

For the nominal parameter values of Table V the ratio between the temporal and the spatial diversity

$$\gamma = \frac{X_t}{X_\ell} = \frac{VT/R_o}{L/2R_o} \ll 1 \quad (32)$$

and the root mean square performance for the range R_o and

spatial bearing $\sin\theta_\ell$ are simply given by equations 20a and 20b. However, the cross-coupling plays an important role on the estimation of the aircraft's speed v and temporal bearing $\sin\theta_t$. Adapting the results of Eq. IV-80 and IV-81 for the coupled SAMS, to the discrete spatial baseline satellite configuration of Fig. 25, we obtain for the Cramer-Rao performance

$$\sigma_v \approx G_d^{-1/2} (M_d^{-1})^{1/2} \approx G_d^{-1/2} \frac{\lambda}{2\pi} \frac{v}{R_o} \frac{3\sqrt{3} \cos\theta_t}{\cos\theta_\ell} \frac{1}{X_\ell X_t} \quad (33a)$$

$$\sigma_{\sin\theta_t} \approx G_d^{-1/2} (M_d^{-1})^{1/2} \approx \sigma_v \frac{\sin\theta_t}{v} \quad (33b)$$

where G_d is given by Eq. 17.

3.5.3 ML - System Discussion

We assume the values of Table V (unless otherwise specified). For the signal to noise ratio SNR at the user site we consider as a nominal value

$$\text{SNR} = 0 \text{ dB} \quad (34a)$$

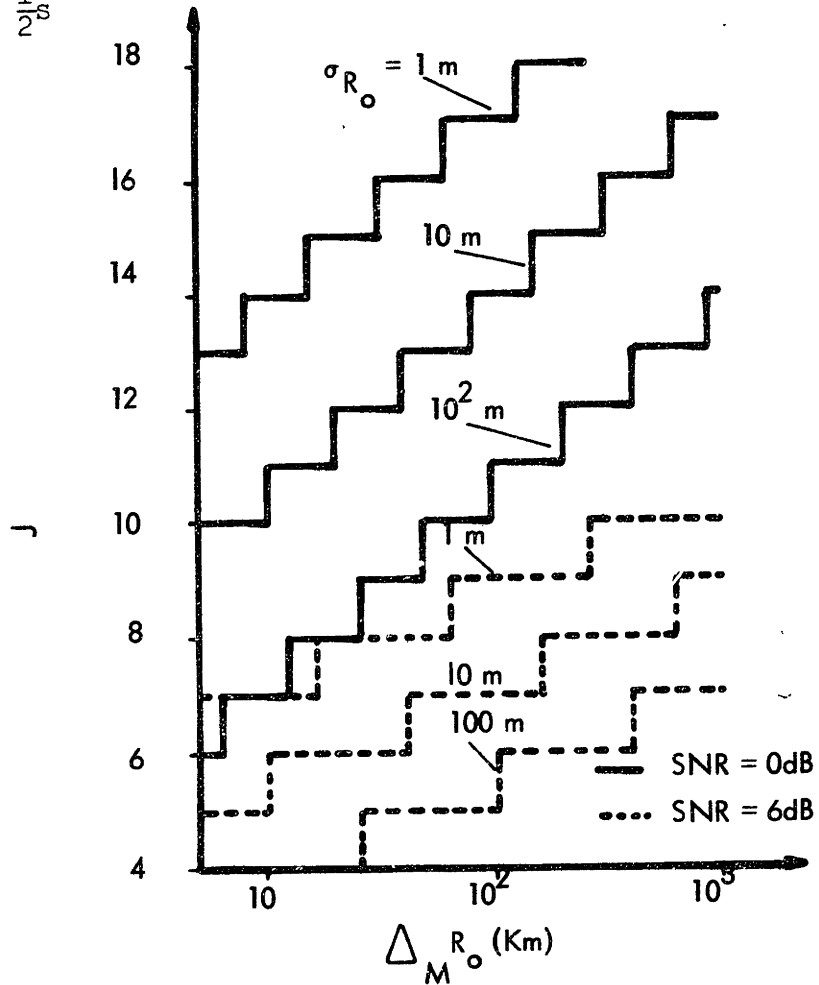
and as comparison value

$$\text{SNR} = 6 \text{ dB} \quad (34b)$$

The total time interval for the range global acquisition is the elementary observation interval ΔT of Table V

$$\Delta T = \frac{1}{2} s$$

(34c)



Number of Updates versus A priori Range Uncertainty

Figure 26

Range Accuracy . Figure 26 studies the total number of steps given by Eq. 30c

$$J \geq J_{R_o} = \frac{\ln(\Delta_M R_o) - \ln \sigma_{R_o}}{\ln(G^{1/2})} \quad (35)$$

necessary to achieve a desired accuracy σ_{R_0} , when the a priori uncertainty is $\Delta_M R_0$. We considered 3 values for σ_{R_0}

$$\sigma_{R_0} = 1\text{m}; 10\text{m}; 10^2\text{m}$$

and the two above indicated SNR values. As an example, we read from the curve that, to go from a relatively large uncertainty

$$\Delta_M R_0 = 10^2 \text{ km} \quad (36a)$$

to a very small final root mean square error

$$\sigma_{R_0} = 10 \text{ m} \quad (36b)$$

with an SNR = 0 dB, requires 14 sequential updates. If the SNR level is increased to 6 dB only 7 steps are necessary. The starting value for λ is, from Eq. 26a

$$\lambda_{R_0}^1 = \Delta_M R_0 (\frac{M^{-1}}{\tilde{d}})^{-1/2} \approx 7750 \text{ m} \quad (36c)$$

and the final value, from Eq. 27b

$$\lambda_{R_0}^{14} \approx \frac{\lambda_{R_0}^1}{(G^{1/2})_d^{13}} \approx \frac{\lambda^1}{2^{13}} \approx 1 \text{ m} \quad (36d)$$

Speed Accuracy

For the example described by Eq. 36 above, we let the a priori speed uncertainty

$$\Delta_M V = 10^2 \text{ m/s} \quad (37a)$$

We obtain from Eq. 33a

$$\left(\frac{M}{\lambda} d^{-1}\right)^{1/2} \frac{1}{V} = \frac{\left(M d^{-1}\right)^{1/2}}{\lambda} = \frac{22.83}{T} \quad (37b)$$

To solve the original uncertainty given by Eq. 37a, the wavelength must be greater than

$$\lambda_V^1 \approx (\Delta_M V) \left(\frac{M}{\lambda} d^{-1}\right)^{-1/2} \approx 4.38T$$

which, for any reasonable T, is much smaller than $\lambda_{R_0}^1$ given by Eq. 36c. The final accuracy is

$$\sigma_V \approx \frac{\lambda}{\sqrt{\text{SNR}}} \left(\frac{M}{\lambda} d^{-1}\right)^{1/2} \frac{1}{V} \approx 8.071 \frac{\lambda}{\sqrt{\text{SNR}}} T^{-3/2} \quad (37c)$$

For

$$\lambda = \frac{13}{\lambda_{R_0}} = 1\text{m} \quad (37d)$$

figure 27 studies the speed accuracy as a function of the acquisition time T_{acq} for two levels of SNR.

If we take

$$T_{\text{acq}} = \Delta T = .5 \text{ sec} \xrightarrow{\text{SNR} = 0\text{dB}} \sigma_V \approx 22.83 \text{ m/s} \quad (37e)$$

while for

$$T_{\text{acq}} = 3\Delta T \xrightarrow{\text{SNR}=0\text{dB}} \sigma_V \approx 4.5 \text{ m/s} \quad (37f)$$

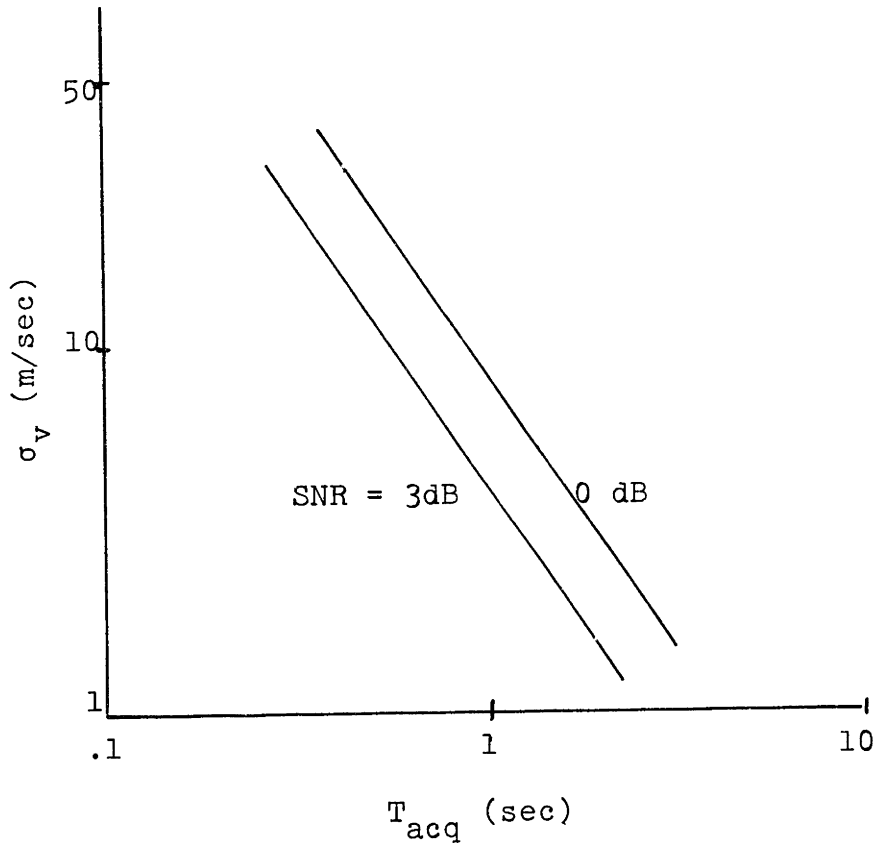


Figure 27

Since the EKB is insensitive to large a priori inaccuracies on the velocity measurements, the range of σ_v of Figure 27 is acceptable for starting the linearized EKB.

Similar considerations could be pursued for the two other parameters.

3.5.4 Extended Kalman Bucy Filter

For the linearized phase tracker, and concentrating the discussion on the range and range rate parameters the steady

state covariance values are, from Eq. V- and V-

$$P_{11} \approx \frac{1}{H_1} (4QH_1)^{1/4} \quad (38a)$$

$$P_{22} \approx \frac{2Q}{(4QH_1)^{1/4}} \quad (38b)$$

For moderate turbulence flight conditions

$$Q \approx \left(\frac{g}{2}\right)^2 \approx 5 \text{ m}^2/\text{sec}^3 \quad (39a)$$

and for

$$\lambda \approx 1\text{m} , \text{ SNR} = 0 \text{ dB} \quad (39b)$$

we obtain

$$P_{11} \approx .1182 \text{ m}; \quad P_{22} = 5.286 \text{ m/s} \quad (39c)$$

The loop bandwidth and the equivalent signal to noise ratio in the bandwidth loop

$$B_L = \frac{3}{8} (4QH_1)^{1/4} \approx 3.546 \quad (39d)$$

$$\alpha \approx \frac{8}{3} \frac{H_1}{(4QH_1)^{1/4}} \approx 22.55 \quad (39e)$$

The average time between cycle skips to occur is

$$T_{\text{skp}} \approx \frac{\pi}{4B_L} e^{2\alpha} \approx 1.4 \times 10^9 \text{ sec} \quad (39f)$$

The results in Eq. 39c and 39f show that the EKB loop performs well within the limitations imposed by the global ML-processor.

Conclusion

We considered two typical navigation problems involving satellites. With orbiting satellites the continuous time formulation of SAMS₀ is particularly suitable.

With geosynchronous satellites we had to adapt the passive tracking results to a discrete space formulation. Although the general principles extend in a straightforward way, the details of the resulting structure depend largely on the number of available satellites, and on ratios of powers of the satellites interspacing ΔL and the wavelength λ . The main issue deals with the ambiguity function periodic structure, and, within each primary cell Ω_1 , with the important secondary lobes which may arise due to aliasing effects.

We presented a sequential updating algorithm, where the wavelength is reduced by a factor equal to the square root of the available signal energy to noise ratio, and which achieves both, the global acquisition, and the desired resolution.

We studied the tradeoffs between the necessary number of updates, the a priori uncertainty, the available signal to noise ratio at the user site, and the desired accuracy, in the context of an SST commercial avionics surveillance ap-

plication, using a constellation of 4 geosynchronous satellites.

The large spatial baseline available allows very accurate final estimates. Starting with a large range a priori uncertainty (100 km), we saw that an accurate estimate ($\sigma_{R_0} \approx 10$ m) could be achieved in 14 steps, with a final wavelength of about 1 m. There is here a tradeoff between computation time and complexity, in that these 14 steps can be processed sequentially in time by a single processor unit, or simultaneously by 14 processor units. We analyzed the EKB performance, and concluded that the linearized performance was within the required accuracies, and that the cycle skip phenomena will not be an issue, unless the EKB is used with larger wavelengths.

4. Monte-Carlo Simulation Results

We report here the results of simulating the ML-processor in the context of the passive positioning with underwater acoustics discussed in Section 2 . The linearized EKB structure has been analyzed in [Mo73a], and the results reported also in [Mo73b]. See Fig. V-7 for some illustrative runs.

There are three main points concerning the Monte Carlo simulations. The first is the actual implementation on a discrete environment (computer) of the simulation of a stochastic problem, with the "discretized" version of a "white" noise process and the design of (stochastic) maximization routines. The second relates to the statistical confidence associated with the simulation results themselves, with a tradeoff between the finiteness of the computation time available, and the number of samples taken in the ensemble average. The third relates to the closeness of the simulation results to the predicted by the theoretical analysis, with the determination of regions where both converge (in a statistical sense).

We discuss briefly each one of these points.

4.1 Algorithms Implementation

We implemented the two-step algorithm mechanizing the ML-estimation receiver for both the SASS and the SAMS₀ contexts.

Due to the discrete environment the noise levels were normalized by the (space and time) sampling intervals, see for example [Mo73a]. If

ΔL = (array) sampling interval

ΔT = time sampling interval

we obtain

$$(\text{SNR})_d = \frac{2P}{\frac{N_0}{\Delta L \Delta T}} = (\text{SNR})_c \Delta L \Delta T$$

where the index d stands for discrete and c for continuous. The maximization algorithm consisted essentially of a search procedure, superimposing grids of varying overall and elementary cell size. This, bounds the accuracy to the size of the smallest elementary cell used (quantization type errors), but avoids the implementation of costlier maximization routines.

Due to the limited computer time availability, we restricted ourselves to testing the local results on the mean square performance, i.e. to the statistical test of the Cramer-Rao bounds by bounding the a priori region of uncertainty so that

$$\sigma_{gl}^2 \ll \sigma_{loc}^2 \rightarrow \sigma_{tot}^2 \approx \sigma_{loc}^2$$

4.2 Confidence Intervals Associated with Statistical Averages

The simulation results had as main objectives to compare the performance predicted by the analysis, with the one computed by statistical averaging the simulated runs.

Due to the stochastic nature of the problem, the performance measures computed by the Monte Carlo runs are random variables themselves. For example, for a random variable with known mean and variance σ_x^2 , the variance computed from the ensemble averaging

$$\hat{\sigma}_x^2 = \frac{1}{N} \sum_{i=1}^N (x_i - \bar{x})^2$$

is, for all practical purposes, an unbiased estimate of σ_x^2 , normally distributed with mean σ_x^2 and variance $\frac{2\sigma_x^2}{N}$.

We have then

$$\Pr \{ (1-\alpha) \sigma_x^2 < \hat{\sigma}_x^2 < (1+\alpha) \sigma_x^2 \} \approx \text{erf} \left(\frac{\alpha}{2} \sqrt{N} \right)$$

where

$$\text{erf}(X) = \frac{2}{\sqrt{\pi}} \int_0^X \exp(-y^2) dy$$

α is a positive constant.

We are particularly interested in the 3σ confidence interval ($\alpha=2$)

4.3 Simulation Results

We simulated one geometry for each problem, for several values of the signal to noise ratio. Table VI summarizes the important data.

$$\lambda = 50 \text{ ft}; R_o = 6 \times 10^3 \text{ ft}$$
$$\sigma_b^2 = 1; \theta_l = 0$$

SASS	SAMS _o
$\Delta L = \frac{\lambda}{2} = 25 \text{ ft}$	$V = 30 \text{ ft/sec}$
$L = 3980 \text{ ft}$	$\theta_t = -15^\circ$
$\Delta T = T = 1 \text{ sec}$	$\Delta L = L = 50 \text{ ft}$
$X_l = .331$	$\Delta T = 5\text{s}, NT = 24$
	$X_t = .287$

Simulated Configuration Parameters

Table VI

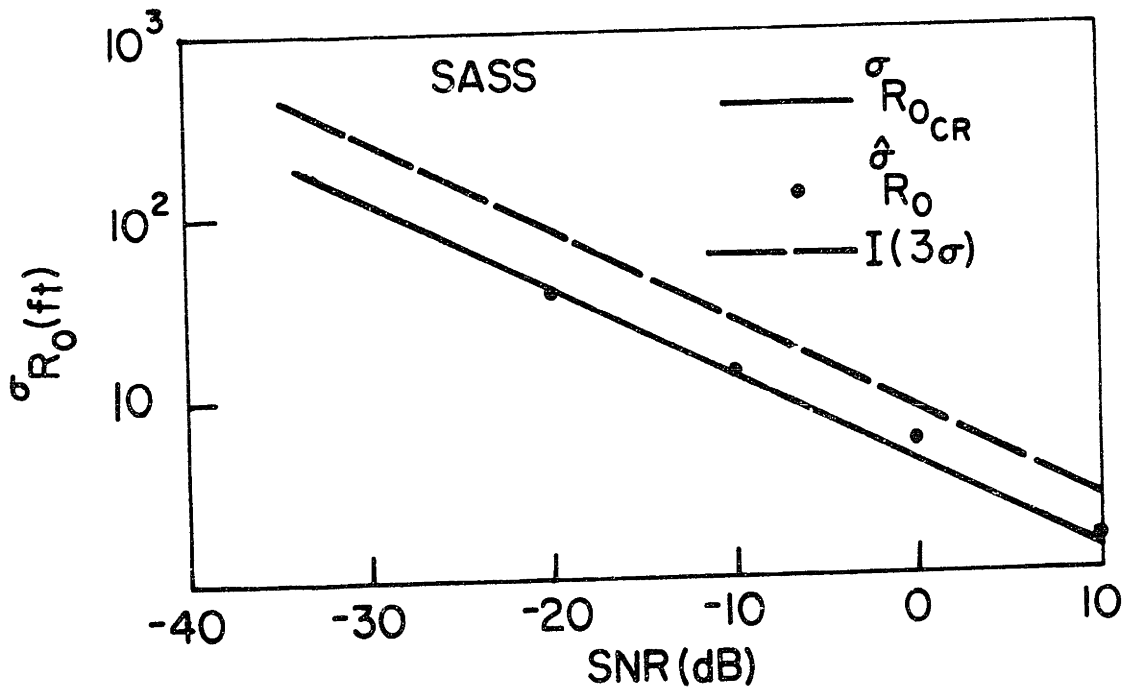
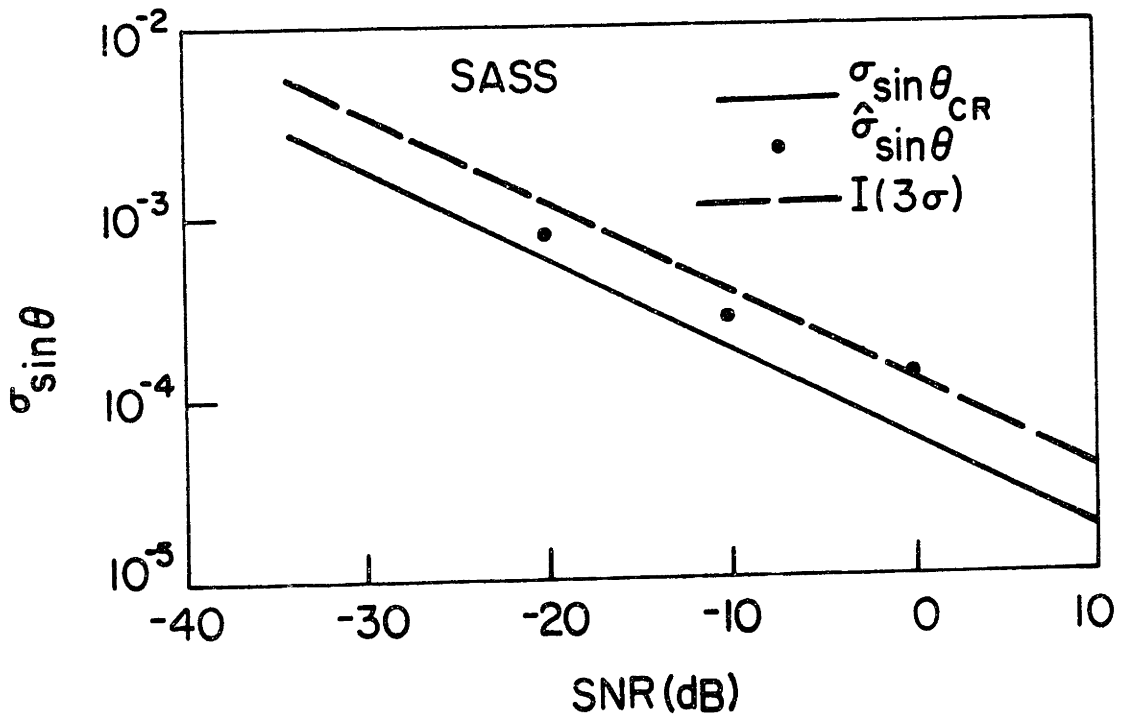
Figure 28 represents the SASS simulation results for 15 Monte Carlo runs. We distinguish a threshold region below

$$\text{SNR} = -30\text{dB}$$

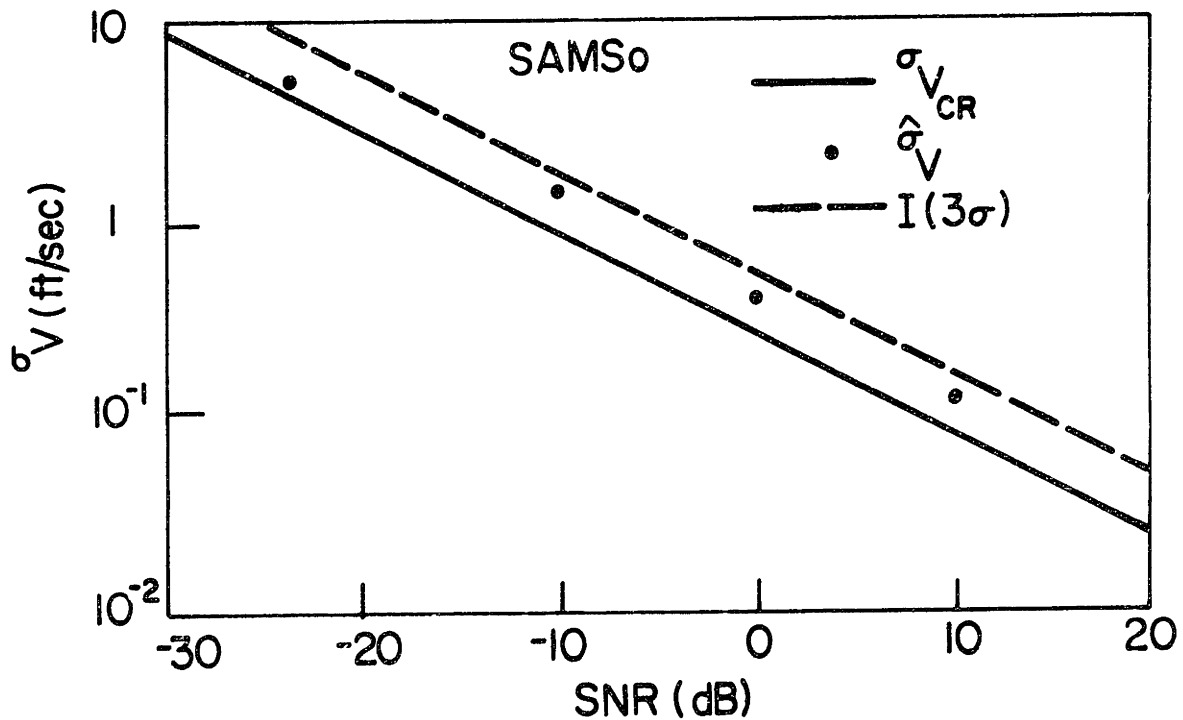
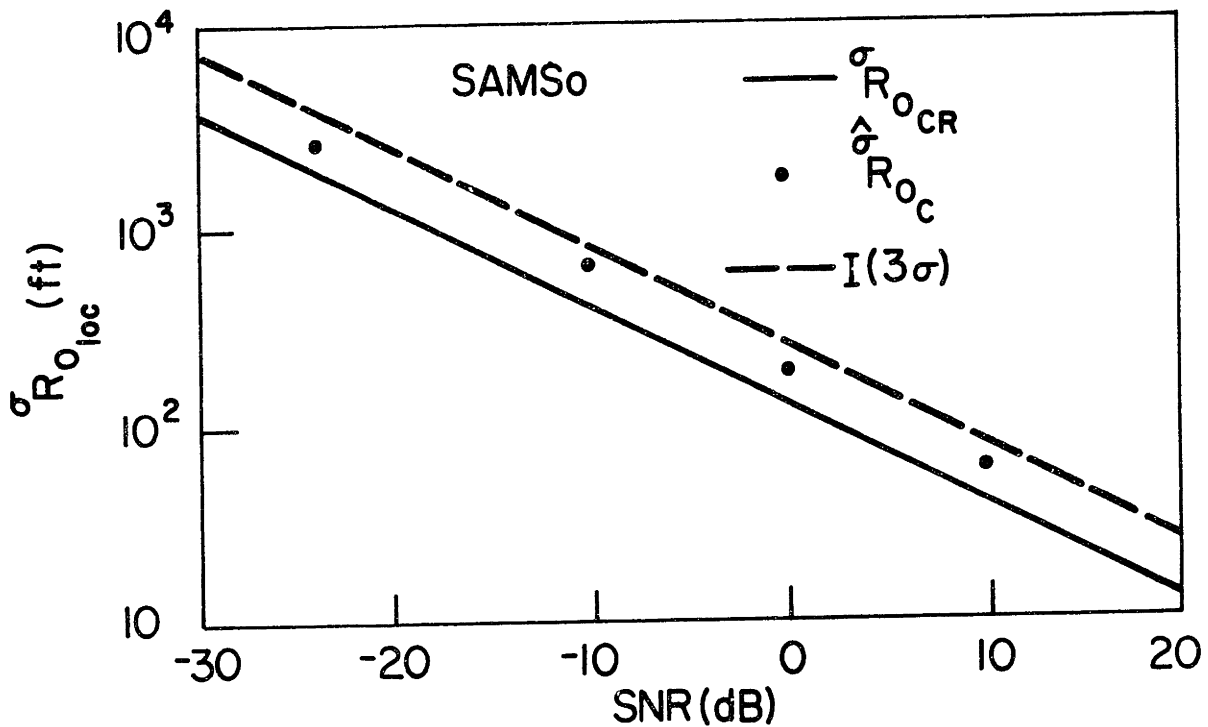
Above this value the statistical results are within a 3σ confidence interval $I(3\sigma)$ of the Cramer-Rao bounds. The point for

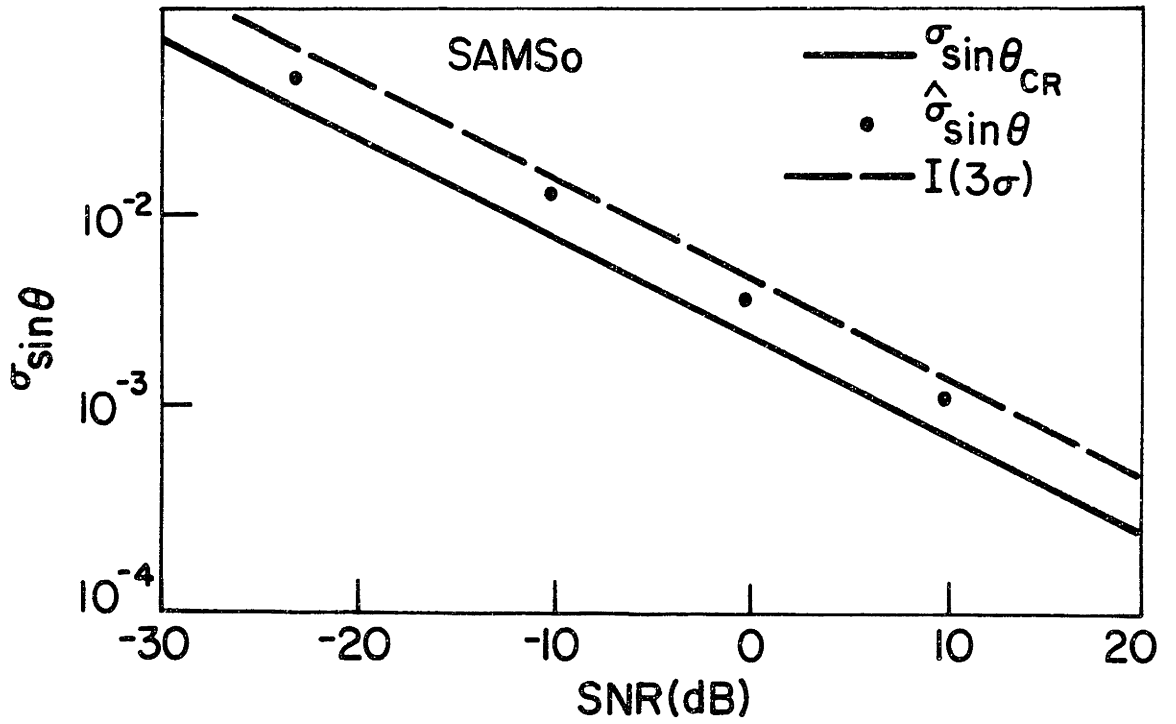
$$\text{SNR} = -34 \text{ dB}$$

SASS - Simulation Results
 Fig. 28



SAMS_o - Simulation Results
 Fig. 29





SAMSo Simulation Results
 Fig. 29 (cont.)

is about one order of magnitude apart from the Cramer-Rao curve.

Figure 29 presents the SAMS₀ simulation results, averaged over 15 runs, for varying SNR. The curves show that all the statistically computed standard deviations are within the 3σ confidence interval I(3σ) of the theoretically computed Cramer-Rao standard deviation.

As a final comment on these simulation results, we note that when the Rayleigh amplitude $|\tilde{b}|$ of the complex multiplicative Rayleigh parameter \tilde{b} is kept constant (unknown) and equal to

$$|\tilde{b}|^2 = 2\sigma_b^2$$

the agreement between the theoretical and the practical results is even closer than the one indicated by Figures 28 and 29. The reason is that, for \tilde{b} a zero mean complex Gaussian random variable, there are runs for which $|\tilde{b}|$ is very small, which, regardless of SNR, deteriorates the statistical performance computed via the Monte Carlo simulations.

CHAPTER VII
CONCLUSIONS EXTENSIONS

1. Conclusions

In this thesis we have considered the passive tracking problem with narrowband and linear constraints.

In Part I (Chapters I to IV) we developed a simple model, designed optimal and suboptimal receivers, and analyzed their structure and associated errors. In summary, the main contributions of the research in these chapters are:

- 1) A simple model which encompasses the fundamental global and local characteristics of the passive tracking problem, and which explicitly exhibits the symmetry between the space and time aspects.
- 2) A systematic treatment of the passive global identifiability of the parameters defining the relative source/receiver geometry. We emphasized the passive global range observability, as obtained from the higher order phase modulations induced on the radiated signal's structure by the spatial and/or temporal diversity.
- 3) Analysis of the global ambiguity structure associated with nonhomogeneous passive narrowband tracking, with bounds on its asymptotic behavior.

We carried out this study using both analytical and graphical techniques.

in more complex receivers, represents a nontrivial improvement on the global identifiability of the source parameters. The order of the estimation problem is reduced with respect to the decoupled situation, requiring only measurements of second order effects on both space and time domains (Fresnel Zone). Once again, by using Taylor series techniques, we arrived at intuitively satisfying analytical expressions, quantifying the mean square spread of the main lobe, and the (local and global) mean square performance bounds (section IV-2, and Appendix D).

In Part II (Chapters V and VI) we presented a practical hybrid receiver for passive tracking, and applied the preceding theory and results to positioning and navigation problems. The main results obtained are:

- 1) A practical hybrid algorithm achieving a compromise between the continuous global estimation of the relative source/receiver geometry, and complexity of implementation.

Global acquisition is accomplished by an ML-processor, requiring a multidimensional stochastic maximization. The local dynamics are recursively tracked by a linearized filter, e.g. an Extended Kalman-Bucy filter.

- 2) Sensitivity analysis of each receiver's block to the geometry, statistical parameters, and modeling assumptions, leading to four characteristic modes for the hybrid algorithm's behavior:

i) For high signal to noise (SNR) applications, the errors associated with global acquisition dominate the hybrid algorithm's behavior, and the results of part I predict well the overall performance. In practice, due to random perturbations, the source deviates from the assumed nominal linear constant path, imposing a maximum acquisition time, after which the error induced are larger than those due to additive measurement noise (see section V-4).

ii) For low SNR (the breakdown being approximately at an equivalent to noise ratio of 0 dB), the errors associated with the EKB nonlinear behavior (cycle skipping phenomena) may significantly deteriorate the EKB performance, with no tracking being possible.

3) An illustrative design of practical passive systems for use in precision landing air traffic control, underwater acoustic positioning, and navigation with orbiting and geostationary satellites.

The precision landing problem (section VI-1) is typically an high SNR application (about 40 dB available receiver's site), with the global acquisition imposing the harder limitations on the hybrid algorithm performance. Flight turbulence conditions determine the maximum acquisition time, and the corresponding ML-mean square error.

The underwater acoustic problem (section VI-2) is highly sensitive to the geometry and statistical parameters.

The ambiguity structure for the distant observer was extensively considered. The range phase was approximated by a truncated n th order Taylor series, and the resulting ambiguity function associated with generalized n th order sinc functions (sections II-3, III-3, and Appendix A). We bounded the asymptotic behavior of these approximate structures, e.g. for the generalized 3th order sinc, the bound was related to an Airy function.

By application of the Method of Stationary Phase, we showed that the general ambiguity function is negligible for large parameter errors. Coupling the analytical studies to graphical displays, we concluded that GAF presents a quadratic ellipsoidal main lobe, with negligible secondary structure (see Chapter III, end of section 3.3).

4) Global and local mean square error bounds. Graphical displays, exploring the effects of the geometry and of the statistical parameters on the mean square performance, were presented.

We considered the distant and close observer situations. We derived, via Taylor series, simple, intuitively pleasing approximate expressions, and showed how they compare to the exact bounds.

Depending solely on the geometry, and in particular, independently of the signal to noise ratio, we concluded that the two step practical implementation of the ML-receiver

exhibits two distinct types of performance behavior:

- i) a local region, where the mean square performance is well approximated by the local bounds and determined by the sharpness and dimensions of the ambiguity structure main lobe; and
- ii) a global region, where decision errors induce, on the average, large inaccuracies and the performance is given by the global bounds. In practice, the latter may be circumvented by means of independent measurements (see sections II-4.3, and III-4.5).
- 5) Study of the space/time factorability and coupling issues in passive tracking.

We analyzed in detail the distant observer situation, and concluded :

- i) When the temporal diversity (source travel) dominates the spatial baseline, the ambiguity structure factors. The spatial bearing angle is observed from the available spatial diversity, and the remaining parameters from the temporally induced modulations. The decoupled receiver consists, intuitively, of a beam steering (spatial operation), and a (bank of) matched filter(s), over a 3-dimensional parameter space (temporal processing). We derived an expression for the total number of steering operations, and by putting the problem in the perspective of previously obtained results, analyzed its mean square performance (section IV-1).
- ii) When the temporal and spatial baselines are comparable, the receiver is not separable. This coupling, although resulting

For higher SNR and certain geometries tracking is possible, with the root mean square path variations determining the maximum allowable performance. For lower SNR, the hybrid algorithm reduces to the acquisition step, with the time updating being nonrecursively accomplished by the ML-processor.

Passive navigation with satellites (section VI-3) presents practical situations, where a large baseline is synthesized (either by an orbiting or geostationary satellites) leading to geometries where accurate ranging is possible; see the tradeoffs and attainable accuracies for the ship navigation and the SST commercial avionics surveillance examples (sections VI-3-2 and VI-3-5).

- 4) Analysis of the sampling effects on the nonhomogeneous second order (Fresnel zone) ambiguity structure.
- 5) A sequential procedure for resolving the ambiguities resulting from discretization effects associated with the geostationary satellite passive navigation.
- 6) Monte Carlo simulation studies (sections V-3 and VI-4), demonstrating the existence of regions of statistical convergence between the theoretical and the simulated results.

2. Extensions

The generalizations and extensions of the present work relate basically to the modelling assumptions and to the receiver's complexity. The following constitutes a selected list:

1) Signal's Assumptions: A narrow band source signature was assumed. In many practical situations a better model is a combination of broadband and narrowband components, e.g. [Pa 74a], while in others the signals are broadband. A forthcoming thesis [Met 75] deals with the latter situations. The results herein may be extended in a straightforward way to the case of a long observation interval, compared to the signal and noise correlation times, and to the travel time of the wavefield across the array. The processes admit a Fourier representation with uncorrelated coefficients, and the problem reduces to a multitone type, where the relative source/receiver geometric parameters enter, as in the singletone model, through phase modulations.

Using the results of [Ban 71], the Fisher information Matrix for the multitone problem is given by

$$J = G \underline{M} \quad 1$$

with

$$G = \left\{ \sum_{k=1}^K \frac{[S_s(w_k) / S_n(w_k)]^2}{1 + G(w_k) \frac{S_s(w_k)}{S_n(w_k)}} \left(\frac{2\pi}{\lambda_k} \right)^2 \right\}$$

Where $S_s(w_k)$, $S_n(w_k)$ are the power spectra of the signal and noise processes at w_k , $G(w_k)$ is the array gain, \underline{M} the mean square spread matrix (normalized by the wavenumber $2\pi/\lambda_k$) as defined in Appendix B. The matrix J , given by equation 1, is the product of a gain, G , incorporating the new signal modelling assumptions (multitone); and of the mean square

spread matrix, reflecting the geometric aspects, which remains the same, as in the singletone situation studied in this thesis.

2) Noise Assumptions: We considered unstructured additive measurement noises, i.e., spatially and temporally white -Gaussian. When the measurement exhibits a significant structure it may be combatted by high resolution array processing methods, e.g. [Bag 73]. It will, however, involve a generalization of these procedures to nonhomogeneous wavefields.

3) Dynamics and Geometry: We assumed nominal linear motions and linear array structures. The effects of nonlinear motions and/or nonlinear receiving structures can be analysed using the approach considered here, by incorporating the new geometry on the range phase function.

4) Higher Order Receivers: The Hybrid Algorithm developed in Chapter V is decoupled in two blocks. From the illustrative studies carried out in Chapter VI, we anticipate that in many practical applications the sensitivity of the global step to the path perturbations constitutes a limiting factor on the Hybrid Algorithm's mean square performance. Higher order receivers, designed using the more sophisticated techniques of nonlinear waveform estimation theory [Bu 72b], may then be necessary. The problems with these techniques relate not only to the added conceptual difficulties, but mainly to the large associated computational effort, [Bu 72b].

BIBLIOGRAPHY

- Abr65 Abramowitz and Stegun, "Handbook of Mathematical Functions", Dover, N.Y., 1965.
- Ach72 Acheson, D.T., "Radiosonde Tracking with Loran-C, Omega and other Transmitters", 2nd Sympos. on Meteor. Obs. and Instr., A.M.S., S.Diego, Calif., March 27-30, 1972.
- Bag73 Baggeroer, A.B., "Space/Time Random Processes and Optimum Array Processing", NUC Report, (Preliminary Copy), 1973.
- Bag74 Baggeroer, A.B., "High Resolution Velocity/Depth Spectra Estimation for Seismic Profiling", IEEE Int. Conf. on Eng. in the Ocean Environm., Part II, 1974.
- Ban71 Bangs, W.J., "Array Processing with Generalized Beam-Formers", Ph.D. Th., Yale Univ., Connecticut, Sept., 1971.
- Ban73 Bangs, W.J., and P.M. Schultheiss, "Space-Time Processing for Optimal Parameter Estimation", in "Signal Processing", edited by J.W.R. Griffiths, P.L. Stocklin and C. van Schooneveld, Academic Press, 1973.
- Bas72 Bass, R.W., R.E. Mortensen, V.D. Norum, B. Shawaf, H.W. Sorensen, "ASW Target Motion and Measurement Models", CSA, Tech Rpt. 72-024-01, Sept. 1972.
- Bec63 Beckmann and Spizzichino, "Scattering of Electromagnetic Waves from Rough Surfaces", Pergamon, 1963.
- Beu72 Beukers, J.M., "Integrated Upper and Meteorological Sounding Systems", 2nd Symposium on Meteorological Observations and Instrumentation, A.M.S., S. Diego, Calif., March 27-30, 1972.
- Beu74 Beukers, J.M., "A Review and Applications of VLF and LF Transmissions for Navigation and Tracking", Navigation: Journal of the Inst. of Navigation, Vol. 21, No. 2, Summer 1974.

- Bu72a Bucy, R.S., "Building and Evaluating Nonlinear Filters", Proc. Symp. on Appl. Math., Stoch. Diff. Eqs., A.M.S., Ap. 1972.
- Bu72b Bucy, R.S., C. Hecht, and K.D. Senne, "An Engineer's Guide to Building Nonlinear Filters", Frank J. Seiler Research Lab., Tech. Rept. SRL-TR-72-0004, Air Force Syst. Comm., May 1972 (2 vols.) DDC nos. AD746921 and AD746922.
- Cha 66 Charles, F.J., and W.C. Lindsey, "Some Analytical and Experimental Phase-Locked Loop Results for Low Signal to Noise Ratios", Proceedings of the IEEE, vol. 54, no.9, 1152-1166, Sept. 1966.
- Cou73 Counselman, C., "Radio Interferometry Course Notes", M.I.T. Dept. of Earth Sciences, Fall Term, 1973.
- Eas72 Easton, R.L., "The Role of Time/Frequency in Navy Navigation Satellites", IEEE Proceedings, vol. 60, no. 5, pp. 557-563, May 1972.
- Ehr72 Ehrlich, E., "The Role of Time/Frequency in Satellite Position Determination Systems", IEEE Proceedings, vol. 60, no.5, pp.564-571, May 1972.
- Fio70 Fiore, A.E., "Earth Satellite Systems for Marine and Transoceanic Air Navigation and Traffic Control", Navigation: Journal of the Institute of Navigation, Vol. 17, no.3, Fall 1970.
- Goo65 Goodman, "Fourier Optics", McGraw Hill, 1965.
- Gra65 Gradshtey and Ryzhik, "Table of Integrals, Series And Products", Academic Press, 1965.
- Hin72 Hinteregger, H.F., "Geodetic and Astronomic Applications of Very Long Baseline Interferometry", Ph.D. Th., Dept. of E.E., M.I.T., June 1972, Cambridge, Mass.
- IEE73 IEEE Proceedings, "Special Issue on Radio and Radar Astronomy", Vol. 61, no.9, p.1169-1376, Sept. 1973.
- IEE74 IEEE Proceedings, "Special Issue on Rays and Beams", Vol. 62, no. 11, pp.1409-1618, Nov. 1974.
- IEE75 IEEE Transactions on Geoscience Electronics" Special Issue on Data Collection from Multiple Earth Platforms", Vol.GE-13, no. 1, Jan. 1975.

- Kay69 Kayton, M. and W.R. Fried, Eds. "Avionics Navigation Systems", New York, Wiley, 1969.
- Kel60 Kelly, E.J., I.S. Reed, and W.L. Root, "The Detection of Radar Echoes in Noise, Part I and II", J. SIAM, 8, 1960.
- Kel61 Kelly, E.J., "The Radar Measurement of Range, Velocity, and Acceleration", IRE Transactions Mil. Electr., MIL-E, 51-57, Ap, 1961.
- Kel65 Kelly, E.J. and R.P. Wishner, "Matched-Filter Theory for High-velocity Targets", IEEE Trans. Mil. Elect., MIL-9, 56-64, Jan. 1965.
- Kol68 Kolb, R.C., and F.H. Hollister, "Bearings Only Target Motion Estimates", U.S. Naval Elect. Lab. Center, 1968.
- Lin72 Lindsey, W.C., "Synchronization Systems in Communication and Control", Prentice Hall, Inc., Englewood Cliffs, New Jersey, 1972.
- Lin73 Lindsey, W.C., and M.K. Simon, "Telecommunication Systems Engineering", Prentice Hall, Inc., Englewood Cliffs, New Jersey, 1973.
- Mac69 MacDonald, V.H. and P.M. Schultheiss, "Optimum Passive Bearing Measurement in a Spatially Incoherent Noise Environment", JASA, Vol. 46, no. 1, (Part I), 1969, pp. 37-43.
- McD73 McDonald, K.D., "A Survey of Satellite-Based Systems for Navigation, Position Surveillance, Traffic Control and Collision Avoidance", Navigation: Journal of the Institute of Navigation, Vol. 20, no. 4, Winter, 1973-74.
- Met75 Metzger, L. Ph.D. Thesis, Dept. of Elect. Eng. and Compt. Sci., MIT, Sept. 1975, Cambridge, Mass.
- Mid65 Middleton, D. and H.L. Groginsky, "Detection of Random Signals by Receivers with Distributed Elements: Optimum Receiver Structures for Normal Signals and Noise Fields", JASA, Vol. 38, pp. 727-737, Nov., 1965.
- Mo73a Moura, J.M.F., "Estimation of the Dynamics of a Moving Source by an Integrated Spatial and Temporal Processing", S.M. Thesis, 1973, Dept. of E.E., M.I.T., Cambridge, Mass.

- Mo73b Moura, J.M.F., H.L. Van Trees, A.B. Baggeroer, "Space/Time Tracking by a Passive Observer", 4th Symposium on Nonlinear Estim. Theory and its Appl., S. Diego, Calif., Sept. 1973.
- Pap67 Papoulis, "Systems and Transforms with Applications in Optics", McGraw-Hill, 1967.
- Pa74a Pasupathy, S. and P.M. Schueltheiss, "Passive Detection of Gaussian Signals with Narrowband and Broadband Components", JASA, Vol. 56, no. 3, Sept. 1974.
- Pa74b Pasupathy, S. and A.N. Venetsanopoulos, "Optimum Active Array Processing Structure and Space/Time Factorability", IEEE Trans. on Aerospace and Electronics Systems, Vol. AES-10, no. 6, pp. 770-778, Nov. 1974.
- Pie58 Pierce, J.N., "Theoretical Diversity Improvement in Frequency-Shift Keying", Proc. IRE, 46, 903-910, May 1958.
- Por73 Porter, R.P., R.C. Spindel, and R.J. Jaffee, "CW Beacon System for Hydrophone Motion Determination", JASA, Vol. 53, no. 6, 1973.
- Rog70 Rogers, A.E.E., "Very Long Baseline-Interferometry with Large Effective Bandwidth for Phase-Delay Measurements", Radio Sci., Vol. 5, pp.1239-1248, Oct. 1970.
- Row67 Rowbotham, J.R., and R.W. Sanneman, "Random Characteristics of the Type II Phase Locked Loop", IEEE Trans. on Aerospace and Electr. Syst., Vol. AES-3, no.4, p. 604-612, July 1967.
- Spi74 Spindel, R.C. and R.P. Porter, "Precision Tracking Systems for Sonobuoys", IEEE Int. Conf. on Eng. in the Ocean Environment, Vol. II, 1974.
- Sus64 Sussman, S.M., "Simplified Relations for Bit and Character Error Probabilities for M-ary Transmission over Rayleigh Fading Channels", IEEE Trans. Commun. Tech., COM-12, no. 4 (Dec. 1964).
- Tan69 Taner, M.T., Koehler, F., "Velocity Spectra-Digital Computer Derivation and Applications of Velocity Function", Geophysics, Vol. 34, no. 6, Dec. 1969, pp. 859-881.

- Urk62 Urkowitz, H., C.A. Hauer, and J.F. Koval, "Generalized Resolution in Radar Systems", Proc. IRE, Vol. 50, pp. 2093-2105, Oct. 1962.
- Van68 Van Trees, H.L., "Detection, Estimation and Modulation Theory: Part I", John Wiley and Sons, N.Y., 1968.
- Va71a Van Trees, H.L., "Detection, Estimation and Modulation Theory: Part II", John Wiley and Sons, N.Y., 1971.
- Va71b Van Trees, H.L., "Detection, Estimation and Modulation Theory: Part III", John Wiley and Sons, N.Y., 1971.
- Van75 Van Trees, H.L., and A.B. Baggeroer, "Multidimensional and Multivariable Processes", John Wiley and Sons, 1975.
- Vit66 Viterbi, A., "Principle of Coherent Communication", McGraw Hill, N.Y., 1966.
- Wes72 Westerfield, E.E., "Determination of Position of a Drifting Buoy by Means of the Navy Navigation Satellite System", IEEE Conf. on Eng. in the Ocean Environment, pp. 443-446, 1972.
- Woo55 Woodward, P.M., "Probability and Information Theory, with Applications to Radar", McGraw-Hill, N.Y., 1955.

Appendix A

Generalized Ambiguity Function

1. Introduction

As discussed in chapter II the Generalized Ambiguity Function (GAF) for the narrowband passive problem is given by

$$\phi(A, \bar{A}) = |\psi(A, \bar{A})|^2 \quad 1$$

where $\psi(A, \bar{A})$ is the signal autocorrelation function

$$\psi(A, \bar{A}) = \frac{1}{2\epsilon} \int_{-\epsilon}^{\epsilon} dx \exp\left[j \frac{2\pi}{\lambda} \Delta R(x, A, \bar{A}) \right] \quad 2$$

With SASS or MASS the parameter vector is two-dimensional

$$A = \begin{bmatrix} R_o \\ \sin\theta_o \end{bmatrix} \quad 3$$

while for SAMS_o

$$A = \begin{bmatrix} R_o \\ v \\ \sin\theta_o \end{bmatrix} \quad 4$$

is 3 dimensional, since we further estimate the relative source/observer speed v .

The analysis for the two dimensional SASS or MASS parallels the one for SAMS₀ and can be obtained as a special case by assuming

$$v = \bar{v} \tag{5}$$

in the final results. In order to reduce to a minimum the unnecessary details, we concentrate the discussion on the more general SAMS₀ configurations of chapter III. In the main text, chapters II and III we specialize and discuss the implications of the results of this appendix.

Since we deal here with SAMS₀ the spatial domain is

$$x = vt \tag{6}$$

and we rewrite the signal auto-correlation as

$$\psi(A, \bar{A}) = \frac{1}{T} \int_{-\frac{T}{2}}^{\frac{T}{2}} dt \exp \left[j \frac{2\pi}{\lambda} \Delta R(t, A, \bar{A}) \right] \tag{7}$$

with the phase difference

$$\Delta R(t, A, \bar{A}) = [R_0^2 + (vt)^2 - 2(vt)R_0 \sin\theta]^{1/2} - [R_0^2 + (\bar{v}t)^2 - 2(\bar{v}t)\bar{R}_0 \overline{\sin\theta_0}]^{1/2} \tag{8}$$

The analysis of GAF is pursued by steps. First we consider polynomial approximations to the phase difference and study the approximate structure of GAF so obtained. Secondly we return to the general expression of GAF and concentrate on presenting bounds on the asymptotic behavior of the function.

2. Polynomial Approximation

The range phase difference is approximated herein by finite degree polynomials, obtained by truncation of Taylor Series expansions. We have

$$\frac{2\pi}{\lambda} \Delta R(t, A, \bar{A}) \approx \sum_{i=0}^n \Delta_i t^i, \quad t \in \left[-\frac{T}{2}, \frac{T}{2}\right] \quad 9$$

where

$$\Delta_i \triangleq \frac{1}{i!} \frac{2\pi}{\lambda} \Delta R_o^{(i)} = \frac{1}{i!} \frac{2\pi}{\lambda} \left. \frac{d^i}{dt^i} [R(t, A) - R(t, \bar{A})] \right|_{t=0} \quad 10$$

We study subsequently a linearized, a second order and a third order polynomial expansion.

2.1 Linearized Analysis

Linearizing the phase difference

$$\Delta R(t, A, \bar{A}) \approx \Delta R_o - \Delta(v \sin \theta) t \quad 11$$

where

$$\Delta R_o = R_o - \bar{R}_o \quad 12$$

$$\Delta(v \sin \theta) = v \sin \theta - \bar{v} \overline{\sin \theta} \quad 13$$

This approximation is valid whenever

$$\frac{\Delta \dot{R}}{\Delta \ddot{R}} = \frac{\Delta(v \sin \theta)}{\Delta\left(\frac{v^2 \cos^2 \theta}{R_o}\right)} \gg \frac{T}{2} \quad 14$$

i.e., when the Doppler mismatch $\Delta \dot{R}$ is much greater than the error $\Delta \ddot{R} \frac{T}{2}$ induced in the Doppler by the range acceleration mismatch. This may happen either because T is small (short observation interval) or $\Delta \ddot{R}$ is small, i.e., we are analyzing the ambiguity structure in the neighborhood of the Doppler-parameter axis.

The ambiguity function is approximately given by

$$\phi(A, \bar{A}) \cong \text{sinc}^2 \left[\frac{2\pi}{\lambda} \Delta(v \sin \theta) \frac{T}{2} \right] \Delta \left(\frac{\sin \left[\frac{2\pi}{\lambda} \Delta(v \sin \theta) \frac{T}{2} \right]}{\frac{2\pi}{\lambda} \Delta(v \sin \theta) \frac{T}{2}} \right)^2 \quad 15$$

For a graphical representation see Figure II-9. The zeroes occur at

$$\Delta(v \sin \theta) = k \frac{\lambda}{T} \quad k = \pm 1, \pm 2, \dots \quad 16$$

and the maxima at

$$\Delta(v\sin\theta) = 0 \quad 17$$

and

$$\Delta(v\sin\theta) = \pm(k + \frac{1}{2}) \frac{\lambda}{T} \quad k=1,2,3,\dots \quad 18$$

The maxima of sinc^2 decrease monotonically as we depart from the origin. The relation between absolute maximum (at the origin) and the second relative maximum is

$$\frac{1}{(\frac{1}{3} \frac{2}{\pi})^2} \approx 22.5 \quad 19$$

i.e., the second maximum is reduced to about 4.5% of the value at the origin. We remark that this relation is independent of the specific values of the parameters, and is in fact an intrinsic relation of the sinc function.

2.2 Quadratic Analysis

The phase variation is approximated by the quadratic expansion

$$\Delta R(t, A, \bar{A}) \approx \Delta R_0 - \Delta(v\sin\theta)t + \Delta\left(\frac{v^2 \cos^2 \theta_0}{R_0}\right) \frac{t^2}{2} \quad 20a$$

where besides equations 12 and 13 we have

$$\Delta\left(\frac{v^2 \cos^2 \theta_0}{R_0}\right) = \frac{v^2 \cos^2 \theta_0}{R_0} - \frac{\bar{v}^2 (1 - \sin^2 \theta)}{\bar{R}_0} \quad 20b$$

This approximation is valid in the region

$$\frac{\ddot{\Delta R}}{\Delta \ddot{R}} = \frac{\Delta\left(\frac{v^2 \cos^2 \theta_0}{R_0}\right)}{\Delta\left(\frac{3v^2 \cos^2 \theta}{R_0} \frac{v \sin \theta}{R_0}\right)} \gg \frac{T}{3} \quad 20c$$

i.e., either whenever T is small, but not so small that relation 14 holds, or ΔR is small (the ambiguity structure is being analyzed in a neighborhood of the $\Delta \dot{R}$, $\Delta \ddot{R}$ plane). For economy of notation we define

$$\Delta_0 = \frac{2\pi}{\lambda} \Delta R_0 \quad 21a$$

$$\Delta_1 = \frac{2\pi}{\lambda} \Delta (v \sin \theta) \quad 21b$$

$$\Delta_2 = \frac{1}{2} \frac{2\pi}{\lambda} \Delta \left(\frac{v^2 \cos^2 \theta}{R_0} \right) \quad 21c$$

so that

$$\frac{2\pi}{\lambda} \Delta R(t, A, \bar{A}) \approx \Delta_0 + \Delta_1 t + \Delta_2 t^2 \quad 21d$$

The GAF is approximately

$$\phi(A, \bar{A}) \approx \left| \frac{1}{T} \int_{-\frac{T}{2}}^{\frac{T}{2}} \exp[j(\Delta_1 t + \Delta_2 t^2)] dt \right|^2 \quad 22$$

and can have the interpretation of being given by the square of the amplitude of the characteristic function of a filter with complex impulse response as illustrated in figure 1.



Complex Impulse Response of Complex Filter

Figure 1

i.e.

$$h(x) = \frac{1}{2Z} \exp[j \Delta_2 x^2] \quad \text{for } |x| \leq Z$$

$$= 0 \quad \text{elsewhere}$$

For large observation interval, i.e., large Z, the filter is essentially an all pass with quadratic phase lag. The characteristic function approaches

$$H(\Delta_1, \Delta_2) \sim e^{j\pi/4} \sqrt{\frac{\pi}{\Delta_2}} \frac{1}{2Z} \exp(-j\Delta_1^2 / 4\Delta_2)$$

and the group delay

$$\theta^1(\Delta_1) = \frac{d}{d\Delta_1} \left(\frac{\Delta_1^2}{4\Delta_2} - \frac{\pi}{4} \right) = \frac{\Delta_1}{2\Delta_2}$$

is linear. This quadratic phase lag filter is unrealizable.

When

$$\Delta_2 = 0$$

GAF has approximately the sinc square structure arrived at in the previous paragraph. We assume therefore

$$\Delta_2 \neq 0$$

and rewrite the right hand side (RHS) of equation 21d as

$$\alpha(x - \beta)^2 + \gamma^2 = \Delta_0 + \Delta_1 x + \Delta_2 x^2 \quad 23$$

where

$$\alpha = \Delta_2 = \frac{\pi}{\lambda} \Delta \left(\frac{v^2 \cos^2 \theta}{R_0} \right) \quad 24a$$

$$\beta = - \frac{\Delta_1}{2\Delta_2} = - \frac{\Delta(v \sin \theta)}{\Delta \left(\frac{v^2 \cos^2 \theta}{R_0} \right)} \quad 24b$$

$$\gamma = \left[\Delta_0 - \frac{\Delta_1^2}{4\Delta_2} \right]^{1/2} \quad 24c$$

We note that α corresponds to a normalized version of the error on the range acceleration parameter, while β is a shift on the observation interval due to the nonzero mismatch on the Doppler and the radial acceleration parameters. γ corresponds to a normalization of the phase reference, and given that we assumed an incoherent phase model, it is ignored in the sequel. We change variables

$$\frac{\pi}{2}t = \sqrt{\alpha} (t-\beta) \quad 25a$$

and define

$$\Sigma_f = \sqrt{\alpha} \left(\frac{T}{2} - \beta \right) \quad 25b$$

$$\Sigma_i = \sqrt{\alpha} \left(-\frac{T}{2} - \beta \right) \quad 25c$$

$$\Delta\Sigma = \Sigma_f - \Sigma_i = \sqrt{\alpha}T \quad 25d$$

$$C = \frac{1}{\Delta\Sigma} \int_{\Sigma_i}^{\Sigma_f} \cos\left(\frac{\pi}{2} t^2\right) dt \quad 25e$$

$$S = \frac{1}{\Delta\Sigma} \int_{\Sigma_i}^{\Sigma_f} \sin\left(\frac{\pi}{2} t^2\right) dt \quad 25f$$

Recall the tabulated Fresnel Integrals [Abr 75]

$$F_c(\Sigma) = \int_0^{\Sigma} \cos\left(\frac{\pi}{2} t^2\right) dt \quad 26a$$

$$F_s(\Sigma) = \int_0^{\Sigma} \sin\left(\frac{\pi}{2} t^2\right) dt \quad 26b$$

with the symmetry relations

$$F_c(\Sigma) = -F_c(-\Sigma) \quad 27a$$

$$F_s(\Sigma) = -F_s(-\Sigma) \quad 27b$$

The integrals in equations 26a and 26b lead to

$$C = \frac{1}{\Delta\Sigma} [F_c(\Sigma_f) - F_c(\Sigma_i)] \quad 28a$$

$$S = \frac{1}{\Delta\Sigma} [F_s(\Sigma_f) - F_s(\Sigma_i)] \quad 28b$$

which leads to the ambiguity function structure

$$\phi(A, \bar{A}) = C^2 + S^2 = \frac{1}{(\Delta\Sigma)^2} \{ [F_c(\Sigma_f) - F_c(\Sigma_i)]^2 + [F_s(\Sigma_f) - F_s(\Sigma_i)]^2 \} \quad 29$$

Alternatively, defining the complex Fresnel Integral

$$F(\Sigma) = F_c(\Sigma) + jF_s(\Sigma) = \int_0^{\Sigma} \exp j\left(\frac{\pi}{2} t^2\right) dt \quad 30$$

the signal auto-correlation function is simply

$$\psi(A, \bar{A}) = \frac{1}{\Delta \Sigma} [F(\Sigma_f) - F(\Sigma_1)] \quad 31$$

with the ambiguity function given by its amplitude squared.

We analyze now the behavior of these functions. Since

$\Delta_2=0$ leads to the sinc² structure, we restrict ourselves to

$$\Delta_2 \neq 0.$$

2.2.1 Radial-Acceleration GAF Type

For

$$\Delta_1=0$$

we obtain

$$\psi(A, \bar{A}) = \frac{1}{\Sigma} F(\Sigma) \quad 32$$

and

$$\phi(A, \bar{A}) = \left| \frac{1}{\Sigma} F(\Sigma) \right|^2 \quad 33$$

where

$$\Sigma = \sqrt{\alpha} \frac{T}{2} = \sqrt{\frac{\pi}{\lambda} \Delta \left(\frac{v^2 \cos^2 \theta}{R_0} \right)} \frac{T}{2} \quad 34$$

The graph of

$$F(\Sigma) = F_c(\Sigma) + j F_s(\Sigma) \quad 35$$

in the complex plane is given by the so called Cornu Spiral (e.g. Papoulis [Pap. 67 or Goodman [Goo. 65]).

In figure II-10 we show eq. 33. The 1st minimum is at

$$\Sigma_m \cong 1.9 \quad 36$$

and the second local maxima at

$$\Sigma_{2m} = 2.26 \quad 37$$

where the ambiguity function is

$$\phi(A, \bar{A}) = .132 \quad 38$$

i.e., GAF is reduced to about 13% of its maximum value 1, occurring at $\Sigma=0$.

We proceed with a local and an asymptotic analysis of expressions 36 and 37. From Abramowitz and Stegun one finds on page 301, that the complex Fresnel integral is equivalent to

$$F(\Sigma) = \Sigma M\left(\frac{1}{2}, \frac{3}{2}, j \frac{\pi}{2} \Sigma^2\right) \quad 39a$$

where $M(a, b, z)$ is a Confluent Hypergeometric Function which is defined by the series

$$M(a, b, z) = 1 + \frac{az}{b} + \dots + \frac{(a)_n z^n}{(b)_n n!} \quad 39b$$

with

$$(a)_n = a(a+1)\dots(a+n-1), (a)_0 = 1 \quad 39c$$

Then letting

$$\xi = \frac{\pi}{2} \Sigma^2 \tag{39d}$$

we obtain

$$\begin{aligned} \psi(A, \bar{A}) &= M\left(\frac{1}{2}, \frac{3}{2}, j\xi\right) \\ &= 1 + \sum_{n=1}^{\infty} \frac{1}{1+2n} \frac{\xi^n}{n!} \end{aligned} \tag{39e}$$

This can be rearranged in its real and imaginary components as

$$\begin{aligned} \psi(A, \bar{A}) &= \left\{ 1 - \frac{\xi^2}{5 \cdot (2)!} + \sum_{k=2}^{\infty} (-1)^k \frac{1}{1+4k} \frac{\xi^{2k}}{(2k)!} \right\} \\ &+ j \left\{ \frac{\xi^2}{3} - \frac{\xi^3}{7 \cdot (3)!} + \sum_{k=2}^{\infty} (-1)^k \frac{1}{3+4k} \frac{\xi^{2k+1}}{(2k+1)!} \right\} \end{aligned} \tag{40}$$

In the neighborhood of $\Sigma=0$ we have the local approximation for the ambiguity function

$$\phi(A, \bar{A}) \cong 1 - \frac{4\xi^2}{45} + \frac{2^4}{3^3 \times 5^2 \times 7} \xi^4 + \text{h.o.t.} \tag{41}$$

For large Σ we obtain from the asymptotic expansion of the Confluent Hypergeometric Function, expression 13.51, pg. 508, Abramowitz and Stegun [Abr 65].

$$\psi(A, \bar{A}) = \Gamma\left(\frac{3}{2}\right) e^{j \frac{\pi}{2}} (j\xi)^{-1/2} + \frac{\Gamma\left(\frac{3}{2}\right)}{\Gamma\left(\frac{1}{2}\right)} \left\{ \frac{e^{j\xi}}{j\xi} \left[1 + (j\xi)^{-1} - \frac{3}{2^2} \xi^{-2} + \frac{3 \cdot 5}{2^3} (j\xi)^{-3} + \sum_{n=4}^{\infty} \frac{1 \cdot 3 \cdot 5 \dots (2n-1)}{2^n} (j\xi)^{-n} + o(\xi)^3 \right] \right\} \quad 42a$$

where the remainder converges to zero as

$$o(|\xi|^{-s}) = \frac{1 \cdot 3 \dots (2s-1)}{2^s} (j\xi)^{-s} \left[\frac{1}{6} - s + (j\xi) + o(|\xi|^{-1}) \right] \quad 42b$$

Up to least order we have

$$\psi(A, \bar{A}) \sim \Gamma\left(\frac{3}{2}\right) e^{j \frac{\pi}{2}} \frac{1}{(j\xi)^{1/2}} \quad 43a$$

and so

$$\phi(A, \bar{A}) \sim \left| \Gamma\left(\frac{3}{2}\right) \right|^2 \frac{1}{\xi} = \frac{1}{2\Sigma^2} \quad 43b$$

2.2.2 General Quadratic GAF

We examine directly the quadratic GAF structure as given by equations 34 and 35. The asymptotic behavior of GAF, as the parameter errors get large is studied by

The method of stationary phase (MSP) [Pap 67]. The MSP studies the integral form

$$N(k) = \int_a^b \exp[j k\mu(x)] dx \quad 44$$

based on the fact that for large k the exponential term varies rapidly and the integral tends to zero. The asymptotic analysis quantifies how fast does it converge, and follows from a Taylor series expansion of the integral 44. As it turns out, the MSP result depends on the particular behavior of the phase $\mu(x)$ in the observation interval, namely on its stationary points in $[-x, x]$, i.e., on

$$x \in [-x, x]$$

where

$$\mu'(x) = 0$$

The MSP analysis can easily be applied to other integral forms where large parameter values are involved (e.g. large observation interval) if, with a suitable change of variable, they can be reduced to 44.

To show that the Fresnel integral defined by equation 33, can in fact be written equivalently as equation 44, let ξ be a fixed constant and define

$$\Sigma = \sqrt{k} \zeta$$

$$\tau = \sqrt{k} \xi$$

We have

$$F(\Sigma) = \sqrt{k} \int_0^{\zeta} \exp(j k \xi^2) d\xi$$

which has the form of 44. Clearly $k \rightarrow \infty$ as $\Sigma \rightarrow \infty$. But, e.g.

[Pap 67]

$$F(x) = \sqrt{k} \int_0^x \exp(j k \xi^2) d\xi \sim \sqrt{\frac{\pi}{2}} \left[\frac{e^{j\pi/4}}{\sqrt{2}} + \frac{e^{j\frac{\pi}{2}x^2}}{j\pi x} + o(x^{-1}) \right] \quad 45$$

where $o(x^{-1})$ is a function such that

$$\lim_{x \rightarrow \infty} x o(x^{-1}) = 0$$

Substituting in equation 35

$$\psi(A, \bar{A}) \sim \frac{\sqrt{\pi/2}}{(\Sigma_f - \Sigma_1) j \pi \Sigma_f \Sigma_1} [\Sigma_1 \exp(j \frac{\pi}{2} \Sigma_f^2) - \Sigma_f \exp(j \frac{\pi}{2} \Sigma_1^2)] \quad 46a$$

Recalling that

$$\Sigma_f = \sqrt{\alpha} \left(\frac{T}{2} - \beta \right) = \sqrt{\Delta_2} \left(\frac{T}{2} + \frac{\Delta_1}{2\Delta_2} \right) \quad 46b$$

$$\Sigma_1 = \sqrt{\alpha} \left(-\frac{T}{2} - \beta \right) = \sqrt{\Delta_2} \left(-\frac{T}{2} + \frac{\Delta_1}{2\Delta_2} \right) \quad 46c$$

we obtain

$$\psi(A, \bar{A}) \sim \sqrt{\frac{\pi}{2}} \frac{\exp j\Delta_2 \left[\left(\frac{T}{2}\right)^2 + \left(\frac{\Delta_1}{2\Delta_2}\right)^2 \right]}{j\frac{T}{2} \left[-(2\Delta_2 \frac{T}{2})^2 + \Delta_1^2 \right]} \left[-(2\Delta_2 \frac{T}{2}) \cos(\Delta_1 \frac{T}{2}) + j\Delta_1 \sin(\Delta_1 \frac{T}{2}) \right] \quad 46d$$

which represents the asymptotic behavior as

$$\Sigma_f \rightarrow \pm \infty$$

and

$$\Sigma_i \rightarrow \pm \infty$$

The ambiguity function behaves asymptotically as

$$\phi(A, \bar{A}) = |\psi(A, \bar{A})|^2 \sim \frac{\pi}{2} \frac{\left[(2\Delta_2 \frac{T}{2})^2 \cos^2(\Delta_1 \frac{T}{2}) + \Delta_1^2 \sin^2(\Delta_1 \frac{T}{2}) \right]}{\left(\frac{T}{2}\right)^2 \left[-(2\Delta_2 \frac{T}{2})^2 + \Delta_1^2 \right]^2} \quad 47$$

Equations 46 and 47 represent usefully the tendencial behavior of the quadratic ambiguity structure for large parameter errors, except at the neighborhood of

$$\Delta_1 = \pm 2\Delta_2 \frac{T}{2} \quad 48$$

When this holds direct substitution in equation 35 leads to

$$\begin{aligned}\psi(A, \bar{A}) &= \frac{1}{\sqrt{\Delta_2 T}} [F(\sqrt{\Delta_2 T})] \\ &= \frac{1}{2\Sigma} F(2\Sigma)\end{aligned}\tag{49}$$

and the quadratic GAF

$$\phi(A, \bar{A}) = \left| \frac{1}{2\Sigma} F(2\Sigma) \right|^2\tag{50}$$

Equations 49 and 50 have the same form of equations 36 and 37. Then the conclusions in part A also hold when 48 is true, with the Σ parameter scale being contracted by a factor of 2. In particular for large Σ we have an hyperbolic decrease, as seen from equation 43.

If $\Delta_2 \rightarrow 0$

$$\phi(A, \bar{A}) \sim \text{sinc}^2\left(\Delta_1 \frac{T}{2}\right)\tag{51}$$

which compares with the linearized structure.

If $\Delta_1 \rightarrow 0$

$$\phi(A, \bar{A}) \sim \frac{1}{\left(\frac{T}{2}\right)^2 (2\Delta_2 \frac{T}{2})^2}\tag{52}$$

and decays hyperbolically with Δ_2^2 as already concluded from equation 43.

From equation 47, and when 48 does not hold we obtain

$$\phi(A, \bar{A}) \sim < \frac{\pi/2}{\left(\frac{T}{2}\right)^2 [\Delta_1 + 2\Delta_2 \frac{T}{2}] \left[1 - \frac{2(2\Delta_2 \frac{T}{2})\Delta_1}{(2\Delta_2 \frac{T}{2})^2 + \Delta_1^2}\right]} \quad 53$$

2.3 Third Order Approximation

We pursue the approximation analysis a step further, since for SAMS₀ third order effects are required for global identifiability of the 3 source parameters, as discussed in the beginning of chapter III

The signal autocorrelation function is simply

$$\psi(A, \bar{A}) \cong \frac{1}{T} \int_{-\frac{T}{2}}^{\frac{T}{2}} \exp j(\Delta_1 t + \Delta_2 t^2 + \Delta_3 t^3) dt \quad 54$$

where, as before, we have ignored the contribution of the phase reference Δ_0 . By a change of variables one obtains

$$\psi(A, \bar{A}) \cong \frac{1}{\Delta \Sigma} \int_{\Sigma_i}^{\Sigma_f} \exp j\omega\tau \exp j\tau^3 d\tau \quad 55a$$

where

$$\omega = \frac{1}{\Delta_3^{1/3}} \left(\Delta_1 - \frac{\Delta_2^2}{3\Delta_3} \right) \quad 55b$$

$$\Sigma_f = \Delta_3^{1/3} \left(\frac{T}{2} + \frac{1}{3} \frac{\Delta_2}{\Delta_3} \right) \quad 55c$$

$$\Sigma_i = \Delta_3^{1/3} \left(-\frac{T}{2} + \frac{1}{3} \frac{\Delta_2}{\Delta_3} \right) \quad 55d$$

$$\Delta\Sigma = \Sigma_f - \Sigma_i = \Delta_3^{1/3} T \quad 55e$$

Along the Δ_3 -axis, i.e., whenever

$$\Delta_1 = 0$$

$$\Delta_2 = 0$$

the GAF is simply

$$\phi(A, \bar{A}) = |\psi(A, \bar{A})|^2 = \left| \frac{1}{\Sigma} \int_0^\Sigma \cos \tau^3 d\tau \right|^2 \quad 56$$

where

$$\Sigma = \Delta_3^{1/3} \frac{T}{2}$$

A picture of this function is represented in figure III-4. Returning to the general third order polynomial GAF structure, equation 55, and assuming that the observation interval goes to infinite, i.e., that

$$\begin{aligned} \Sigma_i &\rightarrow -\infty \\ \Sigma_f &\rightarrow +\infty \end{aligned}$$

we can rewrite the asymptotic ambiguity function structure as

$$\psi(A, \bar{A}) \sim \frac{1}{\Sigma} \int_0^{\infty} \cos(\pm \omega \tau + \tau^3) d\tau \quad 57$$

Recalling from Abramowitz and Stegun [Ab 65, p. 447, 10.4.32] the integral representation of one of the Airy functions

$$A_1\left(\pm \frac{x}{(3a)^{1/3}}\right) = \frac{(3a)^{1/3}}{\pi} \int_0^{\infty} \cos(at^3 \pm xt) dt \quad 58a$$

we see that, asymptotically, the signal correlation function goes as

$$\psi(A, \bar{A}) \sim \frac{\pi}{3^{1/3}} \frac{1}{\Sigma} A_1\left(\frac{\pm \omega}{3^{1/3}}\right) \quad 58b$$

For the Airy functions we have the following asymptotic expansions

$$A_1(z) \sim \frac{1}{2} (\pi^2 z)^{-1/4} e^{-\xi} \sum_0^{\infty} (-1)^k c_k \xi^{-k}$$

$$A_1(-z) \sim (\pi^2 z)^{-1/4} \left[\sin\left(\xi + \frac{\pi}{4}\right) \sum_0^{\infty} (-1)^k c_{2k} \xi^{-2k} - \cos\left(\xi + \frac{\pi}{4}\right) \sum_0^{\infty} (-1)^k c_{2k+1} \xi^{-(2k+1)} \right]$$

where

$$\xi = \frac{2}{3} z^{3/2}$$

$$c_0 = 1$$

$$c_k = \frac{\Gamma(3k + \frac{1}{2})}{54^k k! \Gamma(k + \frac{1}{2})} = \frac{(2k+1)(2k+3)\dots(6k-1)}{216^k k!}$$

In particular the first few terms lead to

$$A_1(3) \sim \frac{1}{2} (\pi^2 z)^{-1/4} e^{-\xi} [1 - \frac{5}{12} \xi^{-1}]$$

$$A_1(-2) \sim (\pi^2 z)^{-1/4} [\sin(\xi + \frac{\pi}{4}) - \cos(\xi + \frac{\pi}{4}) \frac{5}{12} \xi^{-1}]$$

Substitution in equation 58b

$$\psi(A, \bar{A}) \sim \frac{\pi}{3^{1/3}} \frac{1}{2} \frac{1}{2} (\pi^2 \frac{\omega}{3^{1/3}})^{-1/4} e^{-\xi} [1 - \frac{5}{12} \xi^{-1}] \text{ if } \omega > 0 \quad 58c$$

$$\sim \frac{\pi}{3^{1/3}} \frac{1}{2} \frac{1}{2} (\pi^2 \frac{\omega}{3^{1/3}})^{-1/4} [\sin(\xi + \frac{\pi}{4}) - \cos(\xi + \frac{\pi}{4}) \frac{5}{12} \xi^{-1}]$$

$$\text{if } \omega < 0 \quad 58d$$

where now

$$\xi = \frac{2}{3} (\frac{\omega}{3^{1/3}})^{3/2} \quad 58e$$

with

$$\omega = \frac{1}{\Delta_3^{1/3}} \left(\Delta_1 - \frac{\Delta_2^2}{3\Delta_3} \right) \quad 58f$$

Along the Δ_3 -axis, i.e., whenever equation 56 holds

$$\int_0^\Sigma \cos \tau^3 d\tau \rightarrow \int_0^\infty \cos \tau^3 d\tau = \frac{\pi A_1(0)}{3^{1/3}} = \frac{\pi}{3\Gamma(\frac{2}{3})} \quad 58g$$

and so along this line

$$\phi(A, A) \sim \left| \frac{1}{\Sigma} \frac{\pi}{3\Gamma(\frac{2}{3})} \right|^2 \quad 58h$$

2.4 General Expression of GAF

Finally we consider briefly the asymptotic behavior of GAF as given by its general expression. We apply the Method of Stationary Phase (MSP). Let n be the first positive integer for which

$$\Delta R^{(n)}(x_0) \triangleq \frac{d^n \Delta R(x, A, \bar{A})}{dx^n} \neq 0 \quad x_0 \in \left[-\frac{T}{2}, \frac{T}{2}\right] \\ x = x_0$$

As the observation interval increases we have the behavior

$$\int_{-\frac{T}{2}}^{\frac{T}{2}} \cdot \approx 2 f_n(x_0, A, \bar{A}) e^{j\pi/2n} \quad n=\text{even} \quad 59$$

$$\int_{-\frac{T}{2}}^{\frac{T}{2}} \cdot \approx f_n(x_0, A, \bar{A}) 2 \cos \frac{\pi}{2n} \quad n=\text{odd} > 1 \quad 60$$

where

$$f_n(x_0, A, \bar{A}) = e^{j \frac{2\pi}{\lambda} \Delta R(x_0, A, \bar{A})} \frac{\Gamma(1/n)}{n \sqrt{\frac{2\pi}{\lambda} \left. \frac{d^n \Delta R}{dx^n} \right|_{x_0}} / n!} \quad 61$$

For $n=1$ we obtain

$$\int_{-\frac{T}{2}}^{\frac{T}{2}} dx \exp j \frac{2\pi}{\lambda} \Delta R(x, A, \bar{A}) \cdot \frac{1}{j \frac{2\pi}{\lambda}} \left[\frac{\exp \left[j \frac{2\pi}{\lambda} \Delta R \left(\frac{T}{2}, A, \bar{A} \right) \right]}{\left. \frac{d\Delta R}{dx} \right|_{\frac{T}{2}}} - \frac{\exp \left[j \frac{2\pi}{\lambda} \Delta R \left(-\frac{T}{2}, A, \bar{A} \right) \right]}{\left. \frac{d\Delta R}{dx} \right|_{-\frac{T}{2}}} \right] \quad 62$$

The asymptotic behavior of GAF is then given by:

If equation 62 holds

$$\phi(A, \bar{A}) \sim \frac{1}{\left(\frac{2\pi}{\lambda} T \right)^2} \left| \frac{\exp \left[j \frac{2\pi}{\lambda} \Delta R \left(\frac{T}{2} \right) \right]}{\Delta \dot{R} \left(\frac{T}{2} \right)} - \frac{\exp \left[j \frac{2\pi}{\lambda} \Delta R \left(-\frac{T}{2} \right) \right]}{\Delta \dot{R} \left(-\frac{T}{2} \right)} \right|^2 \quad 63$$

which leads, by algebraic manipulation, to

$$\phi(A, \bar{A}) \sim \frac{1}{\left(\frac{2\pi}{\lambda} \frac{T}{2}\right)^2} \frac{1}{\Delta \dot{R}_+^2} \frac{1}{\Delta \dot{R}_-^2} \left\{ \Delta \dot{R}_+^2 + \Delta \dot{R}_-^2 - 2\Delta \dot{R}_+ \Delta \dot{R}_- \cos \frac{2\pi}{\lambda} (\Delta R_+ - \Delta R_-) \right\} \quad 64$$

$$\sim \left\langle \frac{1}{\left(\frac{2\pi}{\lambda} T\right)^2} \left\{ \frac{1}{|\Delta \dot{R}_+|} + \frac{1}{|\Delta \dot{R}_-|} \right\}^2 \right\rangle \quad 65$$

where

$$\Delta \dot{R}_\pm = \Delta \dot{R}\left(\pm \frac{T}{2}, A, \bar{A}\right) \quad 66$$

If equation 59 holds we obtain

$$\phi(A, \bar{A}) \sim \left\{ \frac{1}{T/2} \frac{\Gamma(1/n)}{n \sqrt{\frac{2\pi}{\lambda}} \frac{(n)}{\Delta R} (x_0)/n!} \right\}^2 \quad 67$$

If it is equation 60, this bound 67 multiplies by $\cos^2\left(\frac{\pi}{2n}\right)$

Appendix B

Mean Square Spread Matrix Computation

The mean square spread matrix (mssm) M has been defined, equation II-38 as

$$M = - \frac{1}{2} \left[\frac{\partial^2 \phi(A, A_a)}{\partial A_i \partial A_j} \Big|_{A=A_a} \right]_{i,j} \quad 1$$

This matrix is a measure of how flat the GAF main lobe is, reflecting the effects of the geometry on its structure and on the receiver's performance. The Cramer-Rao bounds are obtained by scaling M with a signal energy to noise ratio dependent factor, and the total number of grid cells in the "largest of" step of the estimation algorithm is directly related to the eigenvalues and eigenvectors of M and in particular to $\det M$.

We compute here the spread matrix expression and work in general with the SAMS_o problem. Writing

$$\phi(A, A_a) = |\Psi(A, A_a)|^2 = \Psi(A, A_a) \Psi^*(A, A_a) \quad 2$$

where

A_a = actual source parameter vector

$\Psi(A, A_a)$ = signal correlation function defined by equation II-15 Differentiating with respect to A_j

$$\frac{\partial \phi}{\partial A_j} = 2 \operatorname{Re} \left\{ \Psi \frac{\partial \Psi^*}{\partial A_j} \right\} \quad 3$$

and then w.r.t. A_1

$$\frac{\partial^2 \phi}{\partial A_1 \partial A_j} = 2 \operatorname{Re} \left\{ \frac{\partial \Psi}{\partial A_1} \frac{\partial \Psi^*}{\partial A_j} + \frac{\partial^2 \Psi^*}{\partial A_1 \partial A_j} \right\} \quad 4$$

Due to the total signal energy normalization

$$\int_{-X}^X |\tilde{s}_n(A)| |\tilde{s}_n(A_a)| dx = 1 \quad 5$$

Differentiating twice this equation, one can easily obtain

$$\left. \frac{\partial^2 \Psi^*}{\partial A_1 \partial A_j} \right|_{A=A_a} = - \left\langle \frac{\partial \tilde{s}_n}{\partial A_1}, \frac{\partial \tilde{s}_n}{\partial A_j} \right\rangle \bigg|_{A=A_a} \quad 6$$

where the inner product notation introduced in equation II-11 has been used. The first term in equation 4 is

$$\left. \frac{\partial \Psi}{\partial A_1} \frac{\partial \Psi^*}{\partial A_j} \right|_{A=A_a} = \left\langle \frac{\partial \tilde{s}_n}{\partial A_1}, \tilde{s}_n \right\rangle \overline{\left\langle \frac{\partial \tilde{s}_n}{\partial A_j}, \tilde{s}_n \right\rangle} \quad 7$$

where $\overline{\quad}$ stands for complex conjugation. The matrix M is then given by

$$M = M_0 - M_1 \quad 8$$

where

$$M_{0 \quad ij} = \text{Re} \left\{ \left\langle \frac{\partial \tilde{s}_n}{\partial A_i}, \frac{\partial s_n}{\partial A_j} \right\rangle \right\} \quad 9$$

$$M_{1 \quad ij} = \text{Re} \left\{ \left\langle \frac{\partial \tilde{s}_n}{\partial A_i}, \tilde{s}_n \right\rangle \left\langle \frac{\partial \tilde{s}_n}{\partial A_j}, \tilde{s}_n \right\rangle \right\} \quad 10$$

All quantities are evaluated at the source location parameters, and \tilde{s}_n is defined by expression II-15b. The Fisher Information Matrix (FIM) is given by

$$J = G'(M_0 - M_1) \quad 11$$

with the gain G' in equation II-44b.

By direct substitution of the signal expression

$$\left\langle \frac{\partial \tilde{s}_n}{\partial A_i}, \frac{\partial \tilde{s}_n}{\partial A_j} \right\rangle = \left(\frac{2\sqrt{T}}{\lambda} \right)^2 \frac{1}{2x} \int_{-X}^X \frac{\partial R(x,A)}{\partial A_i} \frac{\partial R(x,A)}{\partial A_j} dx \quad 12$$

$$\left\langle \frac{\partial \tilde{s}_n}{\partial A_i}, \tilde{s}_n \right\rangle = j \frac{2\sqrt{T}}{\lambda} \frac{1}{2x} \int_{-X}^X \frac{\partial R(x,A)}{\partial A_i} dx \quad 13$$

The matrices M_0 and M_1 are then

$$M_0 = \left(\frac{2\sqrt{T}}{\lambda} \right)^2 \frac{1}{2x} \int_{-X}^X \left[\nabla_A R(x,A) \right] \left[\nabla_A R(x,A) \right]^T dx \quad 14$$

$$M_1 = \left(\frac{2\sqrt{T}}{\lambda} \right)^2 \left[\frac{1}{2x} \int_{-X}^X \nabla_A R(x,A) dx \right] \left[\frac{1}{2x} \int_{-X}^X \nabla_A R(x,A) dx \right]^T \quad 15$$

where $\nabla_A \cdot$ is the gradient column vector operator wrt. the parameter vector A and

$$x = \frac{z}{R_0} \quad 16$$

Computing the integrands and defining

$$f_1(x, \theta) = \frac{1}{\sqrt{2x}} \frac{1-x \sin\theta}{\sqrt{(1-x \sin\theta)^2 + x^2 \cos^2\theta}} \quad 17$$

$$f_2(x, \theta) = \frac{R_0}{v} \frac{1}{\sqrt{2x}} \frac{x \sin\theta}{\sqrt{(1-x \sin\theta)^2 + x^2 \cos^2\theta}} \quad 18$$

$$f_3(x, \theta) = R_0 \frac{1}{\sqrt{2x}} \frac{x}{\sqrt{(1-x \sin\theta)^2 + x^2 \cos^2\theta}} \quad 19$$

we obtain

$$M_{0_{ij}} = \left(\frac{2\pi}{\lambda}\right)^2 \int_{-X}^X f_i f_j dx \quad 20$$

$$M_{1_{ij}} = \left(\frac{2\pi}{\lambda}\right)^2 \left[\int_{-X}^X f_i dx \right] \left[\int_{-X}^X f_j dx \right] \quad 21$$

By application of the Schwartz inequality one can see that

$$M_{0_{ii}} \geq M_{1_{ii}} \quad i=1,2,3 \quad 22$$

except for the degenerate conditions

$$x = 0 \quad (\text{no observer}) \quad 23$$

or

$$\theta = \frac{\pi}{2} \quad (\text{end fire geometry}) \quad 24$$

Performing the computations we obtain

$$M_0 = \left(\frac{2\pi}{\lambda}\right)^2 \left[\begin{array}{ccc|ccc} 1 - \cos^2 \theta_0 H_2 & & & & & \\ \hline \frac{R_0}{v} (-\sin \theta H_1 + \cos^2 \theta H_2) & & & \frac{(R_0)^2}{v} \left(\frac{x^2}{3} - \cos^2 \theta H_2\right) & & \\ \hline -R_0 (H_1 - \sin \theta H_2) & & & \frac{R_0^2}{v} (-\sin \theta H_2 + H_3) & & R_0^2 H_2 \\ \hline \end{array} \right] \quad 25$$

$$M_1 = \left(\frac{2\pi}{\lambda}\right)^2 \left[\begin{array}{ccc|ccc} (F_0 - \sin \theta F_1)^2 & & & & & \\ \hline \frac{R_0}{v} (F_0 - \sin \theta F_1) (F_2 - \sin \theta F_1) & & & \left(\frac{R_0}{v}\right)^2 (F_2 - \sin \theta F_1)^2 & & \\ \hline -R_0 (F_0 - \sin \theta F_1) F_1 & & & \frac{R_0^2}{v} (F_2 - \sin \theta F_1) F_1 & & R_0^2 F_1^2 \\ \hline \end{array} \right] \quad 26$$

where we defined

$$x = \frac{z}{R_0} = \frac{L/2}{R_0} \text{ for SASS or } \frac{vT}{2R_0} \text{ for MASS and SAMS.}$$

$$R = 1 + x^2 - 2x \sin \theta_0 \quad 27$$

$$H_0 = \frac{1}{2x} \int_{-x}^x \frac{1}{R} dx = \frac{1}{\cos \theta_0} \Delta \arctan \quad 28$$

$$H_1 = \frac{1}{2x} \int_{-x}^x \frac{x}{R} dx = \frac{1}{2} \Delta \ln + \tan \theta \Delta \arctan \quad 29$$

$$H_2 = \frac{1}{2x} \int_{-x}^x \frac{x^2}{R} dx = 1 + \sin \theta \Delta \ln - \frac{\cos 2\theta}{\cos \theta} \Delta \arctan \quad 30$$

$$H_3 = \frac{1}{2x} \int_{-x}^x \frac{x^3}{R} dx = 2 \sin \theta + \frac{1 - 2 \cos 2\theta}{2} \Delta \ln - \tan \theta (1 + 2 \cos 2\theta) \Delta \arctan \quad 31$$

$$F_0 = \frac{1}{2x} \int_{-X}^X \frac{1}{\sqrt{R}} dx = \Delta \text{Arsh} \quad 32$$

$$F_1 = \frac{1}{2x} \int_{-X}^X \frac{x}{\sqrt{R}} dx = \Delta\sqrt{R} + \sin\theta \Delta\text{Arsh} \quad 33$$

$$F_2 = \frac{1}{2x} \int_{-X}^X \frac{x^2}{\sqrt{R}} dx = \frac{1}{2} \left[\frac{1}{2} (\sqrt{1+x^2+2x \sin\theta} + \sqrt{1+x^2-2x \sin\theta}) + 3 \sin\theta \Delta\sqrt{R} + (3 \sin^2\theta - 1) \Delta\text{Arsh} \right] \quad 34$$

and where

$$\Delta \arctan = \frac{1}{2x} \left[\text{Arsh}\left(-\tan\theta + \frac{x}{\cos\theta}\right) \right] \Bigg|_{-X}^X = \frac{1}{2x} \left[\arctan\left(\tan\theta + \frac{x}{\cos\theta}\right) - \arctan\left(\tan\theta - \frac{x}{\cos\theta}\right) \right] \quad 35$$

$$\Delta \text{Arsh} = \frac{1}{2x} \left[\text{Arsh}\left(-\tan\theta + \frac{x}{\cos\theta}\right) \right] \Bigg|_{-X}^X \quad 36$$

$$\Delta\sqrt{R} = \frac{1}{2x} [\sqrt{R}] \Bigg|_{-X}^X \quad 37$$

$$\Delta \ln = \frac{1}{2x} [\ln R] \Bigg|_{-X}^X \quad 38$$

Remark: With the SASS or MASS problems the second line and column of M are deleted.

Analysing the elements of M_0 and M_1 in equations 25 and 26, we note that we can rewrite the spread matrix as

$$M = SM'S$$

39

where S is the scaling diagonal matrix

$$S = \begin{bmatrix} \frac{1}{R_o} & 0 \\ 0 & \frac{1}{v} \\ & & 1 \end{bmatrix} \quad 40$$

and M' is the spread matrix for the normalized estimation problem, where the parameter vector is

$$A_n = \begin{bmatrix} R_o/R_{oa} \\ v/v_a \\ \sin\theta \end{bmatrix} \quad 41$$

The elements of M' depend only on the source bearing angle and on the geometric parameter

$$x = \frac{z}{R_o}$$

Appendix C

Asymptotic Behavior of the Mean Square Spread Matrix

1. General Derivation

As discussed in Chapters II and III the Mean Square Spread Matrix (MSSM) M reflects the effects of the geometry on the receiver's performance. We study here its asymptotic behavior for large values of the geometric parameter, i.e., as

$$x = \frac{Z}{R_0} \rightarrow \infty \quad 1$$

or equivalently as

$$Y = \frac{1}{x} \rightarrow 0 \quad 2$$

We start with equations B-25 to B-38 and make the change of variables

$$Y = x^{-1} \quad 3$$

Define the trinomial

$$R_{\pm}(x) = 1 + x^2 \pm 2x \sin \theta \quad 4$$

abbreviated by R_+ or R_- , when the variable is understood from the context.

We work in detail one of the integrals.

$$\begin{aligned} F_1 &= \frac{1}{2x} \int_{-X}^X \frac{x}{\sqrt{R_-}} dx = -\frac{Y}{2} \left\{ \int_{-Y}^{-\infty} \frac{-1}{y^2 \sqrt{R_-}} dy + \int_{\infty}^Y \frac{1}{y^2 \sqrt{R_+}} dy \right\} \\ &= \frac{Y}{2} \int_Y^{\infty} \left[\frac{1}{y^2 \sqrt{R_-}} - \frac{1}{y^2 \sqrt{R_+}} \right] dy \end{aligned} \quad 5$$

These are tabulated integrals, e.g., Gradshteyn/Ryzhik [Gira6], 2.269. The final results for all quantities of interest are given below. Set

$$H_{i_{\pm}} = \frac{Y}{2} \int_Y^{\infty} \frac{1}{y^i R_{\pm}} dy \quad 6$$

$$F_{i_{\pm}} = \frac{Y}{2} \int_Y^{\infty} \frac{1}{y^i \sqrt{R_{\pm}}} dy \quad 7$$

From Gradshteyn/Ryzhik , 1.642

$$\text{Arsh } z = \ln 2z - \sum_{k=1}^{\infty} \frac{(2k)!}{2^{2k} (k!)^2 2k} z^{-2k} \quad 8$$

With

$$|z|^2 = \left| \frac{1 + Y \sin \theta}{Y \cos \theta} \right|^2 > 1 \quad 9$$

which is satisfied whenever

$$\frac{1}{Y} > 1 + \sin \theta \quad 10$$

or equivalently

$$Y < 2 \quad 11$$

we obtain

$$Y \Delta_+ \text{Arsh of the order } Y \text{ Ln } Y + O(Y^{-3}) \text{ as } Y \rightarrow 0 \quad 12$$

But

$$\lim_{Y \rightarrow 0} Y^\epsilon \text{Ln } Y = 0 \quad 13$$

for any $\epsilon > 0$.

The Taylor Series (TS) expansions of B-35 to B-38 lead to

$$\Delta \text{ATAN} \cong 2 \cos \theta Y + O(Y^3) \quad 14$$

$$\ln \frac{R_-}{R_+} \cong -4 \sin \theta Y + O(Y^3) \quad 15$$

$$\Delta_- \text{Arsh} \cong -2 \sin \theta Y + O(Y^3) \quad 16$$

$$\Delta \sqrt{R} \cong -2 \sin \theta Y + O(Y^3) \quad 17$$

$$\sqrt{R_-} + \sqrt{R_+} \cong 2 + \cos^2 \theta Y^2 \quad 18$$

Substituting in the expressions of H_1 and F_1 we obtain

$$H_1 = H_{1-} - H_{1+} = \frac{\pi}{2} \tan \theta Y + \frac{1}{4} \left[\ln \frac{R_-}{R_+} \right] Y - \frac{\tan \theta}{2} [\Delta \text{Atan}] Y \quad 19$$

$$H_2 = H_{2-} + H_{2+} = 1 - \frac{\cos 2\theta}{\cos \theta} \frac{\pi}{2} Y + \frac{\sin \theta}{2} \left[\ln \frac{R_-}{R_+} \right] Y + \frac{\cos 2\theta}{2 \cos \theta} [\Delta \text{ATAN}] Y \quad 20$$

$$H_3 = H_{3-} - H_{3+} = \sin \theta - \frac{1 - 4 \sin^2 \theta}{2} \frac{Y}{2} \left[\ln \frac{R_-}{R_+} \right] - \tan \theta (3 - 4 \sin^2 \theta) \frac{Y}{2} [\pi - \Delta \text{ATAN}] \quad 21$$

$$F_0 = F_{1-} - F_{1+} = [\text{Arsh}(\tan \theta)] Y + \frac{1}{2} [\Delta \text{Arsh}] Y \quad 22$$

$$F_1 = F_{2-} - F_{2+} = \frac{1}{2} \Delta \sqrt{R} + \frac{\sin \theta}{2} [\Delta_+ \text{Arsh}] Y \quad 23$$

$$F_2 = F_{3-} + F_{3+} = \frac{1}{4Y} (\sqrt{R_-} + \sqrt{R_+}) + \frac{3}{4} \sin \theta \Delta \sqrt{R} + \frac{Y}{4} (3 \sin^2 \theta - 1) [\Delta_+ \text{Arsh}] \quad 24$$

where

$$\Delta \text{ATAN} = \text{ATAN}(-\tan \theta + \frac{Y}{\cos \theta}) + \text{ATAN}(\tan \theta + \frac{Y}{\cos \theta}) \quad 25$$

$$\Delta \sqrt{R} = \sqrt{R_-} - \sqrt{R_+} = \sqrt{1 + Y^2 - 2Y \sin \theta} - \sqrt{1 + Y^2 + 2Y \sin \theta} \quad 26$$

$$\Delta_+ \text{Arsh} = \text{Arsh}(\frac{1}{Y \cos \theta} - \tan \theta) + \text{Arsh}(\frac{1}{Y \cos \theta} + \tan \theta) \quad 27$$

All these expressions can be expanded in a Taylor series (TS) about

$$Y=0$$

except Δ_+ Arsh. But we note that

$$\lim_{Y \rightarrow 0} Y \Delta_+ \text{Arsh} = 0 \quad 28$$

$$H_1 \cong \frac{\pi}{2} \tan\theta Y - 2\sin^2\theta Y^2 \quad 29$$

$$H_2 \cong 1 - \frac{\cos 2\theta}{\cos\theta} \frac{\pi}{2} Y + (\cos^2\theta - 3\sin^2\theta) Y^2 \quad 30$$

$$H_3 \cong \sin\theta \left[1 - (3 - 4\sin^2\theta) \frac{\pi Y}{2\cos\theta} + 4 \cos(2\theta) Y^2 \right] \quad 31$$

$$F_0 \cong Y [\text{Arsh}(\tan\theta) - \sin\theta Y] \quad 32$$

$$F_1 \cong -\sin\theta Y + \frac{\sin\theta}{2} [\Delta_+ \text{Arsh}] Y \quad 33$$

$$F_2 \cong \frac{1}{2Y} + \frac{Y}{4} [(\cos^2\theta - 6\sin^2\theta) + (3\sin^2\theta - 1) [\Delta_+ \text{Arsh}]] \quad 34$$

The asymptotic behavior of MSSM up to first order in

$$Y = \frac{1}{x} = \frac{R_0}{z} \quad 35$$

is given by

$$\begin{aligned}
M^{-1} &= \left(\frac{2\pi}{\lambda} \right)^2 \left[\begin{array}{l} \sin^2 \theta + \cos \theta \cos \left(2\theta \frac{\pi Y}{2} \right) \frac{R_0}{v} \left[\cos^2 \theta - \frac{1}{2} \left[\text{Arsh}(\tan \theta) - \frac{\sin^2 \theta}{2} \Delta + \text{Arsh} \right] \right. \\ \left. - \frac{\pi}{2} \frac{Y}{\cos \theta} (\cos^4 \theta + \sin^4 \theta) \right] \\ \hline = \left(\frac{R_0}{v} \right)^2 \left[\frac{1}{12Y^2} - \frac{3\cos^2 \theta + 2\cos 2\theta}{4} \right. \\ \left. + \frac{\cos^2 \theta}{4} \Delta + \text{Arsh} + \cos \theta \cos \left(2\theta \frac{\pi Y}{2} \right) \right] \\ \hline R_0 \left(-\sin \theta + \frac{\pi}{2} \sin \left(2\theta \frac{\pi Y}{2} \right) \right) \frac{R_0^2}{v} \left[\frac{\sin \theta}{2} \left(1 - \frac{1}{2} \Delta + \text{Arsh} \right) - \frac{\pi}{2} Y \sin 2\theta \right] \\ \hline R_0^2 \left(1 - \frac{\cos 2\theta}{\cos \theta} \frac{\pi}{2} Y \right) \end{array} \right]
\end{aligned}$$

36

Before tackling the inversion of this 3-dimensional matrix, we consider first the diagonal elements, then the principal minors, and finally return to the full 3-dimensional matrix.

2. Limiting Behavior of Diagonal Elements

This analysis provides the asymptotic behavior when only one parameter is to be estimated, with the other two assumed a priori known. We obtain

$$\lim_{Y \rightarrow 0} M^{-1} = \lim_{Y \rightarrow 0} \frac{\left(\frac{\lambda}{2\pi} \right)^2}{R \sin^2 \theta + \cos \theta \cos \left(2\theta \frac{\pi Y}{2} \right)} = \left(\frac{\lambda}{2\pi} \right)^2 \frac{1}{\sin^2 \theta} \quad 37$$

$$\lim_{Y \rightarrow 0} M^{-1} = \lim_{Y \rightarrow 0} \frac{1}{M_{22}} \sim \left(\frac{\lambda}{2\pi}\right)^2 \left(\frac{Y}{R_0}\right)^2 12Y^2 \quad 38$$

$$\lim_{Y \rightarrow 0} M^{-1} = \lim_{\sin\theta Y \rightarrow 0} \frac{\left(\frac{\lambda}{2\pi}\right)^2}{R_0^2 \left(1 - \frac{\cos 2\theta}{\cos \theta} \frac{\pi}{2} Y\right)} = \left(\frac{\lambda}{2\pi}\right)^2 \frac{1}{R_0^2} \quad 39$$

3. Limiting Behavior of Principal Minors

3-1) Range/Angle Estimation:

$$M_{R_0, \sin\theta} = \left(\frac{2\pi}{\lambda}\right)^2 \left[\begin{array}{c|c} \sin^2\theta + \cos\theta \cos\left(2\theta \frac{\pi}{2} Y\right) & R_0 \left[-\sin\theta + \frac{\pi}{2} \sin(2\theta) Y\right] \\ \hline \text{-----} & \text{-----} \\ = & R_0^2 \left[1 - \frac{\cos 2\theta}{\cos \theta} \frac{\pi}{2} Y\right] \end{array} \right] \quad 40$$

The determinant is

$$\text{Det } M_{R_0, \sin\theta} \sim \left(\frac{2\pi}{\lambda}\right)^4 R_0^2 \frac{\pi}{2} \frac{Y}{\cos\theta} \quad 41$$

The inverse is

$$M_{R_0, \sin\theta}^{-1} \approx \left(\frac{\lambda}{2\pi}\right)^2 \left[\begin{array}{c|c} \frac{2}{\pi} \frac{\cos\theta}{Y} - \cos 2\theta & \frac{\sin 2\theta}{R_0} \left[\frac{1}{\pi y} \cos\theta\right] \\ \hline \text{-----} & \text{-----} \\ = & \frac{1}{R_0^2} \left[\frac{2}{\pi} \frac{\cos\theta \sin^2\theta}{Y} + \cos^2\theta \cos 2\theta\right] \end{array} \right] \quad 42$$

We study briefly the normalized spread function

$$f_R(\theta, Y) = \frac{2}{\pi} \frac{\cos \theta}{Y} - \cos 2\theta \quad 43$$

$$f_\theta(\theta, Y) = \frac{1}{R_0} \frac{2}{\pi} \left[\frac{2}{\pi} \frac{\cos \theta \sin^2 \theta}{Y} + \cos^2 \theta \cos 2\theta \right] \quad 44$$

$$f_{R\theta}(\theta, Y) = \frac{\sin 2\theta}{R_0} \left[\frac{1}{\pi Y} - \cos \theta \right] \quad 45$$

First note that f_R and f_θ are even functions of θ and $f_{R\theta}$ is odd.

3-1-1) Mean Square Range Spread: From equation 43 we obtain

$$\frac{d^{2n+1}}{d\theta^{2n+1}} f_R(\theta, Y) = (-1)^n \left[-\frac{2\sin \theta}{\pi Y} + 2^{2n+1} \sin 2\theta \right], \quad n=0, 1, 2, \dots \quad 46$$

$$\frac{d^{2n}}{d\theta^{2n}} f_R(\theta, Y) = (-1)^{n+1} \left[-\frac{2\cos \theta}{\pi Y} + 2^{2n} \cos 2\theta \right], \quad n=1, 2, \dots \quad 47$$

In particular the zeroes of the first derivative for $\theta \in [0, \frac{\pi}{2})$ are

$$\frac{df_R(\theta, Y)}{d\theta} = 0 \rightarrow \begin{cases} \theta = 0 \\ \text{or} \\ \cos \theta = \frac{1}{2/Y} \end{cases} \quad 48$$

$$\text{At } \theta=0 \quad \ddot{f}_R = 2\left(-\frac{1}{\pi Y} + 2\right) \rightarrow \begin{cases} \ddot{f}_R < 0 & \text{if } Y < \frac{1}{2} \\ = 0 & Y = \frac{1}{2} \\ > 0 & Y > \frac{1}{2} \end{cases} \quad 49$$

$$\text{At } \cos\theta = \frac{1}{2\sqrt{Y}} \rightarrow \ddot{f}_R = -4 \sin^2\theta < 0 \quad \text{for } \theta \neq 0 \quad 50$$

$$\text{For } \theta=0, y=\frac{1}{2\sqrt{Y}} \rightarrow \ddot{f}_R=0 \text{ but } f_R^{(IV)} = -12 < 0 \quad 51$$

Conclusions:

- For a) $Y > \frac{1}{2\sqrt{Y}}$, $\theta=0$ is a local minimum
 b) $Y \leq \frac{1}{2\sqrt{Y}}$, $\theta=0$ is a local maximum

In case a) a local maximum occurs at $\cos\theta = \frac{1}{2\sqrt{Y}}$, while in case b) the function monotonically decreases to 1 at $\theta = \frac{\pi}{2}$.

3-1-2) Mean Square Bearing Spread

We observe that

$$f_\theta(0) = 1 \quad 52$$

$$f_\theta\left(\frac{\pi}{2}\right) = 0 \quad 53$$

and

$$\dot{f} = 0 \quad \text{for } \theta=0 \text{ which is a stationary point.} \quad 54$$

For

$$Y \ll \frac{1}{\pi} \quad 55$$

a second stationary point, which is a maximum, occurs at approximately

$$\cos \theta \approx \frac{1}{\sqrt{3}} \rightarrow \theta \approx 55^\circ \quad 56$$

A pictorial representation of these functions is given in chapter II, figures 18 and 19.

3-2) Range/Velocity Estimation

We obtain from equation 36 the inverse range/velocity minor

$$M_{R_o, v}^{-1} \sim \left(\frac{\lambda}{2\pi} \right)^2 \left[\begin{array}{c} \frac{1}{\sin^2 \theta} - \frac{v_1 12Y^2}{R_o} \frac{1}{\sin^2 \theta} [\cos^2 \theta - \frac{1}{2} [\text{Arsh}(\tan \theta) \\ - \frac{\sin^2 \theta}{2} \Delta_+ \text{Arsh}]] \\ \hline = \left(\frac{v}{R_o} \right)^2 12Y^2 \end{array} \right] \quad 57$$

where the determinant

$$\det M_{R_o, v} \sim \left(\frac{2\pi}{\lambda} \right)^2 \left(\frac{R_o}{v} \right)^2 \frac{\sin^2 \theta}{12Y^2} \quad 58$$

Up to lowest order

$$(M_{R_o, v}^{-1})_{R_o} \rightarrow \left(\frac{\lambda}{2\pi} \right)^2 \frac{1}{\sin^2 \theta} \quad 59$$

$$(M^{-1})_{R_0, v} \rightarrow \left(\frac{\lambda}{2\pi}\right)^2 \left(\frac{v}{R_0}\right)^2 12Y^2 \quad 60$$

3.3) Velocity/Bearing Estimation

Again from equation 36 we obtain for the inverse of the velocity/bearing minor

$$M^{-1}_{v, \sin\theta} \sim \left(\frac{\lambda}{2\pi}\right)^2 \begin{bmatrix} \left(\frac{v}{R_0}\right)^2 12Y^2 & \frac{v}{R_0} \frac{\sin\theta}{2} [1 - \frac{1}{2}\Delta_+ \text{Arsh}] 12Y^2 \\ \vdots & \vdots \\ \frac{1}{R_0} & \vdots \end{bmatrix} \quad 61$$

$$\text{Det } M_{v, \sin\theta} \sim \left(\frac{2\pi}{\lambda}\right)^4 \frac{R_0^4}{\sqrt{2}} \frac{1}{12Y^2} \quad 62$$

Finally we consider the full 3-dimensional problem.

4. SAMS - Mean Square Spread Matrix

The determinant and M^{-1} are computed directly from equation 36

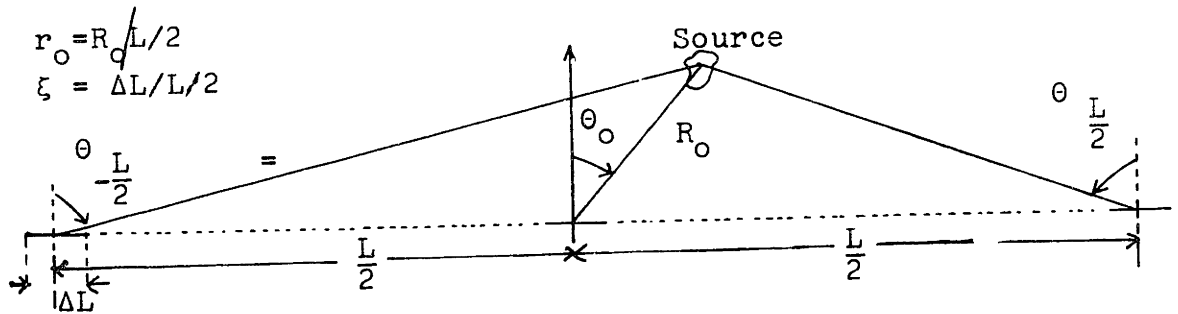
$$\text{Det } M \sim \left(\frac{2\pi}{\lambda}\right)^6 \frac{R_0^4}{\sqrt{2}} \frac{\pi}{2} \frac{1}{12} \frac{1}{\cos\theta} \frac{1}{Y} \quad 63$$

$$\begin{aligned}
M^{-1} \sim \left(\frac{\lambda}{2\pi}\right)^2 & \left[\frac{2\cos\theta}{\pi Y} - \cos 2\theta \left| \frac{v}{R_o} \left[1 - \frac{\sin^2\theta}{2} - \frac{1}{2} \text{Arsh}(\tan\theta) \right] \right| \frac{2}{\pi} 12 \cos\theta Y \right. \\
& \left. - \frac{1}{R_o} \frac{\sin 2\theta}{\pi Y} \right] \\
= & \left(\frac{v}{R_o} \right)^2 12 Y^2 \\
& \left[-\frac{v}{R_o} \sin\theta \left[1 - \frac{\sin^2\theta}{2} - \frac{1}{2} \text{Arsh}(\tan\theta) \right] \right] \frac{2}{\pi} 12 \cos\theta Y \\
= & \left[\frac{2\cos\theta \sin^2\theta}{\pi Y} + \cos^2\theta \cos 2\theta \right] \frac{1}{R_o^2}
\end{aligned}$$

64

5. Very Long Baseline Interferometry (Range/Bearing)

Figure 1 illustrates a linear observer composed of three short colinear arrays placed far apart of each other. We derive the Cramer-Rao performance bounds for the range and bearing parameters, under suitable assumption made explicit below.



Long Baseline (3-element) Staved Linear Array

Figure 1

Assumptions:

H-1) $R_0 \gg \Delta L$, i.e., the source/observer's center separation is much larger than the physical dimensions of the individual linear sensors;

H-2) $R_0 \ll L$, i.e., the source/receiver's center separation is much smaller than the total observer's system dimension.

Under H-1) we linearize the range phase function across each individual stave about its geometric center. We obtain

$$R(x) = \sqrt{r_0^2 + x^2 - 2xr_0 \sin\theta_0} \approx r_0 - \sin\theta_0 x \quad \text{for } x \in (-\epsilon, \epsilon) \quad 65$$

$$\approx R(1) - \sin\theta_{\frac{L}{2}}(x-1) \quad \text{for } x \in (1-\epsilon, 1+\epsilon) \quad 66$$

$$\approx R(-1) - \sin\theta_{\frac{L}{2}}(x+1) \quad \text{for } x \in (-(1+\epsilon), -(1-\epsilon)) \quad 67$$

But

$$\sin\theta_{\frac{L}{2}} = \cos\left(\frac{\pi}{2} - \theta_{\frac{L}{2}}\right) = -\cos\left(\frac{\pi}{2} - |\theta_{\frac{L}{2}}|\right) \quad 68$$

By H-2)

$$\theta_{\frac{L}{2}} \approx -\theta_{\frac{L}{2}} = \theta_L \quad 69$$

and we can approximate

$$\cos\left(\frac{\pi}{2} - |\theta_{\frac{L}{2}}|\right) \approx 1 - \left(\frac{\pi}{2} - \theta_L\right)^2 \frac{1}{2} \quad 70$$

Also by H.2)

$$\frac{\pi}{2} - \theta_L \approx \sin\left(\frac{\pi}{2} - \theta_L\right) \approx \tan\left(\frac{\pi}{2} - \theta_L\right) = \frac{R_o \cos\theta_o}{\frac{L}{2} - R_o \sin\theta_o} \approx r_o \cos\theta_o \quad 71$$

So that

$$\sin\theta_{\pm \frac{L}{2}} \approx \mp \left[1 - \frac{r_o^2 \cos^2\theta_o}{2}\right] \quad 72$$

We have than

$$R(x) \approx \begin{cases} r_o - \sin\theta_o x & x \in [-\epsilon, \epsilon] & 73 \\ R(1) + \left(1 - \frac{r_o^2 \cos^2\theta_o}{2}\right) (x-1) & x \in [1-\epsilon, 1+\epsilon] & 74 \\ R(-1) - \left(1 - \frac{r_o^2 \cos^2\theta_o}{2}\right) (x+1) & x \in [-(1+\epsilon), -(1-\epsilon)] & 75 \end{cases}$$

To compute the spread matrix we need the gradient of $R(x)$ with respect to the parameter vector

$$A = \begin{bmatrix} R_o \\ \sin\theta_o \end{bmatrix} \quad 76$$

Because of the Rayleigh model, we ignore in subsequent computations the presence of the zeroth order term in the phase approximations 73 to 75. We arrive at

$$M = \left(\frac{2\pi L/2}{\lambda} \right)^2 \frac{1}{3} \epsilon^3 r_o^2 \left[\begin{array}{c|c} \frac{\cos^4 \theta_o}{(L/2)^2} & - \frac{\cos^2 \theta_o}{(L/2)} \sin \theta_o r_o \\ \hline - & \frac{1}{r_o^2} + \sin^2 \theta_o r_o^2 \end{array} \right] \quad 77$$

$$\det M = \left[\left(\frac{2\pi L/2}{\lambda} \right)^2 \frac{1}{3} \epsilon^3 r_o^2 \right]^2 \frac{\cos^4 \theta_o}{(L/2)^2 r_o^2} \quad 78$$

$$M^{-1} \approx \frac{1}{m} \left[\begin{array}{c|c} \left(\frac{L/2}{\cos^2 \theta} \right)^2 + \left(\frac{L/2 \sin \theta r_o^2}{\cos^2 \theta} \right)^2 & \frac{L/2 \sin \theta r_o^3}{\cos^2 \theta} \\ \hline - & r_o^2 \end{array} \right] \quad 79$$

where

$$m = \left(2\pi \frac{L/2}{\lambda} \right)^2 \frac{1}{3} \epsilon^3 r_o^2 \quad 80$$

The Cramer Rao bounds are given by

$$\sigma_{R_o} \approx G^{-1/2} (M^{-1})_{11}^{1/2} \approx G^{-1/2} \sqrt{3} \frac{1}{\pi} \sqrt{\frac{L/2}{\Delta L}} \left(\frac{L/2}{R_o \cos \theta} \right)^2 \frac{1}{\Delta L} R_o \left[1 + \frac{r_o^4 \sin^2 \theta}{2} \right] \quad 81$$

$$\sigma_{\sin \theta} \approx G^{-1/2} (M^{-1})_{22}^{1/2} \approx G^{-1/2} \sqrt{3} \frac{1}{\pi} \sqrt{\frac{L/2}{\Delta L}} \left(\frac{1}{\Delta L / \lambda} \right) \quad 82$$

But from equation II-44c

$$G^{-1/2} = \frac{\alpha}{\sqrt{\text{SNR}_{\text{eff}}}} \frac{1}{\sqrt{LT}} \quad 83$$

we obtain

$$\sigma_{\sin\theta} \approx \frac{\alpha}{\sqrt{\text{SNR}_{\text{eff}}}} \frac{1}{\sqrt{\Delta L T}} \sqrt{\frac{3}{2}} \frac{1}{\pi} \left(\frac{1}{\lambda}\right) \quad 84$$

and

$$\sigma_{R_o} \approx \sigma_{\sin\theta} \tan^2\theta_L R_o \quad 85$$

Appendix D

We present here the local analysis expressions for the mean square spread matrix M , its classical adjoint \tilde{M} , the inverse M^{-1} and for the determinant $\text{Det } M$. Due to the extension of the results, we restrict, most of the time, them to the last order terms. However in actual computations we have used the required higher order terms to obtain the exact coefficients for the terms of interest in $\text{Det } M$, and also to preserve the positive definite character of M . In particular, we stress that below, when certain equalities between elements of M or M^{-1} occur, such as

$$\tilde{M}_{33} = \frac{\tilde{M}_{22}}{v^2} \sin^2 \theta_2$$

they are intended only as an economy of notation, and it is to be understood that the equality holds only for the least order terms exhibited in this appendix and not for the higher order terms which have to be considered when manipulating the matrices.

We use below the notation

$$X_{1c} = X_1 \cos \theta_1 = \frac{L}{2R_0} \cos \theta_1$$

$$X_{2c} = X_2 \cos \theta_2 = \frac{vT}{2R_0} \cos \theta_2$$

$$X_{is} = X_i \sin \theta_i, \quad i=1,2$$

Mean Square Spread Matrix

$$M_{11} = \left(\frac{2\pi}{\lambda}\right)^2 \frac{1}{9} (X_{c_1}^4 + 5X_{c_1}^2 X_{c_2}^2 + X_{c_2}^4)$$

$$M_{22} = \left(\frac{2\pi}{\lambda}\right)^2 \left(\frac{R_0}{v}\right)^2 X_2^2 \left[\frac{\sin^2 \theta_2}{3} + \frac{X_1^2}{9} \cos \theta_1 \cos(\theta_1 + 2\theta_2) + \frac{(\cos \theta_2 X_2)^2}{5} \left(\frac{4 \cos^2 \theta_2}{9} - 3 \sin^2 \theta_2 \right) \right]$$

$$M_{ii} = \left(\frac{2\pi}{\lambda}\right)^2 R_0^2 X_{\alpha_i}^2 \left[\frac{1}{3} - \frac{\cos \theta_{\alpha_j}}{9 \cos^2 \theta_{\alpha_i}} X_{\alpha_j}^2 \cos(\theta_{\alpha_j} + 2\theta_{\alpha_i}) + \frac{X_{\alpha_i}^2}{5} \left(\frac{31 \sin^2 \theta_{\alpha_i}}{9} - 1 \right) \right]$$

for $i=3, \alpha_i=2, \alpha_j=1$; for $i=4, \alpha_i=1, \alpha_j=2$

$$M_{12} = \left(\frac{2\pi}{\lambda}\right)^2 \frac{R_0}{v} X_2^2 \left[\frac{X^2}{5} \left(\sin^2 \theta_2 - \frac{2 \cos^2 \theta_2}{9} \right) - \frac{X_1^2 \cos \theta_1}{9} \cos(2\theta_2 + \theta_1) \right]$$

$$M_{1i} = \left(\frac{2\pi}{\lambda}\right)^2 R_0 \frac{X_{\alpha_i}^2}{9} \left[\frac{11 \cos \theta_{\alpha_i} \sin \theta_{\alpha_i}}{5} X_{\alpha_i}^2 + 2 \cos \theta_{\alpha_j} \cos(\theta_{\alpha_i} - \theta_{\alpha_j}) \right]$$

same convention as above for i, α_i, α_j .

$$M_{23} = \left(\frac{2\pi}{\lambda}\right)^2 \frac{R_0^2}{v} X_2^2 \left[\frac{\sin \theta_2}{3} + \frac{\sin \theta_2}{2} X_2^2 \left(\frac{3 \sin^2 \theta_2}{5} - \frac{7 \cos^2 \theta_2}{9} - \frac{1}{5} \right) - \frac{\cos \theta_1}{9 \cos \theta_2} X_1^2 \sin(\theta_1 + 2\theta_2) \right]$$

$$M_{24} = \left(\frac{2\pi}{\lambda}\right)^2 \frac{R_o^2}{v} \frac{X_1^2 X_2^2}{9 \cos \theta_1} [-\sin(2\theta_1 + 2\theta_2) - \cos \theta_2 \sin \theta_2 - \sin \theta_1 \cos \theta_1 \sin^2 \theta_2]$$

$$M_{34} = \left(\frac{2\pi}{\lambda}\right)^2 R_o^2 \frac{X_1^2 X_2^2}{3} \left[\frac{\cos \theta_1 \sin \theta_2^2}{3 \cos \theta_2} + \frac{\cos \theta_2 \sin \theta_1^2}{3 \cos \theta_1} + \sin \theta_1 \sin \theta_2 - \frac{2 \cos \theta_1 \cos \theta_2}{3} \right]$$

Classical Adjoint Matrix M

$$\tilde{M}_{11} = \left(\frac{2\pi}{\lambda}\right)^6 \frac{R_o^6}{v^2} \frac{X_1^2 X_2^4}{3^4 \cos \theta_2} \left[\frac{4}{5} X_2^2 + X_1^2 \right]$$

$$\tilde{M}_{22} = \left(\frac{2\pi}{\lambda}\right)^6 R_o^4 \frac{X_1^2 X_2^2}{3^4} \left[\frac{X_2^4}{5} + X_1^2 X_2^2 + \frac{X_1^4}{5} \right]$$

$$\tilde{M}_{33} = \frac{\tilde{M}_{22}}{v^2} \sin^2 \theta_2$$

$$\tilde{M}_{44} = \left(\frac{2\pi}{\lambda}\right)^6 R_o^4 \frac{1}{3^5 \times 5} \frac{\cos^2 \theta_1}{\cos \theta_2} X_1^2 X_2^2 \left[X_2^4 + \frac{4}{5} X_1^2 X_2^2 + X_1^4 \right]$$

$$\tilde{M}_{12} = \left(\frac{2\pi}{\lambda}\right)^6 \frac{R_o^5}{v} \frac{X_1^2 X_2^4}{3^4} \left[\frac{2}{5} X_2^2 + X_1^2 \right]$$

$$\tilde{M}_{13} = -\frac{\tilde{M}_{12}}{v} 12 \sin \theta_2$$

$$\tilde{M}_{23} = -\frac{\tilde{M}_{22}}{v} \sin \theta_2$$

$$\begin{aligned} \tilde{M}_{14} = & -\left(\frac{2\pi}{\lambda}\right)^6 \frac{R_o^5}{v^2} \frac{X_1^2 X_2^2}{3^5 \times 5} [2\cos\theta_2(3\cos\theta_1\sin\theta_2 + 2\cos\theta_2\sin\theta_1)X_2^4 + \\ & + \frac{\cos^2\theta_1(25\cos\theta_1\sin\theta_2 + 44\cos\theta_2\sin\theta_1)}{5\cos\theta_2} X_1^2 X_2^2 \\ & + \frac{11\cos\theta_1^4 \sin\theta_1 X_1^4}{\cos\theta_2^2}] \end{aligned}$$

$$\begin{aligned} \tilde{M}_{24} = & -\left(\frac{2\pi}{\lambda}\right)^6 \frac{R_o^4}{v} \frac{X_1^2 X_2^4}{3^5 \times 5} \{ \cos\theta_2^3(3\cos\theta_1\sin\theta_2 + 2\cos\theta_2\sin\theta_1)X_2^4 \\ & + \frac{\cos\theta_1^2 \cos\theta_2(25\cos\theta_1\sin\theta_2 + 22\cos\theta_2\sin\theta_1)}{5} X_1^2 X_2^2 \\ & - \frac{\cos\theta_1^4(\cos\theta_1\sin\theta_2 - 9\cos\theta_2\sin\theta_1)}{\cos\theta_2} X_1^4 \} \end{aligned}$$

$$\tilde{M}_{34} = -\tilde{M}_{24} \sin\theta_2$$

Inverse Matrix: We only present explicitly the diagonal elements.

$$(M^{-1})_{11} = \left(\frac{\lambda}{2\pi}\right)^2 \frac{3^2 \cdot 5}{X_{c1}} \left[1 - \frac{X_{2c}^4}{X_{1c}^4 + \frac{4}{5}X_{1c}^2 X_{2c}^2 + X_{2c}^4} \right]$$

$$(M^{-1})_{22} = \left(\frac{\lambda}{2\pi}\right)^2 \frac{v^2}{R_o^2} \frac{3^2 \cdot 5 \cos^2\theta_2}{\cos^2\theta_1} \frac{1}{X_1^2 X_2^2} \left[1 - \frac{4}{5} \frac{1 - X^2}{4} p_{eqc} \right] \frac{1 + \frac{4}{5} X^2 p_{eqc}}{p_{eqc}}$$

$$(M_{33})^{-1} = \frac{(M^{-1})_{22}}{v^2} \sin^2 \theta_2$$

$$(M^{-1})_{44} = \left(\frac{\lambda}{2\pi}\right)^2 \frac{3}{x_1^2}$$

where

$$x_{peq_c}^2 = \frac{1}{\frac{1}{x_{1c}^2} + \frac{1}{x_{2c}^2}}$$

Determinant of M:

$$\text{Det } M = \left(\frac{2\pi}{\lambda}\right)^8 \frac{R_o^6}{v^2} \frac{1}{3^{6.5}} \frac{\cos^2 \theta_1}{\cos^2 \theta_2} x_1^4 x_2^4 [x_{c_1}^4 + \frac{4}{5} x_{c_1}^2 x_{c_2}^2 + x_{c_2}^4]$$

BIOGRAPHICAL NOTE

José Manuel Fonseca de Moura was born in Beira, Mozambique, on January 9, 1946.

He attended the Instituto Superior Técnico, Universidade Técnica de Lisboa, from 1963 to 1969, where he received the degree of "Engenheiro Electrotécnico" (Electrical Engineer) in April /1970. From March to May/1969, and from July/1969 to August/1970, he held a research assistantship at Centro de Estudos de Electrónica, Comissão de Estudos de Energia Nuclear. On February/1970 he joined, as an instructor, the Electrical Engineering Department of Instituto Superior Técnico, where he taught Digital Systems theory and was in charge of a Telecommunications Laboratory course.

He entered M.I.T. Graduate School in September/1970, with a scholarship of Instituto de Alta Cultura, and will be returning, upon graduation, to Instituto Superior Técnico and Centro de Estudos de Electrónica, Lisboa, Portugal.

He is a member of Sigma X₁, AAAS and student member of IEEE.